



HAL
open science

Dynamics of hybrid rod-like viruses and spherical gold nanoparticles self-assemblies : from matchstick-like particles to colloidal stars

Arantza Zavala Martinez

► **To cite this version:**

Arantza Zavala Martinez. Dynamics of hybrid rod-like viruses and spherical gold nanoparticles self-assemblies : from matchstick-like particles to colloidal stars. Physics [physics]. Université de Bordeaux, 2022. English. NNT : 2022BORD0177 . tel-04587103

HAL Id: tel-04587103

<https://theses.hal.science/tel-04587103>

Submitted on 24 May 2024

HAL is a multi-disciplinary open access archive for the deposit and dissemination of scientific research documents, whether they are published or not. The documents may come from teaching and research institutions in France or abroad, or from public or private research centers.

L'archive ouverte pluridisciplinaire **HAL**, est destinée au dépôt et à la diffusion de documents scientifiques de niveau recherche, publiés ou non, émanant des établissements d'enseignement et de recherche français ou étrangers, des laboratoires publics ou privés.

THÈSE PRÉSENTÉE POUR OBTENIR LE GRADE DE
DOCTEUR DE L'UNIVERSITÉ DE BORDEAUX

ÉCOLE DOCTORALE DES SCIENCES PHYSIQUES ET DE L'INGÉNIEUR
SPECIALITÉ: LASERS, MATIÈRE ET NANOSCIENCES

Par Arantza Berenice ZAVALA-MARTINEZ

**Dynamics of hybrid rod-like viruses and spherical gold
nanoparticles self-assemblies: from matchstick-like
particles to colloidal stars**

Sous la direction de: **Eric GRELET**

Soutenue le 23 Mai 2022

Membres du jury :

M. Luis M. LIZ-MARZÁN	Directeur de Recherche	CIC biomaGUNE	Rapporteur
M. Eric FREYSSINGEAS	Maître de conférences	ENS de Lyon	Rapporteur
Mme. Laurence RAMOS	Directrice de Recherche	CNRS	Examinatrice
M. Olivier SANDRE	Directeur de Recherche	CNRS	Examineur
M. Alois WÜRGER	Professeur	Université de Bordeaux	Examineur
Mme. Cécile ZAKRI	Professeure	Université de Bordeaux	Examinatrice
M. Eric GRELET	Directeur de Recherche	CNRS	Directeur de Thèse

Présidente du jury : Mme. Cécile ZAKRI

Acknowledgments

I would like to express sincere gratitude to the following people who have helped me in many ways to undertake this research project.

First, thanks to my supervisor, Eric Grelet, who has always shown interest and participation in my work. For your kind support, encouragement, and patience in the tough moments, I really thank you.

I sincerely thank my thesis committee Luis M. Liz-Marzán, Eric Freyssingéas, Laurence Ramos, Olivier Sandre, Alois Würger and Cécile Zakri for your time evaluating my research and for your feedback. It was very pleasant to have a discussion with all of you.

I would like to thank all people at CRPP who were there at every step: administrative staff, IT team, permanent and non-permanent. A special thanks to the ones who actively participated in this research: Thomas Beneyton, Lionel Buisson, Nicolas Mano and Claire Stines. Thank you for your assistance and guidance in your expertise. I learned a lot from you and I really appreciate that you helped me when I needed it.

Thanks should also go to my teammates. Andrii and Hanna, thank you for teaching me how to do everything in the lab and for letting me continue a bit of both your projects. Lachlan, thank you for showing me that friendship is possible no matter where we come from or the language we speak. Henri and Eloise thank you for welcoming me and showing me good food and French traditions.

Furthermore, I would like to thank all my friends at CRPP who have been part of this journey. Thank you, Flavia, Ale, Fer, Rajam, Simone, Fred, David, Etienne, Sarah, Nathan, Wael, Tatjana and Gabi for making my everyday life abroad really pleasant.

Lastly, I would like to thank the support received from my family and friends in Mexico.

Agradezco al arquitecto Antonio Vilchis López quien, a través de la Fundación de la Universidad Veracruzana, me brindó su apoyo para llevar a cabo mi doctorado en el extranjero.

Agradezco a mi familia, especialmente a mis abuelos, mis padres y hermano, quienes siempre han sido mi mayor soporte para superarme y seguir con mis sueños y metas. Agradezco que me hayan hecho sentir en casa a pesar de estar del otro lado del mundo. Familia, los amo y les dedico todos mis logros.

Mi sincero agradecimiento a mi novio, Jorge Arroyo, quien ha sido uno de mis pilares más fuertes en este tiempo. Gracias por echarme porras y ayudarme a tomar fuerzas para seguir en cada momento de debilidad que tuve. Sólo puedo amarte más por eso. Gracias.

Résumé

Dans cette thèse, nous étudions la diffusion d'auto-assemblages hybrides à base des virus en forme de filament et des nanoparticules d'or. Dans ce but, nous utilisons des bactériophages qui ont été génétiquement modifiés afin de posséder des groupements cystéines exposés à leur extrémité proximale. La présence des ponts disulfure à l'une de leurs pointes leur permet ainsi de se lier aux nanoparticules métalliques par une liaison covalente de coordination. La morphologie des différents colloïdes hybrides formés dépend de l'excès molaire initial entre virus et nanoparticules. Lorsque les deux éléments sont placés dans la même proportion, leur interaction conduit à la formation de particules en forme d'allumettes («matchstick-like») qui consiste en un virus de 1 μm long attaché par sa pointe à une seule nanoparticule d'or. Cependant, si les virus sont en grand excès, cela se traduit par la formation de structures colloïdales en étoile («colloidal stars») formées par plusieurs virus attachés à une seule nanoparticule d'or.

La dynamique brownienne de ces structures en régime dilué et dense a été étudiée par diffusion dynamique de la lumière et par suivi temporel des particules individuelles en microscopie optique. L'un des avantages majeurs de l'utilisation combinée de ces deux techniques est la possibilité d'étudier séparément les différents éléments qui composent les colloïdes hybrides. Plus précisément, la forte diffusion de la lumière associée aux nanoparticules d'or permet la détermination des propriétés dynamiques de la structure en observant principalement la nanoparticule liée, alors que le marquage du virus avec des colorants fluorescents permet la mesure de leurs coefficients de diffusion par microscopie optique.

Nos résultats sur la diffusion des particules «matchstick-like» en fonction de la taille des nanoparticules soulignent la flexibilité de la liaison virus-nanoparticule. Étant donné que ces structures sont intrinsèquement asymétriques, nous avons aussi évalué la possibilité d'induire une autopropulsion par effet thermophorétique afin d'obtenir des colloïdes hybrides actifs.

Nous avons également étudié quantitativement l'auto-organisation et la diffusion des «colloidal stars» en fonction de leur fraction volumique. Lorsque la concentration augmente, on observe un arrêt progressif de leur dynamique liée à l'interdigitation des virus qui suggère un état vitreux en régime dense.

Dans la dernière partie de cette thèse, nous formulons de nouveaux mutants de bactériophages qui ont la propriété de se lier à des nanoparticules métalliques aux deux extrémités. Ceci conduit au développement de nouvelles superstructures hybrides avec un

design plus versatile.

Mots clés: Diffusion dynamique de lumière, bactériophage filamenteux, auto-assemblage, nanoparticule d'or, colloïdes hybrides, état vitreux, auto-assemblage, diffusion, auto-propulsion

Abstract

In this thesis, we report on the study of the self-diffusion of hybrid gold-virus self-assemblies formed by spherical gold nanoparticles and rod-like viruses. For this purpose, we use genetically modified mutants of filamentous bacteriophages which possess cysteine residues exposed at their proximal end. The presence of the resulting disulfide bridges allows them to bind to metal nanoparticles by one of their tips forming a weak covalent bond. The control of the resulting self-assembled structures is achieved by tuning the molar excess of viruses with respect to nanoparticles. When both components are set in similar proportion, their interaction leads to the formation of *matchstick-like* particles composed by a 1 μm long virus attached by its tip to a single gold nanobead. However, if the viruses are in big excess, the resulting structures are *colloidal stars* formed by multiple viruses attached to a single gold nanobead.

The Brownian dynamics of these structures is characterized in dilute and dense regimes both by Dynamic Light Scattering (DLS) and single particle tracking using optical microscopy. An advantage of using both techniques resides in the possibility to study separately the different components forming the hybrid particles. Specifically, the high scattering signal coming from the gold nanoparticle facilitates the determination of the dynamic properties of the structure by observing mostly the bound bead, whereas the labeling with fluorescent dyes allows the direct determination of the virus diffusion coefficient by fluorescence microscopy.

Our findings on the self-diffusion of the matchstick-like particles as a function of the nanoparticle size evidence the flexibility of the virus-bead link. Considering the intrinsic asymmetry of the matchstick-like structure, the possibility to induce self-propulsion by self-thermophoresis has been investigated in order to get active hybrid particles overcoming their Brownian motion.

We quantitatively study the self-organization and diffusion of the colloidal stars as a function of the volume fraction. When the particle concentration increases, a progressive dynamical arrest related to the interdigitation of the star viral arms is observed suggesting a glassy state in the dense regime.

In the last part of this thesis, we construct optimized new mutants of filamentous bacteriophages which are engineered to bind metal nanoparticles to both tips. This results in the development of novel hybrid superstructures with more versatile design.

Keywords: Dynamic light scattering, filamentous bacteriophage, self-assembly, gold nanoparticles, hybrid colloids, glassy state

Contents

Résumé	iii
Abstract	v
1 General Introduction	1
1.1 Colloids	2
1.1.1 Phase diagram of ideal colloidal spheres and rods	3
1.2 Hybrid Colloids	5
1.2.1 Potential Applications	5
1.3 Outline of the thesis	7
2 Design of bacteriophage based hybrid colloids	9
2.1 Phage display for the production of hybrid colloids	10
2.2 Genetic engineering of M13KE bacteriophages	13
2.2.1 Mutants with gold binding affinity	14
2.2.2 Virus production	17
2.3 Production of gold-virus colloids	20
2.3.1 Colloidal star particles	24
2.3.2 Matchstick-like particles	26
2.3.3 Dumbbell-like particles	30
2.4 Conclusion and perspectives	35
3 Experimental techniques	37
3.1 Study of colloidal systems	38
3.2 Single particle tracking	38
3.2.1 Optical microscopy observation	39
3.2.2 Mean square displacement analysis	43
3.3 Dynamic light scattering principles	47
3.3.1 Spectral distributions of molecules of arbitrary shape	48
3.3.2 Dynamic light scattering experiment of isotropic particles	53
3.3.3 Intensity correlation function of rod-like particles	55
3.3.4 Diffusion coefficients from Intensity correlation function	57

Appendix I. CONTIN analysis details	63
4 Dynamics of matchstick-like and dumbbell-like particles	67
4.1 Hybrid gold-virus colloids	68
4.2 Dynamic light scattering of gold-virus systems	69
4.2.1 Rod-like viruses: M13C7C strain	69
4.2.2 Spherical gold nanoparticles (Au NPs)	74
4.2.3 Mixture of Au NPs and rod-shaped viruses	76
4.3 Diffusion of matchstick-like particles	78
4.3.1 Diffusion coefficient considering a flexible link	81
4.3.2 Nanoparticle size and concentration dependence	84
4.4 Diffusion of dumbbell-like particles	86
4.5 Discussion and conclusions	88
Appendix I. DLS analysis of other matchstick-like particles	90
Matchstick-like made of Au NPs of $D = 10$ nm	90
Matchstick-like made of Au NPs of $D = 18$ nm	94
Matchstick-like made of Au NPs of $D = 31$ nm	97
5 Towards the self-propulsion of hybrid colloidal particles	103
5.1 Artificial active particles at colloidal scale	104
5.1.2 Designing artificially self-propelled particles	104
5.2 Brownian motion versus Active Brownian motion	107
5.3 Hot Brownian motion	109
5.3.2 Experimental setup	111
5.4 Diffusion of Janus Au-Silica particles	112
5.5 Heat induced motion of matchstick-like particles	117
5.5.2 Effect of convention in the intensity correlation function	118
5.6 Discussion and conclusions	121
6 Colloidal stars as model system of soft spheres	123
6.1 Soft colloidal particles	124
6.1.2 Phase diagram of soft colloids	124
6.2 Dynamics and structure of colloidal star particles	127
6.2.1 Dilute regime	129
6.2.2 Dense regime	133
6.3 Discussion and conclusions	140
7 General conclusions and perspectives	143

Chapter 1

General Introduction

1.1	Colloids	2
1.1.1	Phase diagram of ideal colloidal spheres and rods	3
1.2	Hybrid Colloids	5
1.2.1	Potential Applications	5
1.3	Outline of the thesis	7

1.1 Colloids

The term “colloid” was first used by Thomas Graham in 1861 [1] to describe a particular substance characterized by little or no tendency to diffuse through membranes. These *colloidal particles* remain on the membrane simply because of their linear dimension. In the modern science, the term colloid is usually applied to the combinations of particles or droplets within the size range from 10 nm to 10 μm dispersed in a continuous phase or *dispersion medium* [2]. As shown in figure 1.1, many organic, inorganic and biological systems correspond to the colloidal scale.

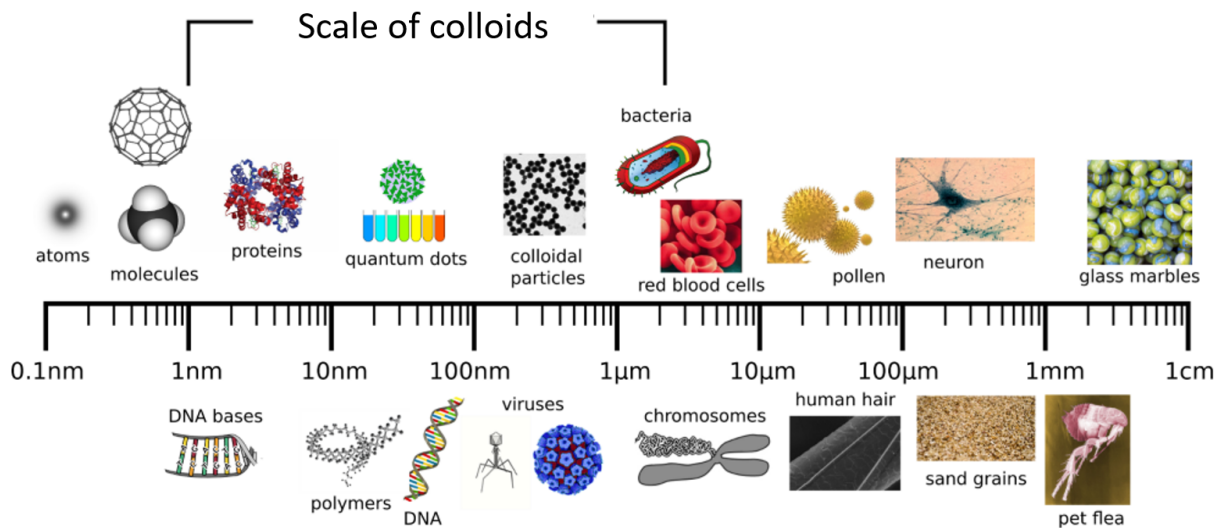


Figure 1.1: **Colloidal length scale.** Graphical comparison of the colloidal scales with atomic and macroscopic ones. Image was taken from reference [3]

A characteristic of colloidal particles immersed in a fluid is their irregular random walk due to the collision between molecules of the surroundings and the particle itself. Such an effect, known as Brownian motion, is named after the Scottish botanist Robert Brown who firstly observed the erratic movement of pollen grains in water [4]. The theoretical explanation of this motion was derived in 1905 by Albert Einstein [5]. He showed that the translational and rotational diffusion coefficients of a spherical particle of radius r are given by

$$D_T = \frac{k_B T}{6\pi\eta r} \quad \text{and} \quad D_R = \frac{k_B T}{8\pi\eta r^3}, \quad (1.1)$$

with k_B the Boltzmann constant, T the temperature and η the solvent viscosity. Jean Perrin [6], awarded by the Nobel Prize in Physics in 1926, proved these theoretical predictions by measuring the Avogadro’s number via the mean square displacement of colloidal particles observed with optical microscopy. The works of Einstein and Perrin show that colloids are subject of thermal motions and behave similarly to small molecules or atoms which obey the same laws of statistical physics. Thus, combined with the fact that their dimensions allow

for visualizing them via optical microscopy, colloids provide a suitable mean to investigate the link between the properties of a system from the behavior of their single components.

Another important feature of colloids is their ability to self-assemble, i.e., to spontaneously form organized structures. Isolated colloidal particles move freely in suspension but, for a given particle concentration, they start to interact with each other through a combination of forces such as electrostatic and van der Waals [7]. The control of the potential interaction between colloidal particles can be achieved by varying conditions of the dispersion medium or particle surface. For instance, colloidal particles which are charged due to the ionization of their surface molecules repel each other when they are in suspension. However, by increasing the concentration of salts the strength of their repulsion is decreased. These tuneable interactions between colloidal particles lead to their self-organization into a variety of phases or states of matter.

1.1.1 Phase diagram of ideal colloidal spheres and rods

A “phase diagram” summarizes the phases that a colloidal suspension could experience function of the key parameter that influences their organization such as temperature or concentration.

The hard-core interaction of monodisperse colloidal spheres results in the simplest phase diagram. These *hard spheres* interact only through an infinite repulsion on contact, but otherwise they do not have any interaction. As result of this potential, the internal energy is zero and then, the phase behavior is driven only by entropy. For this type of systems, the observed phases depend only on the particle shape and volume fraction, ϕ , and are independent of temperature. Synthetic spherical particles have a charged surface and

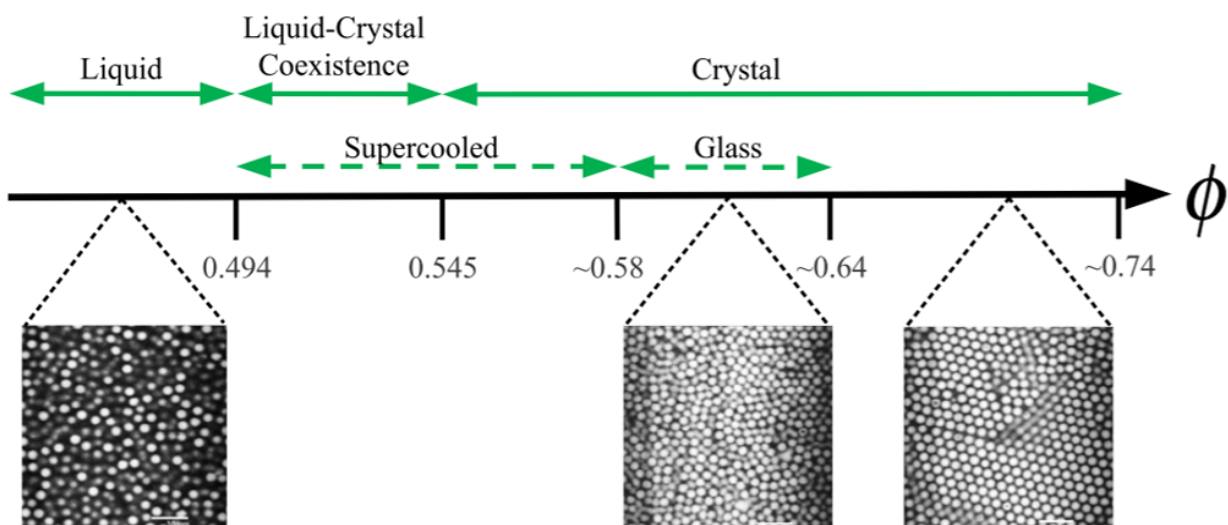


Figure 1.2: **Hard spheres phase diagram.** Top: As function of ϕ , the solid arrows indicate equilibrium phases, whereas dashed ones the non-equilibrium states. Bottom: confocal microscopy images of the analogous phase in a colloidal suspension with 5% polydispersity. Image was taken from reference [8].

polydispersity which affect the liquid-crystal coexistence volume fraction concentration and glass formation [8]. In order to suppress the van der Waals attraction and long range electrostatic repulsion so they behave approximately as hard spheres, nanoparticles made of polymer or from inorganic material such as silica are dispersed in a high ionic strength, index matched, polar solvent. As shown in figure 1.2, the phase diagram of hard spheres, exhibits liquid, liquid-crystal coexistence, crystal and glass states by increasing the particle concentration.

Introducing shape anisotropy in the particle system with hard-core interaction results in novel phases since anisotropic particles have not only the positional order but also orientation one. For instance, compared with spherical particles, rod-shaped ones exhibit liquid crystalline phases such as the *nematic* and *smectic* by increasing concentration. Well-defined rod-shaped colloids of a variety of materials such as silica, iron hydroxide or polymer have shown to form these crystalline phases in equilibrium [9–11]. Bio-organic materials such as *fd*-viruses also exhibit the *columnar* phase [12] (see figure 1.3).

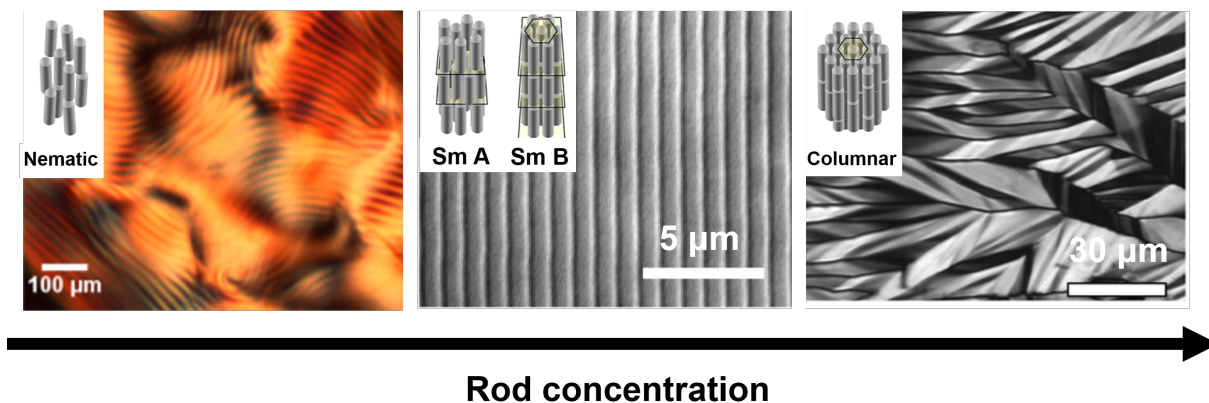


Figure 1.3: **Liquid crystalline phases formed by *fd*-virus suspensions.** **Left:** Chiral nematic phase for which the particles are orientationally ordered but positionally disordered [13]. **Middle:** Smectic A (Sm A) which has liquid-like order within the layers and Smectic B (Sm B) which in turns are organized in a hexagonal positional order [14]. **Right:** Columnar phase for which the rod-like viruses are organized into liquid-like hexagonal lattices [12].

When we consider that a simple modification in the shape of colloidal particles with specific interaction display a richer phase behavior one question is raised: can we selectively drive their self-assembly into a specific organization or structure? By varying either the shape, surface chemistry or introducing highly selective interactions, colloidal particles have been used to assemble into complex architectures which could lead to original material properties. In this way, we start to think of colloids as building blocks or “Lego” for the creation of novel materials with desirable functionalities.

1.2 Hybrid Colloids

When two or more colloidal particles of different origin are combined into a single *hybrid* nanoparticle a route is opened towards engineering nanomaterials of enhanced properties with applications in fields such as photonics [15], bio-medicine [16] and nanotechnology [17]. The fabrication of original hybrid architectures requires developing suitable colloidal building blocks. The synthesis techniques of inorganic nanoparticles are pioneers towards controlling the shape and size of the resulting structures.

Metal nanoparticles, specifically made of gold, have proven to be promising multi-functional templates because of their large surface bio conjugation chemistry and optical properties which are influenced by their shape and size [18–20]. For example, Au NPs which possess high extinction coefficient, i.e., the ability to strongly absorb light at a given wavelength, are visible at lower concentrations when compared with organic materials. Moreover, large Au NPs strongly scatter light [20]. Since this is in the visible spectrum, it is possible to follow the position of individual nanoparticles by means of optical microscopy techniques such as Dark field whose implementation relies on the scattering coming from the particles. Furthermore, when AuNPs are irradiated at the plasmonic resonance, they absorb electromagnetic radiation and convert it into thermal energy [21].

As shown in figure 1.4, Au NPs have been synthesized in a wide range of sizes and shapes. The typical properties of each vary with the size, shape and metal structure [22]. For instance, suspensions of spherical Au NPs change from an intense red color to purple as the particle size increases [18]. The chemical nature of their stabilizing ligands allows their conjugation with different materials such as silica [23], polymers [24, 25], antibodies [18], filamentous viruses [26, 27], etc. The strategy for the design of hybrid colloids using Au NPs requires to consider the applications of the resulting material. In this thesis we investigate hybrid colloids composed by spherical gold nanoparticles and rod-shaped viruses. The study of the structural and dynamic properties of these assemblies is essential to control and predict their collective behavior.

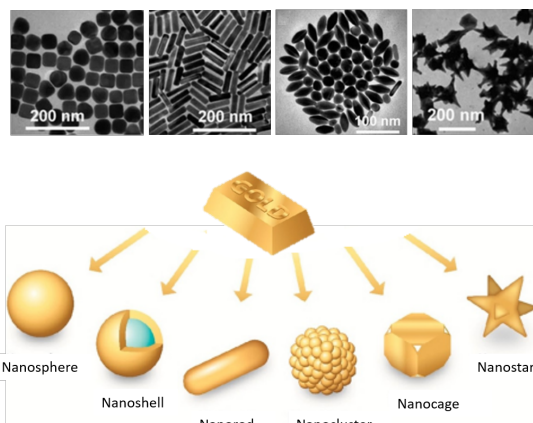


Figure 1.4: **Gold nanoparticles.** Transmission electron microscopy image and scheme of different shapes. Image was adapted from reference [21]

1.2.1 Potential Applications

Significant advances in the fabrication of hybrid colloids have been made in recent years [28, 29]. The combination of different inorganic and organic materials has resulted in a wide range

of shapes and compositions, such as hybrid polymer-NP hydrogels [30], nanofibers made of magnetic NPs and polymer [31], nanoparticle lattices linked by DNA [32], etc. The novel optical and electronic properties of these assemblies are particularly attractive for their use in different fields. Here, we provide a brief overview of the potential applications of hybrid materials.

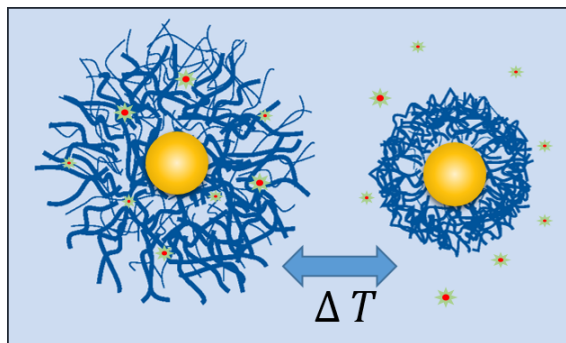


Figure 1.5: **Sketch of a microgel hybrid particle.** The drug is released from the swollen microgel under the right temperature stimuli.

Drug delivery

Drug delivery has attracted much attention not only in basic science but also in clinical medicine [33, 34]. In an ideal case, the drug is released selectively at the location of the targets. One way to achieve selective drug delivery is stimulus-responsive drug release. Stimuli that are specific at target sites may include low pH, high levels of certain enzymes, and externally applied physical signals such as temperature, light, magnetic field and ultrasound.

For such a job, many “smart” materials, i.e., the ones that respond and adapt to changes in their environments, have been developed. Au NPs and polymer have shown to be promising building blocks for the assembly of thermo-responsive microgels which could function as drug delivery systems [35, 36]. Microgels are composed of a cross-linked polymer network of colloidal size that is swollen for given conditions. As shown in figure 1.5, for hybrid gold-polymer microgels consisting of a core Au NP covered by a uniform polymer shell, the right stimuli induce its collapse and then to release of the contained drug.

Imaging

Optical and magnetic resonance based imaging techniques allow clinicians to obtain relevant information for patient diagnosis and treatment [38]. Thanks to their intrinsic properties, metallic nanoparticles are good candidates as contrast agents to improve the resolution, scanning times, and quality of data that can be obtained [39].

Hybrid materials made of filamentous viruses and iron-oxide nanoparticles have been used for this purpose [37]. As shown in figure 1.6, their assembly results in a hybrid rod-like structure.

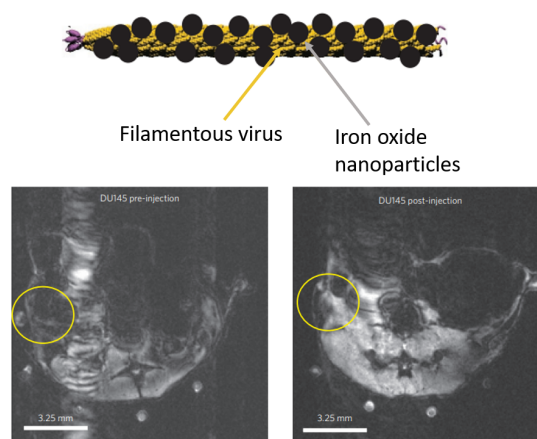


Figure 1.6: **Hybrid virus and iron oxide assemblies.** Virus capped with iron oxide nanoparticles (top) have shown to improve magnetic resonance images (bottom) used for tumor detection [37].

Thanks to the virus capability to display ligands (by phage display) which bind target molecules, these hybrid materials can be placed in the location of a tumor. In this way, they have shown to improve the contrast of magnetic resonance images (see figure 1.6).



Figure 1.7: **Colloidal nanowires.** Filamentous virus capped with cobalt manganese spinel oxides on their surface function as templates for the fabrication of battery electrodes. [40]

have shown considerable advances in this direction [27, 40]. As shown in figure 1.7, the surface modification of viruses allows for binding cobalt manganese spinel oxides. These nanowires suggest a promising route for the design of electrode structures for high capacity batteries.

Energy storage

The current increasing demand of smaller and smarter electronic devices has pushed the development and improvement of energy storage systems [41]. In this context, the development of hybrid colloids which acquire the specific characteristics of metal nanoparticles takes an important role. Compared with conventional battery materials, nanoparticles based ones offer higher ionic transport and electronic conductivity.

The work of Angela M. Belcher and coworkers in the development of nanowires which combine filamentous viruses and inorganic nanoparticles

1.3 Outline of the thesis

Due to their potential applications in many fields, our group had the research project to use Au NPs and filamentous viruses as building blocks for original hybrid colloidal architectures. The aim of this PhD thesis is therefore to investigate novel assembling routes and to characterize the dynamics and structure of the resulting morphologies.

In chapter 2, we describe our approach for the fabrication of hybrid gold-virus colloids. Our method is based in the genetic modification of the virus genome to display peptides only at the virus tips which enables to selectively graft Au NPs at *one* or *both* virus tips. Thus, we report our advances in their genetic engineering which paves the way for developing complex architectures. Furthermore, we present the main hybrid colloidal structures studied in this work: *matchstick-like particles* and *colloidal star molecules*.

We introduce in chapter 3 the experimental techniques used to characterize the dynamics and structure of our hybrid colloidal suspensions: Dynamic Light Scattering (DLS) and optical microscopy. We give a complete background on the experimental tools and principles

involved for their study and visualization. We also provide a detailed description of the methods of data analysis from which we obtain the dynamics of our systems.

In chapter 4, we report a complete DLS study on the matchstick-like morphology. We explore the influence of concentrations and nanoparticle size in the dynamics. Our results are compared with the ones obtained by single particle tracking using optical microscopy techniques. Our observations evidence the flexibility of the proteins at the virus tip.

In chapter 5, we explore the possibility to induce self-propulsion and therefore to make our hybrid particles “active” by combining the temperature gradient created when the Au NPs are excited at the plasmonic resonance and the intrinsic asymmetry of the matchstick-like structure. We present our observations in the laser induced thermophoresis for different concentrations and power intensities.

In chapter 6, we investigate the dynamics and self-organization of colloidal star molecules. We characterize briefly the phase diagram of this “soft colloidal spheres” when the particle concentration is increased. Moreover, we explore their self-assembly induced by depletion.

In the general conclusion, we summarize all the results obtained from the genetically modified phages for the design of novel hybrid colloids to the results found from their structural and dynamical study. Furthermore, we give some perspectives which include the improvements needed for the assembly of other novel architectures which might possess (even) richer properties.

Chapter 2

Design of bacteriophage based hybrid colloids

2.1	Phage display for the production of hybrid colloids	10
2.2	Genetic engineering of M13KE bacteriophages	13
2.2.1	Mutants with gold binding affinity	14
2.2.2	Virus production	17
2.3	Production of gold-virus colloids	20
2.3.1	Colloidal star particles	24
2.3.2	Matchstick-like particles	26
2.3.3	Dumbbell-like particles	30
2.4	Conclusion and perspectives	35

2.1 Phage display for the production of hybrid colloids

Filamentous phages are very stable viral particles which use bacterial cells as host for replication. They are composed of a long cylindrical protein coat, named capsid, that encapsulates its RNA or DNA (see figure 2.1 (a)) [42, 43]. In 1985, George P. Smith, awarded of the Nobel Prize in 2018, introduced the so-called phage display technique [44] in which external peptides or proteins are expressed on the outside of a phage while the genetic material encoding it resides on the inside. As shown in figure 2.1 (b), when a foreign gene fragment (gF) encoding a polypeptide is united with the coding one of the phage surface protein, the resulting fused polypeptide is displayed on the phage surface maintaining a relatively stable structure and biological activity. Since the invention of this approach, many phage display peptide and protein libraries have been developed with the aim to find a variant of interest in the library [45]. To do so, once constructed, this goes through a bio-panning selection, a process that consists in the screening and isolation of a selected variant. This procedure, represented in figure 2.1 (c), starts with the incubation of a primary library on a plate coated with a target molecule such as antibodies, enzymes or other proteins. Then, the non-binding phages are washed off and binders are eluded and amplified by infecting host bacteria. This binding/amplification process is repeated 3 to 5 times in order to enrich the pool in favor of binding sequences [46]. Finally, monoclonal phage populations are separated and characterized by DNA sequencing.

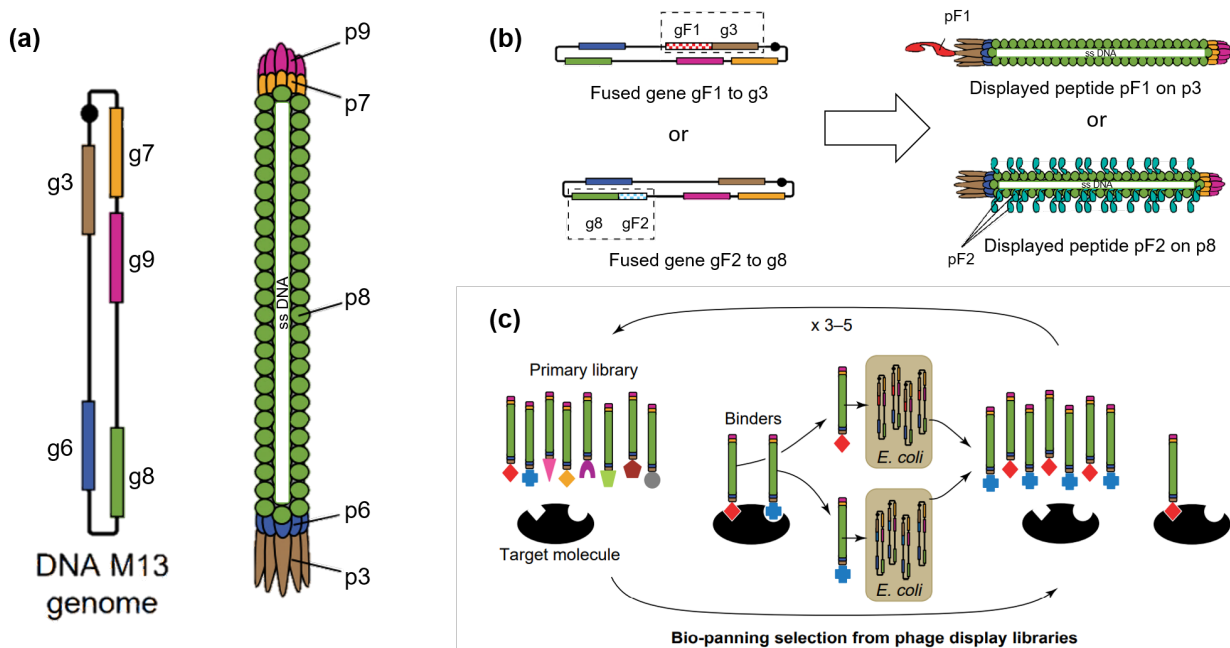


Figure 2.1: **The principle of phage display.** (a) The M13 phage genome consists of single-stranded circular DNA that carries the genes responsible to encode the five different phage coat proteins. (b) A foreign protein, pF (encoded by gene gF), can be displayed at the coat proteins p3 or p8 (encoded by genes g3 or g8) if gF is fused to g3 or g8. This gene fusion ensures that pF is linked to the coat proteins when the phage particle is assembled. (c) A target peptide is isolated by bio-panning selection from a phage display primary library. Figure was adapted from reference [46].

All coat proteins of M13 phages have been used to display peptides [47]. The minor coat protein p3, located at one of the virus tips, is the most widely used, followed by the major coat protein p8 which is at the outer surface of the phage (see figures 2.1 (a) and (b)). When these are modified to express peptides with specific material recognition or affinity by phage display, the M13 viruses can also be used as templates for the construction of hybrid colloidal particles such as the ones shown in figure 2.2. Belcher and co-workers have implemented the phage display of M13 viruses to bind inorganic nanoparticles either at the tip of the M13 phage or at its body surface [28, 48–50] (see figures 2.2 (i) and (ii)). These advances have enabled the fabrication of colloidal particles with applications in energy storage [51], imaging [37, 52] and sensing [53, 54].

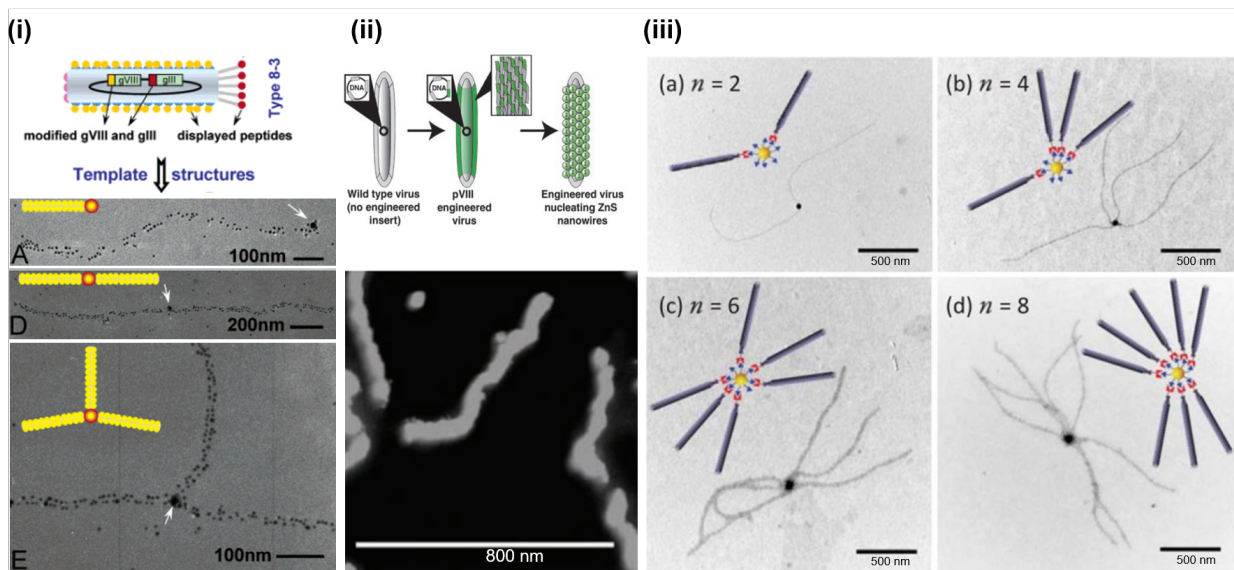


Figure 2.2: **Hybrid colloidal particles made of M13 phages.** (i) Nanoarchitectures made of gold nanoparticles bind to the virus surface and streptavidin-coated nanoparticles at one virus tip [48]. (ii) Nanowires produced by the binding of Zinc sulfide on the virus surface [50]. (iii) Multiarm self-assemblies obtained from the reaction of tip-biotinylated phages and streptavidin coated nanoparticles obtained here at the Center of Research Paul Pascal [26].

In our group the M13KE and M13C7C phages, strains of the M13 viruses, have been used to produce colloidal star molecules made of a gold (Au) core surrounded by a viral corona through the single tip binding of the phages to metal nanoparticles (NPs) [55] (see figures 2.2 (iii) and 2.3). Recent works on phage display through the p7 and p9 proteins of the M13 phages [56, 57], located at the second virus tip, have paved the way for constructing more complex structures by the genetic modification of this virus tip combined with the previously done on the p3 proteins of the other tip. As shown in figure 2.3, a single tip binding has allowed for designing structures that range from asymmetric rod-like particles made of a single Au NP at one virus tip to colloidal star particles. It is expected that having double tip binding enables the creation of more complex arrangements such as oligomeric chains or lattice structures.

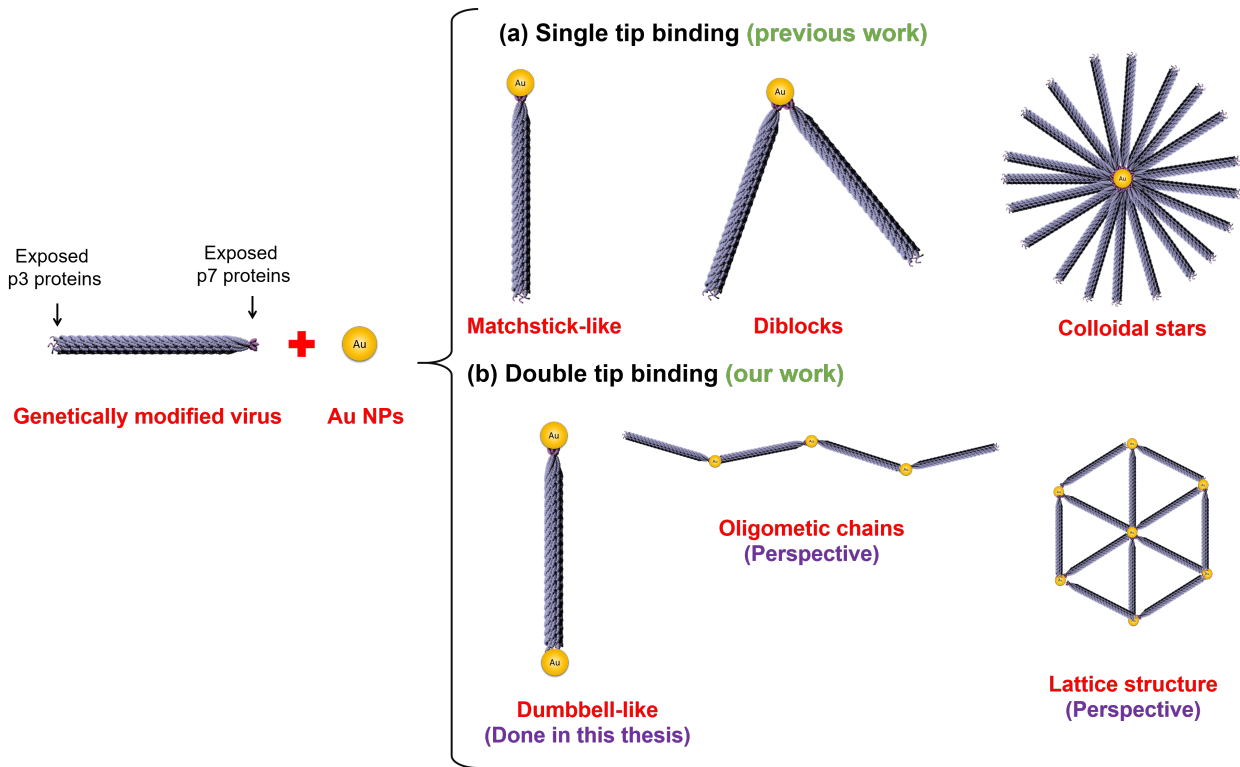


Figure 2.3: **Schematic representation of bacteriophage based hybrid colloids.** (a) The genetic modification on one virus tip paves the way for the production of different structures such as matchstick-like particles, diblocks or colloidal stars while (b) the modification on both tips allows for the formation of dumbbell-like structures, oligomeric chains or lattice-like structures.

Here we introduce the method we use to design bacteriophage based hybrid colloids. Our approach is founded on the formation of a weak covalent bond between metal NPs and disulfide bridges created by the presence of cysteine groups at the p3 proteins of that virus tip. In conjunction with the conditions that promote their interaction with metal NPs, our gold-virus hybrid colloids are formed by self-assembly. This technique is a simpler way to bind Au NPs by the virus tip than others found in literature [26, 28] which are based on the streptavidin-biotin interaction between streptavidin activated nanoparticles and chemically biotinylated viruses. Thus, we extend this concept to genetically modify the M13KE phage in order to obtain a double tip binding.

In this chapter, we present first our advances in the genetic modification done on one and both virus tips for the assembly of our hybrid gold-virus colloids. Next, we discuss the conditions to be considered for their interaction with Au NPs in order to get different architectures such as *matchstick-like* particles and colloidal stars. The second tip binding efficiency of our new mutants $M13s(CgbpC)_2$ and $M13l(CgbpC)_2$ is tested by implementing them to assemble *dumbbell-like* particles made of a single virus bound to individual Au NPs by each tip (see figure 2.3). The chapter ends with conclusions and perspectives for the future optimized production of original hybrid gold-virus colloids.

2.2 Genetic engineering of M13KE bacteriophages

Filamentous phage is a specie of bacterial viruses that specifically infects and replicates within strains of *Escherichia coli* (E.coli) containing the male sex factor in their genetic material [58, 59]. They are released from infected cells while they continue to grow and divide [60]. The virions of M13KE of about $1\ \mu\text{m}$ in length and $7\ \text{nm}$ in diameter are composed of a cylinder of five different types of coat proteins that enclose a single-stranded DNA (ssDNA) (see figure 2.4). The capsid is built from ~ 3000 copies of the major coat protein p8 and 3-5 copies of minor proteins p3, p6, p7 and p9. p3 and p6 on the proximal end and p7 and p9 on the distal end of the virus as shown in figure 2.4 [42, 61]. The main p8 protein has an α -helix structure and is composed of 50 amino acid units which provide to the surface a helical charge distribution of approximate $7\ e^-/\text{nm}$ at physiological pH [62].

The bending stiffness or persistence length P of filamentous viruses has been determined by the implementation of different methods such as force extension and dynamic light scattering [63, 64]. One of the most direct methods is the visualization of the equilibrium conformations [65] of higher accuracy compared to the electron microscopy imaging method [66] which could have drying artifacts. The M13 phage persistence length of $P = 2.2\ \mu\text{m}$ [64] indicates that they are semi-flexible rod-like particlesⁱ.

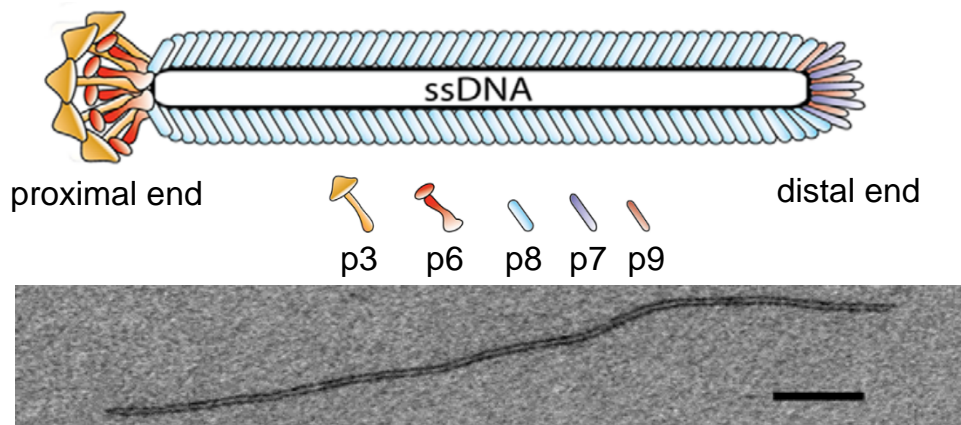


Figure 2.4: **Filamentous phage.** **Top:** Schematic representation of filamentous phage composed of ~ 3000 copies of major coat protein p8 and about 5 of the minor coat proteins p3, p6, p7 and p9. Figure was adapted from reference [56]. **Bottom:** Transmission electron microscopy image of a M13KE virus after negative staining with uranyl acetate. Scale bar represents $100\ \text{nm}$.

One of the common approaches for genetic engineering is the molecular cloning showed in figure 2.5 [68]. This procedure consists in exchanging and joining DNA between two molecules in selected cloning sites [69]. First, restriction enzymes are used to cut the DNA

ⁱIf the persistence length is large compared to its contour length, i.e. $P \gg L$ a filament appears relatively straight and is recognizable as a rigid rod, whereas for $P \ll L$, the filament adopts more flexible shapes [67].

fragments which then are fused to make a recombinant plasmid ⁱⁱ containing the target gene. This is introduced into bacterial host to undergo a transformation process in which some bacteria take up the foreign genetic material. As the plasmid typically contains an antibiotic gene, the bacteria that took it up can be selected from nutrient plates containing the antibiotic. Bacteria without the plasmid die, while the ones carrying it live and reproduce. Each surviving bacterium gives rise to a small colony which can be isolated. Finally, the DNA sequencing is extracted from selected positive clones in order to confirm the correct insertion of the target gene. In this way, a DNA fragment that encodes a desired peptide is inserted in the M13KE genome. Then, by choosing the region corresponding to the coat protein genes g3, g6, g7, g8 or g9, the fused proteins are selectively displayed on the virus capsid after the replication process. But, how do we encode a peptide with stable binding affinity for Au NP's?

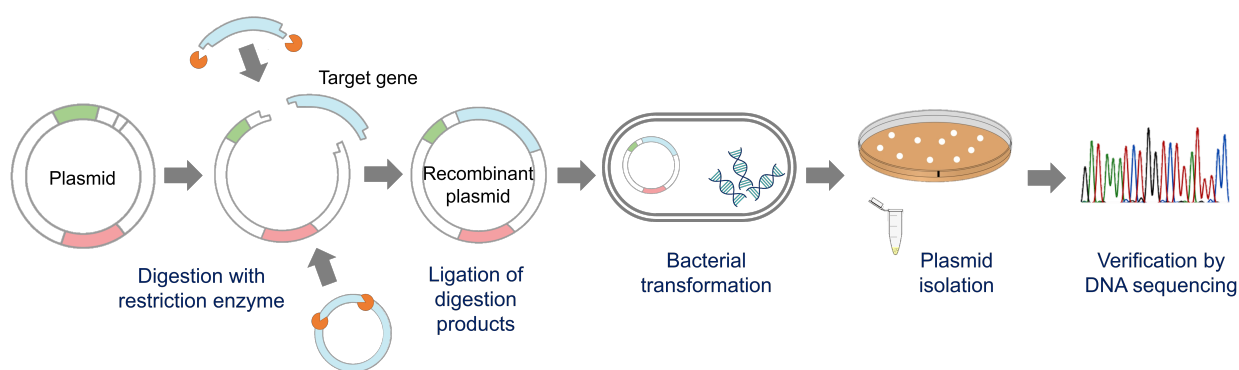


Figure 2.5: **Genetic engineering of phages.** The DNA from two different molecules is combined, one serves as a template and one contains the target genes. Restriction enzymes locate a region of interest and cut open the circular plasmids. The sticky ends of the fragments attach to each other forming recombinant plasmids. Then a transformation process is done in bacteria. The bacterium that take the foreign DNA is isolated and replicated. The DNA sequencing confirms that the target gene is properly inserted in the genome.

2.2.1 Mutants with gold binding affinity

The binding affinity of a ligand for a receptor is given by the dissociation constant K_d [71]. The lower K_d value is, the more stable is the ligand complex and thus the affinity is stronger. Thanks to the phage display technique, gold binding peptides (GBP) have been identified from libraries [72, 73]. However, their dissociation constants of about 3×10^{-6} M make them less stable than indirect methods of conjugation using a mediator between the phage and Au NPs [26, 28, 74]. For instance, the method proposed by Alexis de la Cotte et al. from our group [26] based on the streptavidin-biotin reaction, considered as the strongest non-covalent bond found in nature, exhibits a $K_d = 1 \times 10^{-15}$ M. Nevertheless, these methods require multiple steps that do not ensure the colloidal stability of the products such as the release with time of the bound streptavidin [55].

ⁱⁱPlasmids are circular DNA molecules consisting of few genes that can replicate independently [70].

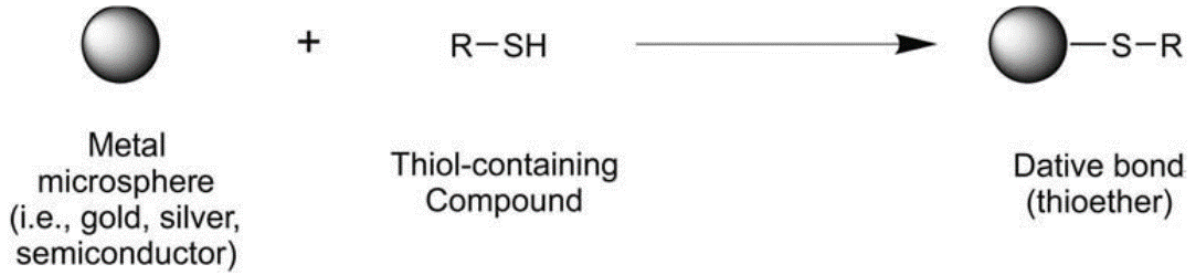


Figure 2.6: **Thiol-metal dative bond.** Dative bonds, also known as coordinate covalent bonds, are formed by two electrons coming from a single atom. The unshared pair from the sulfur atom is given to the metal atom. Image was taken from reference [75].

Here, we use a simpler method of conjugation based on dative bonds formed between the Au NPs and thiol groups (-SH). It is known that noble metals can interact with thiol-containing molecules [75–77]. As shown in figure 2.6, the unshared pair of electrons on the sulfur atom is able to form a weak covalent bond with a metal atom. This monodentate thiol-metal linkage, stronger than any non-covalent bond, is weaker than a true covalent bond. However, its strength is increased for derivatives with multiple thiol groups such as the case of disulfide bridges (S-S) [75].

The M13KE mutant possess disulfide groups formed between cysteine residues (Cys-Cys) only at the end of the p3 proteins [45, 78]. Among these disulfide bridges, only the last one is assumed to be accessible for its conjugation (see figure 2.7). Thus, we have used the M13KE phage as a template for designing mutants with single and double tip binding affinity for Au NPs. In order to increase the strength of the first tip bond as well as for its incorporation at the second virus tip, we have genetically modified the p3 and/or p7 proteins of the virus tips with disulfide constrained peptides. The design and production of different mutants have been done at the Center of Research Paul Pascal with the help of Thomas Beneyton, Geir Åge Løset and Eric Grelet. These are summarized in table 2.1 and described below.

Table 2.1: Summary of M13KE mutants with tip binding affinity for Au NPs.

Name	p3 modification	p7 modification	Type
M13C7C	✓	×	Single tip binding
M13s(<i>CgbpC</i>) ₂	✓	✓	Double tip binding
M13l(<i>CgbpC</i>) ₂	✓	✓	Double tip binding

2.2.1.1 M13C7C strain

The M13C7C is a rod-shaped bacteriophage grown from the phage display peptide library kit (New England Biolabs, Beverly MA). This is nearly identical to the M13KE except for an alteration in the minor coat protein p3 of the proximal end. The M13C7C has an additional

13 amino acids inserted before its terminal amine: GGGCXXXXXXXXCA-NH₂ where X's are seven random amino acids flanked between two cysteines, C.

As shown in figure 2.7, the M13C7C strain displays another accessible disulfide bridge compared with the M13KE phage. The presence of two disulfide bridges on the virus tip promotes their binding to Au NP. Thus, we expect that the probability of interaction increases by increasing the number of functional groups available for reaction.

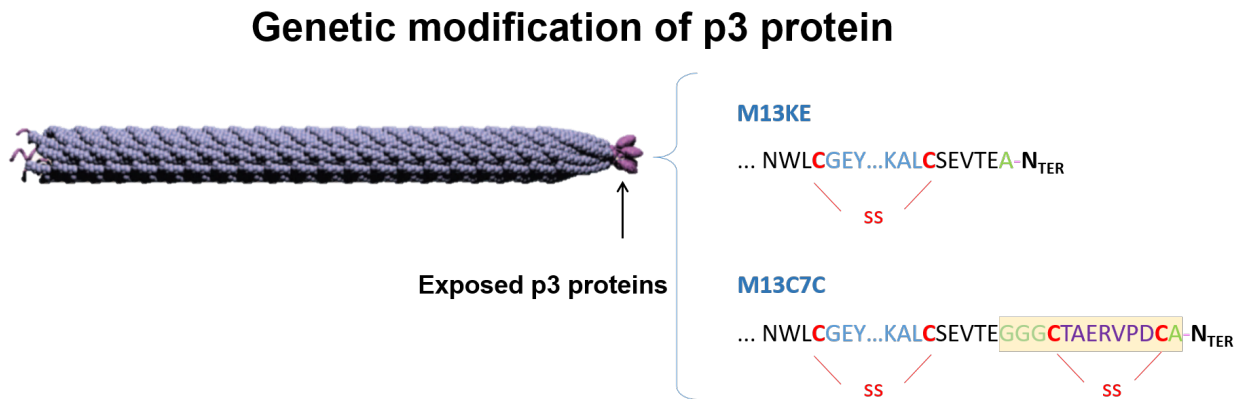


Figure 2.7: **Schematic representation of the amino acid sequence corresponding to the minor coat protein p3.** The M13KE virus possesses two cysteine groups which form a disulfide bridge while the genetically engineered M13C7C strain has an additional fused sequence (highlighted) with two other cysteine residues also linked via a disulfide bridge.

2.2.1.2 M13_s(C*gbp*C)₂ and M13_l(C*gbp*C)₂ strains

The M13_s(C*gbp*C)₂ and M13_l(C*gbp*C)₂ are two mutants genetically modified on the p3 and p7 proteins of the virus tips. These mutants have an inserted gold binding peptide (*gbp*) [73] between two cysteine groups: CGTGSQASC (C*gbp*C), that forms a disulfide bridge at both virus tips.

As shown in figure 2.1, the coat proteins of the distal end (p7) of the M13KE virus are not as exposed as the ones of the proximal end (p3) [42]. For this reason, the p7 proteins exhibit an extra spacer in order to make the disulfide bridge more accessible for their interaction with Au NPs. On one hand, for the M13_s(C*gbp*C)₂ strain we have inserted as a short spacer (*s*) the FLAG1, developed as a small hydrophilic peptide, consisting of only eight amino acids: DYKDDDDK [79]. On the other hand, the FLAG3 peptide: DYKDHDGDYKDHDIDYKDDDDK, developed with a strong net negative charge and a low pI [80], has been added as a long spacer (*l*) in the M13_l(C*gbp*C)₂ mutant. A schematic representation of the amino acid sequence for both tips of these strains is shown in figure 2.8. The role of the negative charge carried by the FLAG1 and FLAG3 spacers is to separate the C*gbp*C from the main virus body which also has negative charge.

The efficiency of the *s* and *l* modification done at the p7 proteins of these mutants is tested in subsection 2.3.3 by comparing their tip reactivity with Au NPs in similar conditions.

Genetic modification of p7 and p3 proteins

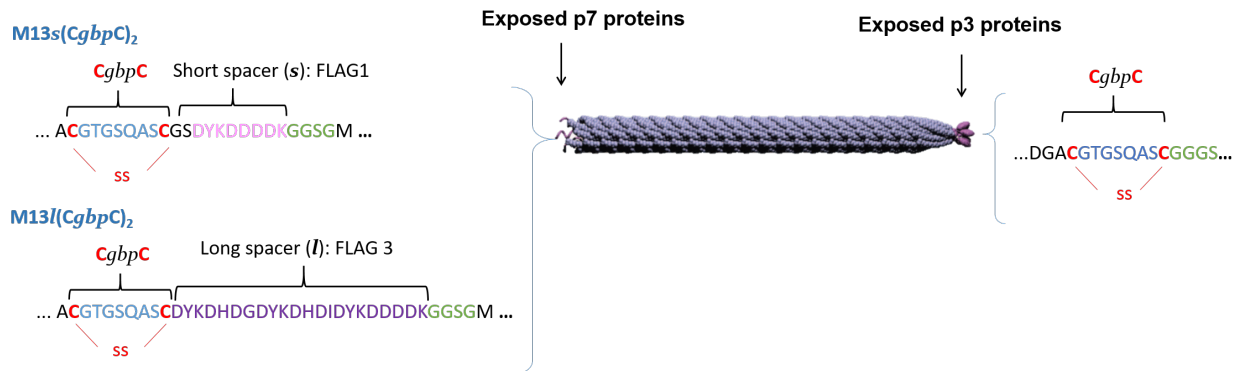


Figure 2.8: **Schematic representation of the amino acids sequence of the exposed p3 and p7 proteins.** Both $M13s(CgbpC)_2$ and $M13l(CgbpC)_2$ have an inserted gold binding peptide (*gbp*) between two cysteine groups (C) that form a disulfide bridge at both virus tips. Since the p7 proteins are more buried than the p3 ones, a short or long spacer (*s* or *l*) is added at the p7 end in order to make more accessible the disulfide bridge for its interaction with Au NPs.

2.2.2 Virus production

The infection of *E. coli* is specifically mediated by the coat protein p3 of the phage which is located at one end of the phage particle. It interacts with the protein membrane of the bacteria allowing for the introduction of the phage ssDNA into the bacterial cytoplasm [82]. As shown in figure 2.9, the viral DNA is immediately converted into a double-stranded (ds) which will transcribe and replicate resulting in a pool of dsDNA molecules [81, 83].

For the production of all the viruses described in the previous subsection, we have used Lysogeny Broth (LB) as growth medium and *E. coli* ER2738, a strain sensitive to the male-specific bacteriophage that expresses resistance to the antibiotic tetracycline. A schematic representation of this procedure is shown in figure 2.10.

First, the bacteria is pre-amplified. We start by preparing a Petri dish with the *E. coli* ER2738. After its growth overnight at 37° C, we place an isolated colony of bacteria in 3 ml of LB media and incubate it for 5-8 hours at 230 rpm and 37° C. Then, the whole content is used to infect another 100 ml of LB media containing 2×10^{-2} mM of tetracycline which

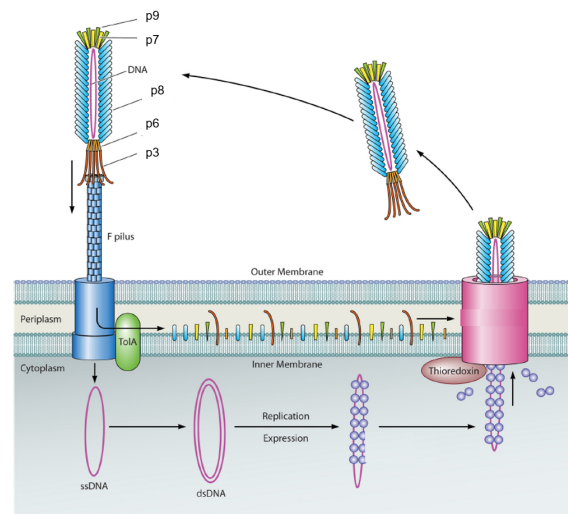


Figure 2.9: **Schematic representation of the infection of *E. coli*.** Mediated by the p3 proteins of the phage and the TolA protein of the membrane, the virus introduces its ssDNA which is immediately converted into a dsDNA. Figure was adapted from reference [81]

is let grown overnight at 230 rpm and 37° C. Subsequently, 6 liters of LB media, divided into 3 Erlenmeyer containing 2 liters each, are infected with 10 ml per liter of pre-amplified bacteria and 0.5 ml per liter of infecting solution of viruses which contains around 1×10^9 infecting phages per ml. This process is carried at 230 rpm and 37° C. The virus growth is tracked by measuring the optical density (OD) at $\lambda = 600$ nm and stopped when the value of OD reaches a plateau (see figure 2.10).

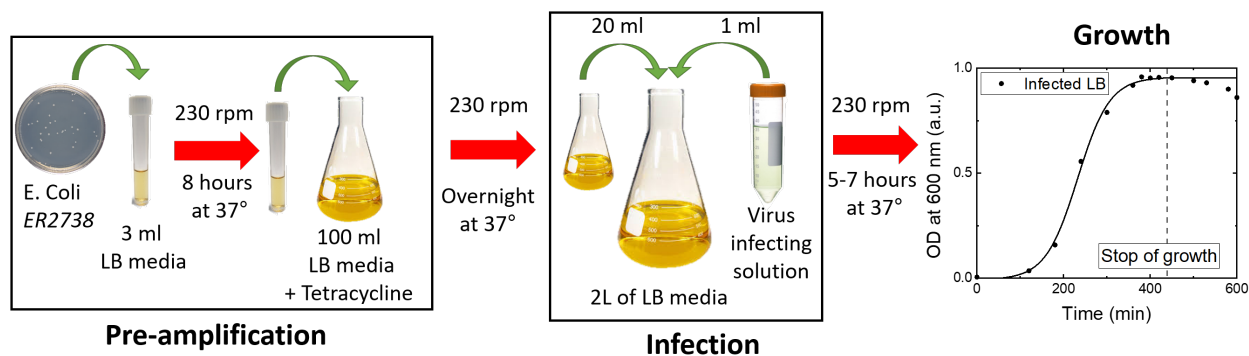


Figure 2.10: **Illustration of the virus production protocol.** During the **pre-amplification**, an isolated colony of bacteria grows in 3 ml of LB at 230 rpm and 37° C for their later growth in another 100 ml of LB media. Then, the **infection** is carried out by adding 20 ml of pre-amplified bacteria and 1 ml of virus infecting solution to 2 liters of LB media. Finally, the virus **growth** is tracked by measuring the absorption at $\lambda=600$ nm and stopped when the plateau is reached.

After this procedure, we have produced 6 liters of virus-bacteria mixture. Then, we proceed with the purification process which consists in the separation of viruses from the bacteria solution by several centrifugation steps achieved as follows. First, *E. coli* cells are removed by centrifuging the cultures twice at 6000 g for 20 minutes and collecting the supernatant each time. Later, we deplete for 1 hour the viruses by adding 15 g per liter of sodium chloride (NaCl) and 20 g per liter of polyethylene glycol with average molecular weight 8 kDA (PEG8K) to induce the depletion of the phages. Then, the supernatant is centrifuged again resulting in the precipitation of a viral mass in the pellet and a clear supernatant which is removed without disturbing the pellet.

The pellet is re-dispersed in a few milliliters of distilled water. The remaining pieces of bacteria are removed by a centrifugation step of 20 000 g for 45 minutes. In this step, the bacteria are placed in the pellet and the supernatant is kept. Finally, in order to remove the remaining polymer used for the depletion step as well as most of the molecular bioproducts, the viruses are sedimented by a centrifugation step of 200 000 g (45000 rpm) for 3 hours. The resulting pellet is then redispersed and dialyzed against the desired buffer for future reaction with Au NPs.

The concentration of viruses is determined by measuring the light absorption at $\lambda = 269$ nm corresponding to the maximum absorbance wavelength of M13 viruses. The optical density of a suspension at 1 mg/ml across a 1 cm path is equal to 3.84 cm²/mg [84]. The

ratio between absorbance at 269 nm and 244 nm is used to approximate the purity of the M13 viruses [85]. If the ratio is lower than expected, it may indicate the presence of contaminants which absorb at 244 nm. A ratio of 1.41 indicates less than 1% of impurities [85]. The usual yield for wild-type virus production is 20 mg/liter of LB medium while for the M13s(*Cgbc*C)₂ and M13l(*Cgbc*C)₂ strains the yield is slightly lower, i.e., about 15 mg/liter of LB medium.

After the production, we verify by DNA sequencing that the genetic modifications of the virus tips are correctly inserted in the mutants. Moreover, we analyze their length and dispersity by Transmission Electron Microscopy (TEM). Samples of about 1×10^{-3} mg/ml are settled onto O₂ plasma treated carbon-coated grids and stained with 2% uranyl acetate. Then, they are characterized from the images recorded with an AMT CCD camera mounted on a Hitachi H-600 electron microscope operating at 75 kV.

In figure 2.11, the length distributions measured using ImageJ software of the M13s(*Cgbc*C)₂ and M13l(*Cgbc*C)₂ are plotted. The black line indicates a Gaussian fit to the data indicating an average contour length of 1074 ± 99 nm and 1057 ± 43 nm respectively. Moreover, we have calculated for both mutants a polydispersity index (PDI) (see section 3.3.2.1) of 0.09 and 0.04 respectively indicating a high monodispersity. Thus, we find that their average length of $L = 1.1 \mu\text{m}$ is slightly higher compared with the M13C7C and M13KE strains for which it is found $L = 1 \mu\text{m}$ [55]. This is consistent with the fact that the virus length is proportional to the DNA length. Since our mutants have extra inserted peptides it is expected that they are longer compared to the wild-type.

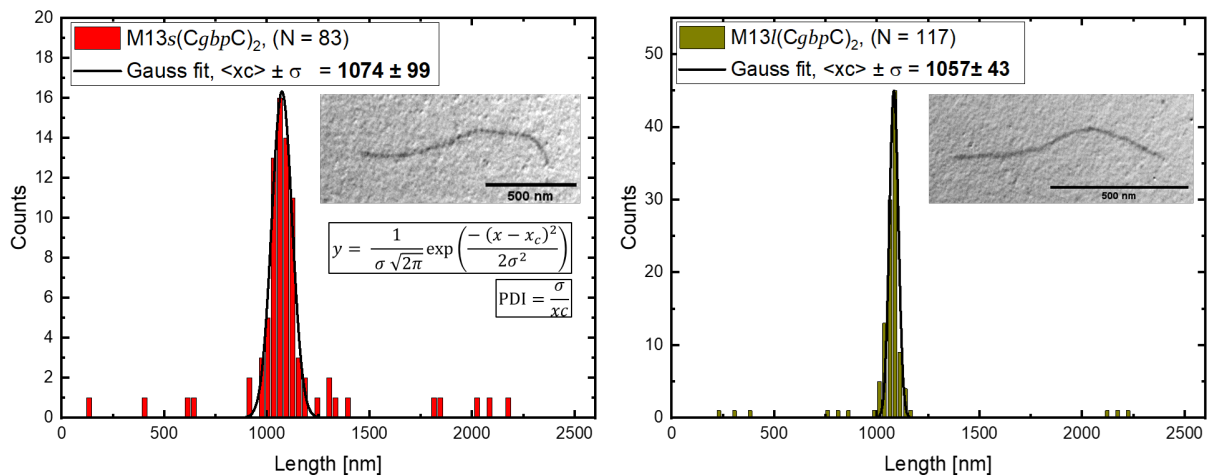


Figure 2.11: **Characterization after virus production.** Distribution of contour length measured from TEM images (insets) for M13s(*Cgbc*C)₂ (left) and M13l(*Cgbc*C)₂ (right). The Gaussian fits indicates contour lengths of 1074 ± 99 nm and 1057 ± 43 nm as well as polydispersity index (PDI) of 0.09 and 0.04 respectively.

2.2.2.1 Viruses functionalized with fluorescent dyes

The functionalization of the virus surface is possible thanks to the terminal amino acids and Lysine of p8 proteins [42]. As shown in figure 2.12, a N-hydroxysuccinimide (NHS) ester

bound to a dye molecule links to the NH_2 groups at the virus surface.

For the labeling process, a suspension of viruses at concentration of 1 mg/ml is dialyzed against phosphate buffer (PBS) at $I = 200$ mM and pH 7.8 and mixed with red or green fluorescent dyes dissolved in a Dimethylformaide (DMF) solution. The excess of dyes is set to be 3 dyes per major p8 coat protein taking care that the amount of DMF does not exceed 20% of the volume. Then, the reaction is carried under stirring at 300 rpm for 2 hours at room temperature and overnight at 4°C . The resulting suspension is then extensively dialyzed against Tris/HCl buffer at $I = 10$ mM and pH 8.2 to remove the free dyes. After this purification, the number of dyes per virus can be calculated form the absorbance spectra of the aqueous suspensions of the pure dye, the pristine mutant and the labeled suspension (see reference [13] and supplementary material of [86]).

For the production of some of our hybrid gold-virus colloids we have used different fractions of full body labeled viruses with Alexa Fluor 488 or Dylight 550 which excitation and emission spectra are shown in figure 2.12 (b). This modification, that does not affect the virus length but only the diameter, is designed to allow for the direct visualization of the viruses by fluorescence microscopy (see section 3.2.1). For a dilute suspension of rods of high aspect ratio, i.e, $L/d \gg 1$, the diffusion is almost insensitive to the rod diameter (see chapter 3). Hence, we expect that the labeling does not affect significantly the virus behavior in colloidal suspensions.

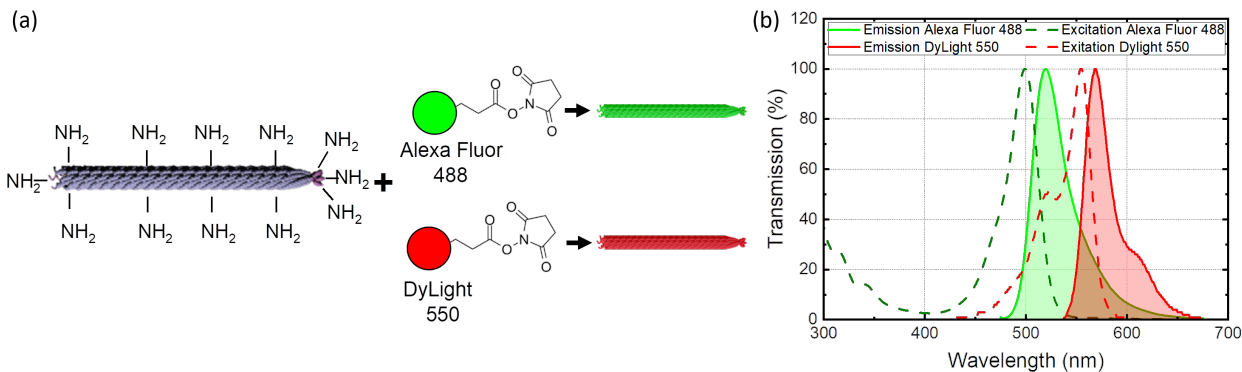


Figure 2.12: **Scheme of labeling process on M13C7C viruses.** (a) The full body functionalization with fluorescent dyes can be performed by the reaction between NH_2 groups and NHS ester functionalized dyes. (b) Excitation (dashed line) and emission (filled full line) spectra of Alexa Fluor 488 and Dylight 550.

2.3 Production of gold-virus colloids

As described in the previous section, the displayed double cysteines at the exposed coat proteins p3 and p7 of the phages form disulfide bridges. This allows for binding metal nanoparticles to the virus tips by a weak covalent bond [75]. In addition with the ionic conditions that promote their interaction, we have constructed hybrid colloids made of gold nanoparticles (Au NPs) bound to the tips of M13 mutants by self-assembly.

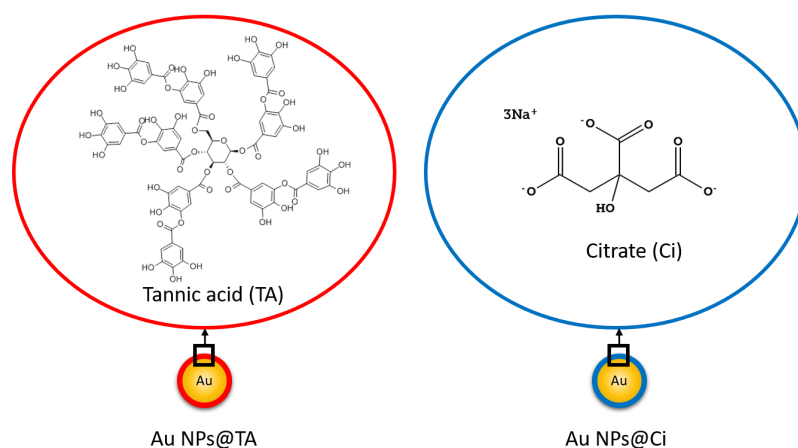


Figure 2.13: Different surface ligands at gold surface used for the production of hybrid gold-virus colloids. Tannic acid (left) and citrate (right) capped gold nanoparticles.

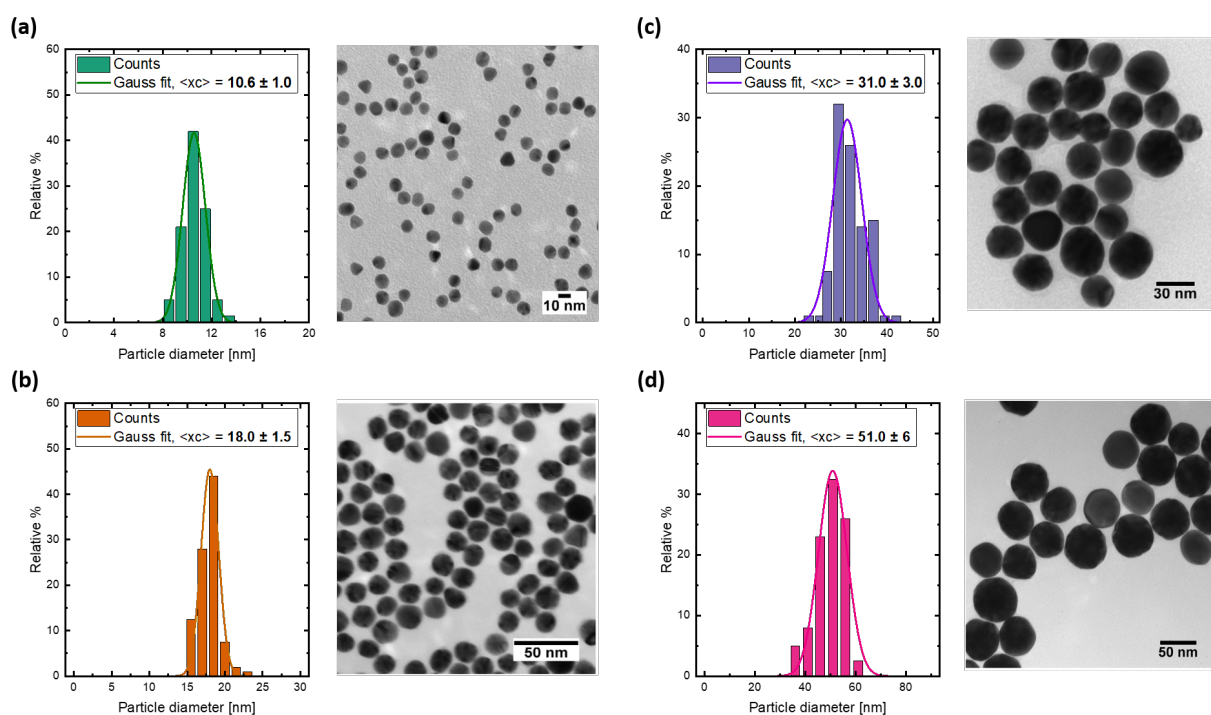


Figure 2.14: Characterization of the different Au NPs suspensions. Size distributions and TEM images for the batches of mean diameter (a) 10.6 nm, (b) 18 nm, (c) 31 nm and (d) 51 nm. Data was provided by the supplier. From dynamic light scattering experiments it is found a PDI = 0.05, 0.07, 0.10 and 0.10 respectively.

For the production of the different hybrid gold-virus structures of this work, we have used tannic acid stabilized Au NPs of average diameters $D = 10.6$, 18 and 51 nm as well as citrate stabilized Au NPs of $D = 31$ nm, all purchased from NanoComposix (see figure 2.13). TEM images and size distributions for the different batches are shown in figure 2.14. The PDI of each one has been estimated by Dynamic Light Scattering (DLS) as described in section 3.3.2.1. The values found, PDI = 0.05, 0.07, 0.10 and 0.10 for the Au NP suspensions

of diameters 10.6, 18, 31 and 51 nm respectively, indicate a high monodispersity, i.e., PDI ≤ 0.1 [87].

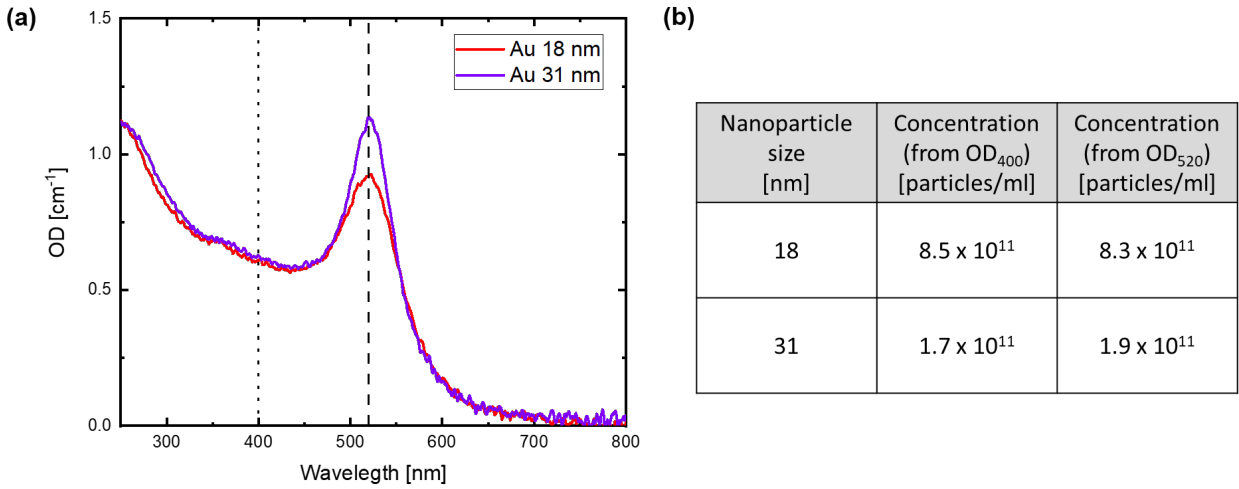


Figure 2.15: **Concentration of Au NPs calculated from light absorption.** (a) UV-Vis spectra measured for stock suspensions of Au NPs of $D = 18$ nm and 31 nm. (b) Calculated concentration from OD at 400 nm and 520 nm according to equations 2.1 and 2.2.

The concentration of the Au NPs is determined based on the UV-Vis light absorption measured by NanoDrop One, Thermo., due to the plasmonic resonance. Two main methods based on the absorption at 400 nm and at 520 nm are commonly used.

(i) Absorption at 400 nm:

The molar extinction coefficient of Au NPs at 400 nm, $\varepsilon_{400} = 2400 \text{ M}^{-1}\text{cm}^{-1}$ can be used to determine the molar concentration of Au as $C_{\text{Au}(0)} = OD_{400}/\varepsilon_{400}$ [88]. Assuming that the particles are spherical, the mass of one particle is calculated as: $m = \rho_{\text{Au}} V_{\text{AuNPs}}$ with $\rho_{\text{Au}} = 19.3 \text{ g/cm}^3$ the density of Au and $V_{\text{AuNPs}} = \frac{\pi D^3}{6}$ the volume of the Au sphere of diameter D . Then, the particle concentration is calculated as:

$$C_{\text{AuNPs}} = \frac{C_{\text{Au}(0)} M_W}{m}, \quad (2.1)$$

with $M_W = 197 \text{ g/mol}$ the molecular weight of Au.

(ii) Absorption at the plasmonic resonance:

From the specific molar extinction coefficient, ε_{520} , which depends on the nanoparticle diameter D in nm as $\varepsilon_{520} = 64714.9D^{(3.2)} \text{ M}^{-1}\text{cm}^{-1}$ for $D \lesssim 50 \text{ nm}$ [55], the particle concentration is calculated by:

$$C_{\text{AuNPs}} = \frac{OD_{520} N_A}{\varepsilon_{520}}, \quad (2.2)$$

with N_A the Avogadro's number.

In figure 2.15 are plotted the UV-Vis spectra measured for Au NPs of $D = 18$ nm and 31 nm. The optical density (OD) is taken from the spectra at 400 nm and 520 nm. Then, the concentration is calculated using equations 2.1 and 2.2. As shown in the figure 2.15 (b), the values of concentration obtained for Au NPs using the methods described above are consistent with each other. For the estimation of the Au NPs concentration needed to manufacture our hybrid gold-virus colloids, we have mostly used the method (ii) as it is dependent of the NP size.

The production steps that promote the interaction of the different M13KE mutants with Au NPs by their tips depend on the following conditions:

- *Electrostatic repulsion.* Both elements are negatively charged so they repel each other. In order to allow for their interaction, the electrostatic repulsion has to be screened. To do so, we increase the number of free ions in suspensions by dialyzing the suspension against different buffers in a range of ionic strength conditions from $I = 20$ mM to $I = 200$ mM.
- *Intensity of electrostatic repulsion.* We know that the isoelectric point of viruses is $pI_E = 4.5$ [62], while the Au NPs are at $pH = 5.4$ for NPs stabilized with tannic acid ($pK_a = 6$) and $pH = 7.2$ for NPs stabilized with citrate ($pK_a = 6.4$) [89, 90]. A pH close to pI_E decreases the overall charge of both components and consequently their electrostatic repulsion. Thus, the pH of the suspension is varied by changing the buffer used for reaction. For example, Tris/HCl buffer at $pH 8.2$ is changed for MES^{iii} buffer at $pH 6.2$.
- *Number of particles available for reaction.* The molar excess ratio, α , defined as the number of Au NPs per number of viruses available for reaction, influences in the resulting final structure. This is expressed in terms of the particle concentration as:

$$\alpha = [AuNPs]/[Viruses]. \quad (2.3)$$

On one hand, when the number of viruses is reduced compared with the number of available beads, for instance $\alpha \sim 3$, their reaction leads to the assembly of a single virus to one NP with a lot of remaining unreacted Au NPs. On the other hand, if the NPs are in significantly less amount compared with viruses, i.e., $\alpha \ll 1$, it is expected that multiple viruses could assemble to a single NP.

- *Virus concentration.* The virus concentration at which the reaction is performed influences the probability of gold-virus interaction and hence the resulting final

ⁱⁱⁱMES is the common name for the compound 2-(N-morpholino)ethanesulfonic acid, a buffering agent that has pK_a value of 6.15 at $20^\circ C$.

structure. The overlap concentration C^* is the concentration after which two viruses start to overlap. As shown in figure 2.16, C^* is calculated as the concentration of fictitious close packing spheres of diameter equal to one virus length, L . Thus, C^* scales as:

$$C^* \sim \frac{M_{M13}}{\frac{4\pi}{3} \left(\frac{L}{2}\right)^3 N_A}, \quad (2.4)$$

with $M_{M13} = 1.86 \times 10^{10}$ mg/mol the filamentous viruses molecular weight and N_A the Avogadro's number. For equimolar conditions, i.e., one bead per virus, working at a virus concentration below C^* reduces the chance that more than one virus interacts with a single bead, while working at concentrations above C^* does the opposite.

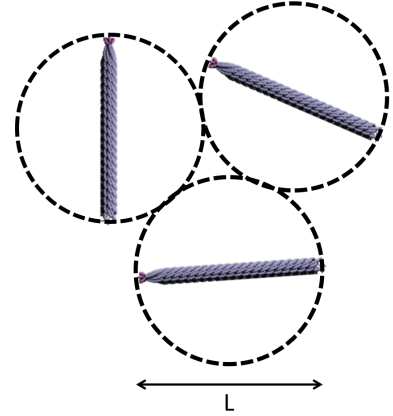


Figure 2.16: **Sketch of C^* concentration.** This is calculated assuming spheres of diameter equal the virus length.

In this work, we combine the M13C7C strain with Au NPs to produce *colloidal star particles* made of multiple viruses attached to a single bead as well as hybrid gold-virus colloids made of a individual virus attached to a single nanoparticle called *matchstick-like particles* (see figure 2.3). The mutants M13s(*Cgbc*)₂ and M13l(*Cgbc*)₂, are used to create hybrid colloids made of a single virus with one nanoparticle attached to each tip named *dumbbell-like particles*. The detailed production steps of each structure is described below.

2.3.1 Colloidal star particles

For the design of a suspension of colloidal star particles with valency n defined as the number of viral arms per Au NP, we have used highly monodisperse Au NPs of $D = 51$ nm (PDI = 0.1) and M13C7C viruses. The choice of the NP size was made considering the findings in our group about the influence on the nanoparticle size on the average valency [55] which proved that for a higher NP surface a higher number of viruses can be grafted.

The production is performed by mixing a suspension of Au NPs at concentration $C_{AuNPs} = 1.1 \times 10^{11}$ particles/ml with the corresponding amount of viruses in such a way that the molar excess is $1/\alpha = 100$, i.e., that for 100 viruses there is 1 Au NP available to react. Moreover, we have chosen to work at a virus concentration above C^* in order to promote the interaction of a single bead with multiple viruses. According to equation 2.4, for a virus length of 1 μm and close packing spheres having a volume fraction of 0.74, $C^* = 0.043$ mg/ml. Thus, we have worked at a concentration $C \sim 8.5C^* = 0.34$ mg/ml. The virus mass needed for the reaction, m_{M13} , is calculated as

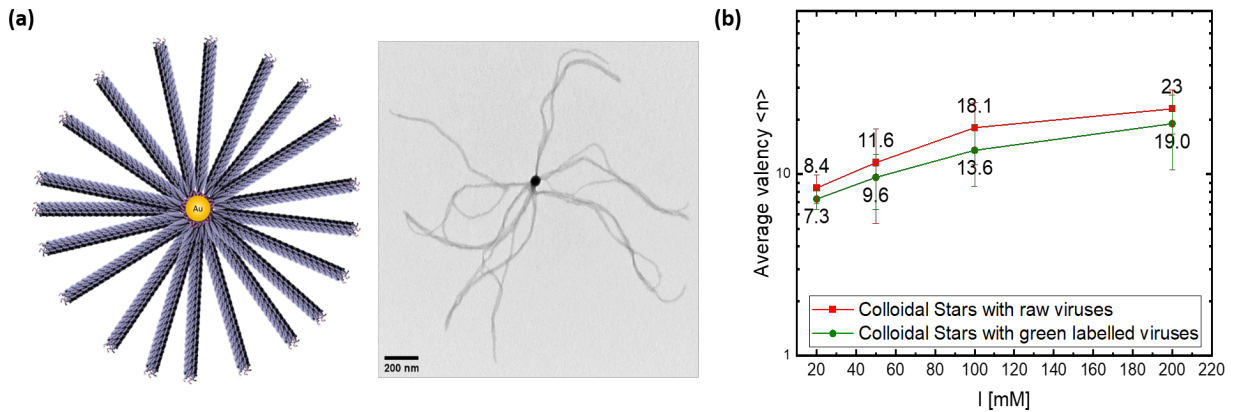


Figure 2.17: **Colloidal star particles.** (a) Schematic representation and TEM image of the structure made of multiple viruses attached to a single Au nanobead. (b) Average valency, $\langle n \rangle$, i.e., number of viral arms, of the colloidal star particles as function of ionic strength used for the reaction.

$$m_{M13} = \frac{C_{AuNPs} \cdot V_{AuNPs}}{\alpha} \cdot \frac{M_{M13}}{N_A}, \quad (2.5)$$

with V_{AuNPs} the volume of the Au NPs suspension. Next, the gold-virus mixture is dialyzed against $I = 20$ mM Tris/HCl buffer at pH 8.2 to screen their electrostatic repulsion leading to their assembly. The reaction takes place overnight at room temperature and at stirring rate of 300 rpm. Then, the ionic strength of the suspension is increased stepwise from $I = 50$ to 100 and 200 mM by dialysis followed by overnight reactions under stirring at room temperature for each ionic condition.

The average valency, $\langle n \rangle$, is determined from TEM images taken after each reaction by counting the number of viral arms attached per Au NP (see figure 2.18). In figure 2.17 are plotted the average valencies found for each step of the reaction. As shown in figure 2.17 (b), $\langle n \rangle$ increases with ionic strength and nearly reaches a plateau for $I > 100$ mM.

Once the plateau is reached, the reaction is stopped by decreasing the ionic strength via dialysis against a $I = 0.5$ mM Tris/HCl buffer. The free viruses are then removed by centrifugation. The resulting colloidal star particles are pelleting by applying 4000 g for 30 minutes. The supernatant containing the free viruses is carefully removed leaving in the pellet only the star-like structures. These are redispersed and the procedure is repeated a few times until the percentage of free viruses is below 10%.

As a result, we get a suspension of colloidal star particles with average valency of 23 viruses per gold nanoparticle. In figure 2.18 is shown a large field of view TEM image of the colloidal star particles as well as the distribution of valency found. From the Gaussian fit, we obtain a $PDI = 0.26$ indicating a moderate polydispersity in the valency [91] (see section 3.3.2.1). For the optical microscopy observation of these structures, we have produced them with 3 to 5 red-labeled viruses as well as a batch made of only green-labeled viruses. As shown in figure 2.17 (b), the use of labeled viruses does not affect significantly the average valency of the resulting colloidal stars.

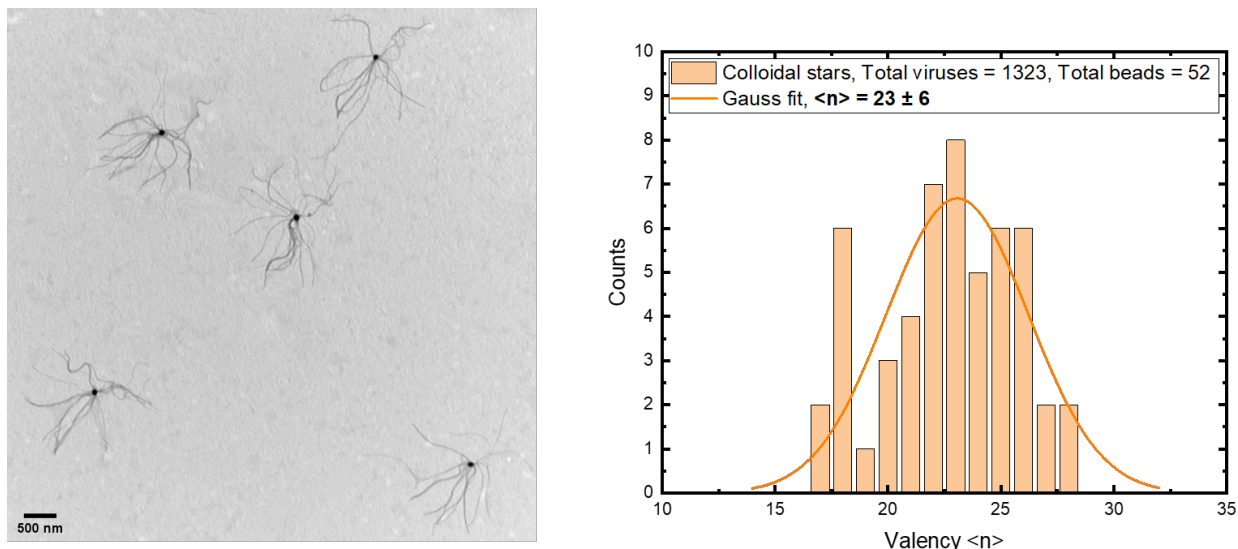


Figure 2.18: **Valency of colloidal star particles.** Large field of view TEM image of the clean suspension, i.e., after removal of free viruses, (left) with average valency of $\langle n \rangle = 23 \pm 6$ and PDI = 0.26 calculated from the Gaussian fit of the distribution (right).

2.3.2 Matchstick-like particles

The production of matchstick-like particles mostly depends on the initial molar excess α . Since we want to produce structures made of a single NP attached to a single virus tip, we have to ensure that only one NP will interact with a single virus. Thus, we set a molar excess of $\alpha = 3$ and perform the reaction at a virus concentration below C^* ($C = 0.009$ mg/ml $\simeq 1/5C^*$) to reduce the probability of interaction of more than one virus per Au NP. The choice of the previous conditions with an excess of beads results in the assembly of a high number of matchstick-like particles compared with other structures such a diblocks made of two viruses attached by one of their tips to a single NP. After the reaction, the excess of non-reacted beads is removed by centrifugation.

To produce matchstick-like particles made of NPs of different sizes ($D = 10.6, 18$ and 31 nm) we mix Au NPs at concentration $C_{\text{AuNPs}} \sim 1 \times 10^{12}$ particles/ml with M13C7C viruses. The mass of viruses needed, calculated with equation 2.5, is added to the suspension of Au NPs. Then, in order to screen their electrostatic repulsion the suspension is dialyzed against the selected buffer. For tannic acid stabilized Au NPs ($D = 10$ and 18 nm) the ionic strength is increased in one step to $I = 20$ mM while for citrate stabilized Au NPs ($D = 31$ nm) it is increased stepwise from $I = 10$ to 20 mM increasing 5 mM each time. The previous conditions assure that the citrate stabilized Au NPs do not aggregate due to their lower stability compared with the tannic stabilized ones explained by the difference in their surface ligand [55] (see figure 2.13). The reaction occurs under stirring and at room temperature overnight. Usually, the number of viruses which have grafted Au NPs after the reaction at $I = 20$ mM is $\sim 90\%$. A higher yield could be expected if we continue to increase ionic strength. However, aggregation of Au NPs has been observed above $I = 40$ mM for

tannic acid stabilized NPs and above $I = 25$ mM for citrate stabilized ones [55]. Hence, we stop the reaction at these conditions.

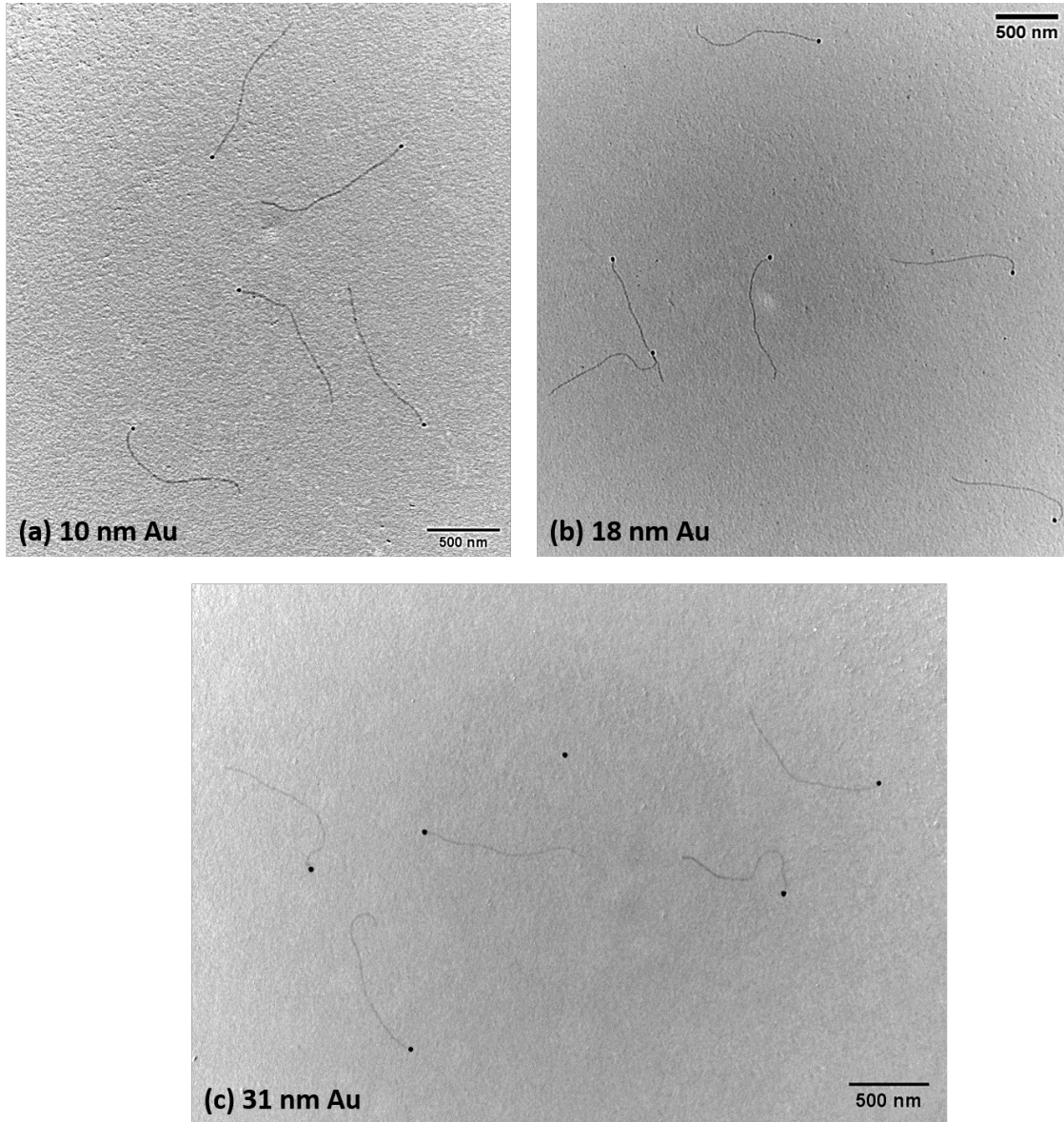


Figure 2.19: **TEM characterization of matchstick-like particles.** Large field of view for viruses based structures made of Au NPs of (a) $D = 10$ nm, (b) $D = 18$ nm and (c) $D = 31$ nm as diameter after purification of the free Au beads.

The difference in density and shape of the two elements in suspension allows us to separate them by simple centrifugation steps. To proceed with the purification, where the NPs that are not involved in hybrid structures go to the pellet while the matchstick-like particles stay in the supernatant, we decrease the ionic strength to $I = 0.5$ mM by dialysis. At these ionic conditions, we assure that the Au NPs do not aggregate when they are concentrated in the pellet. For a height of the suspension, l , we apply during a time t , the acceleration:

$$a = \frac{l}{S \cdot t}, \quad (2.6)$$

where S is the sedimentation coefficient defined as the time for a particle to reach a maximum speed as it falls through the suspension due to the applied acceleration [92]. This occurs when the sum of the drag force and the buoyancy is equal to the centrifugal force. At the infinite dilute regime, S depends on the density and shape of particles [92, 93].

In order to have an easy separation and purification by centrifugation, the sedimentation coefficient of the matchstick-like particles must be at least of one order of magnitude higher than the one of the free NPs. For our spherical Au NPs, S depends on the particle diameter D and is calculated as [55]:

$$S_{\text{AuNPs}} = \frac{\rho_{\text{Au}} - \rho_s}{18\eta} \cdot D^2, \quad (2.7)$$

where $\rho_{\text{Au}} = 19.4 \text{ g/cm}^3$ is the density of gold and ρ_s and η the density and dynamic viscosity of the solvent. For water, the latest correspond to $\rho_s = 1.0 \text{ g/cm}^3$ and $\eta = 0.001 \text{ Pa} \cdot \text{s}$ at $T = 293 \text{ K}$.

For rod-shaped particles of high aspect ratio ($L/d \gg 1$), the sedimentation coefficient in terms of the mass, m , and volume of the particle, V_p , is given by [55, 93]:

$$S_{\text{rod}} = \frac{\ln\left(\frac{L}{d}\right)}{3\pi\eta L} (m - \rho_s V_p), \quad (2.8)$$

where L and d are the length and diameter of the rod. For the matchstick-like particles, we use the approximation that the volume of the Au NP at the tip of the rod is homogeneously spread on the surface of the rod, thus we estimate the sedimentation coefficient as in equation 2.8 resulting in [55]:

$$S_{\text{matchstick}} = \frac{\ln\left(\frac{3L^3}{2D^3+3Ld^2}\right)}{6\pi\eta L} \cdot \left[\frac{\pi D^3}{6} (\rho_{\text{AuNPs}} - \rho_s) + \frac{\pi L d^2}{4} (\rho_M - \rho_s) \right], \quad (2.9)$$

with $\rho_M = 1.285 \text{ g/cm}^3$ the density of the filamentous virus [94]. From equation 2.9, it follows that for $L = 1 \text{ } \mu\text{m}$ and $d = 7 \text{ nm}$, $S_{\text{matchstick}} = 1.1 \times 10^{-11} \text{ s}$, $3.5 \times 10^{-11} \text{ s}$ and $1.51 \times 10^{-10} \text{ s}$ for matchstick-like particles made of Au NPs of $D = 10, 18$ and 31 nm respectively.

The calculated S_{AuNPs} and $S_{\text{matchstick}}$ as well as the applied conditions for the different productions are summarized in table 2.2. Note that S_{AuNPs} of $D = 10 \text{ nm}$ and 18 nm changes by one order of magnitude with respect to the corresponding $S_{\text{matchstick}}$. For this reason, the experimental conditions applied are the same as the theoretical ones. However, for Au NPs of $D = 31 \text{ nm}$, the sedimentation coefficients are of the same order of magnitude and some structures start to go to the pellet when the theoretical value is applied. Hence, we decrease the acceleration and repeat the procedure many times in order to keep the maximum of structures as possible and therefore not decrease too much the yield. The sample is characterized by TEM and the centrifugation is applied until the percentage of free beads is below 10%.

For the TEM characterization of the resulting suspension, we estimate the fraction of

Table 2.2: Summary of Au NPs sedimentation coefficients and applied centrifugation conditions for a suspension of height 3 cm.

Diameter [nm]	S_{AuNPs} [s]	$S_{\text{matchstick}}$ [s]	Theoretical $a \times t$ [$10^3\text{g} \times \text{s}$]	Experimental $a \times t$ [$10^3\text{g} \times \text{s}$]
10	1.0×10^{-10}	1.1×10^{-11}	11.7×2700	11.0×2700
18	3.3×10^{-10}	3.5×10^{-11}	5.0×1800	5.0×1800
31	9.8×10^{-10}	1.5×10^{-10}	1.7×1800	0.5×1800

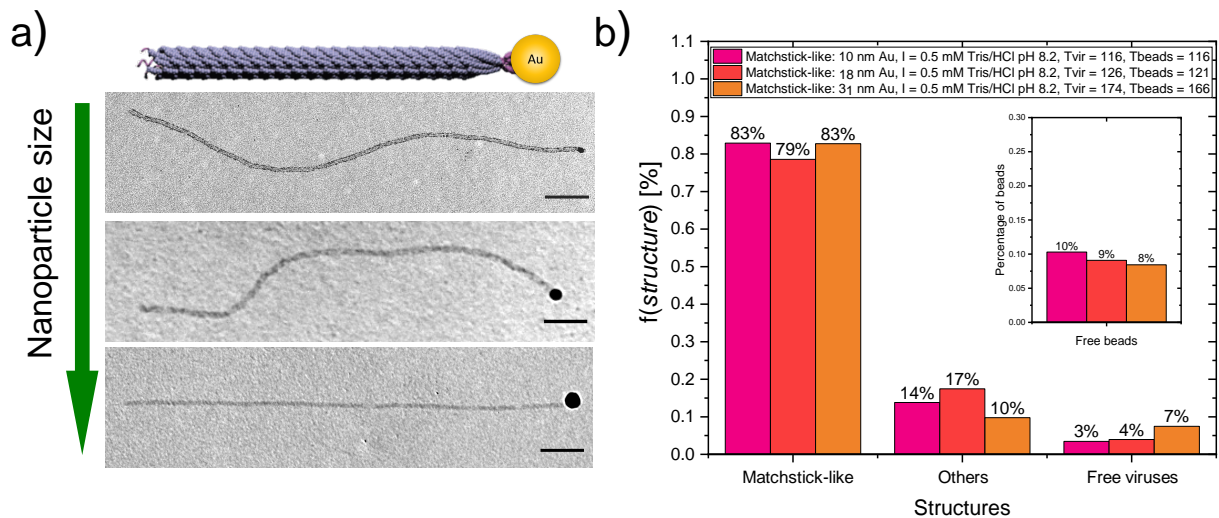


Figure 2.20: **Production of matchstick-like particles.** (a) TEM images of matchstick-like particles made with different nanoparticle sizes, $D = 10$ nm, 18 nm and 31 nm from top to bottom. (b) Histogram representing the fraction of colloidal structures and free breads found in each batch. The fractions, $f(\text{structure})$, are calculated as function of the total number of viruses, T_{vir} , for the structures and as function of the total number of beads, T_{beads} , for the percentage of free NPs.

structures $f(\text{structure}) = T_s/T_{\text{vir}}$ as the ratio between the total number of viruses involved in a given structure, T_s , and the total number of virus, T_{vir} . In figure 2.20 are shown the distributions of our matchstick-like suspensions. For the three NP sizes, we find $\sim 80\%$ of matchstick-like particles, $\sim 15\%$ of other structures (mostly two viruses bind to a single NP) and $\sim 5\%$ of free viruses. Moreover, we have estimated, in terms of the total number of beads, T_{beads} , that the percentage of free beads is below 10% (see inset of figure 2.20). In figure 2.19 are shown large field of view TEM images of the different batches of matchstick-like particles made of Au NPs of $D = 10$, 18 and 31 nm taken after the purification of non-reacted beads.

As final step, we estimate the concentration of structures for a given sample. This is calculated from the OD of the suspension and given in terms or the virus concentration assuming that for each bead there is a virus that has reacted with one tip, i.e.,

$$C_v = C_{\text{matchstick}} = \frac{C_{\text{AuNPs}} M_{\text{M13}}}{N_A} \quad (2.10)$$

with C_{AuNPs} given by equation 2.2 and $M_{\text{M13}} = 1.86 \times 10^{10}$ mg/mol the molecular weight of the viruses.

2.3.3 Dumbbell-like particles

In order to create dumbbell-like particles, we have worked with the virus mutants $\text{M13s}(\text{CgbpC})_2$ and $\text{M13l}(\text{CgbpC})_2$ for which we expect to bind two Au NP one at each virus tip. The reaction conditions are similar as the ones for the matchstick-like particles. However, for this case we have increased the excess of Au NPs according to the two virus tips to be functionalized. Thus, we set a molar excess of $\alpha = 6$ and perform the reaction at a virus concentration below C^* ($C = 0.02$ mg/ml). Since we want to avoid that more than one virus reacts with the same NP we also have chosen to work with a small NP size ($D = 10$ nm). The amount of viruses added to the Au NP suspension at $C_{\text{AuNPs}} \sim 10^{12}$ part/ml is calculated according to equation 2.5. After both components are mixed, the suspension is dialyzed against the selected buffer. First we use a Tris/HCl buffer at pH 8.2 and increase stepwise the ionic strength from $I = 20$ mM to 40 mM. Then, in order to decrease the intensity of the electrostatic repulsion, the pH is changed to 6.2 by dialysis against a MES buffer at $I = 40$ mM. Each reaction takes place at stirring rate of 300 rpm and at room temperature.

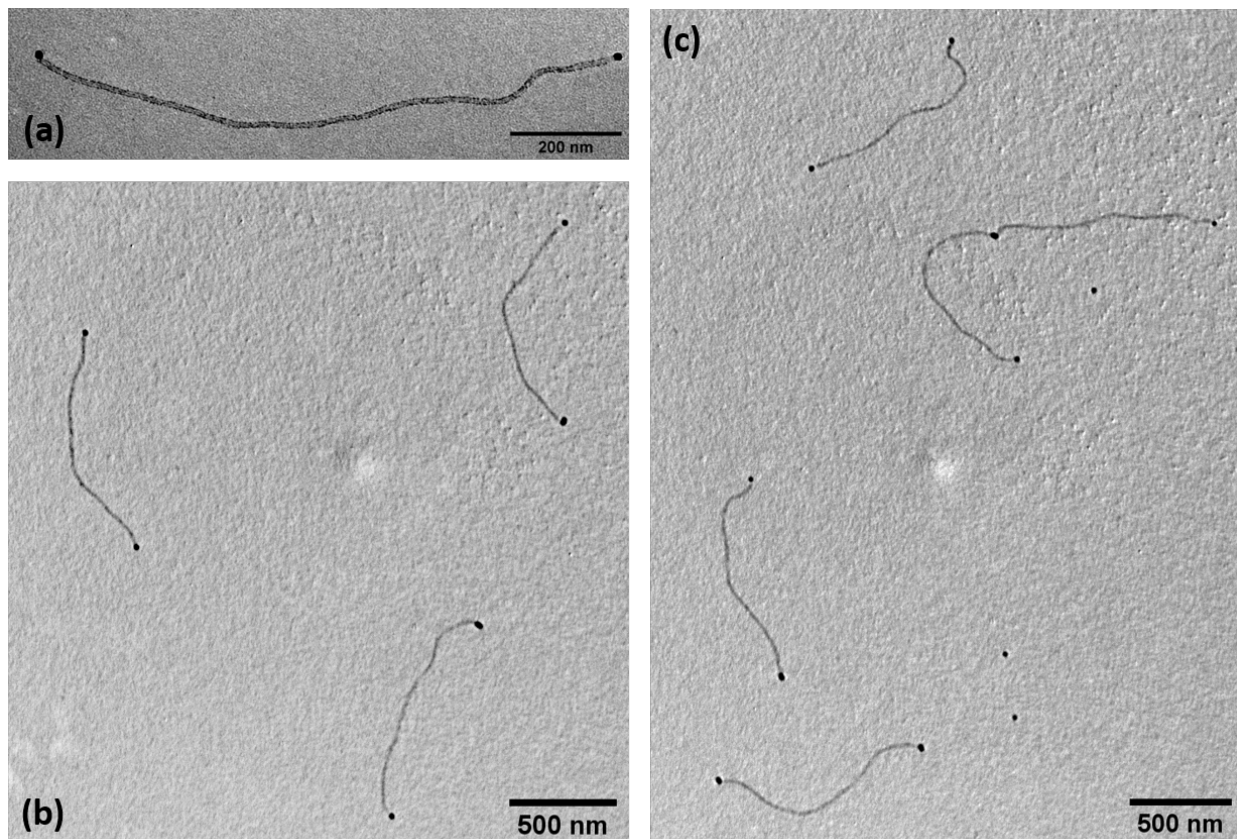


Figure 2.21: TEM characterization of the $\text{M13l}(\text{CgbpC})_2$ reaction with Au NPs of $D = 10$ nm. (a) Dumbbell-like particle. (b)-(c) Large field of view of the structures where also three free NPs can be seen in (c).

In figure 2.21 are shown TEM images of the suspension after purification of the non-reacted beads by centrifugation.

2.3.3.1 Influence of the virus mutant

We have studied the influence of the p3 and p7 genetic modifications done for the M13s(*Cgbc*)₂ and M13l(*Cgbc*)₂ strains by quantifying the percentage of functionalized tips after their interaction with Au NPs in similar conditions.

The double tip binding affinity of these mutants allows for the formation of more complex morphologies such as the ones shown in figure 2.22. These hybrid colloids are called in terms of the number of Au NPs and viruses that are involved in the structure as **A:B** with **A** the number of Au NPs and **B** the number of viruses. For instance, a matchstick-like made of 1 NP and 1 virus is called **1:1** while the dumbbell-like made of two beads and one virus is called **2:1**. Relative to each one, the yield of reaction is calculated dividing the number of tips that have bound to Au NPs over the total number of tips. Thus, for the 1:1 as well as for 1:2 structures, whose viruses have reacted only by one virus tip the yield is 50%, while

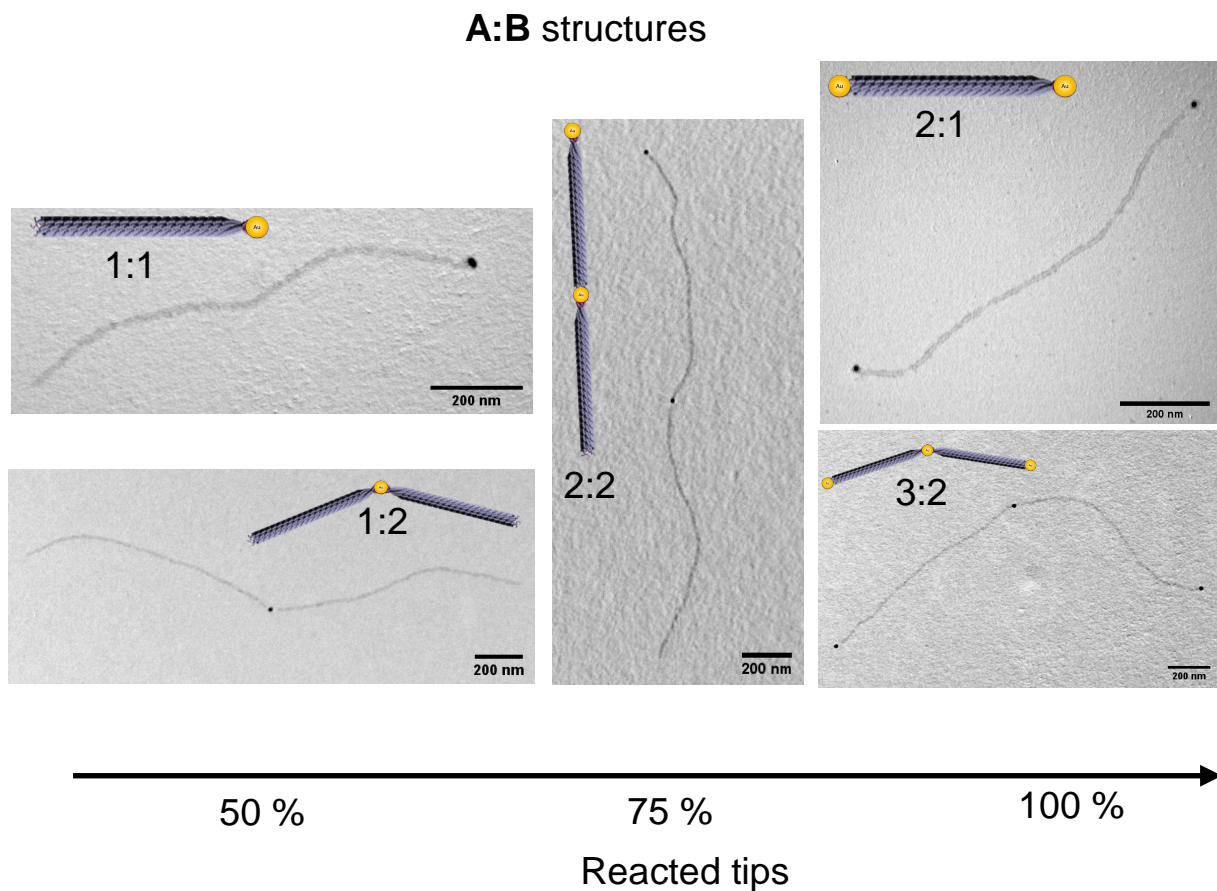


Figure 2.22: **A:B structures as function of reacted tips**. **A** represents the number of Au NPs involve in the morphology while **B** the number of viruses. The yield of reaction is estimated by the ratio between the number of tips that have been bound to Au NPs and the total number of virus tips.

for the 2:1 and 3:2 whose virus tips are completely bounded to Au NPs, the yield is 100% (see figure 2.22).

In the following we describe our observations after each set of conditions for both mutants having cysteine groups displayed at both virus ends.

- **M13s(CgbcC)₂**

In figure 2.23 are summarized the distribution of structures, percentage of reacted tips and molar excess found by TEM after each step.

After the reaction at $I = 20$ mM and pH 8.2, the M13s(CgbcC)₂ mutant exhibits a yield of $\sim 50\%$ tips that have linked to Au NPs mainly involved in the 1:1 morphology. As the ionic strength is increased to $I = 40$ mM, the yield rises up to $\sim 72\%$ and the distribution is balanced between 1:1 and 2:1 structures. Under these conditions, some aggregation of Au NPs is observed which is associated with a decrease of the initial molar excess α . Finally, when the pH is decreased to 6.2, a maximum yield of $\sim 80\%$ is reached. Moreover, a majority of 2:1 structures is found. The final state of this suspension is composed of $\sim 40\%$ dumbbell-like and $\sim 30\%$ matchstick-like particles.

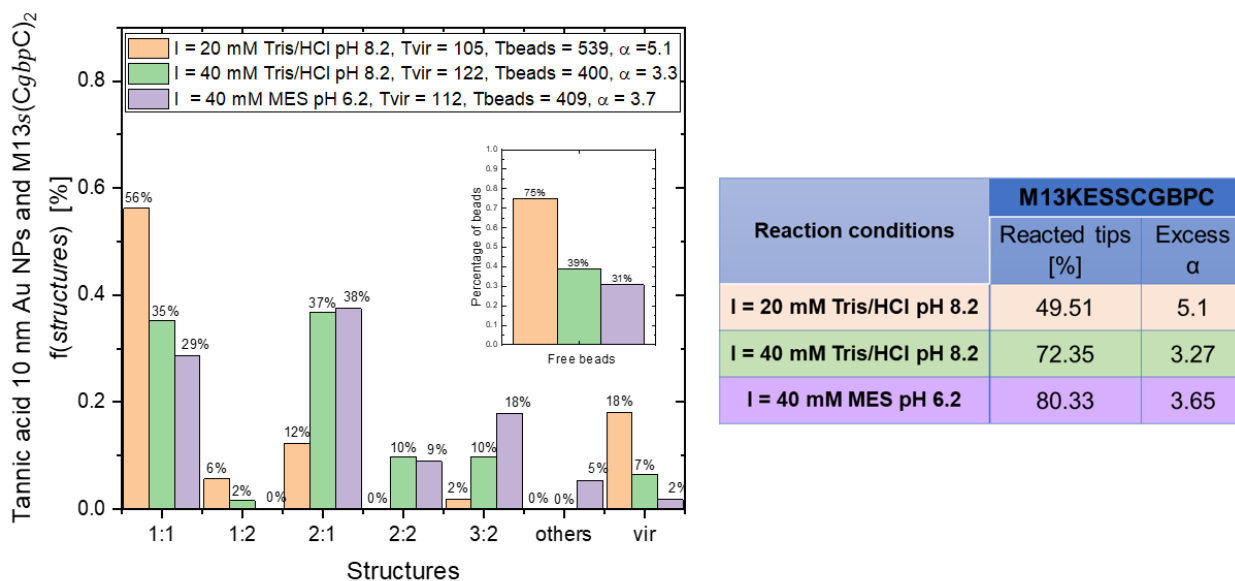


Figure 2.23: **Reaction of M13s(CgbcC)₂ strain and Au NPs of $D = 10$ nm.** Left: Distribution of $A:B$ structures and free beads. Right: Summary of reacted tips and molar excess after each set of reaction conditions.

- **M13l(CgbcC)₂**

For the M13l(CgbcC)₂ mutant, the distribution of structures, percentage of reacted tips and molar excess found by TEM after each set of conditions are summarized in figure 2.24.

Similar as the previous mutant reaction results, at $I = 20$ mM and pH 8.2, about 50% of

the M13l(*CgbcC*)₂ tips have bound to Au NPs. When the ionic strength is raised to $I = 40$ mM, a significant increase of the yield is observed. In this case, the percentage of reacted tips reaches $\sim 84\%$ which are involved mostly in the 2:1 morphology. Last, when the pH is decreased to 6.2 at the same ionic conditions, the yield reaches $\sim 88\%$ and the number of 2:1 increases even more. The conditions are not push further since beyond, aggregation of free NPs starts to prevail. The distribution at the final conditions corresponds to $\sim 60\%$ dumbbell-like structures and $\sim 20\%$ matchstick-like particles.

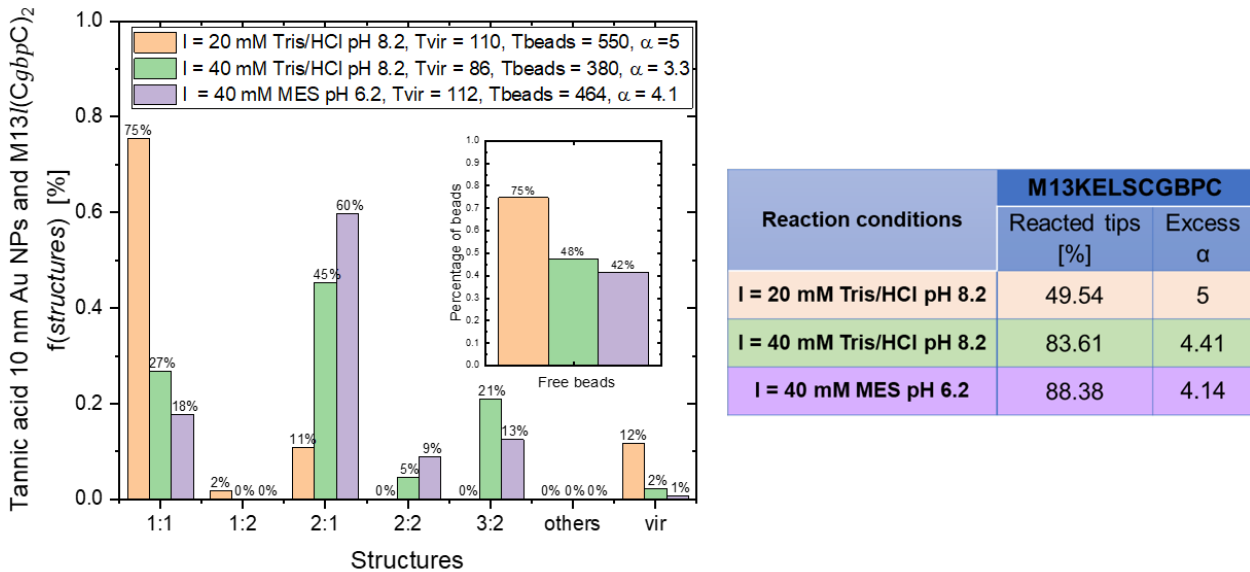


Figure 2.24: **Reaction of M13l(*CgbcC*)₂ strain and Au NPs of $D = 10$ nm.** **Left:** Distribution of $A:B$ structures and free beads. **Right:** Summary of reacted tips and molar excess after each set of reaction conditions.

The previous observations have a direct relation with the genetic modification of both mutants. As described in section 2.2.1, the binding affinity of the virus tips is directly related with the presence of cysteine groups (cys-cys) accessible for interaction with Au NPs via a weak covalent bond.

The p3 protein modification of these mutants is similar as the one of the M13C7C strain, i.e., the vector added close to the N terminal have a peptide encoded by seven amino acids flanked by two cysteines. This genetic modification allows us for comparing our findings with the previously obtained for the production of matchstick-like particles. For an excess of Au NPs and virus concentration below C^* , about 45% of the M13C7C tips have been grafted to one bead. In the same conditions, both of our new mutants exhibit $\sim 50\%$ of tips that have bound to Au NPs. Assuming that the reactivity of the proximal (p3) tip is the same as for the M13C7C mutant, it is expected that the $\sim 5\%$ difference in the number of reacted tips at these conditions stems from the interaction of beads via the second tip (distal end, p7). However, since the p7 proteins are not as exposed as the p3 ones, they are not as accessible for binding Au NPs until the repulsive interaction of both component is screened even more.

For this reason, we do not observe a significant increase until the ionic strength reaches $I = 40$ mM with pH 6.2 for which a maximum percentage of reacted tips of 80% and 88% is found for the $M13s(CgbpC)_2$ and $M13l(CgbpC)_2$ respectively.

The difference in the final yields of these mutants is related to the spacer used before the *CgbpC* sequence at the p7 protein end (see figure 2.8). This gives us an insight of the efficiency of these spacers to make the cysteine groups more exposed for their interaction with Au NPs. Considering that 45% of the yield corresponds to the binding at the first tip, we estimate $\sim 35\%$ and $\sim 43\%$ the yield of the second tip for the short and long spacer respectively. Thus, we conclude that the encoded spacer in the $M13l(CgbpC)_2$ is more efficient to make the cysteine groups accessible for reaction with Au NPs.

2.3.3.2 Purification steps

For the future study of dumbbell-like particles, we have proceeded with the removal of free beads present in suspension produced with $M13l(CgbpC)_2$ where the maximum amount of this morphology is found. This sample is a mixture of multiple structures of unknown sedimentation coefficients. For this reason, we have applied lower acceleration for the centrifugation than the estimated one for Au NPs of $D = 10$ nm (see table 2.2). In this case, we have done multiple steps of $5000 g \times 30$ min. However, even for gentle centrifugation conditions, some structures are sedimented in the pellet. The final distribution of structures is summarized in figure 2.25. This sample is used for the study of its dynamics in chapter 4.

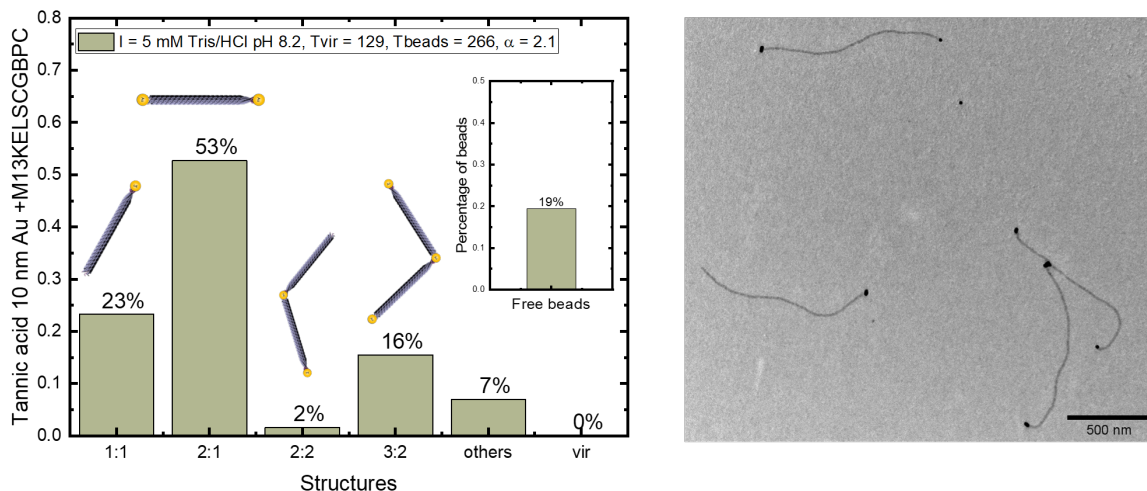


Figure 2.25: **Characterization of the dumbbell-like morphology after the purification steps.** **Left:** Histogram representing the fraction of A:B structures found. **Right:** Large field of view TEM image of the final state of the structures (3 dumbbell-like + 1 matchstick-like particles).

2.4 Conclusion and perspectives

In this chapter, we have introduced the genetic modification of the M13KE phage designed to promote the grafting of Au NPs at one and two virus tips with the aim to construct complex structures. This tip binding affinity for Au NPs has been designed based on the interaction of cysteine groups at the virus tips and Au NPs via a weak covalent bond.

We have used the M13C7C mutant, a genetically modified strain which possesses extra cysteine groups only at the p3 proteins of that virus tip, to reproduce matchstick-like and colloidal star structures previously found in literature [26, 55]. Our contribution is the study of the consequences of the genetic modification done at the p7 proteins of the M13KE virus which are not as exposed to the solvent for their functionalization as the p3 proteins. This genetic modification has allowed us for producing a novel gold-virus colloid, the dumbbell-like structure made by a single virus with one bead attached to each tip.

Here, we have introduced the mutants M13*s*(C*gbp*C)₂ and M13*l*(C*gbp*C)₂ for which it has been inserted at both virus tips a gold binding peptide between two cysteine groups C*gbp*C, a peptide sequence similar to the one at p3 of the M13C7C mutant. These novel strains differ with each other by the spacer that have been added before the encoded peptide at the p7 proteins with the aim to make it more accessible for their interaction with Au NPs.

The binding affinity for Au has been tested by measuring the percentage of reacted tips at the same reaction conditions. We have found a maximum yield of 80% and 88% when the conditions are $I = 40$ mM pH 6.2 for the M13*s*(C*gbp*C)₂ and M13*l*(C*gbp*C)₂ respectively. Considering that 45% of the yield corresponds to the binding at the p3 proteins, these represent a maximum of $\sim 35\%$ and $\sim 43\%$ for the binding at the p7 proteins. Thus, we conclude that the long negatively charged spacer used in the M13*l*(C*gbp*C)₂ mutant promotes a higher efficiency of the second tip binding affinity by making more accessible the cysteine groups for their interaction with gold.

Our findings have proved that the p7 proteins can be modified to promote the grafting of Au NPs. However, in comparison with the p3 proteins, the electrostatic repulsion has to be screened significantly more in order to interact with Au NPs. This is a process that can still be optimized. In this direction, we expect that varying some features such as the charge and length of the spacer used to expose the p7 proteins could improve the binding affinity of the second tip.

After an optimization of the binding affinity for Au (mostly in the distal end), a new type of hybrid colloids such as lattice structures and oligomeric chains could be constructed. For their production other reaction conditions have to be explored. For instance, in order to produce oligomeric chains we suggest to work at a virus concentration close to the overlap one, C^* . This reaction could be carried in two steps in order to assure that no more than two virus tips will interact with a single bead. First, the production of matchstick-like particles could be performed at low ionic conditions with a high molar excess. Then, after the removal of non-reacted beads, the concentration of the suspension could be increased to $\sim C^*$ and

the ionic conditions could be changed to promote the reaction with each other. Similarly, for the construction of lattice structures both nanoparticle size and virus concentration have to be tuned in order to find optimal conditions.

Chapter 3

Experimental techniques

3.1	Study of colloidal systems	38
3.2	Single particle tracking	38
3.2.1	Optical microscopy observation	39
3.2.2	Mean square displacement analysis	43
3.3	Dynamic light scattering principles	47
3.3.1	Spectral distributions of molecules of arbitrary shape	48
3.3.2	Dynamic light scattering experiment of isotropic particles	53
3.3.3	Intensity correlation function of rod-like particles	55
3.3.4	Diffusion coefficients from Intensity correlation function	57
	Appendix I. CONTIN analysis details	63

3.1 Study of colloidal systems

Colloids are suspensions of insoluble particles in the size range of ~ 10 nm to ~ 1 μm dispersed in a fluid medium [2]. These particles exhibit the so called Brownian motion, a spontaneous and random movement attributed to the thermal fluctuations characteristic of these scales [95]. The research interest of these systems stems from both a fundamental perspective and for their relevance in technological applications [25, 96, 97].

Recent advances in the chemical synthesis and fabrication of hybrid colloidal systems composed of inorganic materials and organic components have resulted in a wide variety of complex structures such as shape-anisotropic particles [98], micro-capsules [99] and patchy particles [100]. These novel hybrid colloidal molecules have specific characteristics given by their organization and by the materials that composed them. Investigating the dynamics and structure of these particles is a necessary step towards the understanding of their properties as well as their potential applications in many fields [51, 54, 101].

One of the difficulties in the study of colloidal systems lies in obtaining accurate information at these time and length scales which is essential to extract the dynamics. Common experimental techniques include X-ray, neutron, laser and light scattering as well as various optical microscopy modalities such as fluorescence, differential interference contrast and confocal microscopy. On one hand, light scattering techniques provide extensive information on the spatial and temporal correlations between particles, typically in the form of structure factors and intermediate scattering functions [102–104]. On the other hand, optical microscopy, paired with image recognition algorithms directly examine the dynamics and structural evolution of colloidal systems [105, 106]. However, existing limitations regarding particle sizes, volume fractions and accessible time scales as well as restrictions relative to the optical properties of the particles and solvent have to be considered when examining a particular system.

In chapter 2, we have introduced the bacteriophage based hybrid structures subject of study of this work. These are composed of spherical gold nanoparticles and rod-like bacteriophages. In this chapter we outline the principles of the techniques we use for the understanding of the dynamics and structure of these systems: single particle tracking and dynamic light scattering.

3.2 Single particle tracking

Single-particle tracking (SPT) is a popular tool used to quantify the dynamics of individual particles in colloid science and soft matter physics [106]. This technique is based in the possibility of directly visualize colloids. By means of optical microscopy techniques, multiple particles are located on a continuous sequence of frames in order to reconstruct and analyze the resulting single-particle traces. From this approach it is possible to measure the mean squared displacement to describe the motion and the radial distribution function to

characterize structure [107, 108].

In order to obtain an accurate SPT measurement, the quality of our video microscopy recording has an important impact. In the following, we identify the optical microscopy principles implemented for the observation of our hybrid gold-virus colloids.

3.2.1 Optical microscopy observation

A precise visualization of particles depends on the shortest distance between two points on a plane that can still be distinguished by the observer as separate entities. This, also known as the optical resolution, is limited by diffraction [105]. For a microscope objective lens with no aberrations, the three dimensional diffraction pattern near the focal point is symmetrically periodic along the axis of the microscope as well as radially around this axis. When the three-dimensional diffraction pattern is projected in the focal plane, it is observed as two-dimensional diffraction pattern, the *Airy disk* (see figure 3.1).

For objects illuminated with a large-angle cone of light, the light waves that form adjacent Airy disks are incoherent and thus do not interfere with each other. Then, it is possible to determine the minimum separation that can be resolved with a particular microscope in the image plane. Let's define D as the center-to-center distance of two adjacent illuminated particles with r_{spot} equal the radius of the Airy disk. As shown in figure 3.1 (a), the sum of the diffraction patterns for $D < r_{spot}$ results into a single spot and into barely two spots for $D = r_{spot}$, while for $D > r_{spot}$ it is clearly retrieve the two patterns.

Hence, for well-corrected objective lenses with uniform circular aperture, the smallest distance resolvable between two adjacent points is found when the centers of their Airy disks are separated by $D = r_{spot}$. This, also known as Rayleigh criterion, is given by [105]:

$$d_{min} = \frac{1.22\lambda}{2N.A.} = \frac{1.22\lambda}{2n \sin(\alpha)}, \quad (3.1)$$

where λ is the wavelength of the light, $N.A.$ is the numerical aperture of the objective, n is the index of refraction of the immersion medium between the sample and the objective, and α is half the maximum light-collecting angle of the objective (see figure 3.1 (b)). Thus, the optical resolution can be increased by using high-index immersion medium, i.e., water or oil instead of air and by increasing the light-collecting angle of the objective α , i.e., the numerical aperture.

From equation 3.1, it follows that for a microscope with an oil immersion objective of $N.A. = 1.3$ and green illumination of $\lambda = 532$ nm the limit of resolution is about $d_{min} = 250$ nm. Despite this, an object with size much smaller than d_{min} can still be visible in a standard optical microscope if the light intensity of the object is high enough compared to the overall background intensity, i.e., if the image has sufficient contrast and if the acquisition time of observation is shorter than its dynamics. However, its image results in a spot having a radius of $r_{spot} = d_{min}$ [109]. The elements that compose our hybrid gold-virus assemblies

are rod-shaped filamentous viruses of length $L = 1 \mu\text{m}$ and diameter $d = 7 \text{ nm}$ as well as spherical gold nanoparticles of diameters from 10 to 50 nm. Since the diameter of our viruses are lower than the optical resolution we expect from our observations to be able to visualize $1 \mu\text{m}$ rods of hundreds of nanometers in diameter. Similarly, that our gold nanoparticles are imaged as spots of hundred of nanometers which won't differ too much in size.

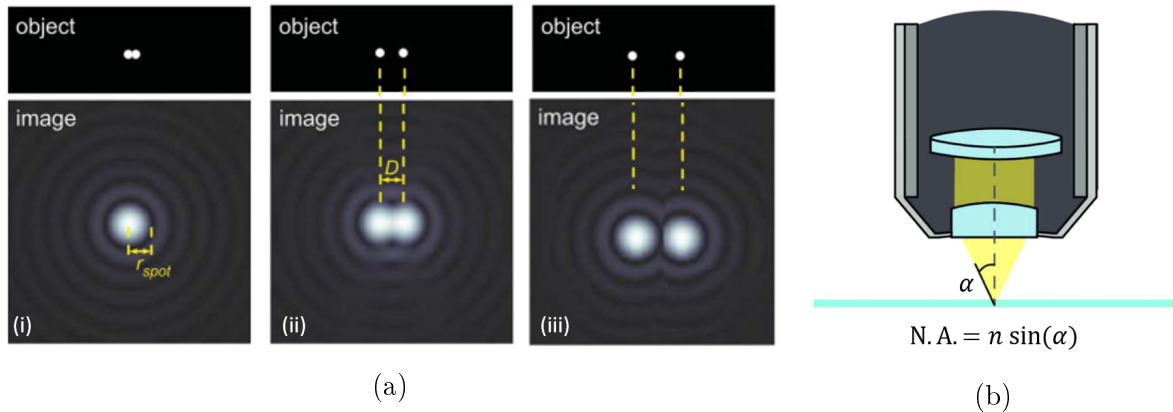


Figure 3.1: **(a) Schematic representation of the Rayleigh criterion.** Diffraction limit (lower panel) of two objects (upper panel) when **(i)** $D < r_{spot}$, **(ii)** $D = r_{spot}$ and **(iii)** $D > r_{spot}$. Adapted from reference [109]. **(b) Scheme of the objective numerical aperture.** The resolution limit of optical microscopes depends on the numerical aperture of the system defined as $N.A. = n \sin(\alpha)$.

In the same way that the lateral resolution is defined for distances within the plane of focus, we can describe the depth over which the fine focusing control of the microscope can be adjusted without diminishing the sharpness of the image. This, also known as *depth of field* or *depth of focus*, is proportional to the wave optical depth [109]:

$$d_z \simeq \frac{\lambda n}{(N.A.)^2}. \quad (3.2)$$

Note from equations 3.1 and 3.2 that the depth of focus is reduced inversely proportionally with the square of $N.A.$ while the lateral resolution with the first power of $N.A.$ Thus, the axial resolution is more affected than the lateral one by the objective $N.A.$

From an oil immersion objective ($n = 1.52$) of $N.A. = 1.3$ and green illumination of $\lambda = 532 \text{ nm}$ it follows that the axial resolution is $d_z \sim 480 \text{ nm}$ while the lateral one, i.e., in the XY plane is $d \sim 250 \text{ nm}$. As result, when an object is vertically displaced on the order of d_z it will be imaged as a blur spot.

Thus, with optical microscopy observation it is possible to visualize objects in a thin optical section for which a microscope can produce clear images of focal planes. The optical microscopy techniques used for the visualization of our structures are described below.

3.2.1.1 Fluorescence microscopy

Fluorescence microscopy is a technique that allows to study materials which can be made to fluoresce either in its natural form or when treated with labeling dyes. When a fluorescent particle is irradiated at the absorption wavelength it results in the emission of fluorescent light which has commonly a longer wavelength [95] (see figure 2.12). A filter cube, consisting of excitation and emission filters and a dichroic mirror, is placed in the optical path to separate the emission signal (see figure 3.2 a)). This ensures that only the emitted light arrives to the camera resulting in fluorescing areas shining against a dark background with sufficient contrast to allow detection.

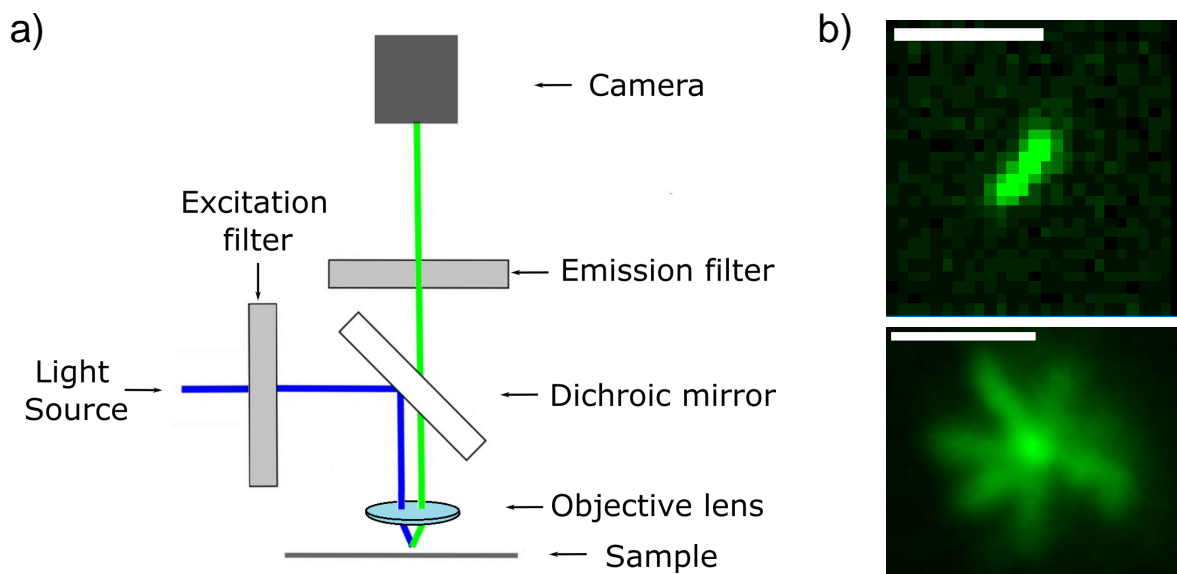


Figure 3.2: **Fluorescence microscopy.** a) Schematic diagram of the fluorescence microscopy setup. b) Images showing matchstick-like (top) and colloidal star particles (bottom). Scale bars represent $2 \mu\text{m}$.

For our fluorescence microscopy observations we use an inverted microscope Olympus IX71 equipped with a 100x oil-immersion objective PlanAPO of $N.A. = 1.4$, a Omicron LedHub light engine as excitation light source and a Neo sCMOS camera. In figure 3.2 b), are shown fluorescence microscopy images of matchstick-like and colloidal star particles made of viruses labeled with fluorescent dye molecules (see section 2.2.2). Note that the single virus is pictured as a $L \sim 1 \mu\text{m}$ rod of diameter $d \sim 300 \text{ nm}$ which is consistent with the lateral resolution of our experiment.

Thanks to this technique it is possible to visualize only the viruses composing the structures to extract the dynamics information. However, two main limitations of this technique have to be considered. The first one is due to the intrinsic weak signal of the fluorescent dyes which sometimes does not provide the sufficient contrast for visualization and the second is that the observation time is limited by the fluorescence lifetime of the dye,

i.e., the maximum time before it photo-bleaches, which complicates long time recordings.

3.2.1.2 Dark-field microscopy

A scheme of dark-field microscopy configuration is shown in figure 3.3. For this arrangement, the objective must have smaller numerical aperture than the dark-field condenser [110]. This forms a hollow cone of light when the sample is illuminated (see figure 3.3). Due to the lower $N.A.$ of the objective, only the light scattered by particles whose refractive index is different from the surrounding medium arrives to the camera. Thus, the particles in the sample appear bright with a dark background.

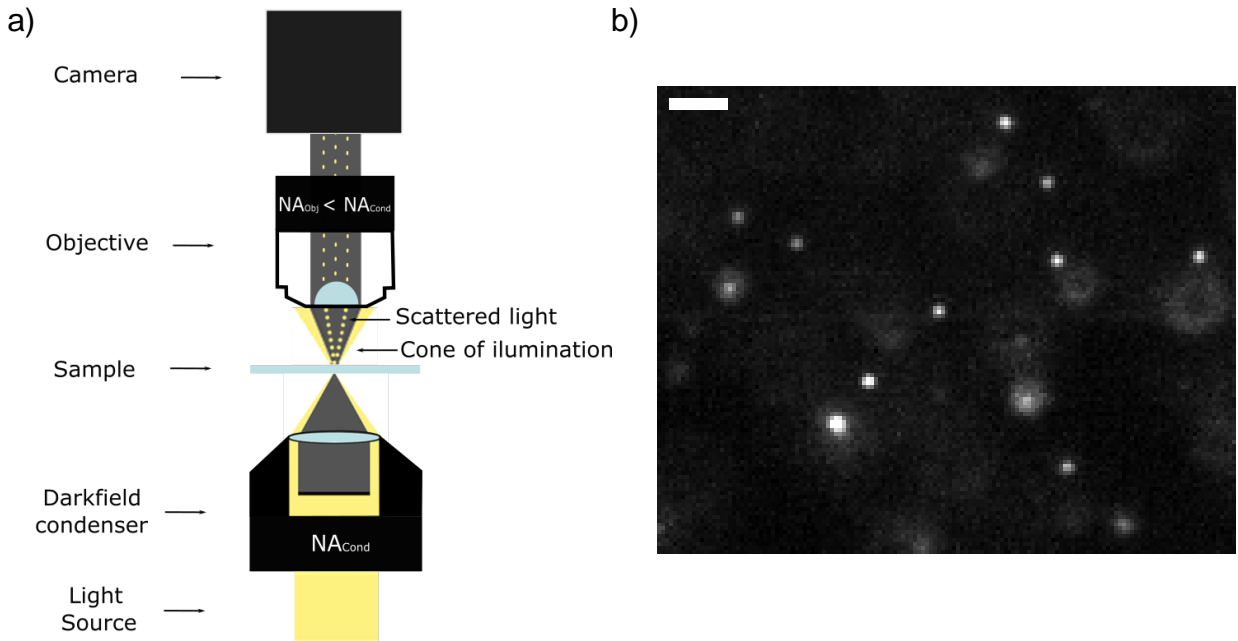


Figure 3.3: **Dark field microscopy.** a) Schematic representation of the dark-field microscopy setup. b) Image of colloidal star particles made of 50 nm gold nanobeads. Scale bar represents 2 μm .

Here, we performed dark-field imaging using an Olympus UPlanFLN 100x Oil Objective of adjustable $N.A.$ (from 0.6-1.3) and a Olympus U-DCW oil dark field condenser ($N.A.$ 1.2-1.4). In figure 3.3 b) it is shown a dark-field image of colloidal star particles made of 50 nm gold beads. The contrast in the image comes from the absorption and scattering of the light illumination by the gold nanoparticles. The variation of scattering intensity can be in part attributed to size effects ⁱ.

With this technique we are able to extract the information of the dynamics from the direct visualization of the gold nanobeads composing the structures without limitation of recording time. The main constrain of this method is the nanoparticle size. As the diameter decreases, the scattered intensity does the same in a power of sixth resulting in a low contrast. Moreover, smaller NPs experience higher diffusivity which makes the visualization more

ⁱAccording to the Rayleigh scattering theory the scattering intensity increases with the power sixth of the particle diameter, i.e., $I \sim (\frac{d}{2})^6$ [103].

difficult. The virus attached the Au NPs composing our matchstick-like structures slows them down enabling their visualization. Nevertheless, for particles smaller than 30 nm in diameter the intensity signal is not enough to have sufficient contrast for their detection.

3.2.2 Mean square displacement analysis

In order to characterize the dynamics of our hybrid gold-virus colloids, the Mean Squared Displacement (MSD) is calculated relying on the individual trajectories traced down by optical microscopy observation. For this purpose, a custom-written MATLAB code is used. The procedure of extracting a particle trajectory is represented in figure 3.4 and achieved as follows. First, an optical microscopy technique is chosen accordingly to the system of study. For example, fluorescence microscopy allows visualizing the center of mass at the viruses composing the matchstick-like particles while dark field microscopy enables the observation of the bead at the center of the colloidal star structures. Next, a series of images are taken at a given frame rate. For each particle in a frame the center of mass is determined by the localization of the intensity peaks. In this way, the positions of each particle are determined with pixel accuracy. Then, the acquired positions are linked to reconstruct the trajectories using an implementation based on the work by Crocker and Grier [111].

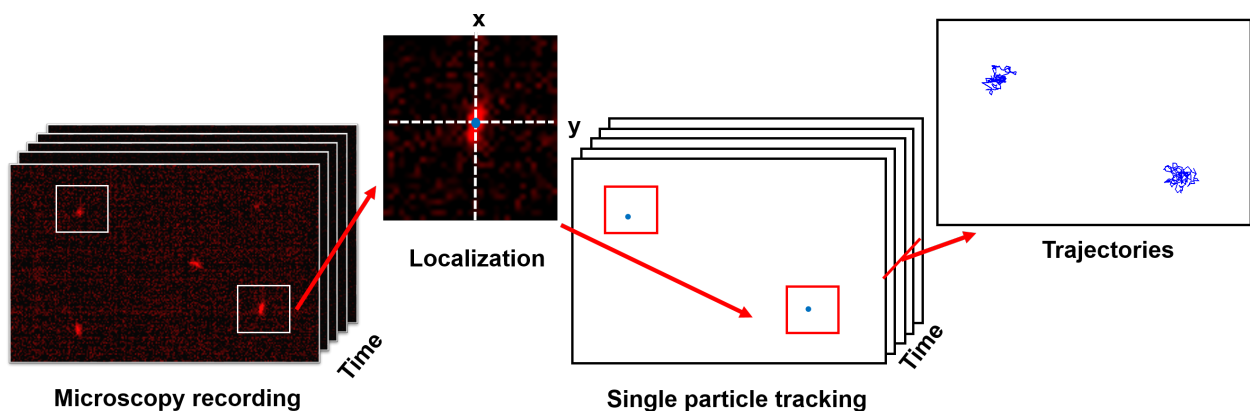


Figure 3.4: **Steps of single particle tracking.** The trajectory reconstruction consists of several steps. First, a series of images are recording with optical microscopy and the individual particles are localized at a given time. Then, the positions are related in time to reconstruct the trajectories of a single particle.

For multiple trajectories, the MSD is calculated as the average of the squared distance between the particle's start and end positions for all lag time in one trajectory as[108]:

$$\text{MSD}(t_{lag} = m\Delta t) \equiv \frac{1}{N - m} \sum_{i=1}^{N-m} [\mathbf{r}(t_i + m\Delta t) - \mathbf{r}(t_i)]^2, \quad (3.3)$$

where $\mathbf{r}_j(t_i + m\Delta t)$ is the particle position with $\mathbf{r}_j(t_i)$ as the starting point at the time interval of $m\Delta t$, N is the total frames of the particle trajectory, Δt is the acquisition time

of each frame and m is an integer. The MSD can also be defined as an ensemble average over the probability density $G_s(\mathbf{r})$ of finding a particle at position $\mathbf{r}(t)$ at time t [112]:

$$\text{MSD} = \int G(\mathbf{r}, t) \mathbf{r}^2 d\mathbf{r}. \quad (3.4)$$

$G(\mathbf{r}, t)$ is known as the self-Van Hove function and can be directly calculated from the particles positions as:

$$G(\mathbf{r}, t) = \frac{1}{N} \sum_{i=1}^N \delta[\mathbf{r}(t) + \mathbf{r}_i(0) - \mathbf{r}_i(t)]. \quad (3.5)$$

In complex systems, the MSD is generalized for n dimensions by the power law [113]:

$$\text{MSD} = 2n D_{\parallel, \perp} t_{\parallel, \perp}^{\gamma}, \quad (3.6)$$

where $D_{\parallel, \perp}$ and $\gamma_{\parallel, \perp}$ are the diffusion rate and diffusion exponent in the parallel (\parallel) and perpendicular (\perp) directions to the particle axis respectively. As shown in figure 3.5 for the simplest case, $\gamma = 1$ corresponds to a random Brownian motion with D_T the translational diffusion coefficient, $\gamma < 1$ represents subdiffusive behavior which is characteristic of crowded systems and $\gamma > 1$ is signature of superdiffusion which can be observed for self-propelled motion, i.e., particles with speed v for which is found $\text{MSD} \sim v^2 t^2$ [114].

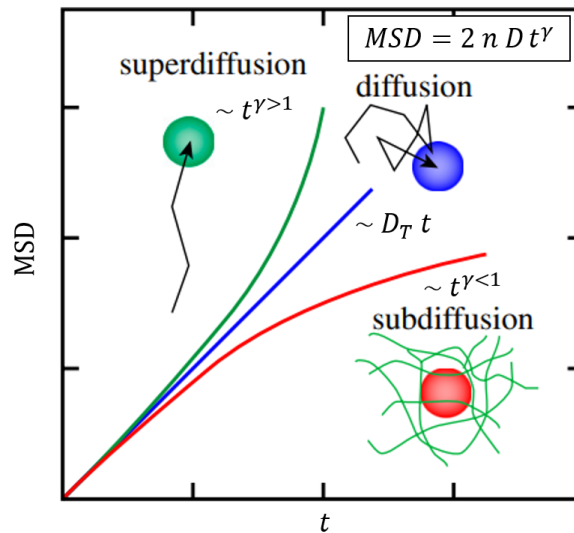


Figure 3.5: **Typical diffusion regimes characterized by MSD.** In equilibrium (blue line), a linear dependence on t is expected for motion in simple liquids. In crowded environments (red line), a subdiffusive regime is expected. By contrast, a superdiffusive motion (green line) often indicates self-propulsion. Adapted from reference [115].

From equation 3.6, it follows that for Brownian diffusion, i.e., $\gamma = 1$, the self-diffusion coefficient can be determined from the slope of a linear fit to MSD vs time. At the infinite dilute regime, the translational diffusion coefficient, D_T^{sphere} , of spherical particles of radius a is given by equation 1.1. For the case of rod particles of length L and diameter d [102]:

$$D_T^{\text{Rod}} = \frac{1}{3}(D_{\parallel} + 2D_{\perp}) = \frac{k_B T}{3\pi\eta L} \ln\left(\frac{L}{d}\right) \quad \text{and} \quad D_R^{\text{Rod}} = \frac{3k_B T}{\pi\eta L^3} \ln\left(\frac{L}{d}\right) \quad (3.7)$$

with

$$D_{\parallel} = \left(\frac{k_B T}{2\pi\eta L}\right) \ln\left(\frac{L}{d}\right) \quad \text{and} \quad D_{\perp} = \frac{1}{2}D_{\parallel} = \left(\frac{k_B T}{4\pi\eta L}\right) \ln\left(\frac{L}{d}\right) \quad (3.8)$$

the diffusion coefficients parallel and perpendicular to the rod axis in the slender rod limit, i.e., $L \gg d$.

In this way, from the particles trajectories extracted by SPT it is possible to get information on the dynamics of a particular system. In order to get reliable information on the diffusion coefficient, it is needed to evaluate above 60 tracks and to lower the variance in the calculated value around 90 traces [116]. Moreover, other experimental parameters such as the frame rate have to be considered to have access to all the dynamic information. For instance, to derive the speed of self-propelled systems one needs to achieve a frame rate sufficiently high enough for the acquisition time to be significantly lower than the relaxation time, $\tau = (D_R)^{-1}$, equal to the inverse of the rotational diffusion coefficient of the particles being studied.

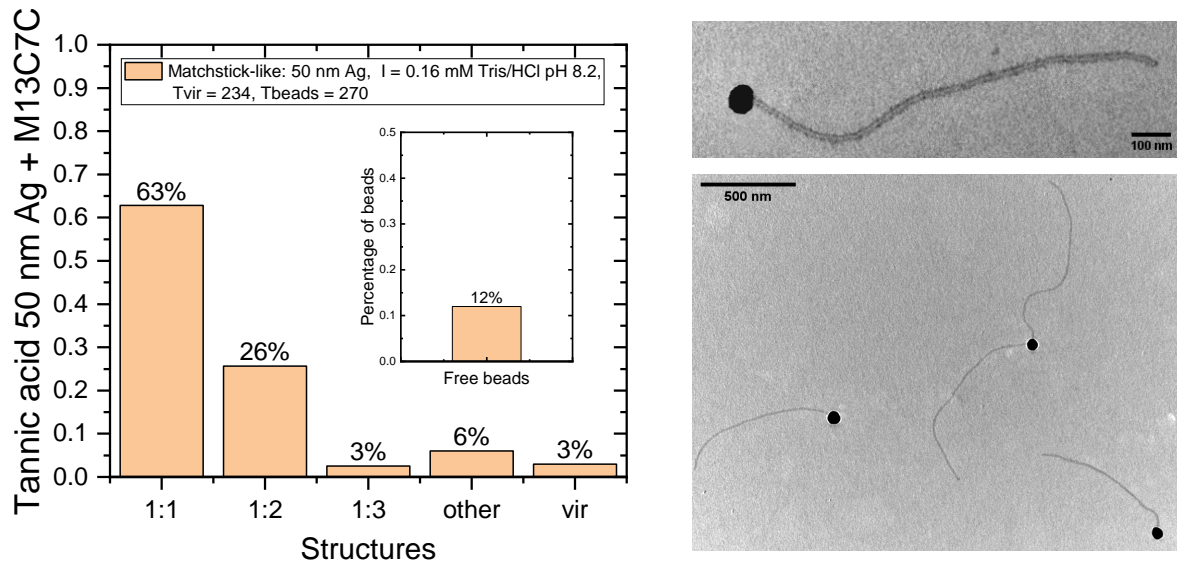


Figure 3.6: **TEM statistics of the matchstick-like particles of $D = 50$ nm Ag** Left: Distribution of structures in percentage of viruses. **Right:** TEM images of the structures found in suspension.

In the following example we report the results of the MSD calculation on matchstick-like particles composed of silver nanoparticles of diameter $D = 50$ nm and full body labeled viruses. The structures distribution and TEM image of this system is shown in figure 3.6. For the experiment, we have prepared a suspension of $\sim 50\%$ water-glycerolⁱⁱ mixture of viscosity

ⁱⁱGlycerol is an organic compound containing multiple hydroxyl groups commonly used in fluid mechanics to adapt a liquid density [117].

$\eta = 6.6 \times 10^{-3} \text{ Pa} \cdot \text{s}$ and a structure's concentration of $C_v = 1 \times 10^{-4} \text{ mg/ml}$. These have been observed through fluorescence microscopy allowing us to track the rod-shaped viruses trajectories. The video recording is taken at a rate of 127.9 frames per second (fps), i.e., acquisition time of $\sim 8 \text{ ms}$, in order to have access to all the dynamics of $L = 1 \mu\text{m}$ rods for which it is found $\tau = (D_R)^{-1} \sim 50 \text{ ms}$.

From the SPT analysis of our movies we have extracted the positions of the center of mass of the viruses in a two-dimensional plane (objective focus plane) for ~ 65 traces. From these, we have calculated the MSD of the structure. In figure 3.7 is plotted the log-log representations of the averaged MSD for which it is found a nearly diffusive behavior, i.e., $\gamma = 1$. According to equation 3.6, the linear fit for the MSD in two dimensions corresponds to: $MSD = 4D_T$. Hence, we find that the translational diffusion coefficient of the matchstick-like particles at these conditions is $D_T = 0.34 \mu\text{m}^2/\text{s}$.

Matchstick-like of 50nm Ag in Tris/HCl I = 0.16 mM pH 8.2, 53.2% glycerol

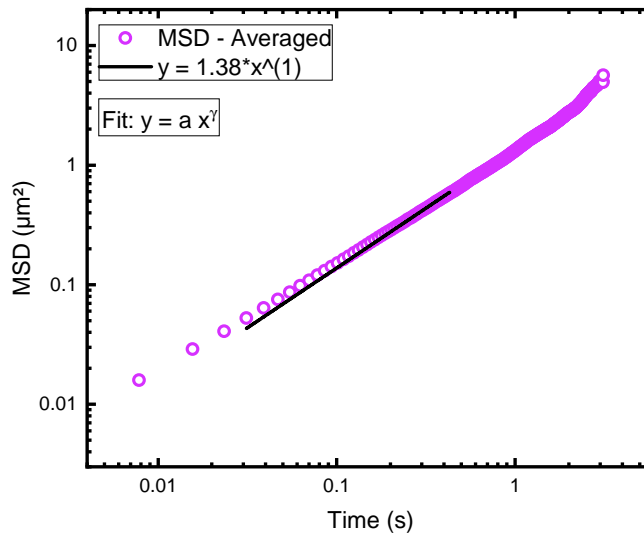


Figure 3.7: MSD of matchstick-like particles made of 50 nm silver. For a virus concentration of $1 \times 10^{-4} \text{ mg/ml}$ in a viscous medium of $\eta = 6.6 \times 10^{-3} \text{ Pa} \cdot \text{s}$ it is found a diffusive regime, i.e., $\gamma = 1$. The diffusion coefficient $D_T = 0.34 \mu\text{m}^2/\text{s}$ is calculated according to equation 3.6 for two dimension.

In our group, it has been previously obtained by SPT the diffusion coefficient, $D_T = 2.25 \mu\text{m}^2/\text{s}$, for matchstick-like particles in water, i.e., at viscosity $\eta = 1 \times 10^{-3} \text{ Pa} \cdot \text{s}$ [55]. This value is consistent with the one we obtain considering the change in viscosity. Moreover, we compare this results with the theoretical value for rods of $L = 1 \mu\text{m}$ given by equation 3.7. For $\eta = 1 \times 10^{-3} \text{ Pa} \cdot \text{s}$ and $\eta = 6.6 \times 10^{-3} \text{ Pa} \cdot \text{s}$ it is found $D_T = 2.0 \mu\text{m}^2/\text{s}$ and $D_T = 0.32 \mu\text{m}^2/\text{s}$ respectively. Thus, from our experimental observations, we conclude that the diffusion of the matchstick-like structure is similar to the one of single rod-shaped viruses.

3.3 Dynamic light scattering principles

Another experimental technique commonly used for particle size analysis and diffusion coefficients determination in colloidal science [118–120] is Dynamic Light Scattering (DLS). When a monochromatic light source impinges on a single molecule of polarizability α , the incident light induces a dipole moment which varies with time [121]. The resulting electric field emitted from each molecule is consecutively a secondary source of light, the scattered light. This secondary source of light will either result in mutual destructive phases or mutual constructive ones which are detectable as intensity fluctuations [103].

For a typical DLS setup, as shown in figure 3.8, a laser beam is used to illuminate a suspension with scattering particles. This incident source of light is a plane electromagnetic wave [102]:

$$\mathbf{E}_i(r, t) = \hat{\mathbf{n}}_i E_0 \exp i [\mathbf{k}_i \cdot \mathbf{r} - \omega_i t], \quad (3.9)$$

of wave length λ , frequency ω_i , amplitude E_0 and polarization $\hat{\mathbf{n}}_i$ perpendicular to the initial propagation vector \mathbf{k}_i . After the light passes through the sample, the scattered intensity is recorded as a function of the observation angle θ where the detector is placed. Assuming that the scattering process is elastic, the magnitude of the final propagation vector \mathbf{k}_f of the scattered electric field $\mathbf{E}(r, t)$ remains the same after the scattering process, i.e.:

$$|\mathbf{k}_i| = |\mathbf{k}_f| = \frac{2\pi n}{\lambda},$$

with n the refractive index of the solvent. Then, the magnitude of the resulting scattering vector $\mathbf{q} \equiv |\mathbf{k}_i - \mathbf{k}_f|$ is given by [102]:

$$q = \frac{4\pi n \sin\left(\frac{\theta}{2}\right)}{\lambda}. \quad (3.10)$$

An analyzer placed in front of the detector permits that only the scattered light of polarization $\hat{\mathbf{n}}_f$ arrives to it. Due to the diffusive behavior of the particles in suspension, the intensity of the scattered light fluctuates with respect to time. In order to determine how rapidly the intensity fluctuates, the correlator computes the second order correlation function or intensity correlation function $G_2(q, t) \equiv \langle I(q, t')I(q, t' + t) \rangle$, expressed as an integral over the product of intensities at time t' and delay time $t' + t$. The $G_2(q, t)$ is commonly expressed in its normalized form as:

$$g_2(q, t) = \frac{\langle I(q, t')I(q, t' + t) \rangle}{\langle I(q, t') \rangle^2}, \quad (3.11)$$

where t is the lag time between two time points. In equation 3.11, the brackets represent average over the duration of the experiment t' , also known as run time.

The intensity correlation function is related to the first-order correlation function

$G_1(q, t) \equiv \langle \mathbf{E}(q, t') \mathbf{E}(q, t' + t) \rangle$ of normalized form:

$$g_1(q, t) = \frac{\langle \mathbf{E}(q, t') \mathbf{E}(q, t' + t) \rangle}{\langle \mathbf{E}(q, t') \mathbf{E}^*(q, t') \rangle}, \quad (3.12)$$

which corresponds to the correlation of the scattered electric fields at time t' and $t' + t$. Assuming that the scattering process is homodyne, i.e., that only scattered light arrives to the detector and that the photon counting is a random Gaussian process, the two autocorrelation functions $g_1(q, t)$ and $g_2(q, t)$ can be coupled to each other thanks to the Siegert relation [118]:

$$g_2(q, t) = 1 + \beta |g_1(q, t)|^2, \quad (3.13)$$

where β is known as the coherence factor that depends on detector area, optical alignment and scattering properties of the particles.

The DLS setup used in this work is an ALV laser goniometer, with a 632.8 nm HeNe linearly polarized laser and an ALV500/EPPⁱⁱⁱ digital correlator of minimum lag time $t = 200$ ns = 2×10^{-4} ms. The range of angles allowed for this experimental setup is $30^\circ < \theta < 150^\circ$ and therefore a range of $6.85 \times 10^{-3} \text{ nm}^{-1} < q < 2.56 \times 10^{-2} \text{ nm}^{-1}$.

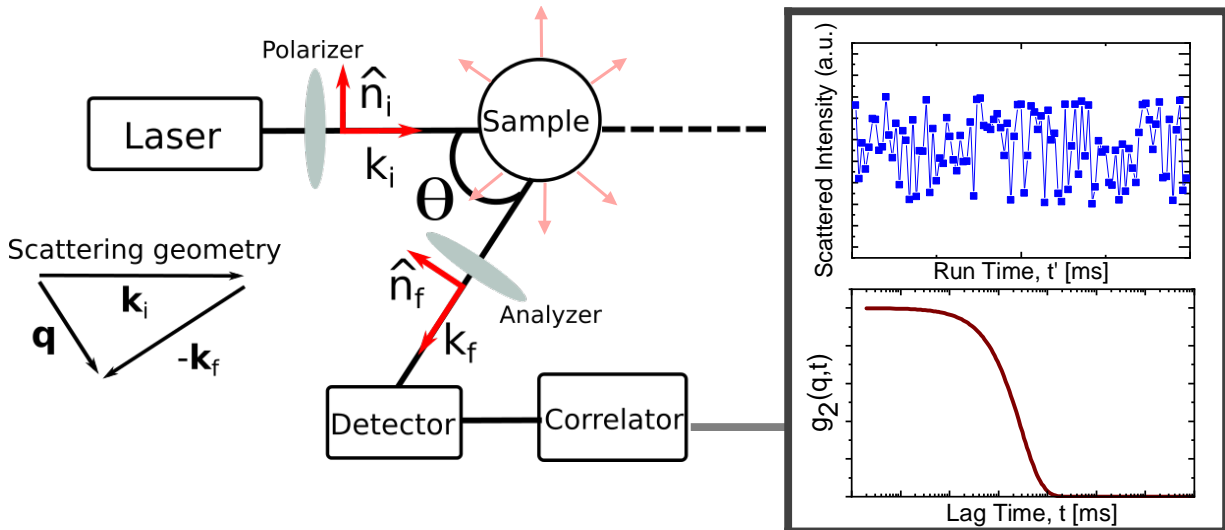


Figure 3.8: **Schematic representation of dynamic light scattering (DLS) experimental setup.** An incident beam of polarization $\hat{\mathbf{n}}_i$ is directed toward the sample which scatters in all directions. The resulting scattering vector \mathbf{q} is defined in terms of the initial and final propagation vector as $\mathbf{q} \equiv |\mathbf{k}_i - \mathbf{k}_f|$. The analyzer selects only the scattered light with polarization $\hat{\mathbf{n}}_f$ that arrives to the detector placed at a given angle θ . For a given run time the detector measures the scattered intensity (top graph) from which the correlator computes the intensity correlation function (bottom graph).

3.3.1 Spectral distributions of molecules of arbitrary shape

In a dilute solution of molecules of arbitrary shape, it is convenient to consider the basic scattering element to be a “segment” of the main molecule. Each one is subdivided into m

ⁱⁱⁱExternal correlator connected to the PC via a EPP board. From ALV-GmbH Technology.

identical segments which are chosen in such a way that its maximum size l is small compared to $1/q$ i.e., $ql \ll 1$. This means that each segment can be considered as a scatter point and that there is no significant intra-segment interference. When these conditions are fulfilled and the solution is sufficiently diluted so segments of different molecules do not interact with each other, the scattered field correlation function is given by [102]:

$$g_1(q, t) = \langle N \rangle \langle \alpha_{if}(0) \alpha_{if}(t) \rangle S(\mathbf{q}, t), \quad (3.14)$$

where N is the number of illuminated molecules, $\alpha_{if} \equiv \mathbf{n}_i \cdot \boldsymbol{\alpha} \cdot \mathbf{n}_f$ is the projection of the polarizability tensor $\boldsymbol{\alpha}$ onto the initial and final polarization directions of the light wave and

$$S(\mathbf{q}, t) \equiv \frac{1}{m^2} \left\langle (\exp(i\mathbf{q} \cdot \mathbf{R}_t)) \left(\sum_{i=1}^m \sum_{j=1}^m \exp(i\mathbf{q} \cdot [\mathbf{r}_i(t) - \mathbf{r}_j(0)]) \right) \right\rangle \quad (3.15)$$

is the dynamic form factor. In equation 3.15, \mathbf{R}_t represents the displacement of the center of mass of a molecule in the lag time t and $\mathbf{r}_{i,j}(t)$ the molecular segmental positions whose summation is done over segments belonging to the same molecule.

Note from equation 3.14 that the elements of the molecular polarizability tensor α_{if} change with time because of the molecular reorientation. Hence, the correlation function $\langle \alpha_{if}(0) \alpha_{if}(t) \rangle$ is purely local and does not depend on q . The only q dependence in equation 3.14 is the dynamic form factor of a single molecule.

Consequently, it is possible to obtain information on the structure of the molecules within a system from the scattered field correlation function $g_1(q, t)$ which is linked to the intensity correlation function measured by DLS through equation 3.13. The dynamic form factors of spheres and rod-like particles have to be considered for the purpose of this work.

3.3.1.1 Form factor of ideal spherical particles

For a system of ideal spherical particles of uniform polarizability and radius r which are divided in m equal segments, the sum in equation 3.15 is not time-dependent since the only relative segmental motion allowed is rotation. This can be seen from the fact that the m identical segments are arranged radially from the center of the sphere (see figure 3.9). Thus, for an ideal sphere, equation 3.15 becomes:

$$S(q, t) = \langle \exp(i\mathbf{q} \cdot \mathbf{R}_t) \rangle S(q), \quad (3.16)$$

where $S(q)$ is the form factor for a sphere which may be written as [102]:

$$S_{\text{Sphere}}(qr) = \left[\frac{3}{(qr)^3} (\sin(qr) - qr \cos(qr)) \right]^2. \quad (3.17)$$

This expression corresponds to an oscillating function whose first minimum is found at $qr = 4.49$ as shown in figure 3.10 (a). In common DLS experiments the wave vector is $q \sim 10^{-2} \text{ nm}^{-1}$ while the radius of spherical nanoparticles can be as small as $r \sim 1 \text{ nm}$. Hence, qr will be in the order of magnitude of 10^{-2} which means that the form factor will be ~ 1 . The latest is consistent with the Guinier approximation which indicates that for small angles, i.e., $q \ll 1$, the form factor will be proportional to the radius of gyration R_g^{iv} as $S(q) \simeq 1 - \frac{(qR_g)^2}{3}$ for spheres until $qR_g \sim 1.3$ [122].



Figure 3.9: Schematic representation of a sphere of radius r divided in m equal segments.

The dynamics of a spherical particle is found in the coefficient of the form factor (equation 3.16). Also known as *self-intermediate scattering function*, $F_s(\mathbf{q}, t) \equiv \langle \exp(i\mathbf{q} \cdot \mathbf{R}_t) \rangle$ is related to the self-Van Hove function $G_s(\mathbf{r}, t)$ (see section 3.2.2) by an inverse Fourier transform as [102]:

$$G_s(\mathbf{r}, t) = (2\pi)^{-3} \int \exp(-i\mathbf{q} \cdot \mathbf{r}) F_s(\mathbf{q}, t) d^3q. \quad (3.18)$$

For a particle to suffer a displacement \mathbf{r} in the time t , $G_s(\mathbf{r}, t) = \langle \delta(\mathbf{r} - \mathbf{R}_t) \rangle$. As time progresses, it is expected that the spherical particle will perform a random walk, i.e., that the particle diffuses by a translational diffusion process of diffusion coefficient, D_T (e.q. 1.1). Then, $G_s(\mathbf{r}, t)$ can be regarded as the solution to the diffusion equation

$$\frac{\partial}{\partial t} G_s(\mathbf{r}, t) = D_T \Delta^2 G_s(\mathbf{r}, t), \quad (3.19)$$

subject to the initial condition $G_s(\mathbf{r}, 0) = \langle \delta(\mathbf{r}) \rangle = \delta(\mathbf{r})$. The spatial Fourier transform of equation 3.19 gives

$$\frac{\partial}{\partial t} F_s(\mathbf{q}, t) = -q^2 D_T F_s(\mathbf{q}, t). \quad (3.20)$$

Subject to the boundary condition $F_s(\mathbf{q}, 0) = 1$, equation 3.20 has as solution:

$$F_s(\mathbf{q}, t) = \exp(-q^2 D_T t) = \exp\left(\frac{-t}{\tau}\right). \quad (3.21)$$

Thus, we conclude that the dynamic form factor of spheres is a single exponential decay

^{iv}The radius of gyration R_g is defined as the root mean-square radius of a macromolecule as: $R_G^2 = \frac{\langle \sum_{i=1}^m (\mathbf{r}_i - \mathbf{R}_t)^2 \rangle}{m}$ [102].

function of decay time $\tau = (q^2 D_T)^{-1}$. Then, equation 3.16 is expressed as [102]:

$$S(q, t) = \exp(-q^2 D_T t) S(q). \quad (3.22)$$

For ideal spheres of radius r , D_T is given by the Stokes-Einstein relation of equation 1.1: $D_T = \frac{k_B T}{6\pi\eta r}$, in terms of the absolute temperature T and viscosity of the solvent η . Since water has a viscosity $\eta \sim 0.001 \text{ Pa} \cdot \text{s}$, the translational diffusion coefficient in aqueous solution at room temperature is $D_T \sim 2r^{-1} \times 10^{-1} \mu\text{m}^2/\text{s}$, with r in μm . For visible light and a scattering angle $\theta \sim 90^\circ$, the wave vector given by equation 3.10 corresponds to $q \sim 10^{-2} \text{ nm}^{-1}$. Then, $q^2 D_T \sim r^{-1} \times 10 \text{ s}^{-1}$ and therefore the decay time is of the order $\tau \sim r \times 10^{-1} \text{ s}$ which means that $F_s(\mathbf{q}, t)$ decays more slowly for larger particles. For instance, for spheres of radius $r \sim 0.01 \mu\text{m} = 10 \text{ nm}$, $\tau \sim 10^{-3} \text{ s}$ while for spheres of radius $r \sim 1 \mu\text{m}$, $\tau \sim 10^{-1} \text{ s}$. In the case of not aqueous solutions, the decay time τ will shift accordingly due to the change of viscosity. A higher viscosity medium will decrease D_T and consequently increase τ while a lower viscosity medium will decrease it.

3.3.1.2 Form factor of thin rod-like particles

For a system of rod-like particles of diameter d negligible compared to the wavelength of the light, i.e., $qd \ll 1$, the m identical optically isotropic segments are arranged along a line of length L (see inset of figure 3.10 (a)). Thus, to the light wave, the rod is a distribution of polarizable segments along a straight line. Since all the segments are arranged along a line, the position of one segment relative to the center of mass of the rod is parallel or anti-parallel to a given vector pointing along the rod. Hence, it only has to be described by the segmental motion along the rod which satisfies a translational-rotational diffusion equation.

For a system of long thin rod-like particles of aspect ratio $p = L/d$, i.e., $p \gg 1$ the translational and rotational diffusion coefficients in the dilute regime are given by equation 3.7. Under the assumption that the rotational and translational motions may be decoupled, the dynamic form factor is expressed as [123]:

$$\begin{aligned} S(q, t) &= \sum_{l \text{ even}} S_{\frac{l}{2}}(qL) \exp(-[q^2 D_T + l(l+1)D_R]t) \\ &= S_0(qL) \exp(-q^2 D_T t) + S_1(qL) \exp[-(q^2 D_T + 6D_R)t] \\ &\quad + S_2(qL) \exp[-(q^2 D_T + 20D_R)t] + \dots \end{aligned} \quad (3.23)$$

where $S_{\frac{l}{2}}(qL)$ is defined in terms of the spherical Bessel functions, j_l , as

$$S_{\frac{l}{2}}(qL) = (2l+1) \left[\frac{2}{qL} \int_0^{\frac{qL}{2}} j_l(z) dz \right]^2. \quad (3.24)$$

From equation 3.23 it follows that the dynamic form factor of a long thin rod-like particle

consists in a sum of exponentials of weighting factors $S_i(qL)$. Then, the form factor of long thin rods is defined as the sum of the weighting factors:

$$S_{\text{Rod}}(qL) \equiv \sum_{l \text{ even}}^{\infty} S_{\frac{l}{2}}(qL). \quad (3.25)$$

The first four terms of the sum, $S_0(qL)$, $S_1(qL)$, $S_2(qL)$ and $S_3(qL)$ are plotted in figure 3.10 (b). In the limit of very low qL , the form factor is only composed by $S_0(qL)$. As qL increases, the following terms increase while $S_0(qL)$ does the opposite. Approximately for $qL > 3$, $S_1(qL)$ starts to contribute to the form factor and for $qL > 5$ it becomes an important part of it. Note that its contribution ranges from 12% of the total $S_{\text{Rod}}(qL)$ at $qL = 5.2$ to $\sim 58\%$ at $qL = 10$ [123]. The terms $S_2(qL)$ and $S_3(qL)$ are negligible for $qL < 8$ but increase to 10% of $S_{\text{Rod}}(qL)$ for $qL = 10$ and $qL = 14.8$ respectively.

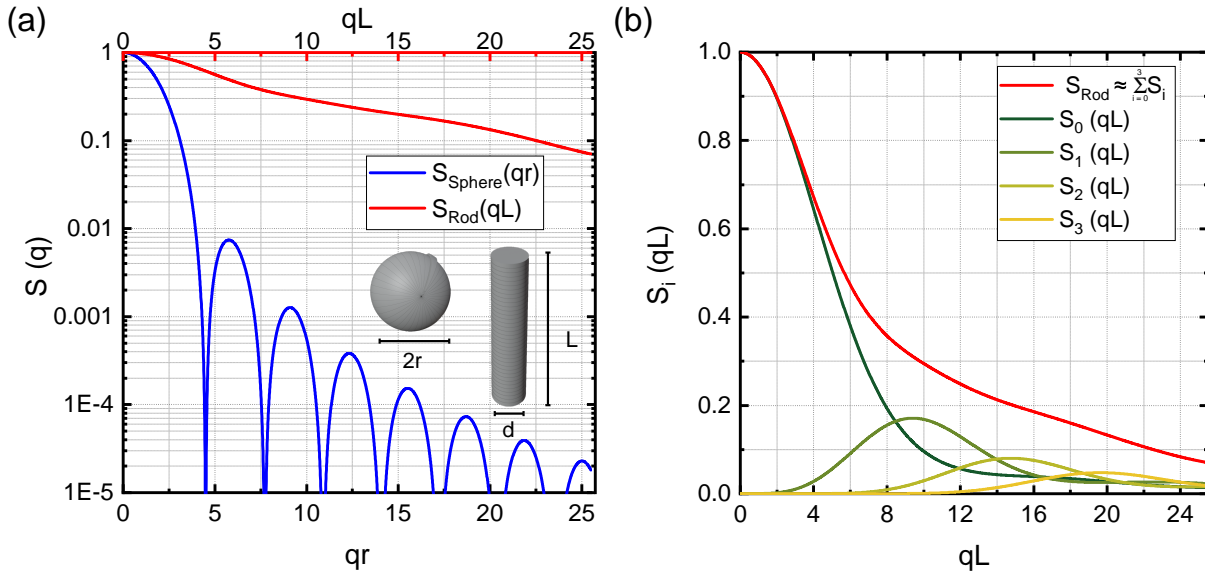


Figure 3.10: **Form factor of simple model systems.** (a) The form factor of a sphere of radius r , $S_{\text{Sphere}}(qr)$, corresponds to an oscillating function which first minimum is found at $qr = 4.49$. For the limit of small angles i.e., $q \rightarrow 0$, the form factor of a rod $S_{\text{Rod}}(qL) \rightarrow 1$ as for the case of spheres. (b) The form factor of a thin long rod $S_{\text{Rod}}(qL)$ is a sum of the elements $S_i(qL)$. The primary mode, $S_0(qL)$, diminishes as qL increases while the following terms do the opposite. The contributions of $S_1(qL)$, $S_2(qL)$ and $S_3(qL)$ rise to about 10% of $S_{\text{Rod}}(qL)$ for $qL > 5$, $qL > 10$ and $qL > 15$ respectively.

Thus, at low qL the dynamic form factor $S(q, t)$ of thin long rods is a single exponential decay which contains only the translational information. As qL increases, $S(q, t)$ corresponds to the sum of exponential decays for which the rotation of the rod also contributes. This contrasts with the dynamic form factor of ideal spherical particles of radius r which does not have any rotational contribution even at $qr \gg 1$. This can be seen from the fact that for a given volume element of a sphere which rotates to a new location there will always be

an identical element to replace it. Moreover, from equations 3.23 and 3.25 it follows that the dynamic form factor is almost insensitive to the rod diameter. For a rod of $L = 1 \mu\text{m}$ measured in a DLS setup of $\lambda = 632.8 \text{ nm}$ in the range of $30^\circ < \theta < 150^\circ$, qL changes from 6.8 made up of multiple exponential decays. For this case, it is recommended to limit the range to $6.8 < qL < 12.2$ ($30^\circ < \theta < 60^\circ$) where $S(qL)$ is composed mostly by the first two terms $S_0(qL)$ and $S_1(qL)$ (see section 3.3.3).

3.3.2 Dynamic light scattering experiment of isotropic particles

To make the connection between the DLS principles and the experimental data, we recall the expression of the scattered field correlation function given by equation 3.14:

$$g_1(q, t) = \langle N \rangle \langle \alpha_{if}(0) \alpha_{if}(t) \rangle S(\mathbf{q}, t), \quad (3.26)$$

where the projection of the polarizability tensor $\alpha_{if} \equiv \mathbf{n}_i \cdot \boldsymbol{\alpha} \cdot \mathbf{n}_f$ has been written in general notation for the geometry defined by the scattering plane formed by the initial and final wave vectors of the light \mathbf{k}_i and \mathbf{k}_f . As shown in figure 3.11, two different polarization configurations are considered. For the *VV* configuration or *Polarized* DLS, the polarization of incident light $\hat{\mathbf{n}}_i$ and scattered light $\hat{\mathbf{n}}_f$ are vertically aligned respectively to the scattering plane. For the *VH* configuration, also called *Depolarized* DLS, the $\hat{\mathbf{n}}_i$ is vertically aligned while the $\hat{\mathbf{n}}_f$ is horizontally oriented within the scattering plane. The Depolarized DLS (DDLS) is highly sensitive to the polydispersity or changes in size or conformation [123]. However, for this configuration there is a high difficulty to obtaining high-quality data due to the weakness of the depolarized signal compared to the polarized one [124]. Hence, we limit our study to the DLS configuration for which we obtained a good quality signal in our systems.

In the DLS experiment for which $\hat{\mathbf{n}}_i = \hat{\mathbf{n}}_f = \hat{\mathbf{z}}$, the projection of the polarizability tensor corresponds to α_{ZZ} and its fluctuation is denoted by $\delta\alpha_{ZZ}$.

For an ideal sphere with isotropic polarizability, $\delta\alpha_{ZZ} = 1$. Hence, combining equations 3.22 and 3.26 the scattered field correlation function reduces to:

$$g_1(q, t) = \langle N \rangle \exp(-q^2 D_T t) S(qr) \quad (3.27)$$

with $S(qr)$ given by equation 3.17. From equation 3.13 and 3.27 it follows that the intensity correlation function, $g_2(q, t)$, of ideal spheres is:

$$g_2(q, t) - 1 = \beta' \exp(-2q^2 D_T t). \quad (3.28)$$

with $\beta' = \beta[\langle N \rangle S(qr)]^2$. Thus, the intensity correlation function of spherical particles is a single exponential decay of decay time $\tau \equiv (2q^2 D_T)^{-1}$. In this case, the hydrodynamic diameter, d_H , can be defined as the diameter of an hypothetical hard sphere that diffuses in

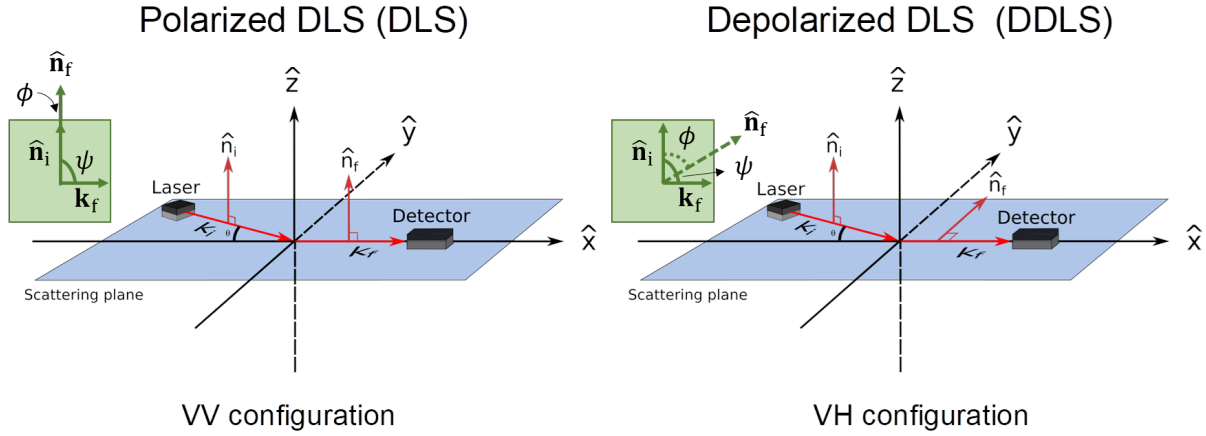


Figure 3.11: **Dynamic light scattering configurations.** For the scattering plane defined by the wave vectors \mathbf{k}_i and \mathbf{k}_f (blue), the *Polarized* DLS configuration (left) places the polarization of the incident light, $\hat{\mathbf{n}}_i$, and scattered light, $\hat{\mathbf{n}}_f$, vertically respectively to it. For the *Depolarized* DLS configuration (right), the $\hat{\mathbf{n}}_i$ is vertically aligned while the $\hat{\mathbf{n}}_f$ horizontally oriented within the scattering plane. ϕ represents the angle between $\hat{\mathbf{n}}_f$ and the plane formed by $\hat{\mathbf{n}}_i$ and \mathbf{k}_f (green) while ψ the angle between \mathbf{k}_f and $\hat{\mathbf{n}}_i$.

the same way as the particle being measured:

$$d_H \equiv \frac{k_B T}{3\pi\eta D_T}, \quad (3.29)$$

with D_T obtained from the analysis of the experimental data with equation 3.28. D_T depends not only on the bare size of the spherical particle but also on any surface structure as well as on the ionic strength of the solvent [125, 126]. Typically, a low ionic strength medium, i.e., high κ^{-1} , reduces the diffusion of a particle which results into a larger apparent hydrodynamic diameter, while a high ionic strength medium (low κ^{-1}) does the opposite resulting into a closer estimation of the bare size [125].

3.3.2.1 Polydispersity of suspension

Another parameter that influences the diffusion measured by DLS is the polydispersity of spherical colloidal particles which production process can result in a size distribution of finite width. For such case, *the cumulants method* proposed by D.E. Koppel [127], provides a mean value of the diffusion coefficient over the set of polydisperse particles. To do so, it is derived the cumulative-generating function $K(-t, \Gamma) \equiv \ln[g_1(q, t)]$. The m^{th} cumulant of the distribution function $k_m(\Gamma)$ is given by the m^{th} derivative of $K(-t, \Gamma)$ as [128]:

$$k_m(\Gamma) = \frac{d^m K(-t, \Gamma)^m}{d(-t)^m} \Big|_{-t=0}. \quad (3.30)$$

The basis of the cumulant method lies in expanding $\ln[g_1(q, t)]$ in terms of the cumulants of the distribution. This relation follows from the fact that the m^{th} cumulant is the coefficient of the $(-t^m)/m!$ term in the Taylor expansion of $K(-t, \Gamma)$ about $t = 0$ expressed as:

$$\ln[g_1(q, t)] = -k_1 t + \frac{k_2}{2!} t^2 - \frac{k_3}{3!} t^3 + \dots + (-1)^n \frac{k_n}{n!} t^n. \quad (3.31)$$

Combining equation 3.31 with the Siegert relation given by equation 3.13, an expression for the measured $g_2(q, t)$ is obtained:

$$g_2(q, t) - 1 = \beta \exp\left(-\bar{\Gamma}t + k_2 t^2 - \frac{k_3}{3} t^3 \dots\right), \quad (3.32)$$

where the first cumulant $\bar{\Gamma}$ is the mean of $\Gamma \equiv 2q^2 D_T$ that yields to the average translational diffusion coefficient \bar{D}_T . The second cumulant k_2 provides a quantitative measure for the polydispersity of the diffusion coefficient distribution by the polydispersity index (PDI). This is defined as the width or spread of the particle size distribution and is given by [103]:

$$PDI = \frac{k_2}{\bar{\Gamma}^2}, \quad (3.33)$$

which is valid for small size polydispersities $\Delta d_H / \langle d_H \rangle \leq 20\%$ [118]. For a Gauss distribution the PDI is given by $PDI = \sigma/d$ with σ the variance and d the mean diameter. A suspension which exhibits $PDI \leq 0.1$ is considered to be highly monodisperse, for values between $0.1 \sim 0.4$ and ≥ 0.4 is considered to be moderately and highly polydisperse respectively [91].

3.3.2.2 Experimental parameters

In order to obtain the characteristic intensity correlation function $g_2(q, t)$ of equation 3.28, the experimental parameters to be tuned are the *run time*, i.e., the duration of the experiment for which the scattering signal is measured and the *range of angles* where the detector is placed. The selection of the run time mostly depends on the typical decay time of the system. The correlator computes the time autocorrelation of the intensity signal which has a decay time $\tau = (2q^2 D_T)^{-1}$ and is proportional to the number of particles. For systems with a higher decay time, i.e., for large particles or dispersion with high viscosity, a run time higher than the decay time decreases the statistical noise of the decay. The choice of angle depends on the contribution of the form factor $S(qr)$. For a typical size of $r = 10$ nm measured in the range of angles $30^\circ < \theta < 150^\circ$ the product qr results in $0.07 < qr < 0.2$ while for $r = 200$ nm, qr results in $1.37 < qr < 5.11$. For the first case, the form factor $S_{Spheres}(qr) \sim 1$ (see figure 3.10) hence there is not preferred angle choice. For the second case, since the form factor has its first minimum at $qr = 4.49$, the choice is preferentially for the lower angles where the form factor is closer to 1.

3.3.3 Intensity correlation function of rod-like particles

For rod-like particles, the components of the polarizability denoted as α_{\parallel} and α_{\perp} will describe how easily electrons are displaced parallel to and perpendicular to the rod axis. If $\alpha_{\parallel} > \alpha_{\perp}$, electrons move preferentially in a parallel direction to the rod axis. This is the case of

synthetic rods of different materials [129, 130]. However, for the case of helical rods such as polypeptides, DNA and viruses there is often much less difference between α_{\parallel} and α_{\perp} [123, 131].

Pecora [102] has shown that in the general case, the spectral density of scattered light by anisotropic particles is represented by the sum of the isotropic and anisotropic components:

$$I(q, \omega) = I_{\text{iso}}(q, \omega) + I_{\text{aniso}}(q, \omega) \quad (3.34)$$

with

$$I_{\text{iso}}(q, \omega) = \frac{\rho}{2\pi} \Lambda^2 \cos^2(\phi) \sin^2(\psi) \alpha_I^2 S(q) S_{\text{iso}}(q, \omega) \quad (3.35)$$

and

$$I_{\text{aniso}}(q, \omega) = \frac{\rho}{30\pi} \Lambda^2 (3 + \cos^2(\phi) \sin^2(\psi)) S_{\text{aniso}}(q, \omega), \quad (3.36)$$

where $\rho \equiv \frac{N}{V}$ is the particle number density, Λ is an optical contrast factor, $\alpha_I \equiv (2\alpha_{\perp} + \alpha_{\parallel})/3$ and $S(q)$ the particle form factor [130]. As represented in the green scheme of figure 3.11, the angle between the wave vector of the scattered light and the polarization of the incident light is denoted ψ , while ϕ is the angle between the polarization vector of the scattered light and the plane formed by the wave vector of the scattered light and the polarization of the incident light. Thus, for the VV configuration it follows that $\cos^2(\phi) \sin^2(\psi) = 1$. The isotropic contribution of the dynamic form factor is given by the Lorentzian

$$S_{\text{iso}}(q, \omega) = \frac{2q^2 D_T}{\omega^2 + (q^2 D_T)^2}, \quad (3.37)$$

while the anisotropic contribution consists of a sum of multiple Lorentzians. For the particular case of particles with cylindrical symmetry whose dynamic form factor is composed by only the first two terms of the sum in equation 3.23, the latter reduces to:

$$S_{\text{aniso}}(q, \omega) = \frac{(\alpha_{\perp} - \alpha_{\parallel})^2}{3} \frac{2(q^2 D_T + 6D_R)}{\omega^2 + (q^2 D_T + 6D_R)^2}. \quad (3.38)$$

The scattered field correlation function, $g_1(q, t)$, is related to the Fourier transform of the isotropic and anisotropic contributions of the dynamic form factor, \tilde{S}_{iso} and \tilde{S}_{aniso} , as [130]:

$$g_1(q, t) = \tilde{S}_{\text{iso}}(q, t) + \tilde{S}_{\text{aniso}}(q, t). \quad (3.39)$$

Therefore, for the VV configuration:

$$g_1^{VV}(q, t) = A \exp(-D_T q^2 t) + B \exp[-(D_T q^2 + 6D_R)t], \quad (3.40)$$

with

$$A = \frac{\alpha_I}{\alpha_I^2 + (\alpha_{\perp} - \alpha_{\parallel})^2} \quad \text{and} \quad B = 1 - A. \quad (3.41)$$

Applying the Siegert relation given by equation 3.13, we get a general equation for the intensity correlation function of anisotropic particles experimentally measured by *Polarized* DLS [123]:

$$g_2^{VV}(q, t) - 1 = \beta \{ A^2 \exp(-\Gamma t) + 2AB \exp[-(\Gamma + \Delta/2)t] + B^2 \exp[-(\Gamma + \Delta)t] \}, \quad (3.42)$$

where $\Gamma \equiv 2D_T q^2$ and $\Delta \equiv 12D_R$. Note that equation 3.40 reduces to the ideal sphere case of equation 3.27 when $\alpha_{\parallel} = \alpha_{\perp}$. This can be seen from the fact that $A \rightarrow 1$ and $B \rightarrow 0$ for equal parallel and perpendicular polarizabilities. Then, the first term of equation 3.40 involves the isotropic part of the polarizability tensor and is independent of the rotations.

As mentioned earlier, the selection of the run time depends on the decay time. For this case, the corresponding decay time is approximately $\tau = 1/\Gamma$ of equation 3.42 since $\Gamma + \Delta \sim \Gamma$. In an aqueous solution, for rods of length $L = 1 \mu\text{m}$ measured at an angle $\theta \sim 90^\circ$, i.e., $q \sim 10 \mu\text{m}^{-1}$, the decay time is of the order of $\tau \sim 1$ ms. Selecting a run time higher than this value will decrease statistical noise. Now, the choice of angle depends on the $S(qL)$ given by equation 3.25 preferring the short angles where $S(qL) \sim 1$. In addition, the range of angles for which the approximation of the dynamic form factor composed only by the first two terms of equation 3.23 corresponds to $0 < qL < 12.2$. Then, for rods of $L = 1 \mu\text{m}$ the preferred choice of angles is $30^\circ < \theta < 60^\circ$.

3.3.4 Diffusion coefficients from Intensity correlation function

In order to gain reliable information on the diffusion coefficients of the particles under investigation we will apply different methods for data analysis. These are described below.

3.3.4.1 CONTIN analysis method

For ideal optically isotropic particles, the intensity correlation function is a single exponential decay:

$$g_2(q, t) - 1 = \beta \exp(-\Gamma t), \quad (3.43)$$

of decay rate $\Gamma \equiv 1/\tau$. A more general expression, which includes the case of anisotropic particles as well as the case of polydisperse systems, comes from a discretization of the previous problem:

$$g_2(q, t) - 1 = \sum_{i=1}^N a_i \exp(-t/\tau_i), \quad (3.44)$$

where the intensity correlation function is given by a sum of exponential decays of decay times $\tau_i = 1/\Gamma_i$. Here, a_i is the weighting factor that involves the coherence factor β and the polarizability terms. The case $i = 1$ reduces to the example of monodisperse spherical particles of equation 3.28 with $a_1 = \beta$, while $i = 3$ corresponds to the case described in equation 3.42 with $a_1 = \beta A^2$, $a_2 = 2\beta AB$ and $a_3 = \beta B^2$. For the limit of $N \rightarrow \infty$, equation 3.44 is written as the inverse Laplace transform (ILT) of a continuous function of decay times $G(\tau)$, as:

$$g_2(q, t) - 1 = \int_0^\infty G(\tau) \exp(-t/\tau) d\tau. \quad (3.45)$$

100 nm Polystyrene in 0.5 mM Tris/HCl - CONTIN Analysis

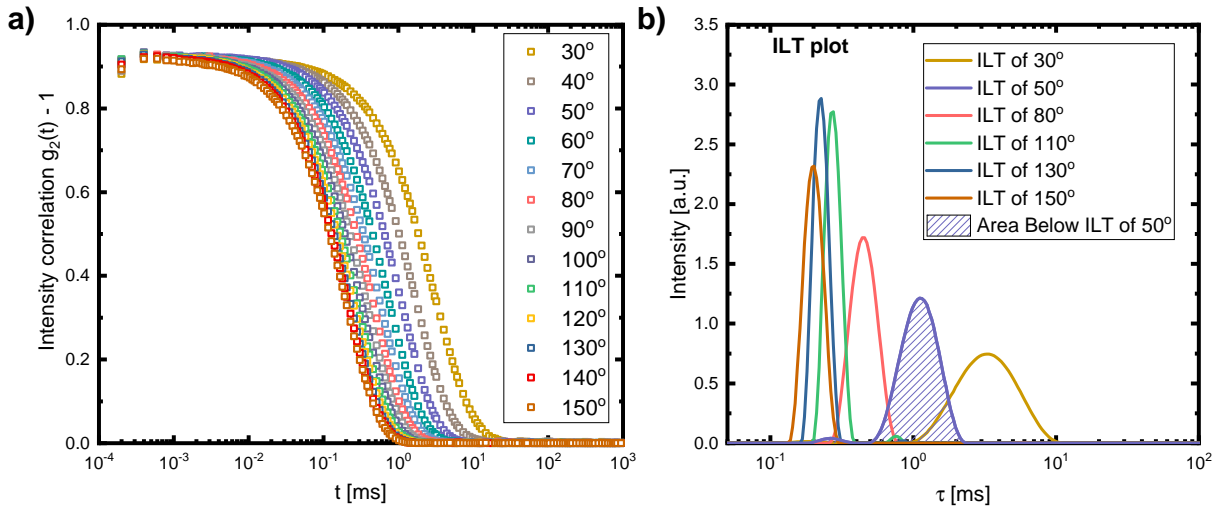


Figure 3.12: **CONTIN analysis of polystyrene nanoparticles of diameter $d = 100$ nm.** **a)** Intensity correlation function in the range of angles $30^\circ \leq \theta \leq 150^\circ$ and angular step 10° . **b)** Inverse Laplace transform (ILT) and integrated area computed for some of the experimental data.

The CONTIN analysis method attempts to retrieve the full decay time distribution by computing the ILT seeking $G(\tau) > 0$ as a sum of δ -peaks which recover equation 3.44. The method has been encoded in a very popular and widely used program package by S. W. Provencher [132]. This package delivers the detailed shape of the decay times of the intensity correlation function by a mathematical linearization of the original problem which results on a continuous distribution of decay times $G(\tau)$ normalized by $\beta\tau$ (see appendix I) .

In the following example, polystyrene nanoparticles of diameter $d = 100$ nm and $PDI = 0.01$ at concentration $C = 7.7 \times 10^{10}$ part/ml in $I = 0.5$ mM Tris/HCl buffer are analyzed by the CONTIN method. The ILT is computed using the CONTIN package of the software Origin 2020 (Origin Lab Corp). The experimental intensity correlation functions obtained by DLS in the range of angles $30^\circ \leq \theta \leq 150^\circ$ and the computed ILTs are plotted in subfigures

3.12 a) and b) respectively.

The decay times τ_i for each intensity correlation function are obtained from the central position of the intensity peaks at the ILT plot. The decay rates $\Gamma_i = 1/\tau_i$ are estimated and plotted versus the square of the scattering vector $q = 4\pi n \sin(\frac{\theta}{2})/\lambda$ in figure 3.13 b). From equation 3.28 it follows that for ideal spherical particles:

$$\Gamma = 2q^2 D_T. \quad (3.46)$$

Hence, the q^2 dependency of Γ_1 is a single straight line with a slope $2D_T$.

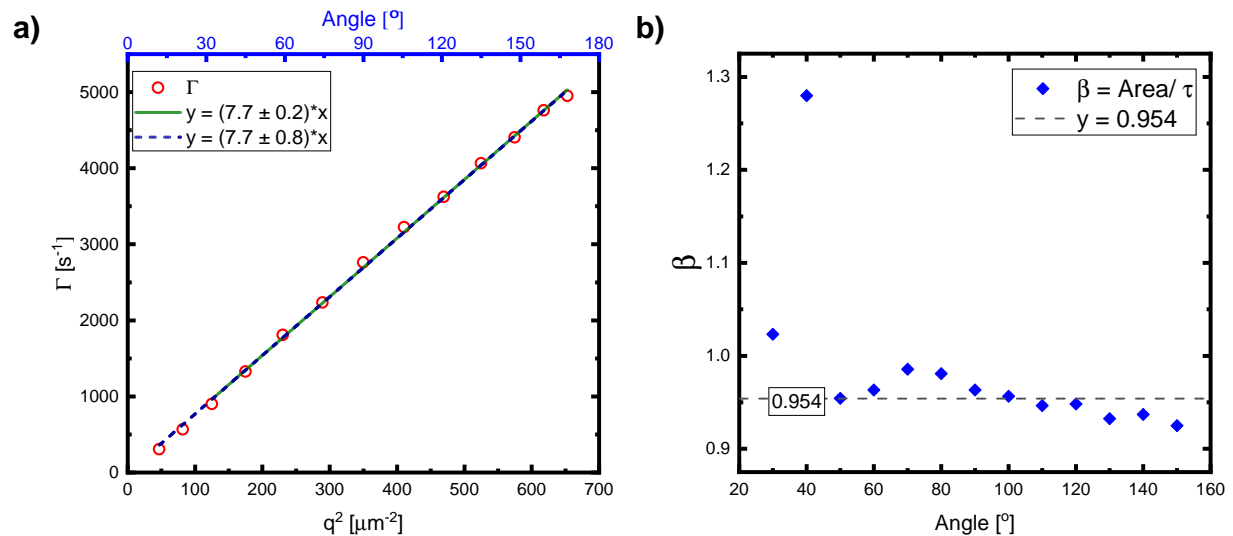


Figure 3.13: **Estimation of D_T from the CONTIN analysis.** **a)** The decay rates $\Gamma = 1/\tau$ are calculated with the τ_i obtained from the central position of the intensity peaks in the ILT plot. The q^2 dependency is a line with slope $2D_T$. **b)** The fitting range is chosen for the angles for which the value of the ratio $Area/\tau = \beta$ is below 10% of the average. Hence, the experimental translational diffusion coefficient of 100 nm polystyrene spheres corresponds to $D_T = 3.85 \pm 0.1 \mu m^2/s$.

As shown in figure 3.13 a), for the full range of angles measured it is found a linear dependency of $\Gamma = (7.7 \pm 0.8 \mu m^2/s)q^2$. In figure 3.13 b) is plotted the ratio between the integrated area below the ILT and the decay time $\beta = Area/\tau$ which indicates the noise in the experimental data (see appendix I). Note that the data points at 30° and 40° are 10% higher than the average value 0.954. As described in the appendix I, we have chosen to discard the data for which β is above 10% in order to reduce the error in the estimation of D_T . Thus, the selected range for the linear fit is $50^\circ < \theta < 150^\circ$. Following equation 3.46, the diffusion coefficient for 100 nm polystyrene nanoparticles measured by DLS corresponds to $D_T = 3.8 \pm 0.1 \mu m^2/s$. For spheres of 100 nm in an aqueous medium ($\eta = 1.005 \text{ mPa} \cdot \text{s}$) at room temperature (273 K), the theoretical value of translational diffusion coefficient (equation 1.1) is $D_T = 4.3 \mu m^2/s$. The observed difference is consistent with the fact that we measure by DLS the hydrodynamic size, i.e., the equivalent sphere diameter d_H given by equation 3.29 from which we obtain $d_H = 112.4 \pm 2.9 \text{ nm}$. The previous value is in agreement

with the expected double layer of ions present around charged particles [125, 126] for which we approximate $d_H \sim d + 2\kappa^{-1}$ with κ^{-1} the Debye screening length^v. For the ionic conditions of our experiment $I = 0.5$ mM, $\kappa^{-1} = 13.6$ nm and hence $d_H = 100$ nm + $2(13.6$ nm) = 127.2 nm.

3.3.4.2 Global fitting method

For a global fit method, a complete set of intensity correlation functions $g_2(q, t)$ measured for different angles are obtained and simultaneously analyzed by fitting equation 3.42 from two different approaches: the *independent global fit* and the *dependent global fit*.

In the first approach, we used the general equation of anisotropic particles (equation 3.42):

$$g_2(q, t) - 1 = \beta \{ A^2 \exp(-2D_T q^2 t) + 2A(1 - A) \exp [-(2D_T q^2 + 6D_R)t] + (1 - A)^2 \exp [-(2D_T q^2 + 12D_R)t] \}, \quad (3.47)$$

where A , D_T and D_R are treated as global parameters, q^2 is fixed depending of the angle according to equation 3.10 and β , which is function of q , i.e. $\beta(q) = \beta(\theta)$ (see section 3.3.2), is allowed to vary between the intensity correlation functions at different angles.

However, it is known that the D_T and D_R are dependent of the dimensions of the object such as r for the case of spheres and L and d for rods (equations 1.1 and 3.7). Thus, in the second approach, for which we consider that our gold nanoparticles are not perfectly spherical (see figure 2.14), we reduce the degrees of freedom by writing the D_T and D_R of equation 1.1 in terms of the correspondent hydrodynamic diameter d_H of equation 3.29. This leads to the *dependent global fit* applicable to spherical particles with a weak anisotropy:

$$g_2(q, t) - 1 = \beta \left\{ A^2 \exp\left(-\frac{2}{3d_H} \Lambda q^2 t\right) + 2A(1 - A) \exp \left[-\left(-\frac{2}{3d_H} \Lambda q^2 t + \frac{3}{d_H^3}\right)t \right] + (1 - A)^2 \exp \left[-\left(-\frac{2}{3d_H} \Lambda q^2 t + \frac{6}{d_H^3}\right)t \right] \right\}, \quad (3.48)$$

where $\Lambda \equiv \frac{k_B T}{\pi \eta}$ is a fixed parameter which depends on the conditions of the system, A and d_H are global parameters, q^2 is fixed for each angle and β varies for different angles. This approach is valid under the assumption that in real systems the spherical particles have some degree of anisotropy either geometrically or optically which makes possible to extract the rotational information.

In figure 3.14 it is shown the *independent global fit* applied to the intensity correlation function obtained by DLS in the range $30^\circ \leq \theta \leq 150^\circ$ for polystyrene nanoparticles of diameter $d = 100$ nm in ionic conditions $I = 0.5$ mM. The intensity correlation functions

^vThe Debye screening length is a measure of the distance that the counter-ions extend away from a charged colloidal surface. For electrolyte solutions, $\kappa^{-1}(\text{nm}) = \frac{0.304}{\sqrt{I(\text{M})}}$, with I the ionic strength [133]

(scattered points) and the global fits (full lines) for different angles are plotted in the subfigure (a) while the resulting fit parameter β is plotted in subfigure (b). The values obtained for the global parameters are $A = 0.962$, $D_T = 3.68 \pm 0.01 \mu\text{m}^2/\text{s}$ and $D_R = 2309.6 \pm 301.7 \text{ s}^{-1}$.

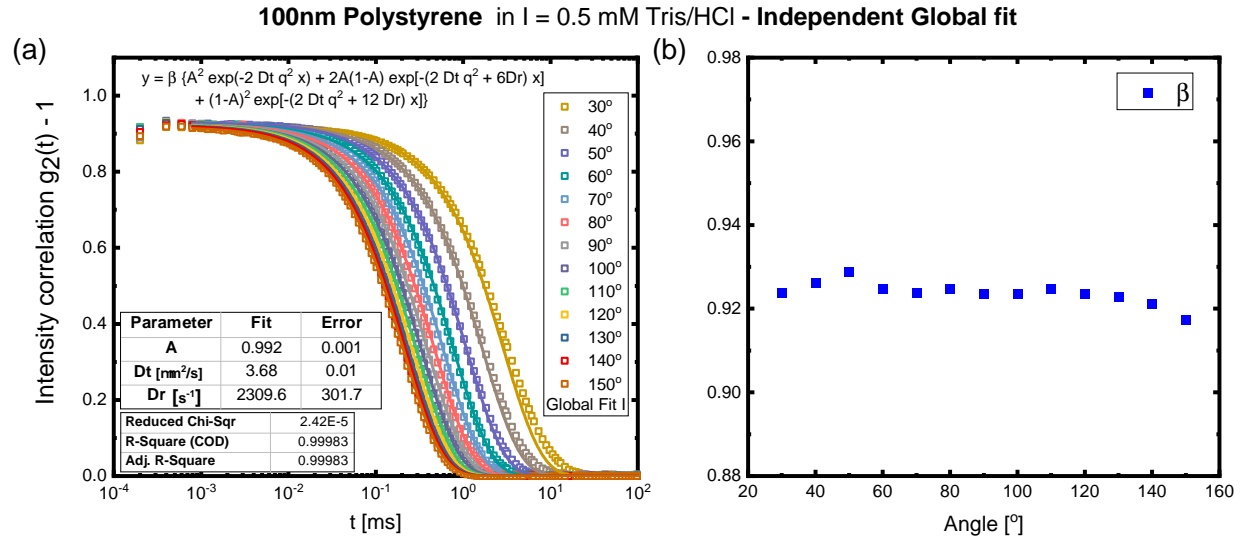


Figure 3.14: **Independent global fit analysis of polystyrene nanoparticles of diameter $d = 100 \text{ nm}$.** (a) Global fit (full lines) of the intensity correlation functions (scattered points) in the range of angles $30^\circ \leq \theta \leq 150^\circ$. (b) Resulting fit parameter β for all the angles. The values found for the global parameters are $A = 0.992 \pm 0.001$, $D_T = 3.68 \pm 0.01 \mu\text{m}^2/\text{s}$ and $D_R = 2309.6 \pm 301.7 \text{ s}^{-1}$.

The expected value of translational diffusion coefficient for 100 nm spheres is $D_T = 4.3 \mu\text{m}^2/\text{s}$. The observed difference with the value obtained from the global fit is consistent if we account for the hydrodynamic diameter of the particles, i.e., $d_H = 116.1 \pm 0.3 \text{ nm}$. For the interpretation of D_R , we compare the experimental value with the one calculated for a sphere of diameter d_H according to equation 1.1: $D_R = 924.5 \pm 7.2 \text{ s}^{-1}$. We observe that the D_R obtained from the global fit differs from about a factor 2.5 from the expected value. This could in part stem from the weak anisotropy of the particles being measured which contribution to the second term of equation 3.42 containing the rotational information is negligible. For this case, we propose to use the dependent global fit for which the link between D_T and D_R facilitates the interpretation of the results, as shown in figure 3.15.

The *dependent* global fit applied to the intensity correlation function of polystyrene nanoparticles of diameter $d = 100 \text{ nm}$ is summarized in figure 3.15. The values obtained for the global parameters are $A = 1$ and $d_H = 113.6 \pm 0.2 \text{ nm}$. From the obtained value of d_H it follows that the diffusion coefficients of the 100 nm polystyrene nanoparticles are $D_T = 3.76 \pm 0.1 \mu\text{m}^2/\text{s}$ and $D_R = 873.9 \pm 4.5 \text{ s}^{-1}$.

The results obtained from each approach agree with each other. Then, it is found that the experimental diffusion of our polystyrene particles of $d = 100 \text{ nm}$ at concentration $C = 7.7 \times 10^{10} \text{ part/ml}$ in I = 0.5 mM Tris/HCl buffer corresponds to $D_T = 3.7 \pm 0.1 \mu\text{m}^2/\text{s}$.

In the following chapters, we implement and combine these methods for the interpretation

of the experimental results.

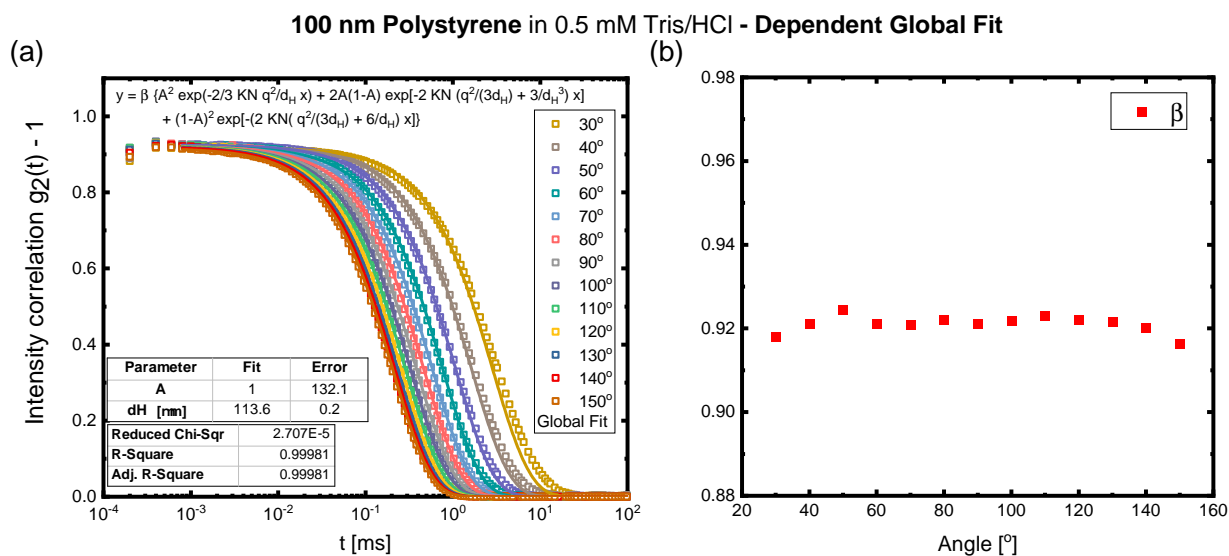


Figure 3.15: **Dependent global fit analysis of polystyrene nanoparticles of diameter $d = 100$ nm.** (a) Global fit (full lines) of the intensity correlation functions (scattered points) in the range of angles $30^\circ \leq \theta \leq 150^\circ$. (b) Resulting fit parameter β for all the angles. The values found for the global parameters are $A = 1$ and $d_H = 113.6 \pm 0.1$ nm.

Appendix I. CONTIN analysis details

In this appendix we review the implementation of the CONTIN, a constrained regularization method for inverting data, emulated in the Origin 2020 software package. For this purpose we have simulated intensity correlation function curves for different examples of equation 3.44 and extracted the dynamics by the implementation of this method.

Ideal spheres

For ideal spherical nanoparticles of translational diffusion coefficient D_T , the simulated intensity correlation function equation corresponds to:

$$y = \beta \exp(-x/\tau), \quad (3.49)$$

where β is the coherence factor and $\tau = 1/\Gamma = 1/(2q^2 D_T)$ with q given by equation 3.10.

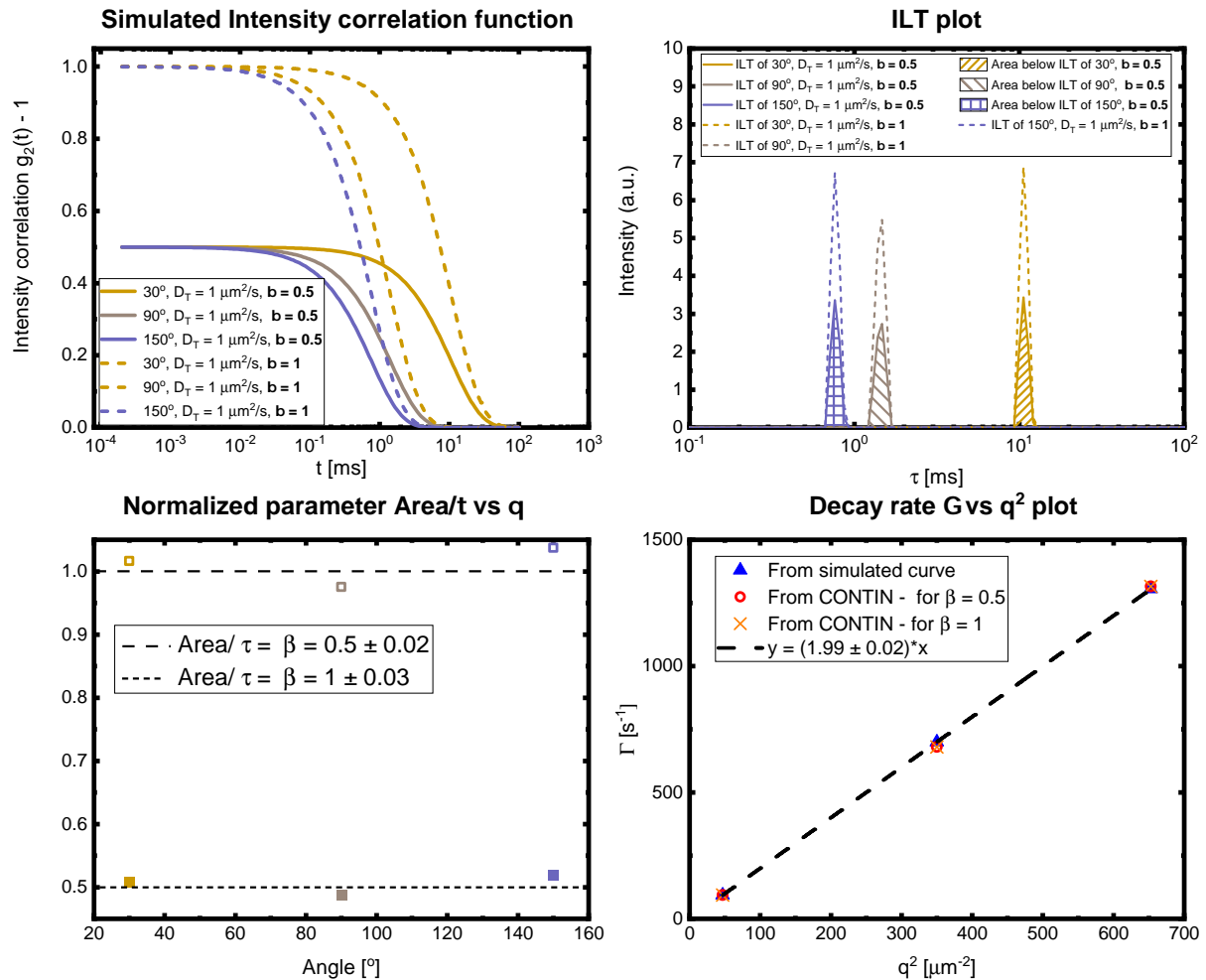


Figure 3.16: Summary of CONTIN analysis method applied to simulated intensity correlation functions of spheres of $D_T = 1 \mu\text{m}^2/\text{s}$, at $\theta = 30^\circ, 90^\circ, 150^\circ$ and coherence factor $\beta = 0.5, 1$.

In figure 3.16 we have plotted the simulated intensity correlation functions for $D_T =$

$1 \mu\text{m}^2/\text{s}$, at $\theta = 30^\circ, 90^\circ, 150^\circ$ and $\beta = 0.5, 1$. In the ILT plot are shown the computed curves using the CONTIN package. Since the simulated curves are composed by a single exponential decay it is expected to find a single peak at center position τ .

To address the question of why the intensity of the peak varies we have calculated the integrated area under the curve around the peak and normalize it by τ . We found that for the curves simulated with $\beta = 1$ the normalized parameter, $Area/\tau$, is 1 with an error bar of 3% while for the curves simulated with $\beta = 0.5$ the normalized parameter is 0.5 with an error bar of 4%. This gives us an insight on the meaning of the intensity of the peaks in the ILT plot which varies in such a way that the **area below the curve corresponds to $\beta\tau$** .

Then, the calculated Γ is plotted as function of q^2 . For this case, the obtained value using the CONTIN method is the same as the one used for the simulated curve with an error bar of less than 3%. Hence, the obtained translational diffusion coefficient from the CONTIN method corresponds to $D_T = 1 \pm 0.01 \mu\text{m}^2/\text{s}$.

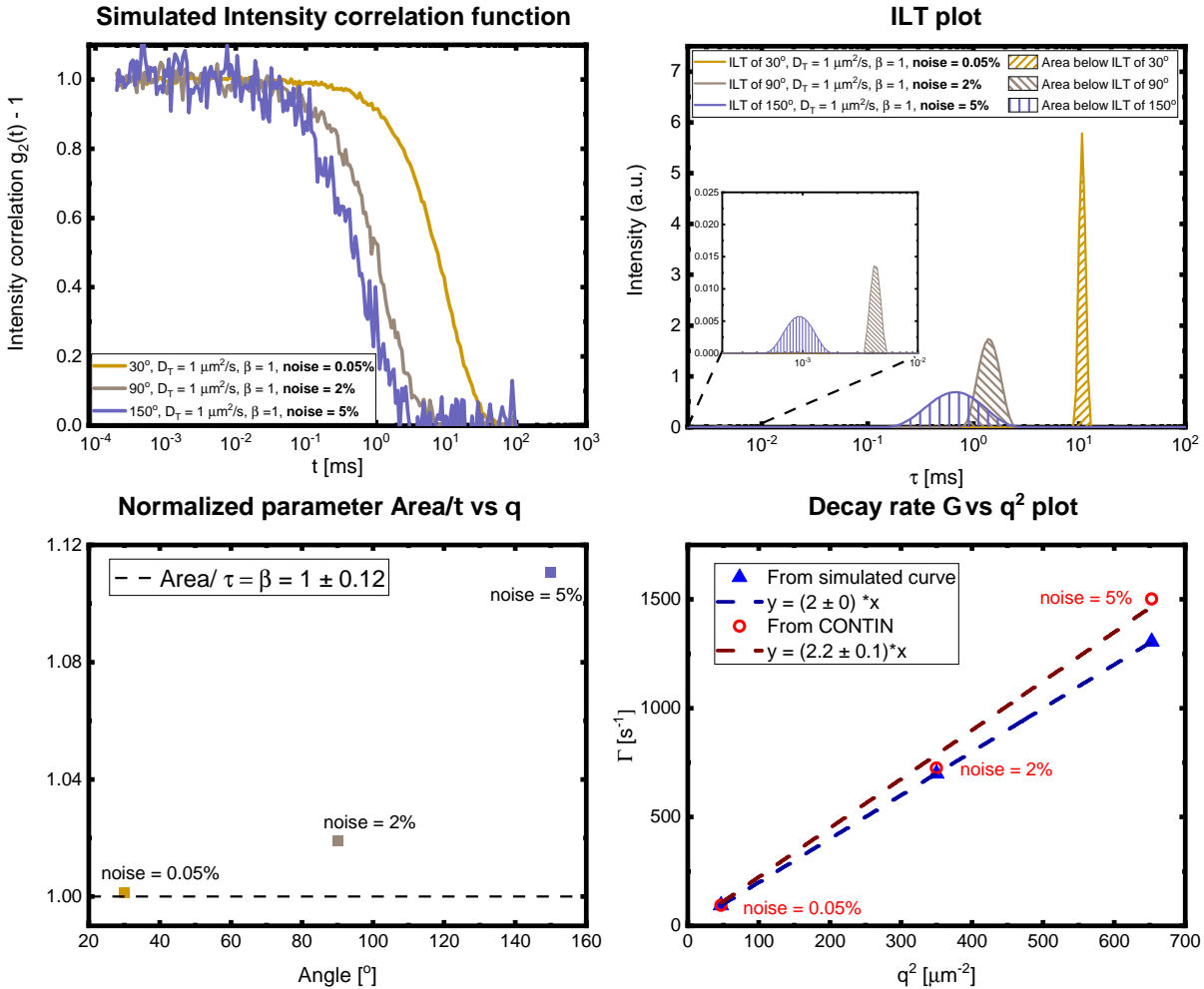


Figure 3.17: Summary of CONTIN analysis method applied to simulated intensity correlation functions of spheres of $D_T = 1 \mu\text{m}^2/\text{s}$, at $\theta = 30^\circ, 90^\circ, 150^\circ$ and coherence factor $\beta = 1$, for different noise levels.

In order to get a better understanding of the results obtained by the CONTIN analysis applied to real data, we simulated curves with an added Gaussian noise. In figure 3.17 we

plotted the simulated intensity correlation functions for a system of $D_T = 1 \mu\text{m}^2/\text{s}$ for the angles $\theta = 30^\circ, 90^\circ$ and 150° with noise of 0.05%, 2% and 5% respectively.

As shown in the ILT plot, the computed curves exhibit a single peak that broadens as the noise increases and consequently the intensity decreases to compensate for keeping constant the area $\beta\tau$. Moreover, as shown in the inset, artificial peaks with no physical meaning are generated due to the presence of noise. The normalized parameter $Area/\tau$ calculated from the area under the main peak and its central position shows a higher dispersion from the expected value as the noise increases, rising the error bar to 12% for a 5% noise. Hence, the calculated Γ from the CONTIN method shows a higher error resulting in a estimated diffusion coefficient of $D_T = 1.12\mu\text{m}^2/\text{s}$. This confirms that for getting a high accuracy in the measurement of D_T , it is required high quality data which depend on the specific experimental conditions of the system. Moreover, it becomes clear that the normalized parameter $Area/\tau$ functions is a measure of how noisy the data is. Then, if one of the experimental data in the set of angles is significantly out of the average, we have to discard it in order to decrease the error of the estimation of D_T through the linear fit of Γ .

Binary mixtures

For an ideal binary mixture, the intensity correlation function could be treated as a sum of two exponential decays of decay times τ_1 and τ_2 . For this case, we use $i = 2$ of equation 3.44:

$$y = \beta [A_1 \exp(-x/\tau_1) + A_2 \exp(-x/\tau_2)], \quad (3.50)$$

where A_1 and A_2 are weighting factors which fulfill $A_1 + A_2 = 1$ [134].

In figure 3.18 are shown the intensity correlation functions of a binary mixture of $D_{T1} = 1 \mu\text{m}^2/\text{s}$, $D_{T2} = 0.25 \mu\text{m}^2/\text{s}$, $\beta = 1$ and $\theta = 30^\circ, 90^\circ$ and 150° for different weighting factors. The ILT plot shows that there are two peaks per curve whose intensity varies in accordance with the weighting factor. For instance, the simulated curve $\theta = 30^\circ$ which has equal weighting factors $A_1 = A_2 = 0.5$ results in equal intensity of the ILT peaks while the simulated curves $\theta = 90^\circ$ and 150° with waiting factors $A_1 = 0.8$ and $A_2 = 0.2$ result in different intensities of the ILT peaks. Hence, the normalized parameter $Area/\tau$ give us an estimation of the weighting factors and thus the contribution of the corresponding exponential decay to the intensity correlation function. Here, there are two calculated Γ plotted as function of q^2 from which we calculate $D_{T1} = 1.03 \pm 0.02 \mu\text{m}^2/\text{s}$ and $D_{T2} = 0.26 \pm 0.01 \mu\text{m}^2/\text{s}$. These values are in agreement with the simulated data.

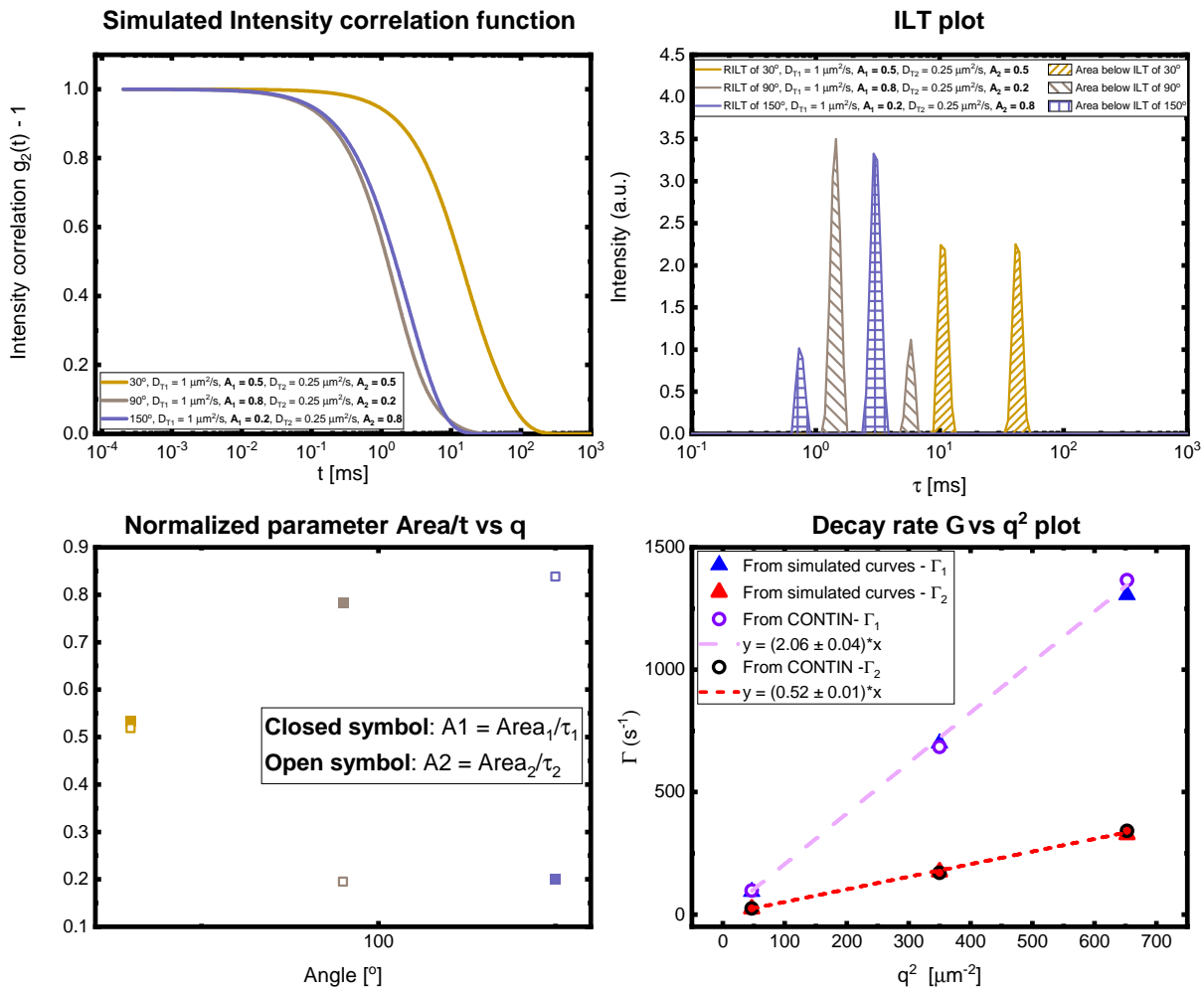


Figure 3.18: Summary of CONTIN analysis method applied to simulated intensity correlation functions of a binary mixture of $D_{T1} = 1 \mu\text{m}^2/\text{s}$, $D_{T2} = 0.25 \mu\text{m}^2/\text{s}$, at $\theta = 30^\circ, 90^\circ, 150^\circ$ and different prefactors A_1 and A_2

Chapter 4

Dynamics of matchstick-like and dumbbell-like particles

4.1	Hybrid gold-virus colloids	68
4.2	Dynamic light scattering of gold-virus systems	69
4.2.1	Rod-like viruses: M13C7C strain	69
4.2.2	Spherical gold nanoparticles (Au NPs)	74
4.2.3	Mixture of Au NPs and rod-shaped viruses	76
4.3	Diffusion of matchstick-like particles	78
4.3.1	Diffusion coefficient considering a flexible link	81
4.3.2	Nanoparticle size and concentration dependence	84
4.4	Diffusion of dumbbell-like particles	86
4.5	Discussion and conclusions	88
	Appendix I. DLS analysis of other matchstick-like particles	90
	Matchstick-like made of Au NPs of $D = 10$ nm	90
	Matchstick-like made of Au NPs of $D = 18$ nm	94
	Matchstick-like made of Au NPs of $D = 31$ nm	97

4.1 Hybrid gold-virus colloids

Hybrid colloidal particles are made of two or more different elements, typically inorganic compounds, such as metallic nanoparticles (NPs), and organic materials, such as biomolecules, DNA, polymers or phages [96, 135]. For this type of hybrid materials, the NPs provide the physical properties of interest, such as optical absorption, scattering or magnetic response while the organic material provides colloidal stability, versatility for further functionalization through suitable surface chemistry and also organization, for instance, rod-shaped viruses which possess liquid crystal properties work as templates for novel architectures [26, 28]. The interest of many research fields in the development and characterization of hybrid colloids lies in their potential applications in energy storage [51], drug delivery [33], stimuli-responsive smart materials [36], etc.

Recently, filamentous phages have been used for the development of novel hybrid materials due to their facility to be genetically modified to display peptides or proteins with specific affinity for desired molecules or materials [27, 74]. Moreover, thanks to their monodispersity in size and their ability to self-assemble into liquid crystalline phases, they are excellent candidates for the design of structurally ordered hybrid materials [136].

In our group we have developed an efficient method for the conjugation of metal NPs with filamentous M13 viruses [26, 55] based in the genetic modification of the M13KE strain. In chapter 2, we have described the specific modification performed on the p3 and p7 proteins to obtain viruses with affinity for noble metal nanoparticles in one or both virus tips (see figure 4.1). The M13C7C mutant which only differs from the M13KE one by the number of cysteine residues displayed on the p3 proteins has shown a high efficiency to graft gold (Au) NPs at one virus tip. The new mutants introduced in chapter 2, M13s(*Cgbc*C)₂ and M13l(*Cgbc*C)₂ are able to bind Au NPs on both tips thanks to the genetic modification we have done on the p7 proteins. These genetically engineered phages are used as building blocks for hybrid gold-virus colloids such as the matchstick-like and dumbbell-like particles shown in figure 4.1.

In this chapter, we investigate by Dynamic Light Scattering (DLS) the self-diffusion of

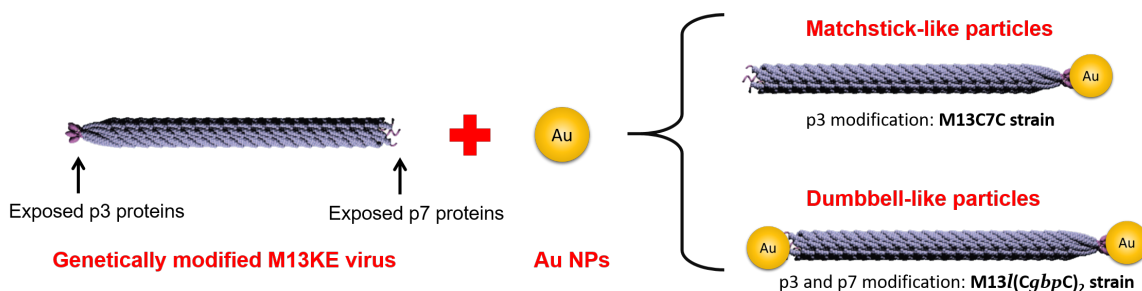


Figure 4.1: **Schematic representation of hybrid gold-virus colloids.** The genetically modified M13KE phage is used as building block for hybrid gold-virus colloids. Their self-assembly with Au NPs results in matchstick-like and dumbbell-like particles.

our hybrid colloids composed by a single virus and one or two Au NPs attached to their tips. For the matchstick-like particles, we explore the effect of the NP size in a wide range of concentrations. Thus, we compare and interpret the differences in the dynamics observed with previous experiments performed by single particle tracking (SPT) [55]. Finally, we evidence and analyze quantitatively the flexibility of p3 proteins of the virus tip.

4.2 Dynamic light scattering of gold-virus systems

The advantage of using the DLS technique for studying our hybrid gold-virus structures comes from the difference in contrast of the elements that compose the structures. For instance, the scattering of Au NPs prevails over the one of the organic viruses which in suspension are mostly transparent.

For this study, we use the DLS theory of spherical particles and long thin rods described in chapter 3 which holds only for the infinite dilution limit, i.e., when the particles do not interact with each other. Here we consider the overlap concentration of the viruses C^* (equation 2.4) as the highest concentration before the structures start to interact. This assumption considers that the diameter of the bead attached to the virus tip, between 10 to 30 nm, is negligible compared to the virus length equal to the one of the structure, $L \sim 1 \mu\text{m}$. Hence, we estimate $C^* = 0.04 \text{ mg/ml}$ for matchstick-like structures made of M13C7C viruses of $L = 1 \mu\text{m}$ and $C^* = 0.03 \text{ mg/ml}$ for dumbbell-like particles considering $L = 1.1 \mu\text{m}$ the length of the M13l(*Cgbc*)₂ mutant that we have used to produce them. As explained in section 2.3.2 the concentration of the structures, C_v , is calculated from the OD of the suspension given by the number of Au NPs involved in the structures (equation 2.10).

In this section, we discuss first the DLS measurements on the two components of our hybrid structures: spherical Au NPs and rod-shaped viruses. For a clear comparison, each of the suspensions is dialyzed against a $I = 5 \text{ mM}$ Tris/HCl buffer. All the DLS measurements have been taken for a running time of 120 s in the range of scattering angles $30^\circ \leq \theta \leq 150^\circ$ (see chapter 3).

4.2.1 Rod-like viruses: M13C7C strain

The first component of our hybrid gold-virus colloids are rod-shaped viruses which have been produced according to the protocol described in section 2.2.2. The TEM characterization of the M13C7C strain (see figure 4.2) shows that it is highly monodisperse and that its average length is $L = 1 \mu\text{m}$ [55]. To study their diffusion, the intensity correlation function is measured for a suspension at $C_v = 0.47C^* = 7.7 \times 10^{11} \text{ part/ml}$. The experimental data is then analyzed with the CONTIN and global fit methods described in section 3.3.4.

The results of the CONTIN analysis method are summarized in figure 4.3. According to the DLS theory of rods, the intensity correlation function of rod-shaped particles is composed by three exponential decays, one directly related to the translational diffusion and the other

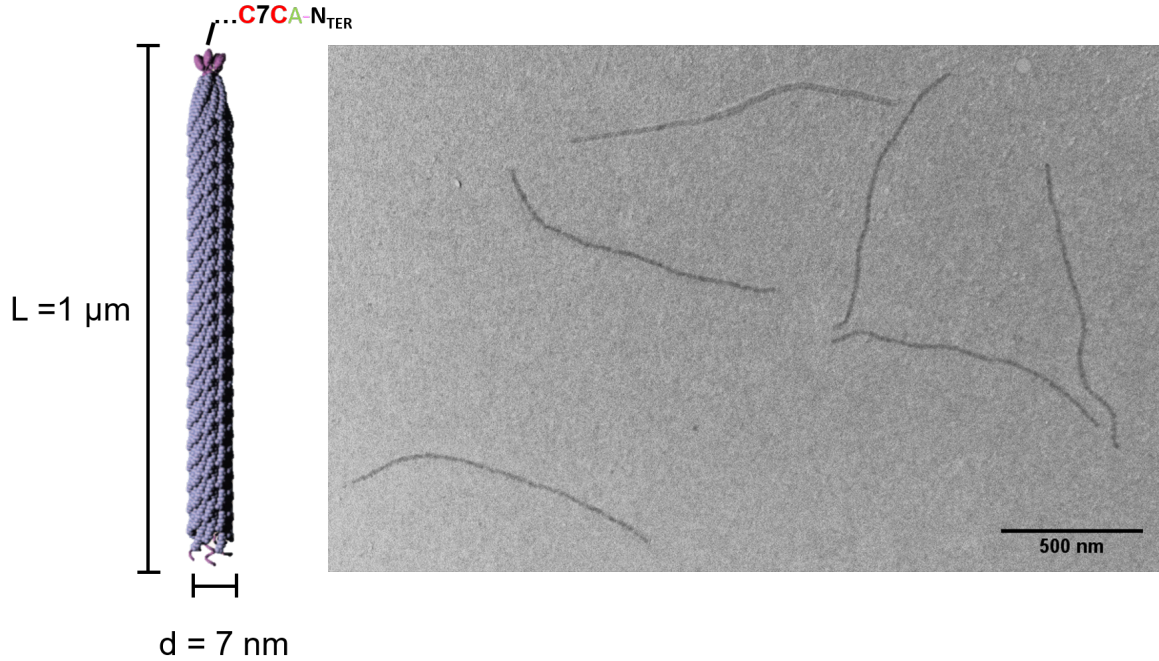


Figure 4.2: **Characterization of M13C7C virus suspension.** **Left:** Schematic representation of M13C7C virus of dimensions $L = 1 \mu\text{m}$ and $d = 7 \text{ nm}$. **Right:** TEM image of the rod-shaped viruses.

two involving translational and rotational diffusions (equation 3.42). The Inverse Laplace Transform (ILT), which seeks for the distributions of decay times τ , exhibits for most of the angles only two peaks. The main peak is found at higher decay times than the second peak of significantly lower intensity.

In order to determine the contribution of each exponential decay to the intensity correlation function, the normalized parameter $Area/\tau$ is calculated (see section 3.3.4). Since $Area_2/\tau_2 < 0.2$, we neglect the second peak. The main contribution is related to the first term of equation 3.42 which involves D_T . The fact that we do not find a significant second peak indicates that our viruses possess a low optical anisotropy since the following terms in equation 3.42 only appear as the optical or geometrical anisotropy increases. Thus, it may not be possible to extract reliable information about the rotational diffusion when measured by DLS in the VV (polarized) mode.

Note that the parameter $Area_1/\tau_1$ has lower dispersion in the range $30^\circ \leq \theta \leq 70^\circ$. This shows that the data in this range has lower noise when compared with the higher angles. Moreover, when the decay rate, $\Gamma = 1/\tau$, is calculated for angles $\theta > 70^\circ$, we find an apparent change of slope. This could be attributed on one hand, to the sensitivity of the CONTIN analysis which in this range does not decompose the signal into the expected multiple peaks and on the other hand, to the flexibility of the M13 viruses.

Song et al. [64] have reported DLS measurements for M13 viruses in a range of q^2 from 21 to $2000 \mu\text{m}^{-2}$ by using laser wavelength at $\lambda = 632.8 \text{ nm}$ and $\lambda = 351.1 \text{ nm}$. Their curves considering the persistence length are compared with the theoretical model of the apparent

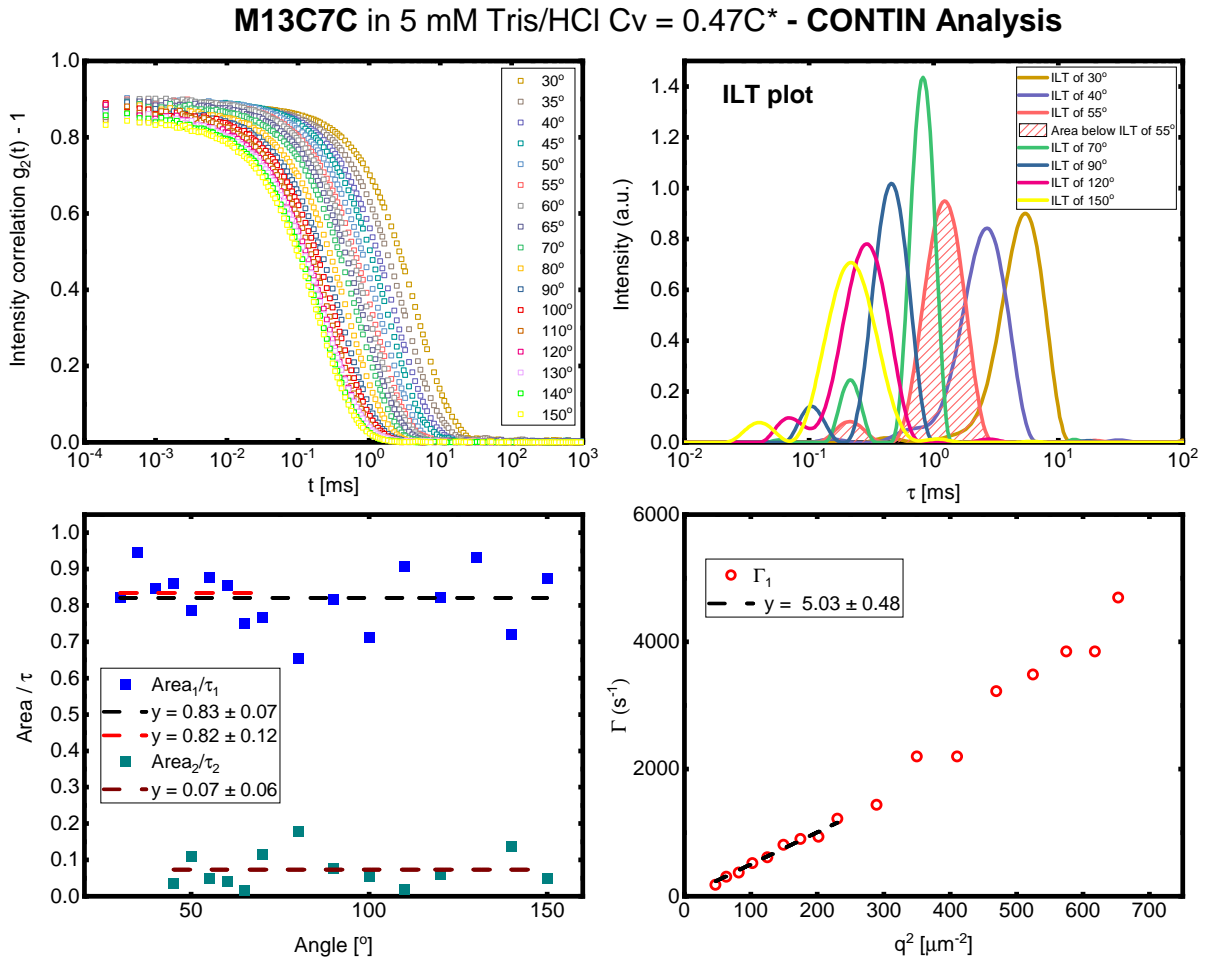


Figure 4.3: **CONTIN analysis of M13C7C rod-like viruses in $I = 5$ mM Tris/HCl buffer at $C_v = 0.47C^*$.** The ILT computed from the experimental data in the range of angles $30^\circ \leq \theta \leq 150^\circ$ shows multiple peaks. The normalized parameter $Area/\tau$ indicates that the second contribution at short times is not significant and that the noise in the data is lower than 10% for the range of angles $30^\circ \leq \theta \leq 70^\circ$. The q^2 dependence of Γ_1 is a single straight line of slope $2D_T$ from which the translational diffusion coefficient is obtained $D_T = 2.5 \pm 0.3 \mu\text{m}^2/\text{s}$.

diffusion coefficient of thin rigid rods of Wilcoxon and Schurr, D_{app}^{WS} , for $L = 0.9 \mu\text{m}$ [137]. As shown in figure 4.4, the apparent translational diffusion coefficient diverges from the rigid rod behavior for $q^2 > 150 \mu\text{m}^{-2}$. This comparison leads to an estimation of the persistence length of $2.3 \mu\text{m}$.

To understand the observed change of slope in our CONTIN analysis, we have calculated the apparent translational diffusion coefficient:

$$D_{app}(q) = D_T(q) = \frac{\Gamma}{2q^2}, \quad (4.1)$$

for our measurements on M13C7C viruses. In figure 4.4, we compare with the work in

ⁱTheir equation has as limit behaviors: $D_{app}^{WS} = D_T$ for $qL \ll 1$ and $D_{app}^{WS} = D_T - \Delta/3 + L^2 D_R/12$ for $qL \gg 1$, with $\Delta = D_{||} - D_{\perp}$, the anisotropy of the translational diffusion coefficients given by equation 3.8.

weakly bending rods of Song et al. [64] where $D_{app}(q)$ at high q^2 differs from the plateau expected for rigid rods as the persistence length, P , decreases. For our experimental data, the calculated $D_{app}(q)$, shows a significant increase for $q^2 > 280 \mu\text{m}^{-2}$ (see inset of figure 4.4). This trend confirms that the persistence length our M13C7C influences the diffusion coefficient measured and hence Γ . For an accurate estimation of the persistence length of our M13C7C viruses, it is necessary to explore higher range of q^2 however, our experimental set up is limited to the range from 47 to 653 μm^{-2} .

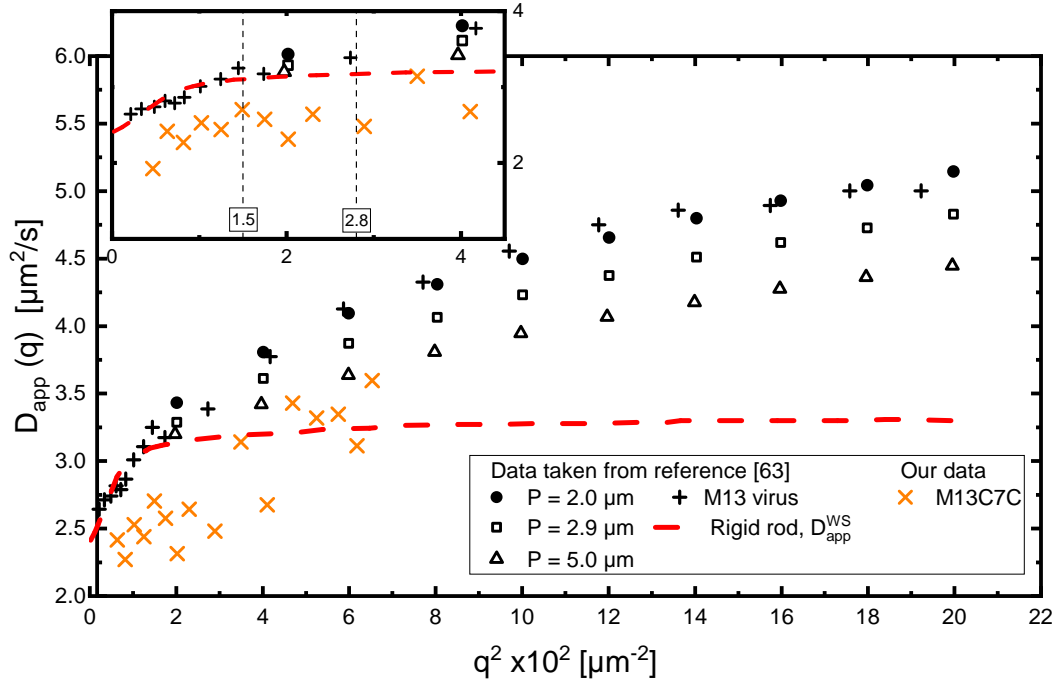


Figure 4.4: $D_{app}(\mathbf{q})$ vs q^2 The translational diffusion coefficient is calculated for each angle according to equation 4.1. Our experimental data on M13C7C is compared with the theoretical and experimental data of Song et al. [64] for different persistence lengths.

In order to extract reliable information on the translational diffusion coefficient, we chose to analyze the range below $q^2 < 280 \mu\text{m}^{-2}$, i.e., $\theta < 80^\circ$. Moreover, we consider the DLS principles described in section 3.3.1, which indicate that the range of validity for which the intensity correlation function is given by equation 3.42 is between $30^\circ \leq \theta \leq 60^\circ$ for stiff rods of $L = 1 \mu\text{m}$. Hence, we limit the fit of Γ to the range of angles for which the flexibility of the viruses does not affect D_T and the q^2 dependence is expected to be a single straight line of slope $2D_T$, i.e., for $30^\circ \leq \theta \leq 70^\circ$.

From the linear fit in this range, it follows that the translational diffusion coefficient of a system of rod-shaped viruses is $D_T = 2.5 \pm 0.3 \mu\text{m}^2/\text{s}$. The error bar in our estimation corresponds to the dispersion in our data from the fit. This value is compatible with the DLS measurements found in literature [138, 139] from which is obtained $D_T = 2.6 \mu\text{m}^2/\text{s}$ as well as with the theoretical value of translational diffusion of stiff slender rods (equation 3.7): $D_T = 2.1 \mu\text{m}^2/\text{s}$.

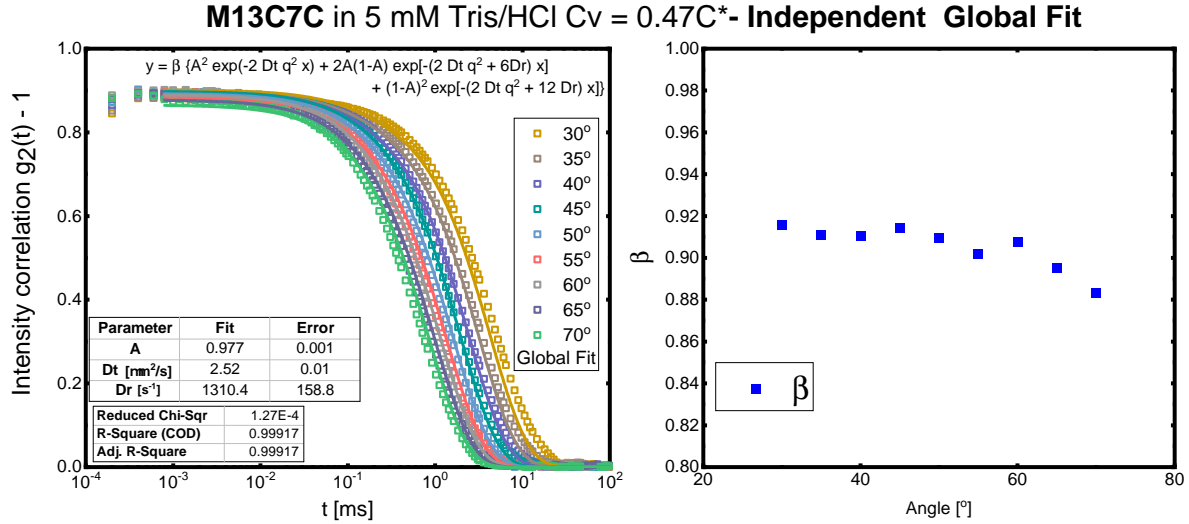


Figure 4.5: **Independent global fit analysis for M13C7C rod-like viruses in $I = 5$ mM Tris/HCl buffer at $C_v = 0.47C^*$.** **Left:** Global fit (full lines) of the intensity correlation functions (scattered points) in the range of angles $30^\circ \leq \theta \leq 70^\circ$. **Right:** Fit parameter β for all the angles. The values found for the global parameters are $A = 0.977$, $D_T = 2.51 \pm 0.02 \mu\text{m}^2/\text{s}$ and $D_R = 1310.4 \pm 158.8 \text{ s}^{-1}$.

For a better understanding of the measured intensity correlation function, we have compared the previous result with the one obtained using the independent global fit method of equation 3.47 in the same range of angles. The results are summarized in figure 4.5. The calculated parameters with error bars equal to the standard error of the fitted values correspond to $A = 0.977$, $D_T = 2.52 \pm 0.01 \mu\text{m}^2/\text{s}$ and $D_R = 1310.4 \pm 158.8 \text{ s}^{-1}$, while the free parameter β remains constant for this range of angles. D_T matches the previous result. However, the value for the rotational diffusion coefficient differs from the expected theoretical value according to equation 3.7: $D_R = 19.1 \text{ s}^{-1}$. According to equation 3.42, for $A = 1$, this is reduced to the sphere case which is independent of rotations. Thus, we conclude that in the stiff rod limit, i.e., $30^\circ \leq \theta \leq 70^\circ$ for which we find $A = 0.97$, our DLS measurements are not sensitive enough to extract the rotational information of the rod-shaped viruses.

At this point, we might consider the effect of the electric double layer formed by the low ionic conditions. However, for rod-like particles of long aspect ratio, i.e., $L/d \gg 1$, the change of diameter is not significant for estimating D_T which scales as $\ln(L/d)$ according to equation 3.7. Thus, the measured value is in the error bar the same as the theoretically expected one. Hence, we conclude that the diffusion of the M13C7C strain experimentally measured by DLS at $C_v = 0.47C^*$ in $I = 5$ mM buffer corresponds to $D_T = 2.5 \pm 0.3 \mu\text{m}^2/\text{s}$.

The next component of our hybrid gold-virus assemblies are spherical Au NPs. As shown in figure 4.6, the suspensions of Au NPs of diameters $D = 10, 18$ and 31 nm used for the production of the matchstick-like particles are highly monodisperse, i.e., PDI= 0.05, 0.07 and 0.10 respectively (see section 3.3.2.1). As we have mentioned earlier, the scattering signal

of the Au NPs is significantly higher than the one of the viruses which allow us to study the matchstick-like particle from the point of view of the dynamics of the Au NP attached to the virus tip. In order to demonstrate it, we discuss next the DLS measurements on a suspension of Au NPs of diameter $D = 18$ nm and on an equimolar mixture of Au NPs and viruses.

4.2.2 Spherical gold nanoparticles (Au NPs)

The measurements of a suspension at $C_{Au} = 7.7 \times 10^{11}$ part/ml are analyzed using the CONTIN method and summarized in figure 4.7.

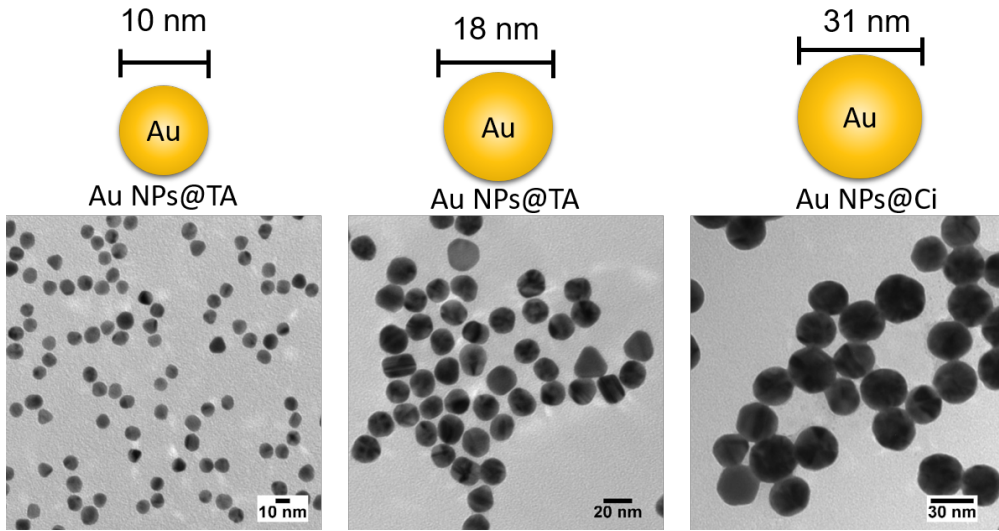


Figure 4.6: **Au NPs used for the production of matchstick-like particles.** TEM image of the Tannic acid (TA) stabilized Au NP suspensions of diameters $D = 10$ and 18 nm and citrate (Ci) ones of $D = 31$ nm of PDI = 0.05, 0.07 and 0.10 respectively (from left to right).

The ILT plot shows a main peak for all the angles and for some of them a second peak at higher decay times for which the parameter $Area_2/\tau_2$ is negligible so it is not taken into account. According to $Area_1/\tau_1$, the data have lower noise in the range of angles $70^\circ \leq \theta \leq 150^\circ$, since their dispersion are around 10%. Thus, we have chosen this range to fit the q^2 dependence of Γ_1 . Following equation 3.46, the measured diffusion coefficient of $D = 18$ nm Au NPs corresponds to $D_T = 14.3 \pm 0.7 \mu\text{m}^2/\text{s}$. This value corresponds to the diffusion of a sphere of hydrodynamic diameter $d_H = 29.9 \pm 1.4$ nm (equation 3.29). Thus, our Au NPs of $D = 18$ nm in $I = 5$ mM buffer diffuse in the same way as hard spheres of $D \sim 30$ nm.

To understand the difference between the value measured of hydrodynamic diameter and the bare one, we have to consider the ionic conditions of the medium used for the measurement. At $I = 5$ mM Tris/HCl buffer, the Debye length corresponds to $\kappa^{-1} = 4.3$ nm. Considering the hydrodynamic diameter as $d_H \approx D + 2\kappa^{-1}$ we obtain $d_H = 26.6$ nm which is consistent with the experimental results. This is in contrast with our observation in the

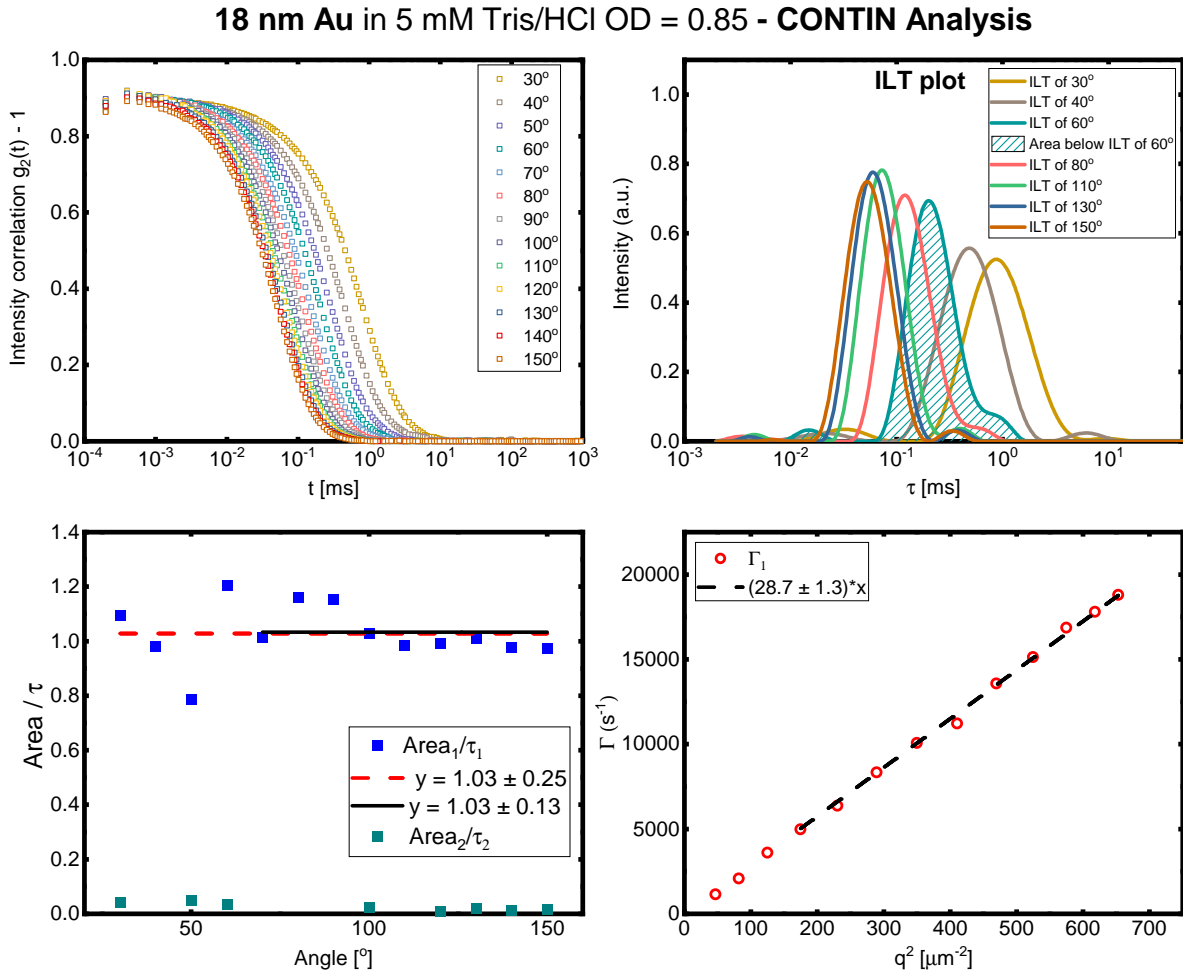


Figure 4.7: **CONTIN analysis of Au NPs of $D = 18 \pm 1.5$ nm in $I = 5$ mM Tris/HCl buffer at $C_{Au} = 7.7 \times 10^{11}$ part/ml = $0.47C^*$.** The ILT is computed from the experimental data in the range of angles $30^\circ \leq \theta \leq 150^\circ$. The normalized parameter $Area/\tau$ indicates that the contribution of lowest intensity is negligible and that the data dispersion of the main contribution is $\sim 10\%$ for the range $70^\circ \leq \theta \leq 150^\circ$. The q^2 dependence of Γ_1 is a single straight line of slope $2D_T$ resulting in $D_T = 14.3 \pm 0.7 \mu\text{m}^2/\text{s}$ which corresponds to an hydrodynamic diameter of $d_H = 29.9 \pm 1.4$ nm.

rod-shaped virus suspension whose diffusion is not significantly affected by the electric double layer.

Knowing that the nanoparticles are not perfectly spherical, we compare the previous result with the approximation proposed in equation 3.48 where the Au NPs are considered as slightly anisotropic particles with d_H given by equation 3.29. Here, we limit the fit to the range of angles where the noise is lower than 10% according to the parameter $Area_1/\tau_1$. The global parameters obtained are $A = 1$ and $d_H = 28.4 \pm 0.2$ nm. As shown in figure 4.8, the β parameter remains constant in this range of angles. Note that $A = 1$ corroborates that the DLS measurements on our Au NPs are only sensitive to the translational diffusion coefficient, D_T .

The results obtained from both analysis give us an estimation of the error bar of our measurements. From the CONTIN analysis we get a diffusion coefficient of $D_T = 14.3 \pm$

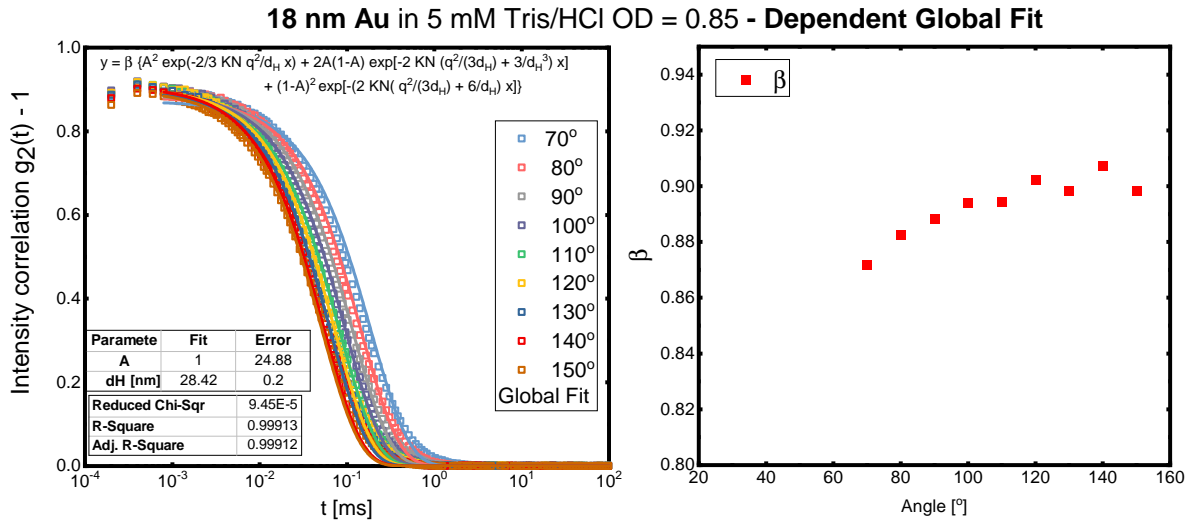


Figure 4.8: **Dependent global fit analysis of Au NPs of diameter $D = 18 \pm 1.5$ nm.** **Left:** Global fit (full lines) of the intensity correlation functions (scattered points) in the range of angles $70^\circ \leq \theta \leq 150^\circ$. **Right:** Fit parameter β for all the angles. The values found for the global parameters are $A = 1$ and $d_H = 28.4 \pm 0.2$ nm.

$0.7 \mu\text{m}^2/\text{s}$. From the dependent global fit analysis, we get a diffusion equivalent to the one of a sphere of $d_H = 28.4 \pm 0.2$ nm, i.e., $D_T = 15.0 \pm 0.1 \mu\text{m}^2/\text{s}$ according to equation 3.29. Here, we take the mean value and include in the error bars the dispersion of our data. Thus, the diffusion of 18 nm Au NPs measured by DLS corresponds to $D_T = 14.7 \pm 1.0 \mu\text{m}^2/\text{s}$.

4.2.3 Mixture of Au NPs and rod-shaped viruses

Since the matchstick-like particles are made of one single nanoparticle attached to a single virus, it is relevant to investigate a equimolar mixture of both elements, i.e., a suspension of both elements present at equal particle concentration $C = 7.7 \times 10^{11}$ part/ml = $0.47C^*$.

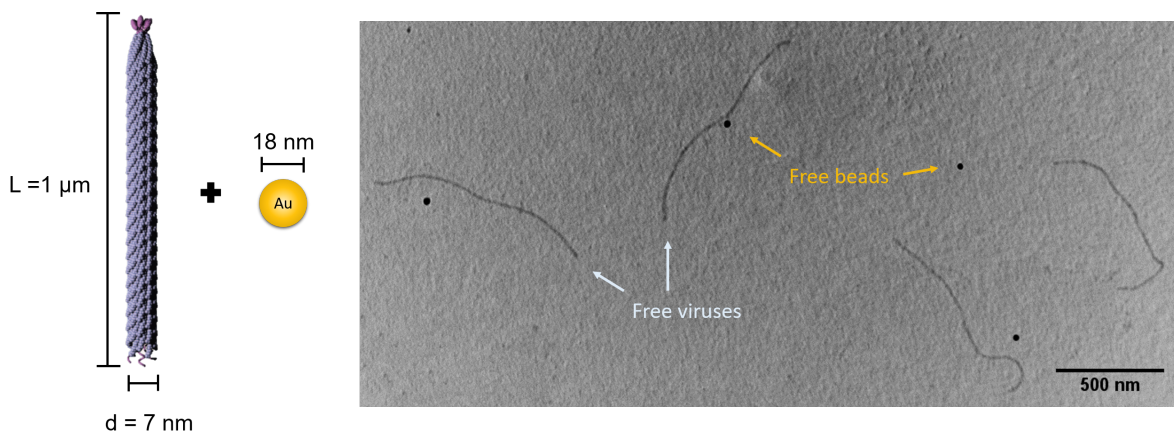


Figure 4.9: **Characterization of the equimolar mixture of M13KE virus and Au NP of $D = 18$ nm.** **Left:** Schematic representation of the mixture composed by one virus particle for one gold particle **Right:** TEM image of the mixture.

In order to avoid that the mixture self-assemble into gold-virus colloids, we have used the M13KE virus described in section 2.2. This strain displays less number of cysteine groups in the p3 protein resulting in a lower yield of tip binding for Au NPs compared to the M13C7C mutant [55]. Additionally, we have chosen to work at low ionic strength conditions to ensure that the electrostatic repulsion between all the particles is high enough to avoid their interaction and then their binding reaction. For this, the mixture is dialyzed against a $I = 5$ mM Tris/HCl buffer and the DLS experiment is performed right after the dialysis is finished. In figure 4.9, a TEM observation done after the experiment shows that there are not gold-virus colloids formed in these conditions.

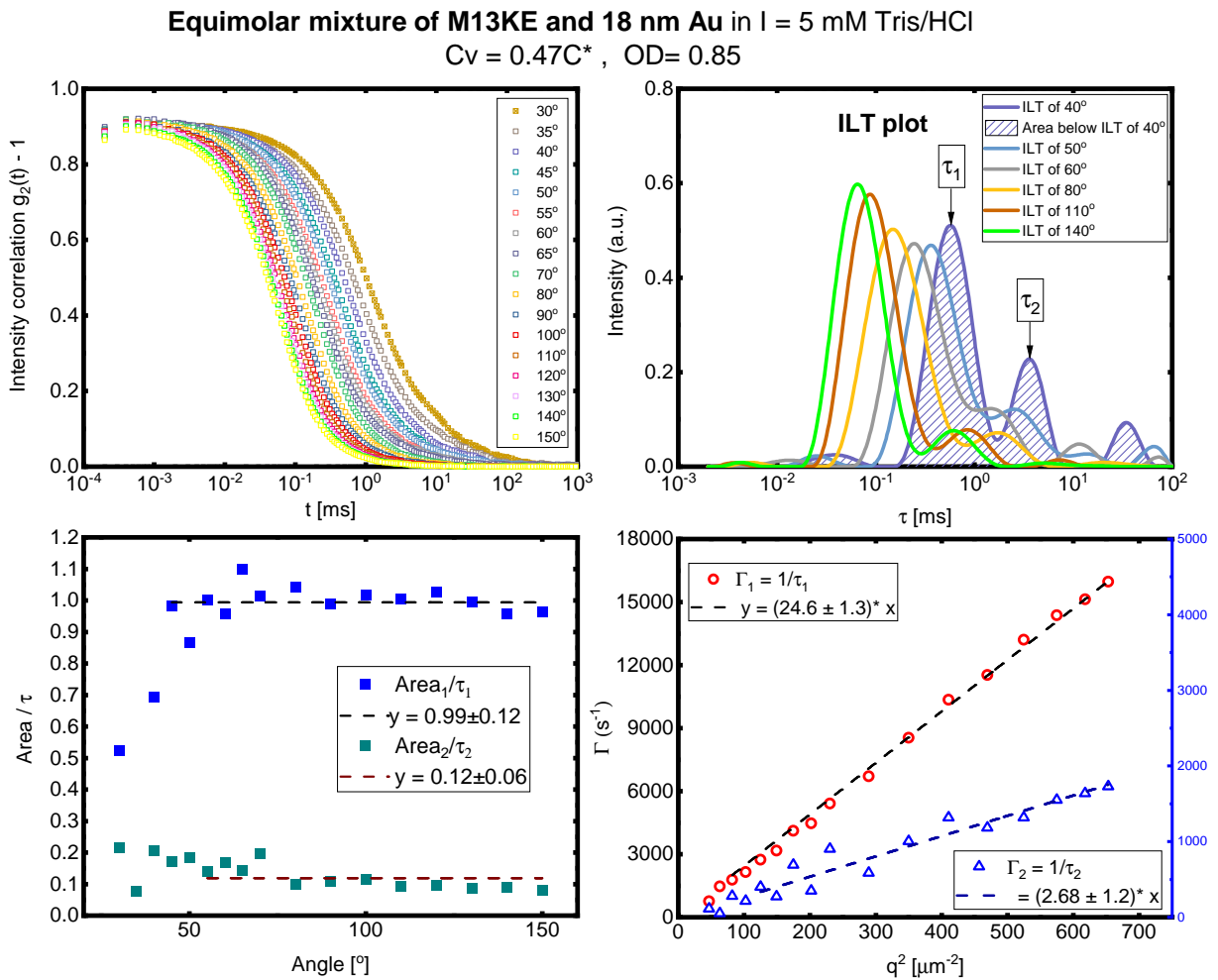


Figure 4.10: CONTIN analysis of an equimolar mixture of M13KE rod-like viruses and Au NPs of $D = 18$ nm in $I = 5$ mM Tris/HCl buffer at $C = 7.7 \times 10^{11}$ part/ml = $0.47C^*$. The ILT computed for the range of angles $30^\circ \leq \theta \leq 150^\circ$ exhibits multiple peaks. The normalized parameter $Area/\tau$ shows that the main and second peaks associated to τ_1 and τ_2 have lower noise for the range of angles $40^\circ \leq \theta \leq 150^\circ$ and $55^\circ \leq \theta \leq 150^\circ$ respectively. The q^2 dependence of Γ_1 and Γ_2 is a single straight line of slope $2D_T$ from which is obtained $D_{T1} = 12.3 \pm 0.7 \mu\text{m}^2/\text{s}$ and $D_{T2} = 1.3 \pm 0.7 \mu\text{m}^2/\text{s}$.

Since the sample is a binary mixture, it is expected that the intensity correlation function is composed by at least two exponential decays: one related to the diffusion of the spherical Au NPs and the other related to the diffusion of the viral rods. The results of the CONTIN

analysis, whose implementation allows us to retrieve the distribution of decay times, are given in figure 4.10. The distributions of decay times exhibit two or more peaks. The main peak is found at shorter decay times compared with the following peaks of lower intensity. The normalized parameter $Area/\tau$ is calculated for the first two significant peaks. The main peak contribution has a minimum noise in the range of angles $40^\circ \leq \theta \leq 150^\circ$ while the second one in the range $55^\circ \leq \theta \leq 150^\circ$. We have analyzed the second peak associated to τ_2 despite the observed low value of the normalized parameter $Area_2/\tau_2$. The calculated decay rates Γ_i exhibit a linear dependence of slope $2D_T$. However, Γ_1 exhibits a lower dispersion than Γ_2 . For the main contribution we find $D_{T1} = 12.3 \pm 0.7 \mu\text{m}^2/\text{s}$ while for the second one $D_{T2} = 1.3 \pm 0.7 \mu\text{m}^2/\text{s}$.

From the results discussed in sections 4.2.1 and 4.2.2, we expect to recover $D_T = 14.7 \pm 1.0 \mu\text{m}^2/\text{s}$ for the Au NPs of $D = 18 \text{ nm}$ and $D_T = 2.5 \pm 0.3 \mu\text{m}^2/\text{s}$ for the rod-like viruses. The latter suggest that the diffusion associated with τ_1 is related to the Au NPs while the second one associated with τ_2 of significantly lower contribution is related to the diffusion of the viruses. The observed difference between the experimental values of the single elements compared with the measured ones from the mixture can be explained as follows. On one hand, the low scattering signal of the viral rods compared with the one of the Au NPs results in a higher error of the estimated diffusion. On the other hand, at this particle concentration for which the viruses are close to interact to each other the Au NPs could be limited in their diffusion due to cage effects.

From these observations, we conclude that the intensity correlation signal of a mixture of Au NPs and rod-shaped viruses mostly comes from the Au NPs. Therefore, we expect to measure the diffusion of our hybrid gold-virus colloids by only probing the Au NPs attached to them.

4.3 Diffusion of matchstick-like particles

For the study of their self-diffusion, matchstick-like particles made of Au NPs of $D = 10, 18$ and 31 nm have been produced according to the protocol described in section 2.3.2. The suspensions, composed by $\sim 80\%$ matchstick-like structures, are tested at different particle concentrations. We discuss next our finding in the suspension made of $D = 18 \text{ nm}$ Au NPs at $C_v = 0.47C^*$. A schematic representation of the structure and a TEM image of this sample are shown in figure 4.11.

In figure 4.12 are the distribution of decay times composed by a main peak and a second peak of negligible contribution at shorter decay times. From our investigations on section 4.2.3, we expect that the main contribution corresponds to the scattering signal coming from the Au NPs.

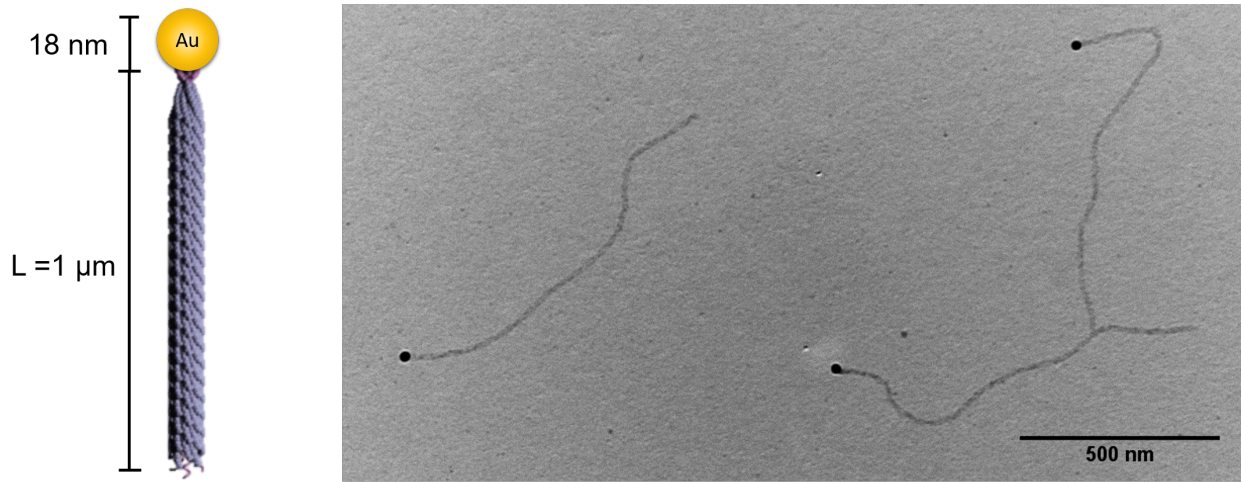


Figure 4.11: **Characterization of matchstick-like particles made of Au NPs of $D = 18$ nm.** **Left:** Schematic representation of matchstick-like particles. **Right:** TEM image of the structures.

Matchstick-like of 18 nm Au in 5 mM Tris/HCl $C_v = 0.47C^*$ - CONTIN Analysis

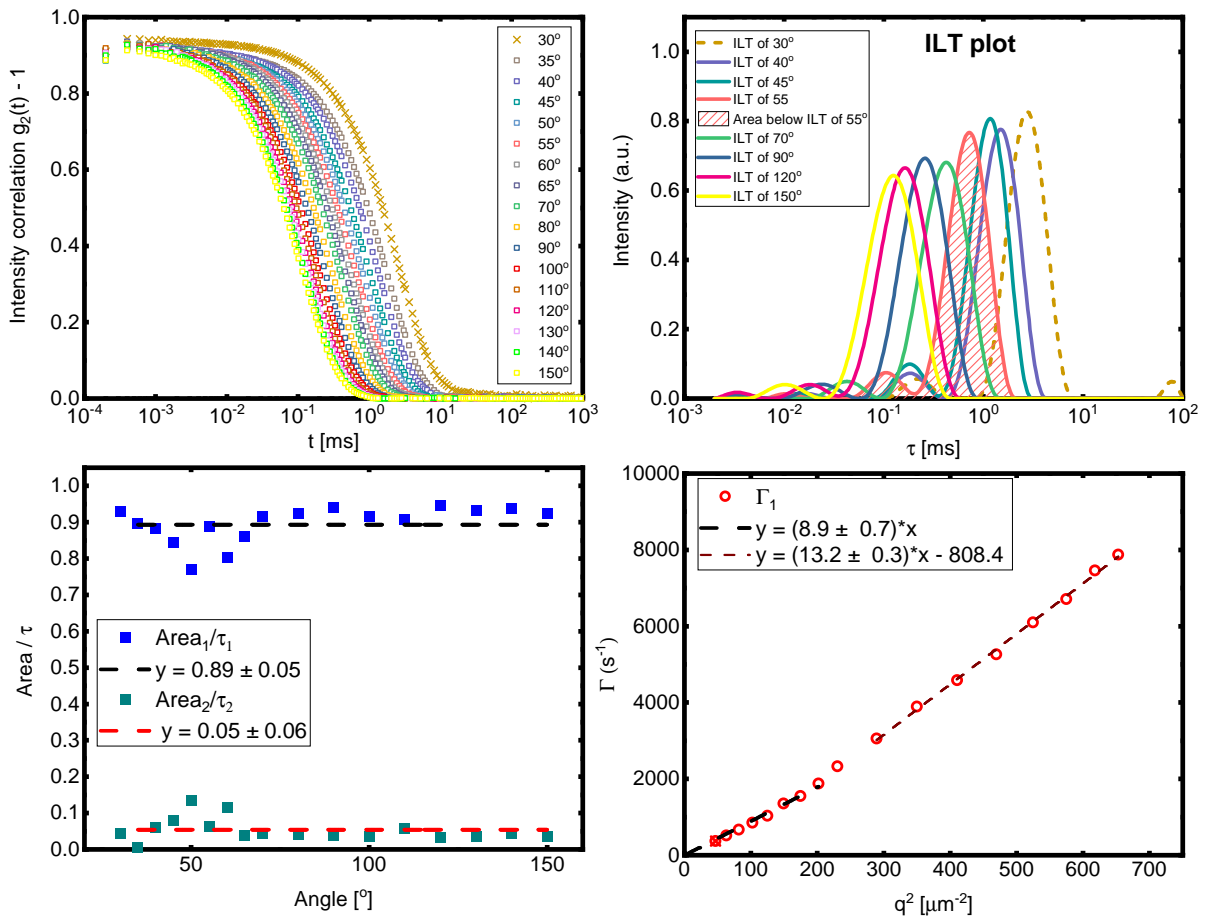


Figure 4.12: **CONTIN analysis of matchstick-like particles made of Au NPs of $D = 18$ nm in $I = 5$ mM Tris/HCl buffer at $C_v = 0.47C^*$.** The ILT is computed from the experimental data in the range of angles $30^\circ \leq \theta \leq 150^\circ$ showing two peaks. The main peak, associated to the diffusion of the Au NPs, exhibits low noise for all the range of θ . The q^2 dependence of Γ_1 is a single straight line of slope $2D_T$ from which is obtained $D_T = 4.5 \pm 0.4 \mu\text{m}^2/\text{s}$.

Even though the noise in the experimental data is found to be lower than 10% for all the range of angles, the q^2 dependence of Γ_1 exhibits two different regimes (see fits of Γ_1). This is similar to the observed change of slope in the rod-shaped viruses suspension (see figure 4.3) for which the persistence length influences the diffusion measured. Thus, in order to obtain the effective D_T of the structure, we consider the angles where Γ_1 has a linear dependence of q^2 with intercept in zero. From the linear fit in the range $35^\circ \leq \theta \leq 65^\circ$, we find a $D_T^{\text{eff}} = 4.5 \pm 0.4 \mu\text{m}^2/\text{s}$.

For comparison, we have also implemented the independent global fit (equation 3.47) for the same range of angles. The global parameters for the fit plotted in figure 4.13 correspond to $A = 0.962$, $D_T = 4.45 \pm 0.02 \mu\text{m}^2/\text{s}$ and $D_R = 2114.6 \pm 141.1 \text{ s}^{-1}$. Even though the D_R value is around a factor two higher than the value experimentally obtained for single viruses (see figure 4.5) the $A \sim 1$ indicates that our results are not sensitive enough to the rotational motion. The latter comes from the fact that the Au NPs under investigation are mostly isotropic in shape and optically which results in a low contribution to the rotational terms in equation 3.47.

Combining the results of both methods, we conclude that the effective diffusion of the matchstick-like particle obtained by probing the Au NP attached to it corresponds to $D_T^{\text{eff}} = 4.5 \pm 0.4 \mu\text{m}^2/\text{s}$.

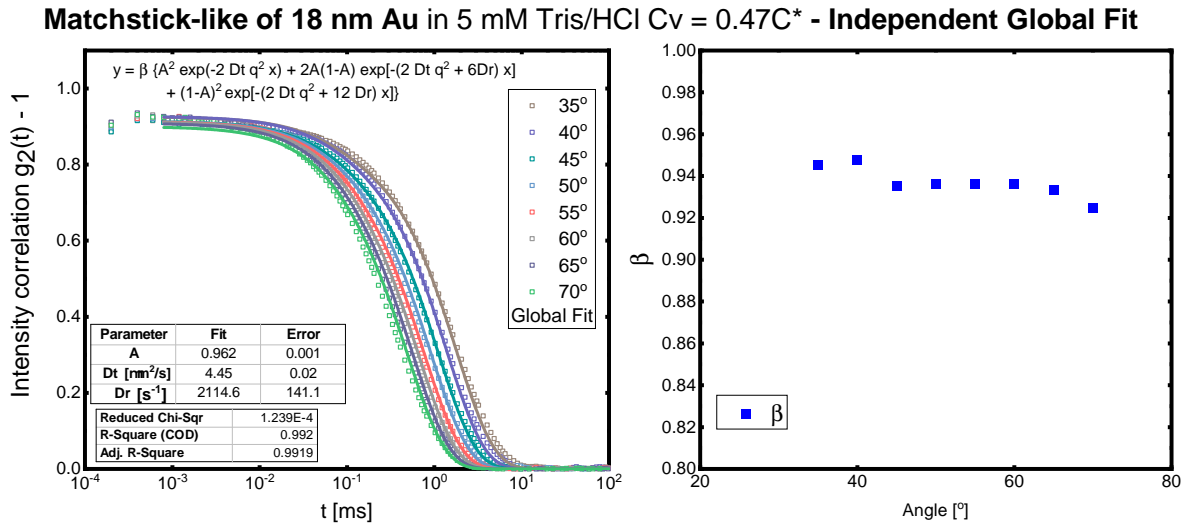


Figure 4.13: **Independent global fit analysis of matchstick-like particles made of Au NPs of $D = 18 \text{ nm}$ in 5 mM Tris/HCl at $C_v = 0.47C^*$.** **Left:** Global fit (full lines) of the intensity correlation functions (scattered points) in the range of angles $30^\circ \leq \theta \leq 70^\circ$. **Right:** Fit parameter β for all the angles. The values found for the global parameters are $A = 0.962$, $D_T = 4.45 \pm 0.02 \mu\text{m}^2/\text{s}$ and $D_R = 2114.6 \pm 141.1 \text{ s}^{-1}$.

Now, we compare these findings with the previously obtained in our group by single particle tracking (SPT) [55], $D_T = 2.25 \mu\text{m}^2/\text{s}$. As discuss in section 3.2.2, the diffusion of a matchstick-like particle suspension using SPT is obtained by probing the virus involved in the structure thanks to fluorescence microscopy. The measured D_T is in agreement with the one

expected for rods of $L = 1 \mu\text{m}$ which for aqueous suspensions corresponds to $D_T = 2.1 \mu\text{m}^2/\text{s}$. However, the D_T^{eff} obtained from the DLS measurements in which we probe the Au NP attached to the structure is up to a factor two higher. How do we explain this increase of diffusion when we observe the bead? Can it be related to a physical quantity?

In the following subsection we discuss the interpretation in terms of the linking point between Au NPs and the virus tip.

4.3.1 Diffusion coefficient considering a flexible link

The main difference in our estimation can be attributed to the fact that by SPT we determine the position of the center of mass of the structure in a focal plane while by DLS we test the diffusion of the bead which has an extra degree of freedom due to the link between the p3 proteins of the virus tip.

It is known that the p3 proteins have certain flexibility that allows their interaction with the membrane for its replication [82, 140] (see figure 2.9). When a single Au NP is attached to this virus tip, the flexibility of the proteins limits the

random walk motion of the bead around the equilibrium position. Thus, we account for this Au bead-p3 protein interaction by a spring-bead model as shown in figure 4.14.

For such a case, an extra contribution coming from this flexible link has to be considered for the interpretation of the scattering signal. From the DLS principles (equations 3.13, 3.21 and 3.27), it follows that for spherical particles the intensity correlation function is related to the intermediate scattering function $F_s(q, t)$, as:

$$g_2(q, t) - 1 = \beta |F_s(q, t)|^2. \quad (4.2)$$

The $F_s(q, t)$ has the contributions from overall translational and rotational diffusions as well as from the spring-bead motion. In the general case, all are coupled. Here, we work with a decoupling approximation for which it is assumed that the dynamics due to the flexible link (flex) does not alter the overall translational (trans) and rotational (rot) diffusions [141], i.e.:

$$F_s(q, t) = F_{\text{trans}}(q, t) \cdot F_{\text{rot}}(q, t) \cdot F_{\text{flex}}(q, t). \quad (4.3)$$

Based on the previously rod-like diffusion of the structure observed by SPT, for the $F_{\text{trans}}(q, t)$ and $F_{\text{rot}}(q, t)$ terms we assume that the translational and rotational motion is given by the virus diffusion. Thus, considering the case of anisotropic particles whose dynamic form factor is composed by only the first two terms of equation 3.23 (see section

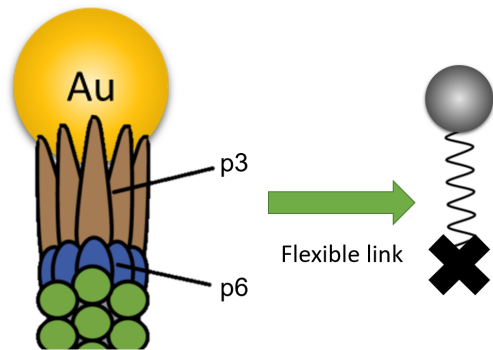


Figure 4.14: Spring-bead model accounting for the flexibility of the p3 proteins at the virus tip bound to Au NP.

3.3.1.2), the expression $F_{trans}(q, t) \cdot F_{rot}(q, t)$ of equation 4.3 results in:

$$F_{trans}(q, t) \cdot F_{rot}(q, t) = A \exp(-D_T q^2 t) + B \exp[-(D_T q^2 + 6D_R)t], \quad (4.4)$$

with A and B given by equation 3.41.

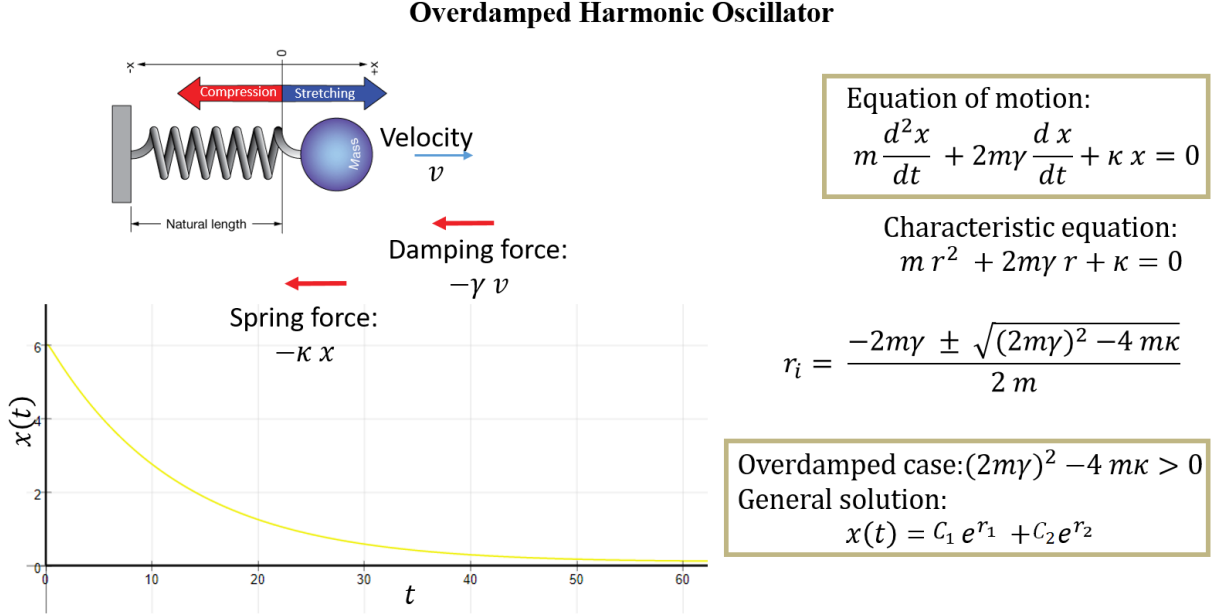


Figure 4.15: **Overdamped harmonic oscillator.** The equation of motion described by the spring constant k and friction coefficient γ has as solution the sum of two exponential decays. This causes that the mass approaches back to zero position.

The motion related to the flexible link is a problem described by the Ornstein-Uhlenbeck process [142]. This is a random walk in a harmonic potential, restricting particle's motion to a small range around an equilibrium position. It can be shown [143], that the Langevin type equation of this process considering high friction results in oscillation solutions describing vibrational motion as the overdamped harmonic oscillator shown in figure 4.15. The derivation of the corresponding intermediate scattering function, found in reference [141], gives us the contribution due to the flexible link:

$$F_{flex} = \exp\{-q^2 \langle r^2 \rangle [1 - \exp(-\lambda t)]\}, \quad (4.5)$$

with

$$\langle r^2 \rangle = \frac{k_B T}{k} \quad (4.6)$$

the mean square displacement, and

$$1/\lambda = \gamma/k \quad (4.7)$$

the relaxation time in terms of the friction coefficient γ and spring constant k . Combining equations 4.2, 4.3, 4.4 and 4.5 it follows that the intensity correlation function of the Au

NPs that compose the matchstick-like structures is given by:

$$g_2(q, t) - 1 = \beta \{ (A \exp(-D_T q^2 t) + B \exp[-(D_T q^2 + 6D_R)t]) \times (\exp\{-q^2 \langle r^2 \rangle [1 - \exp(-\lambda t)]\})^2 \}. \quad (4.8)$$

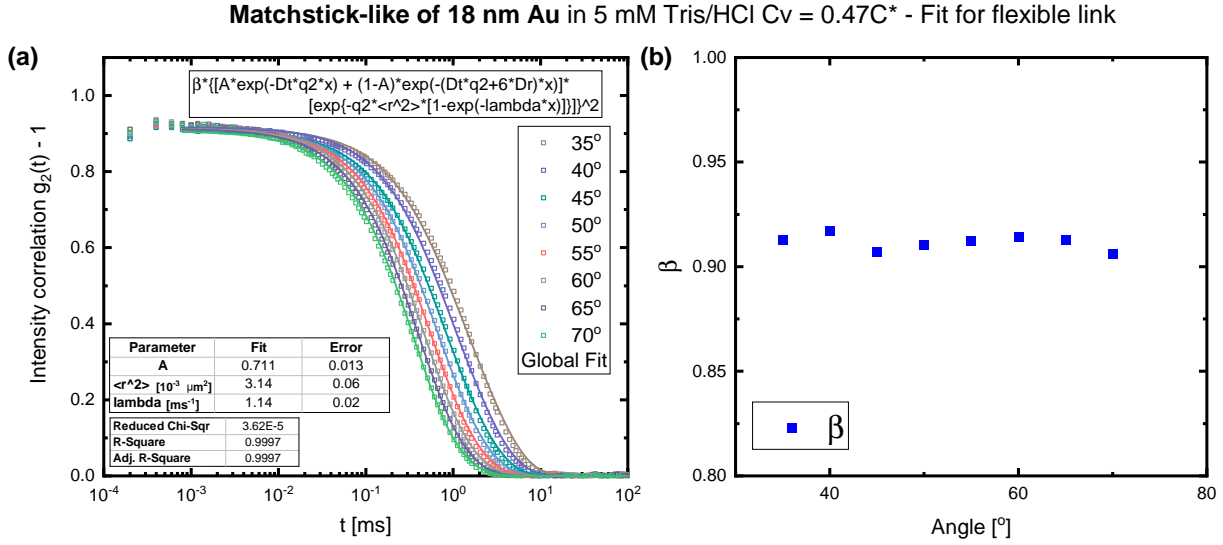


Figure 4.16: **Global fit for the spring-bead model.** (a) The intensity correlation function $g_2(q, t) - 1$ measured for matchstick-like particles made of $D = 18$ nm Au NPs in the range of angles $35^\circ < \theta < 70^\circ$ is analyzed considering a flexible link. For fixed $D_T = 2.5 \mu\text{m}^2/\text{s}$ and $D_R = 21.5 \text{ s}^{-1}$ corresponding to the translational and rotational diffusion coefficients of a stiff rod of $1 \mu\text{m}$ long, we obtain a very good quality of the numerical fit and as global parameters $\langle r^2 \rangle = 3.1 \pm 0.1 \times 10^{-3} \mu\text{m}^2$ and $\lambda = 1.14 \pm 0.02 \text{ ms}^{-1}$. (b) The free parameter β is plotted as function of the scattering angle θ .

In figure 4.16, we have analyzed simultaneously the set of intensity correlation functions in the range of angles $35^\circ < \theta < 70^\circ$ using equation 4.8 for fixed parameters $D_T = 2.5 \mu\text{m}^2/\text{s}$ and $D_R = 21.5 \text{ s}^{-1}$ which correspond to the translational and rotational diffusion coefficients of the rod-shaped viruses measured by DLS. The free parameter β , related to the coherence factor, is plotted as function of the scattering angle in figure 4.16 (b). As global parameters, we obtain $A = 0.71$, $\langle r^2 \rangle = 3.1 \pm 0.1 \times 10^{-3} \mu\text{m}^2$ and $\lambda = 1.14 \pm 0.02 \text{ ms}^{-1}$.

Note that the the root mean square displacement (rmsd), $\text{rmsd} = \sqrt{\langle r^2 \rangle}$, of about 56 nm is comparable with the typical length scale of the p3 protein, i.e., few nanometers [144, 145]. Moreover, from equations 4.6 and 4.7, it follows that the overdamped motion of our model is given by a spring constant of $k = 323 k_B T / \mu\text{m}^2$ and a friction coefficient $\gamma = 0.28 k_B T \text{ s} / \mu\text{m}^2$. The friction coefficient of spheres is related to the diffusion by $D_T = k_B T / \gamma$. Hence, we obtain a diffusion of the bead of $D_T = 3.5 \mu\text{m}^2/\text{s}$ which is self-consistent with the approach where we found $D_T^{\text{eff}} \sim 4.5 \mu\text{m}^2/\text{s}$. The latest comparison indicates that the link between the Au NPs and the p3 proteins allows enough motion to contribute in the observed increase of the dynamics. This result is therefore a direct proof of the flexibility of the p3 proteins.

4.3.2 Nanoparticle size and concentration dependence

Here, we investigate the influence of the concentration on the measured D_T^{eff} for the different suspensions containing $\sim 80\%$ of matchstick-like particles. The range of concentrations possible to explore for each suspension is limited by the scattering properties of the Au NPs. For instance, according to the Rayleigh scattering theoryⁱⁱ, Au NPs of $D = 10$ nm scatter around 34 times less than Au NPs of $D = 18$ nm. In identical conditions, the scattering signal obtained experimentally for $D = 10$ nm Au NPs is not detectable with sufficient accuracy for $C = 0.1C^*$ contrary to the Au NPs of bigger size. Hence, we have explored the concentration range $0.1 < C/C^* < 1$ for matchstick like particles made of Au NPs of $D = 10$ nm, $0.01 < C/C^* < 0.47$ for the ones made of $D = 18$ nm Au NPs and $0.01 < C/C^* < 0.07$ for those made of $D = 31$ nm Au NPs. The CONTIN analysis of each concentration tested are described in the appendix I.

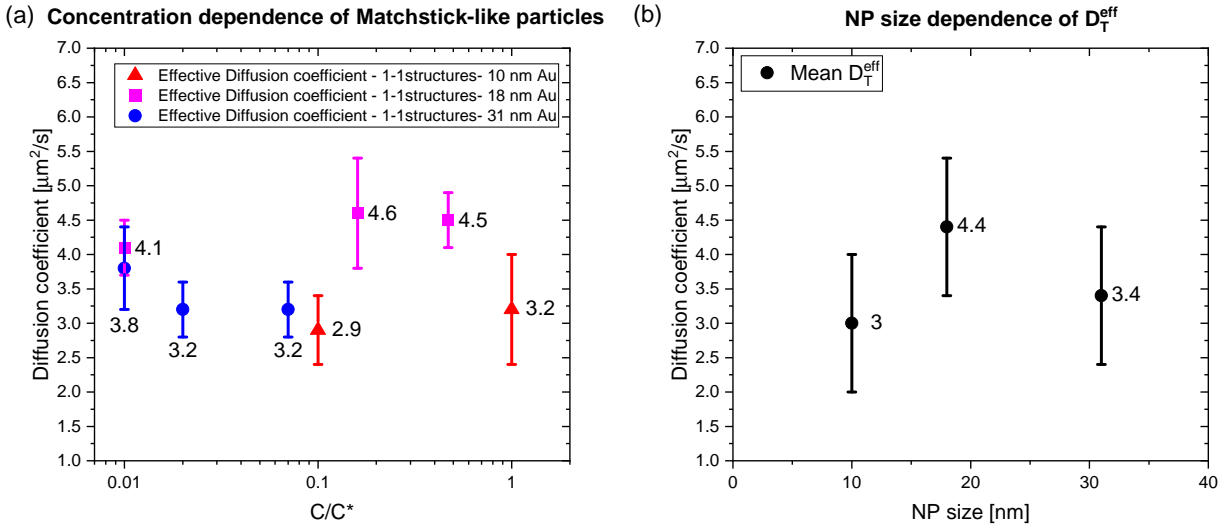


Figure 4.17: **Summary of D_T^{eff} obtained for matchstick-like particles made of Au NPs of $D = 10, 18$ and 31 nm.** (a) Obtained from the CONTIN analysis as function of the normalized concentration C/C^* . (b) Mean value as function of the NP size. The error bars indicate the dispersion of the estimated D_T^{eff} for all the experimental data.

In figure 4.17 (a), the D_T^{eff} values of each sample are summarized. The error bars indicate the highest dispersion in the estimated D_T^{eff} .

For the matchstick-like particles made of Au NPs of $D = 10$ nm we find that the diffusion of the structure is, within the error bar, the same for the concentrations tested $C/C^* = 0.1$ and $C/C^* = 1$. This is similar to the diffusion of matchstick-like particles made of Au NPs of $D = 31$ nm, for which the concentrations tested were between $0.01 < C/C^* < 0.07$. Finally, for the matchstick-like particles made of Au NPs of $D = 18$ nm, D_T^{eff} has the same value for all the range of concentrations. The latter observations confirm our assumption that for $C < C^*$ the structures do not interact with each other and hence their diffusion is independent of the particle concentration.

ⁱⁱThe scattering intensity increases with the power sixth of the particle diameter, i.e., $I \sim (d/2)^6$ [103].

Thus, we have obtained the mean value from the measurements done at different concentrations and consider as error bars the dispersion of the D_T^{eff} estimated for all the data. In figure 4.17 (b), these values are plotted as function of the NP size. We find a mean of $D_T^{\text{eff}} = 3.0 \pm 1.0 \mu\text{m}^2/\text{s}$, $D_T^{\text{eff}} = 4.4 \pm 1.0 \mu\text{m}^2/\text{s}$ and $D_T^{\text{eff}} = 3.4 \pm 1.0 \mu\text{m}^2/\text{s}$ for matchstick-like particles made of $D = 10, 18$ and 31 nm respectively. Thus, the effective diffusion of the matchstick-like structure is also independent of the NP size.

We have also applied the spring-bead model approach of section 4.3.1 for each set of data tested. The fit of each one is show in the appendix I. In figure 4.18, we have summarized for the different structures, the spring constant k , friction coefficients γ and root mean square displacement $rmsd$ with error bars from the standard error of the fitted values as function of the concentration.

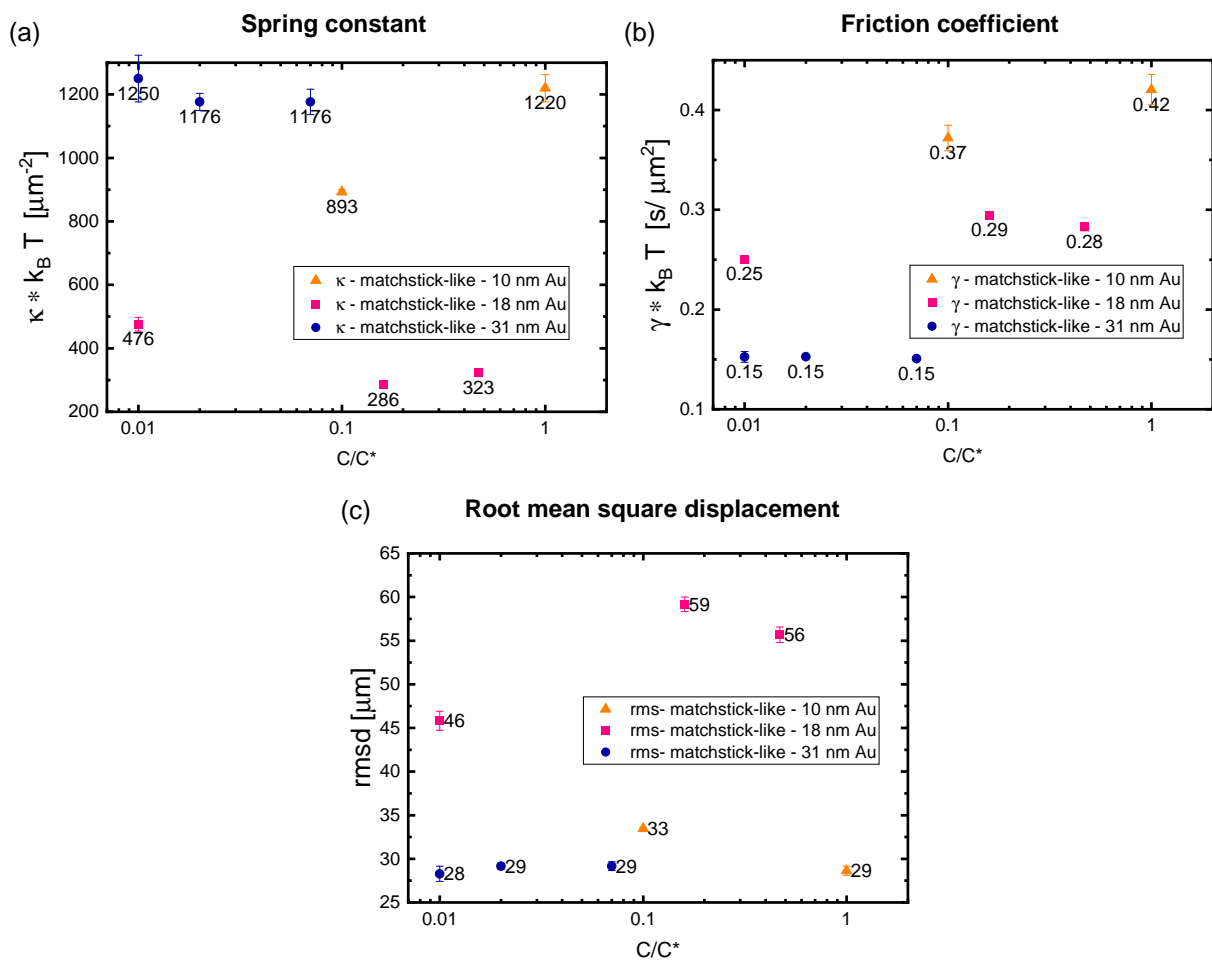


Figure 4.18: **Summary of spring-bead model of matchstick-like particles made of Au NPs of $D = 10, 18$ and 31 nm.** (a) Spring constant, k , (b) friction coefficient, γ , and root mean square displacement, rms , as function of the particle concentration. The error bars are calculated from the standard error of the fitted values.

The parameters k , γ and $rmsd$ are around the same value for all the concentrations. The $rmsd$ of around 30 to 60 nm is compatible with p3 protein length scale. From the friction coefficient, we obtain a diffusion of the beads that ranges from 2.2 to 6.6 $\mu\text{m}^2/\text{s}$ which is self-consistent with the effective diffusion of the matchstick-like particles. The

differences observed between the NP sizes are accounted for the low accuracy of the fit for the matchstick-like particles of 30 nm Au NPs and for the low scattering signal obtained for the ones made of $D = 10$ nm Au NPs (see appendix I). It has to be noted that the exchange ligand of the Au NPs used to produce the structures is different (Tannic acid for Au NPs of $D = 10$ and 18 nm and citrate for the ones of $D = 31$ nm) which could affect the interaction of the Au surface with the p3 proteins of the virus tip. However, our observations do not show a difference when comparing nanoparticles with different ligands.

Thus, we conclude that the parameters obtained from the spring-bead model are nearly as well independent of nanoparticle size and particle concentration.

4.4 Diffusion of dumbbell-like particles

In this section we present the DLS study of the dumbbell-like particle made of Au NPs of $D = 10$ nm. As described in section 2.3.3, the production of this structure involves the formation of other structures. As shown in figure 4.19, our sample at $C_v = 0.5C^*$ is composed mostly by dumbbell-like particles (53%) and matchstick-like structures (23%). The complete distribution of structures is shown in figure 2.25.

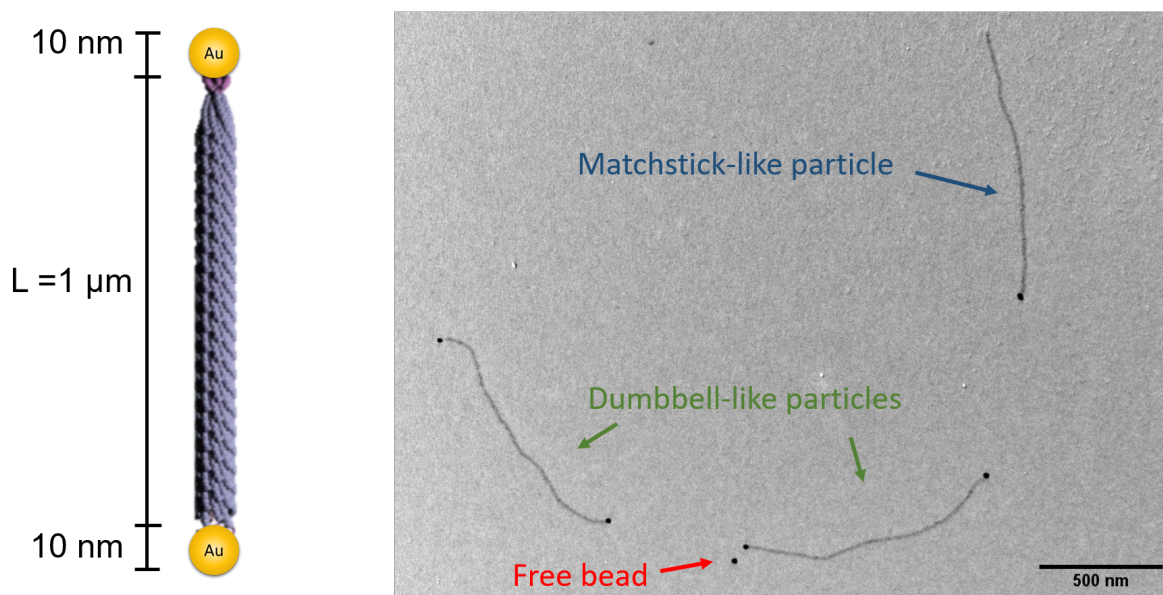


Figure 4.19: **Characterization of the Dumbbell-like suspension.** **Left:** Schematic representation of the Dumbbell-like structure. **Right:** TEM image of the sample composed of 53% of dumbbell-like particles and 23% of matchstick-like particles.

Since the sample is a mixture of different structures, we expect that the distribution of decay times retrieved by the CONTIN method is composed by multiple peaks each one related to the characteristic diffusion of a particular structure. As shown in figure 4.20, the ILT plot exhibits a broad main peak associated to τ_1 and for some angles a second peak of negligible intensity associated to τ_2 . From the main peak we found that the decay rate, Γ_1 , exhibits two regimes. This is similar to our findings for the matchstick-like particles which are

also affected by the persistence length of the virus. Hence, we take the same considerations as for that case and limit the range of analysis to $30^\circ < \theta < 70^\circ$. The normalized parameter $Area_1/\tau_1$ indicates $\sim 14\%$ of noise in this range. From the linear fit of q^2 , we recover an effective translational diffusion coefficient of $D_T^{eff} = 3.45 \pm 0.7 \mu\text{m}^2$.

The value of D_T^{eff} obtained is interpreted as an average diffusion coefficient of the different structures in the suspension. This stems from the resolution limit of the ILT which does not separate the multiple peak contribution coming from the Au NPs belonging to different structures but instead broadens the distribution.

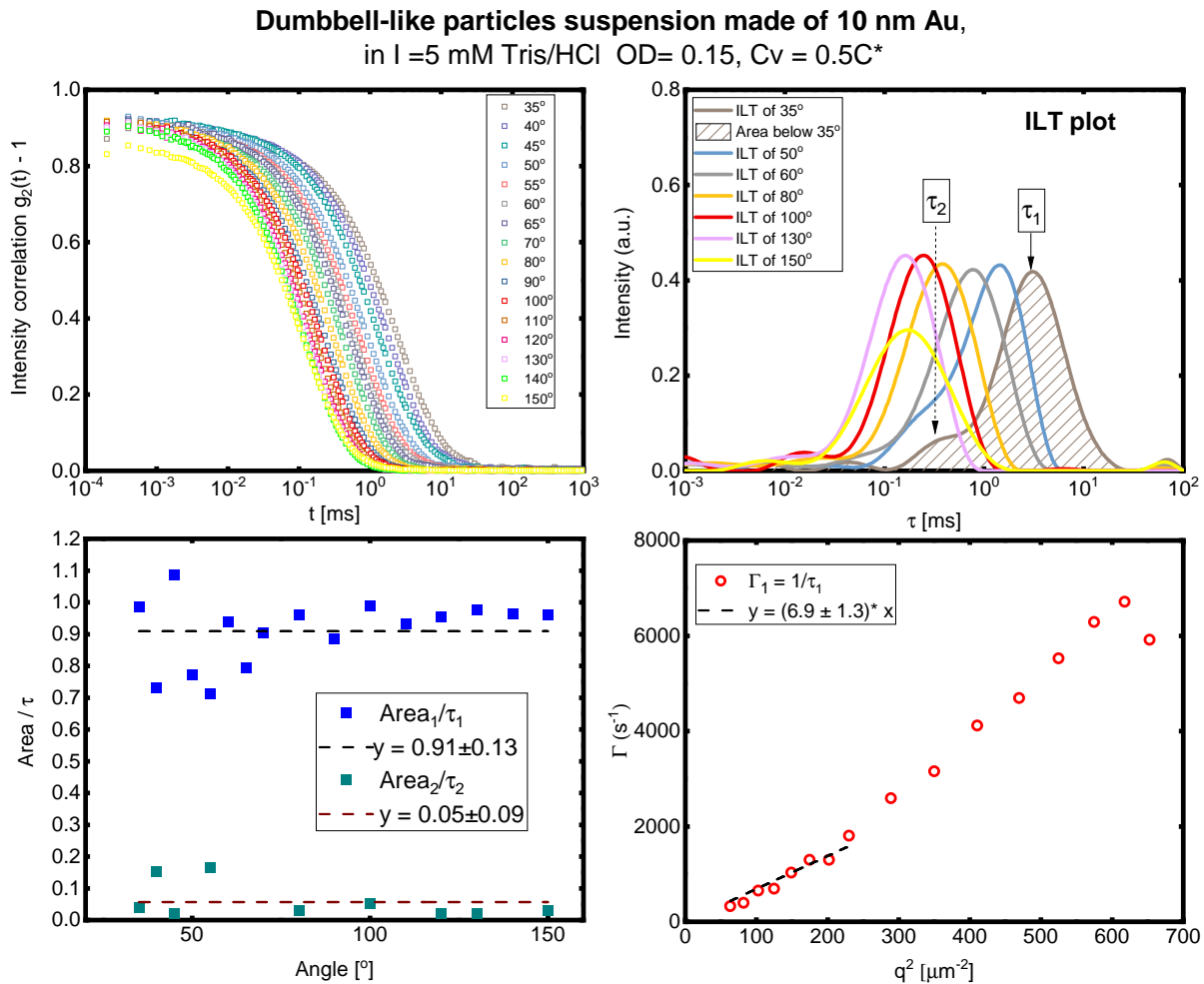


Figure 4.20: **CONTIN analysis of a mixture with 53 % dumbbell-like structures made of Au NPs of $D = 10 \text{ nm}$ in $I = 5 \text{ mM Tris/HCl}$ buffer at $C_v = 0.5C^*$.** The ILT is computed from the experimental data in the range of angles $30^\circ \leq \theta \leq 150^\circ$ showing a main broaden peak. The q^2 dependence of Γ_1 is a straight line of slope $2D_T$ from which it is obtained $D_T = 3.5 \pm 0.6 \mu\text{m}^2/\text{s}$.

Knowing that at least one of the beads of the structures is bound to the p3 proteins which are flexible, we have tested the same spring-bead model approach described in section 4.3.1. As shown in figure 4.21, the global fit for the range of angles $35^\circ < \theta < 55^\circ$ using equation 4.8 for fixed parameters $D_T = 2.5 \mu\text{m}^2/\text{s}$ and $D_R = 21.5 \text{ s}^{-1}$ does not recover the decay of the lower angles. We obtain $A = 1$, $\langle r^2 \rangle = 1.52 \pm 0.03 \times 10^{-3} \mu\text{m}^2$ and $\lambda = 3.1 \pm 0.1 \text{ ms}^{-1}$.

The rmsd of around 39 nm is compatible with the scale length of the virus tip proteins and with the value obtained for the respective matchstick like particles, $rmsd \sim 30$ nm. From equations 4.6 and 4.7, we obtain $k = 657.9 k_B T / \mu\text{m}^2$ and $\gamma = 0.212 k_B T \text{ s} / \mu\text{m}^2$. The friction coefficient is related to the diffusion of $D_T = 4.7 \mu\text{m}^2/\text{s}$ which is higher than the effective diffusion of matchstick-like particles of 10 nm Au NPs, $D_T^{\text{eff}} = 3 \pm 1 \mu\text{m}^2/\text{s}$.

The previous findings show that the diffusion of the dumbbell-like morphology is similar to the one of matchstick-like particles which account for the flexibility of the p3 proteins. Compared with the observations on matchstick-like structures, our results using the single spring-bead model show a higher diffusion. However, since our experimental data is measured from a mixture composed by matchstick-like and dumbbell-like particles the error in our measurements is significant. Thus, we attribute the apparent increase to the experimental uncertainties in the measurements and in then in our fit. For now, we can only confirm that the dumbbell-like particles exhibit a certain degree of flexibility given by the tip-binding proteins. For an accurate estimation of the flexibility of each tip, we have to optimize the monodisperse production of this structure.

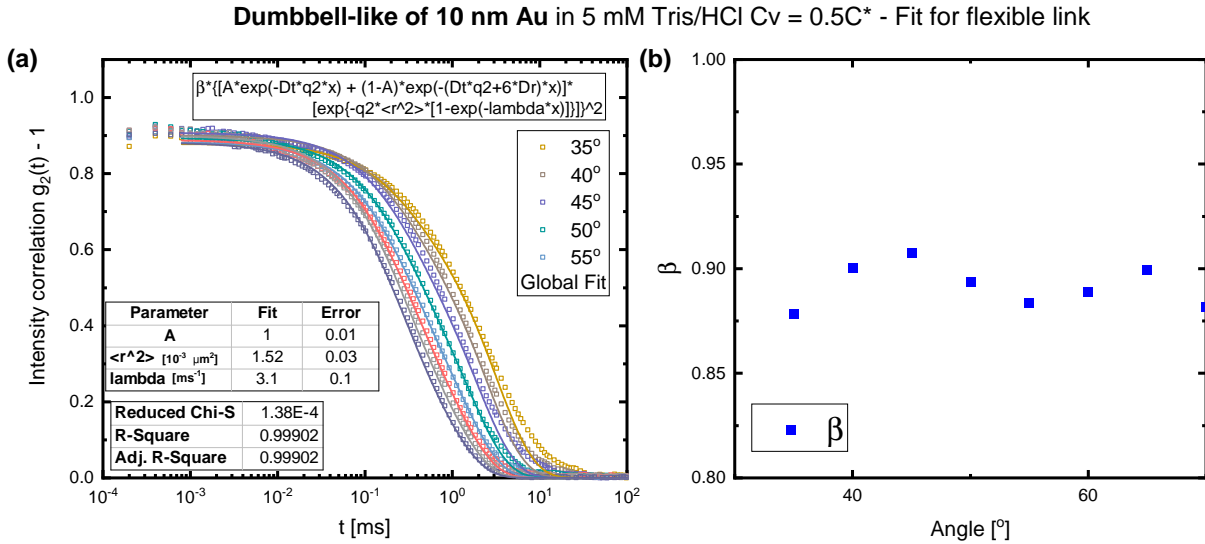


Figure 4.21: **Global fit for the spring-bead model.** (a) The intensity correlation functions for dumbbell-like particles made of $D = 10$ nm Au at $C_v = 0.5C^*$ are simultaneously analyzed considering a flexible link. The global fit for fixed $D_T = 2.5 \mu\text{m}^2/\text{s}$ and $D_R = 21.5 \text{ s}^{-1}$ does not recover the decay of lower angles. We find as global parameters $A = 1$, $\langle r^2 \rangle = 1.52 \times 10^{-3} \mu\text{m}^2$ and $\lambda = 3.1 \text{ ms}^{-1}$. (b) The free parameter β is plotted as function of the scattering angle θ .

4.5 Discussion and conclusions

In this chapter we have studied by DLS the self-diffusion of two of our hybrid gold-virus colloids. The matchstick-like particle, composed by a single virus with one Au NP bound to one tip, and the dumbbell-like particle, composed by a single virus and two beads, one

bound to each tip (see figure 4.1).

Our findings have shown that due to the difference in scattering properties of the elements that constitute the structures, we are able to study by DLS the diffusion of our gold-virus colloids only probing the Au NPs.

We have compared with the results obtained in our group by SPT for which the virus is the element being probed for the dynamics study [55]. A significant increase in the effective translational diffusion coefficient of the structure is observed when the probed component is the Au NPs. Thus, we have implemented a spring-bead model for the interpretation of the scattering signal. Our findings demonstrate that the Au NPs have an extra degree of freedom related to the flexible link at the virus tip. Thus, they are allowed to move around an equilibrium position resulting in higher effective diffusion measured by DLS. This is a direct proof of the flexibility of binding between bead and virus tip.

From a practical point of view, the DLS has shown to be advantageous to recover the diffusion of our structures when compared to SPT which requires more time of analysis and data storage. For example, to analyze ~ 65 particles by SPT a total of 10 movies are stored in few Go and analyzed in a couple of hours while the DLS measurements of a size lower than 1 Mo are analyzed in less than of 30 minutes as soon as the model for data analysis is properly established which requires the right interpretation of the system being studied.

We have explored the influence of the nanoparticle size at concentrations for which the structures do not interact with each other. Our results show that the effective diffusion and spring-bead model parameters of the matchstick-like structures are independent of the nanoparticle size and concentration, as expected from the fact that for $C < C^*$, the structures do not interact with each other.

Our observations in the dumbbell-like structures are not precise enough for concluding that the diffusion coefficient of this morphology is the same as the one of matchstick-like structure. We expect that after the optimization of its production, we might be able to determine the exact value and to evidence or not the flexibility of the second tip binding.

For a further understanding of the flexible link between the elements that compose our structures, we suggest getting and complete our results with a combination of optical microscopy techniques. For instance, we would compare the diffusion of the structure obtained by SPT probing the Au NP via dark-field microscopy and at the same time probing the virus through fluorescence microscopy.

Appendix I. DLS analysis of other matchstick-like particles

In this appendix we summarize the CONTIN and spring-bead model data analysis for matchstick-like particles made of different nanoparticle sizes. Our measurements have been performed for suspension in $I = 5$ mM Tris/HCl buffer at different particle concentrations. The intensity correlation functions are taken in the range of angles $30^\circ < \theta < 150^\circ$ and running time of 120 s.

Matchstick-like made of Au NPs of $D = 10$ nm

In this subsection we present the different concentrations studied for a suspension containing $\sim 80\%$ matchstick-like particles made of Au NPs of $D = 10$ nm as shown in figure 4.22.

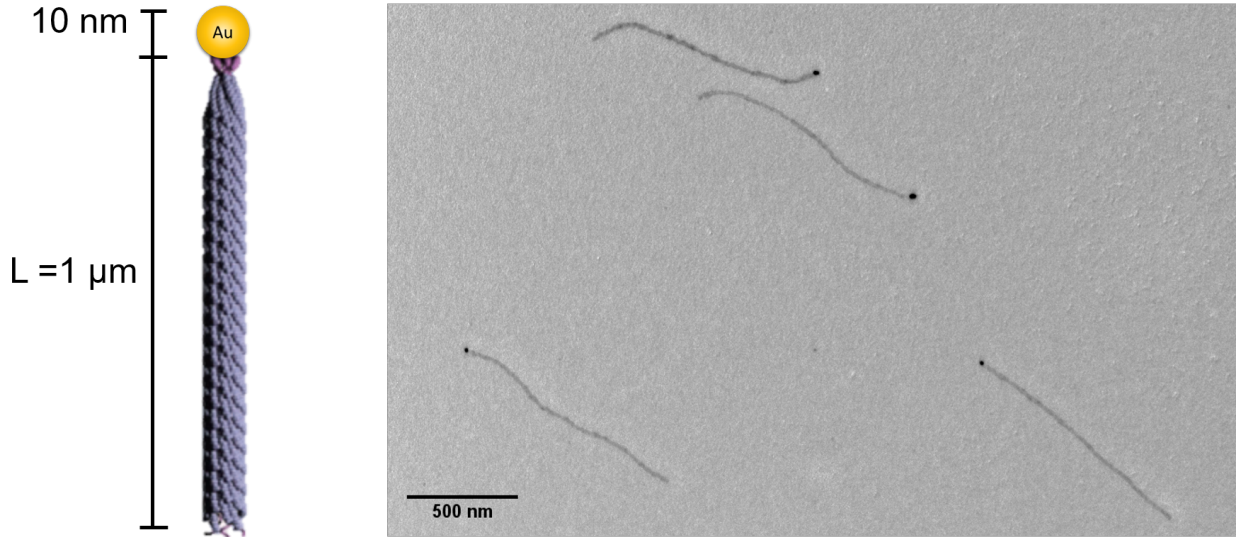


Figure 4.22: **Characterization of matchstick-like particles made of Au NPs of $D = 10$ nm.** **Left:** Schematic representation of matchstick-like particles. **Right:** TEM image of the particle suspension.

- $C_v = 0.1C^*$

As shown in figure 4.23, at this concentration the signal coming from the bead is of the same order of magnitude as the electronic noise coming from the sensor. For this reason, the intensity correlation functions exhibit different coherence factors, β . As observed in the ILT plot, the distribution of decay times is composed by a main peak associated to τ_1 and a second peak at shorter times related to τ_2 . In order to extract the most reliable information from the main peak contribution, we limit the fit of the linear q^2 dependency of Γ_1 to the range $30^\circ < \theta < 55^\circ$ for which we find $D_T = 2.9 \pm 0.5 \mu\text{m}^2/\text{s}$.

Thus, the matchstick-like particles made of Au NPs of $D = 10$ nm at a concentration $C_v = 0.1C^*$ diffuse at $D_T^{\text{eff}} = 2.9 \pm 0.5 \mu\text{m}^2/\text{s}$.

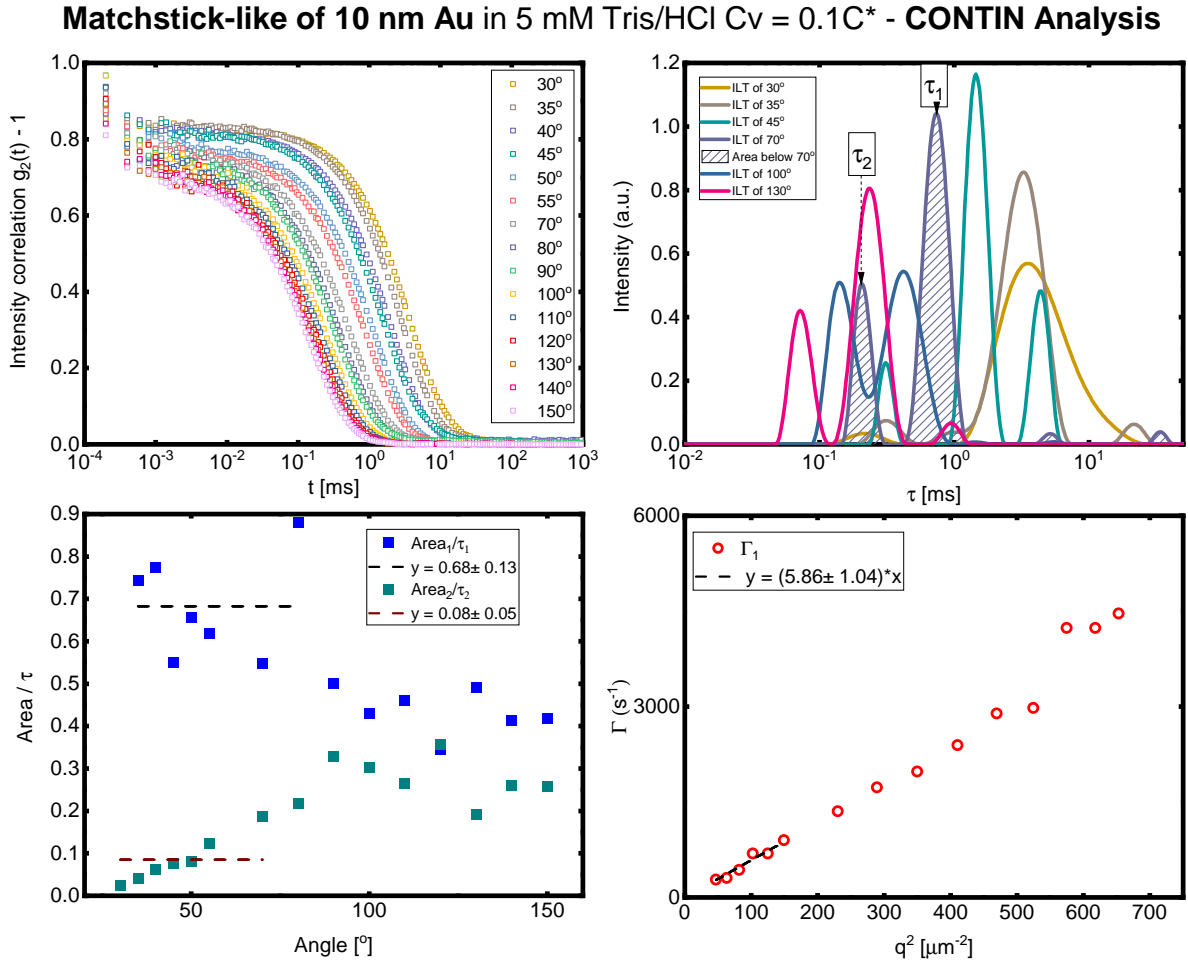


Figure 4.23: **CONTIN analysis of matchstick-like particles made of Au NPs of $D = 10$ nm in $I = 5$ mM Tris/HCl at $C_v = 0.1C^*$.** The ILT computed in the range of angles $30^\circ \leq \theta \leq 150^\circ$ shows multiple peaks. The normalized parameter $Area/\tau$ indicates that the noise in the experimental data is high and that the second contribution is significant for $\theta > 65^\circ$. From the q^2 dependence of Γ is obtained $D_T = 2.9 \pm 0.5 \mu\text{m}^2/\text{s}$.

We have applied the spring-bead model considering as fixed parameters the translational and rotational diffusion of rods $D_T = 2.5 \mu\text{m}^2/\text{s}$ and $D_R = 21.5 \text{s}^{-1}$. As shown in figure 4.24, the global fit for the range of angles $30^\circ < \theta < 55^\circ$ does not recover the decay of the lowest angles. This is accounted to the low intensity of the scattering signal at this concentration which results in a higher error in our measurements. As global parameters, we obtain $A = 1$, $\langle r^2 \rangle = 0.82 \pm 0.03 \times 10^{-3} \mu\text{m}^2$ and $\lambda = 2.9 \pm 0.2 \text{ms}^{-1}$.

Thus, we obtain the parameters $rmsd = 33$ nm, spring constant of $k = 893 k_B T / \mu\text{m}^2$ and a friction coefficient $\gamma = 0.37 k_B T \text{s} / \mu\text{m}^2$.

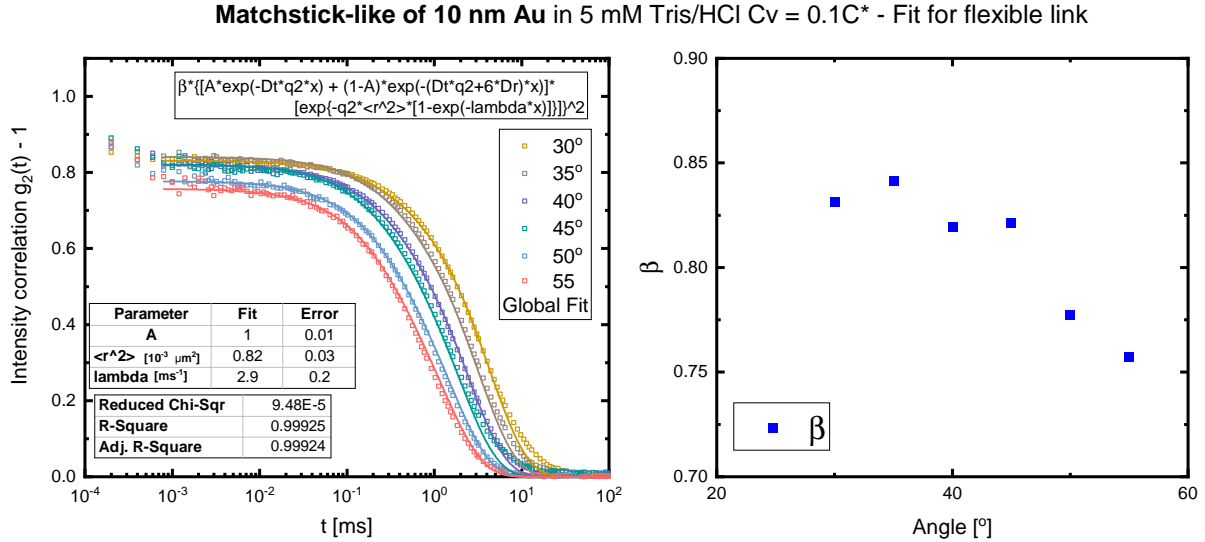


Figure 4.24: **Global fit for the spring-bead model.** (a) Intensity correlation function for matchstick-like particles made of $D = 10$ nm Au NPs at $C_v = 0.1C^*$. The global fit does not recover the decay of the lowest angles. We obtain as global parameters $A = 1$, $\langle r^2 \rangle = 0.82 \times 10^{-3} \mu\text{m}^2$ and $\lambda = 2.9 \text{ ms}^{-1}$. (b) The free parameter β is plotted as function of the scattering angle θ .

- $C_v = C^*$

As the number of particles is higher by a factor 10 compared with the previous set of data, the intensity correlation function exhibits lower noise. Hence, the coherence factor β remains the same for all the range of angles.

The CONTIN analysis, summarized in figure 4.23, shows a distribution of decay times formed by a main peak. We found that the q^2 dependence of Γ_1 has two different regimes. Hence, we limit the fit to the regime $30^\circ \leq \theta \leq 70^\circ$ for which we recover a $D_T^{\text{eff}} = 3.2 \pm 0.8 \mu\text{m}^2/\text{s}$.

For the spring-model analysis of the intensity correlation function we have simultaneously analyzed our data in the range of angles $30^\circ < \theta < 70^\circ$. As shown in figure 4.26, we obtain a good quality fit and as global parameters $A = 1$, $\langle r^2 \rangle = 1.12 \times 10^{-3} \mu\text{m}^2$ and $\lambda = 2.4 \text{ ms}^{-1}$.

The root mean square displacement $rmsd = 29$ nm is consistent with the value found for lower concentration. From equations 4.6 and 4.7, it follows that $k = 1220 k_B T / \mu\text{m}^2$ and $\gamma = 0.42 k_B T \text{ s} / \mu\text{m}^2$. The observed difference of k compared with the obtained value at lower concentration is attributed to the low quality fit of that case due to the low scattering signal.

From the previous results, we conclude that the effective diffusion and spring-bead model parameters are independent of the concentration. For the effective diffusion, we take the mean value and consider as error bars the dispersion of our data. Thus, the mean effective diffusion coefficient of matchstick-like particles made of Au NPs of $D = 10$ nm is $D_T^{\text{eff}} = 3.0 \pm 1.0 \mu\text{m}^2/\text{s}$.

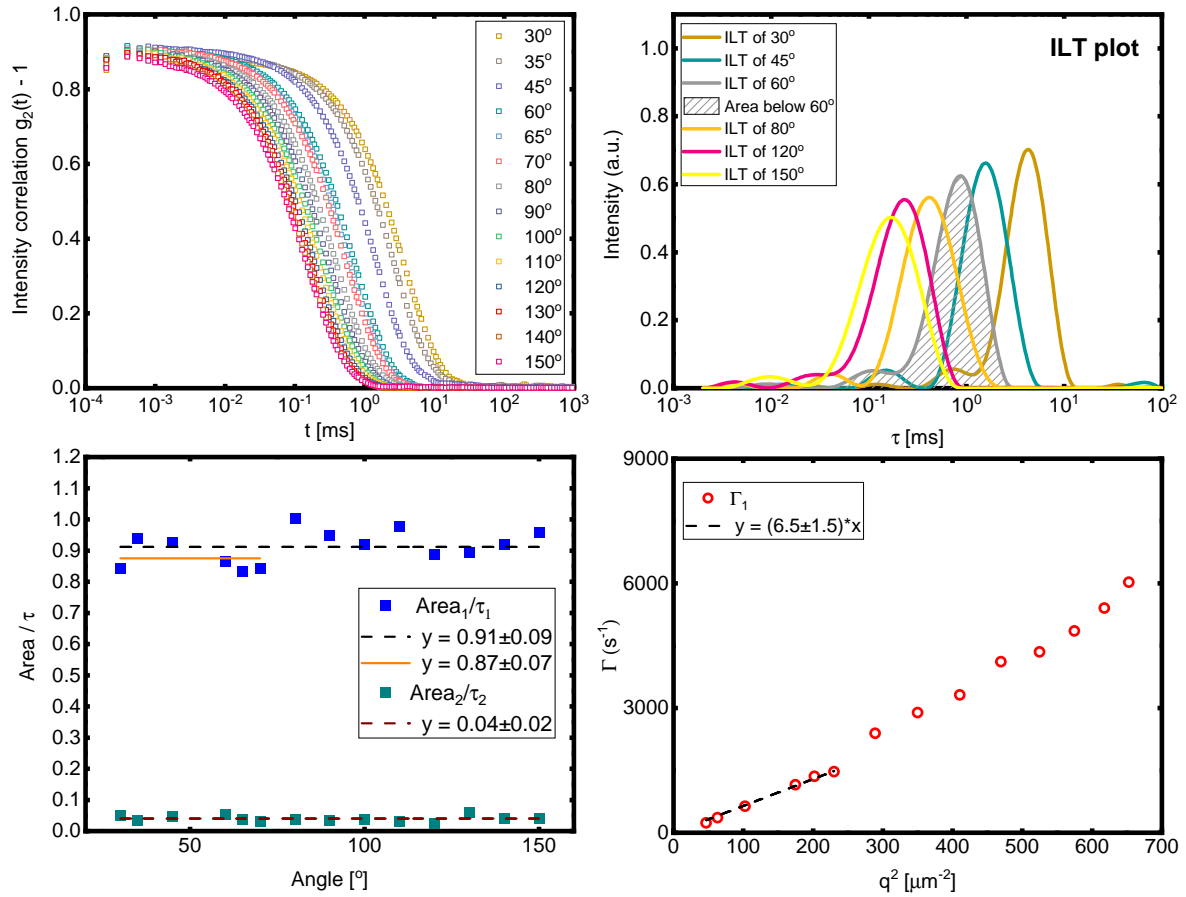
Matchstick-like of 10 nm Au in 5 mM Tris/HCl $C_v = C^*$ - CONTIN Analysis

Figure 4.25: CONTIN analysis of matchstick-like particles made of Au NPs of $D = 10$ nm in $I = 5$ mM Tris/HCl buffer at $C_v = C^*$. The ILT computed in the range of angles $30^\circ \leq \theta \leq 150^\circ$ shows multiple peaks. The normalized parameter $Area/\tau$ indicates that the contribution of the second peak is negligible. From the q^2 dependence of Γ is obtained $D_T = 3.2 \pm 0.8 \mu\text{m}^2/\text{s}$.

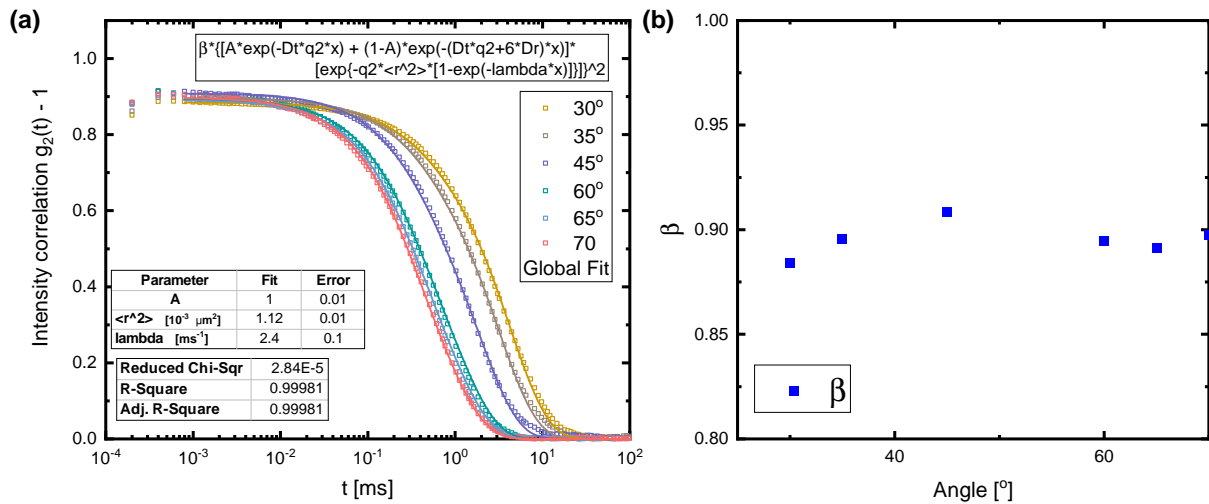
Matchstick-like of 10 nm Au in 5 mM Tris/HCl $C_v = C^*$ - Fit for flexible link

Figure 4.26: Global fit for the spring-bead model. (a) Intensity correlation function for matchstick-like particles at $C_v = C^*$. We obtain a good quality fit and as global parameters $A = 1$, $\langle r^2 \rangle = 1.12 \times 10^{-3} \mu\text{m}^2$ and $\lambda = 2.4 \text{ ms}^{-1}$. (b) The free parameter β is plotted as function of the scattering angle θ .

Matchstick-like made of Au NPs of $D = 18 \text{ nm}$

• $C_v = 0.01C^*$

At this concentration, the intensity signal that arrives to the detector is low compared with the electronic noise and therefore the intensity correlation function exhibits high noise.

The ILT plot of figure 4.27 shows two peaks in the distribution of decay times. According to the calculated normalized parameter $Area/\tau$, both contribution have a high noise and are significant for all the range. We limit the fit of Γ_i to the range where a linear q^2 dependency is found. For the first contribution we find $D_{T1}^{eff} = 4.1 \pm 0.4 \mu\text{m}^2/\text{s}$ while for the second contribution $D_{T2}^{eff} = 10.4 \pm 0.8 \mu\text{m}^2/\text{s}$. The first diffusion is consistent with the expected value for matchstick-like particles. The second one corresponds to the diffusion of spheres of diameter $d_H = 41.1 \text{ nm}$ according to equation 3.29. However, this does not correspond to any expected structure in the sample. We believe that this contribution is an artifact

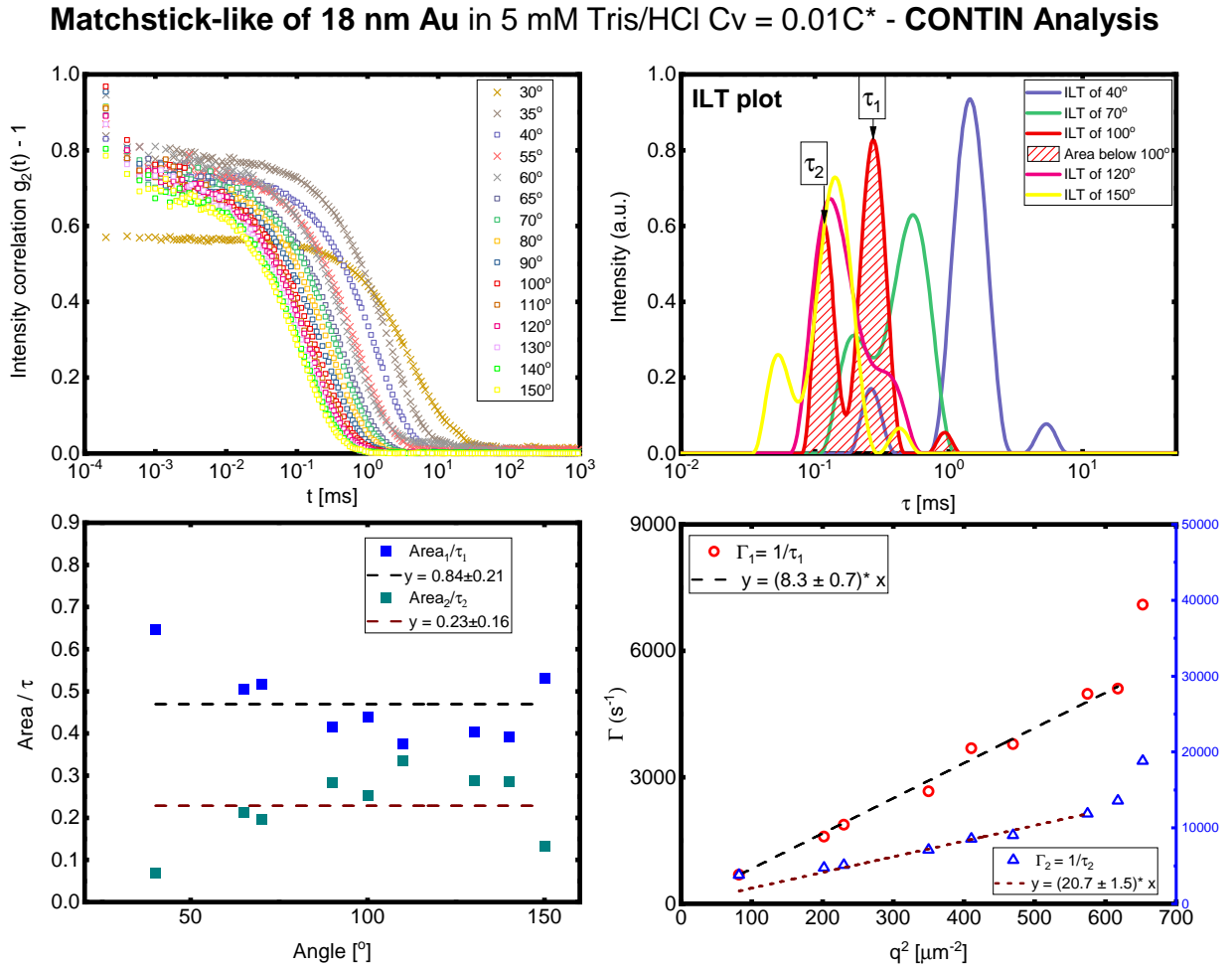


Figure 4.27: CONTIN analysis of matchstick-like particles made of Au NPs of $D = 18 \text{ nm}$ in $I = 5 \text{ mM Tris/HCl}$ buffer at $C_v = 0.01C^*$. The ILT computed in the range of angles $30^\circ \leq \theta \leq 150^\circ$ shows multiple peaks. The normalized parameter $Area/\tau$ indicates that the noise in the experimental data is high and that the second contribution is significant. From the q^2 dependence of Γ_i is obtained $D_{T1} = 4.1 \pm 0.4 \mu\text{m}^2/\text{s}$ and $D_{T2} = 10.4 \pm 0.8 \mu\text{m}^2/\text{s}$.

coming from the high noise of the experimental data.

The spring-model analysis for this case is shown in figure 4.28. We have analyzed data in the range of angles $40^\circ < \theta < 90^\circ$. The quality of the fit is good despite the low scattering signal. The global parameters correspond to $A = 0.55$, $\langle r^2 \rangle = 2.1 \times 10^{-3} \mu\text{m}^2$ and $\lambda = 1.9 \text{ ms}^{-1}$.

From these results, we obtain $rmsd = 46 \text{ nm}$, $k = 476 k_B T / \mu\text{m}^2$ and $\gamma = 0.25 k_B T \text{ s} / \mu\text{m}^2$. Our observations are consistent with the previously observed for higher concentration.

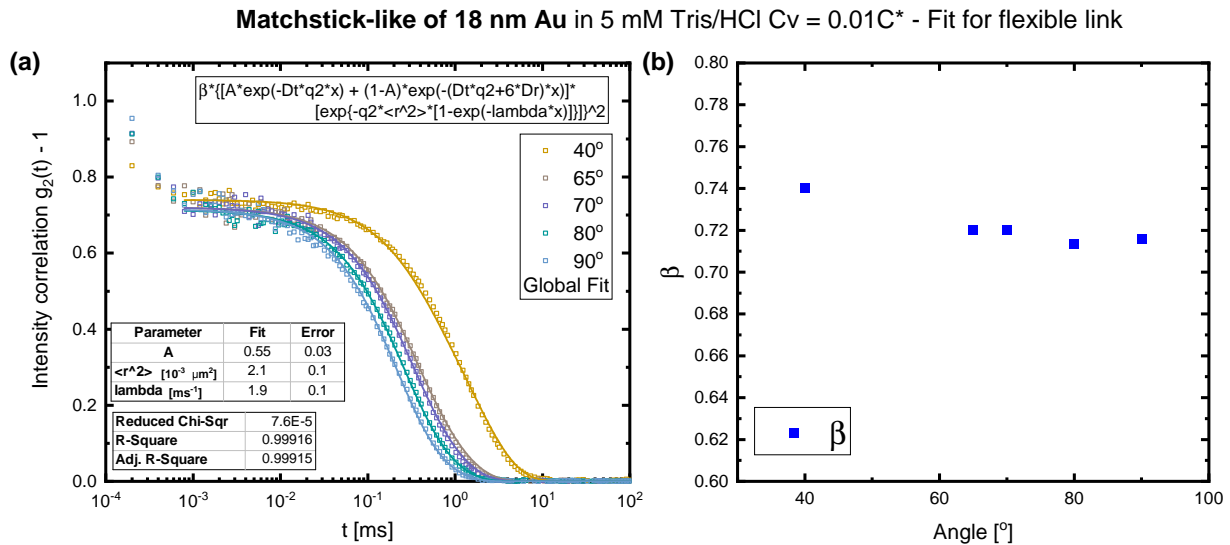


Figure 4.28: **Global fit for the spring-bead model.** (a) Intensity correlation function for matchstick-like particles at $C_v = 0.01C^*$. We obtain a good quality fit and as global parameters $A = 0.55$, $\langle r^2 \rangle = 2.08 \times 10^{-3} \mu\text{m}^2$ and $\lambda = 1.9 \text{ ms}^{-1}$. (b) The free parameter β is plotted as function of the scattering angle θ .

• $C_v = 0.16C^*$

As shown in figure 4.29, for this concentration, the decay times distribution exhibits a main peak (see ILT plot). Here, we limit the fit of the q^2 dependence of Γ_1 to the range of angles $35^\circ \leq \theta \leq 65^\circ$ where it is found a $D_T^{\text{eff}} = 4.6 \pm 0.8 \mu\text{m}^2/\text{s}$.

Summarizing the results obtained for all the concentrations tested we find that the effective diffusion of this structure is independent of the concentration. Thus, for matchstick-like particles made of Au NPs of $D = 18 \text{ nm}$ we obtain a mean $D_T^{\text{eff}} = 4.4 \pm 1.0 \mu\text{m}^2/\text{s}$.

In figure 4.30, we report our findings using the spring bead model. For this analysis, we have worked in the range of angles $35^\circ < \theta < 55^\circ$. We find a good quality fit for most of the angles and as global parameters $A = 0.83$, $\langle r^2 \rangle = 3.5 \times 10^{-3} \mu\text{m}^2$ and $\lambda = 0.97 \text{ ms}^{-1}$. We find a $rmsd = 59 \text{ nm}$ which is consistent with the observations at higher concentration. Moreover, $k = 286 k_B T / \mu\text{m}^2$ and $\gamma = 0.28 k_B T \text{ s} / \mu\text{m}^2$ confirms that the parameters are independent of the concentration.

Matchstick-like of 18 nm Au in 5 mM Tris/HCl $C_v = 0.16C^*$ - CONTIN Analysis

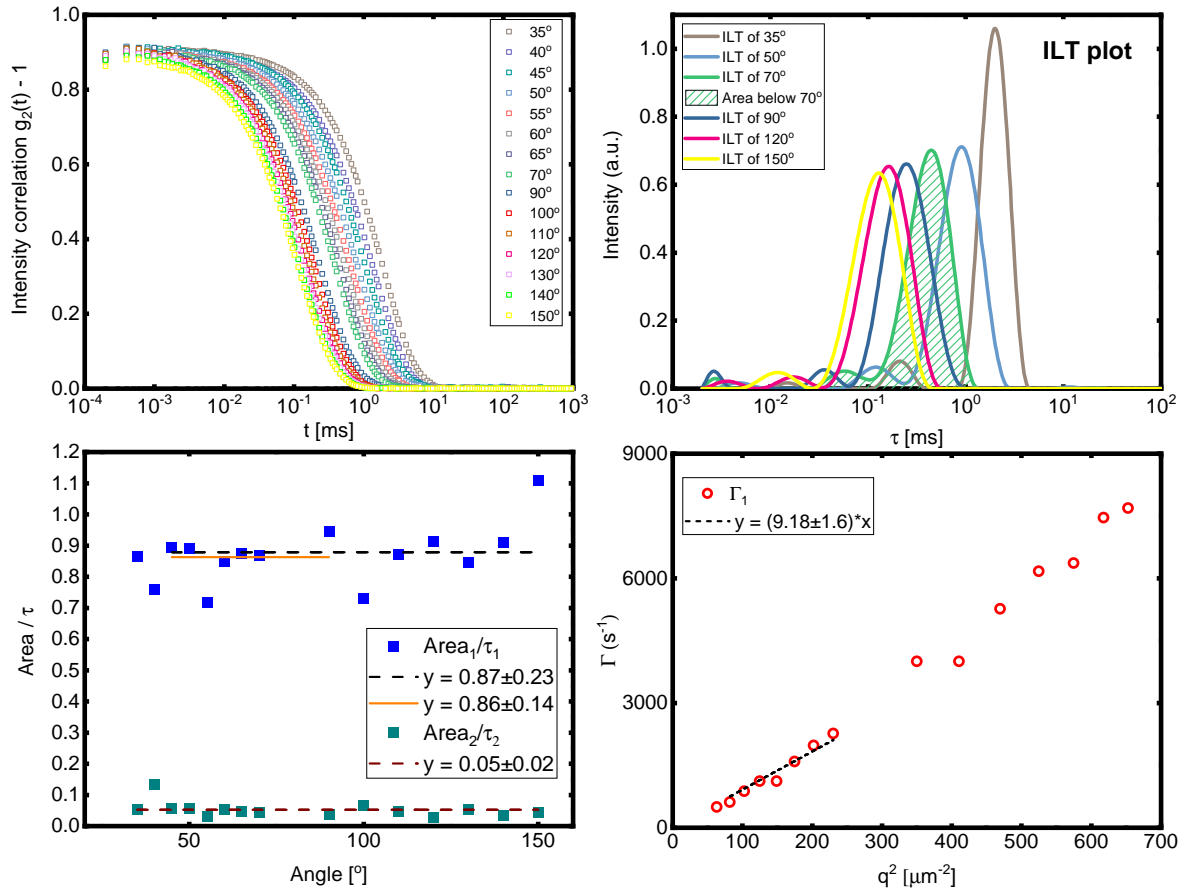


Figure 4.29: CONTIN analysis of matchstick-like particles made of Au NPs of $D = 18$ nm in $I = 5$ mM Tris/HCl buffer at $C_v = 0.16C^*$. The ILT computed in the range of angles $30^\circ \leq \theta \leq 150^\circ$ shows a main peak. From the q^2 dependence of Γ is obtained $D_T = 4.6 \pm 0.8 \mu m^2/s$.

Matchstick-like of 18 nm Au in 5 mM Tris/HCl $C_v = 0.16C^*$ - Fit for flexible link

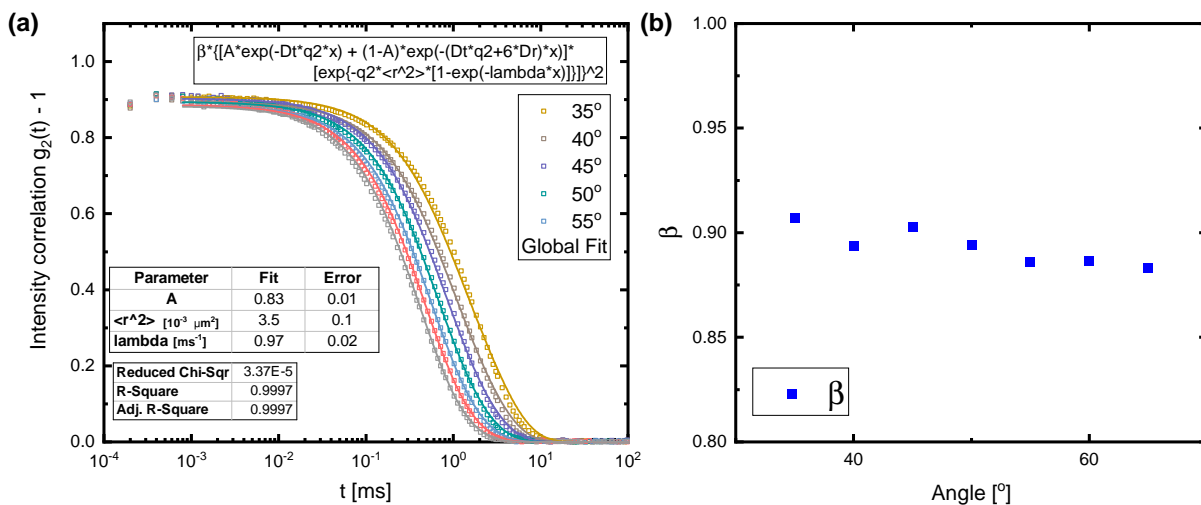


Figure 4.30: Global fit for the spring-bead model. (a) Intensity correlation function for matchstick-like particles at $C_v = 0.16C^*$. We obtain a good quality fit and as global parameters $A = 0.83$, $\langle r^2 \rangle = 3.5 \times 10^{-3} \mu m^2$ and $\lambda = 0.97 ms^{-1}$. (b) The free parameter β is plotted as function of the scattering angle θ .

Matchstick-like made of Au NPs of $D = 31$ nm

Here, we present the different concentrations studied for a suspension containing $\sim 80\%$ matchstick-like particles made of Au NPs of $D = 31$ nm as shown in figure 4.31.

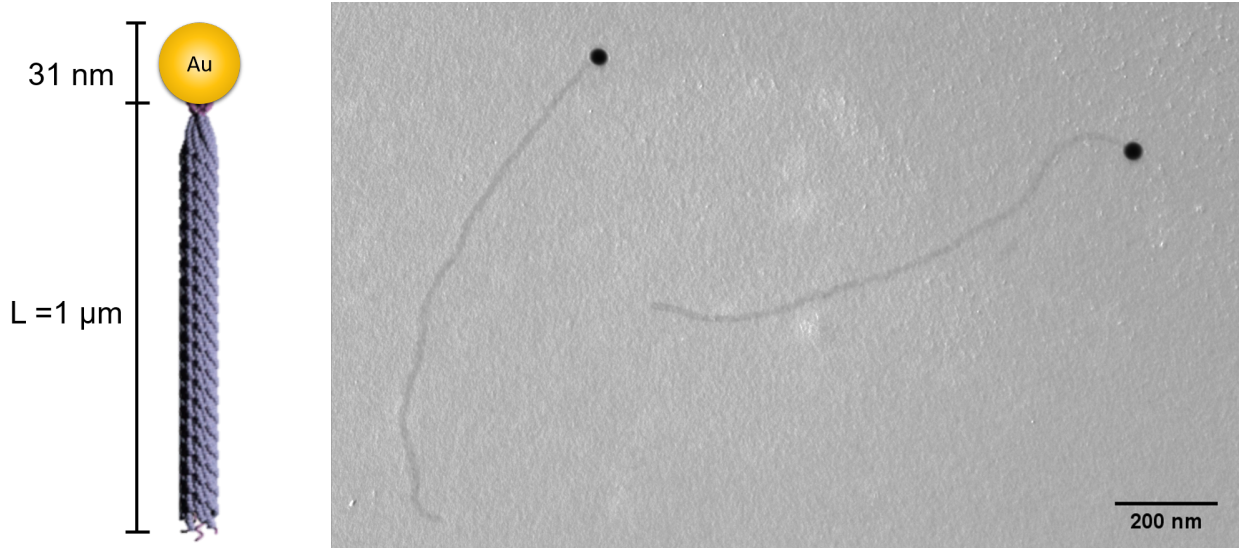


Figure 4.31: **Characterization of matchstick-like particles made of 31 nm Au.** **Left:** Schematic representation of matchstick-like particles. **Right:** TEM image of the particle suspension.

- $C_v = 0.01C^*$

The ILT plot of figure 4.32, shows a distribution of decay times composed by multiple peaks. The normalized parameter $Area/\tau$ shows that there is only a main contribution with low noise in the range of $55^\circ \leq \theta \leq 130^\circ$. The q^2 dependence of Γ_1 results in $D_T^{\text{eff}} = 3.8 \pm 0.6 \mu\text{m}^2/\text{s}$.

We have applied the spring-bead model for data in the range of angles $40^\circ < \theta < 70^\circ$. As shown in figure 4.33, the global fit with fixed parameters $D_T = 2.5 \mu\text{m}^2/\text{s}$ and $D_R = 21.5 \text{ s}^{-1}$ is of lower quality compared with our observations on matchstick-like particles made of $D = 10$ and 18 nm Au NPs.

From the global parameters $A = 0.48$, $\langle r^2 \rangle = 0.8 \times 10^{-3} \mu\text{m}^2$ and $\lambda = 8.2 \text{ ms}^{-1}$, it follows that $rmsd = 28$ nm, $k = 1250 k_B T / \mu\text{m}^2$ and $\gamma = 0.15 k_B T \text{ s} / \mu\text{m}^2$. These values are consistent with the ones found for matchstick-like structures made of 10 nm Au NPs.

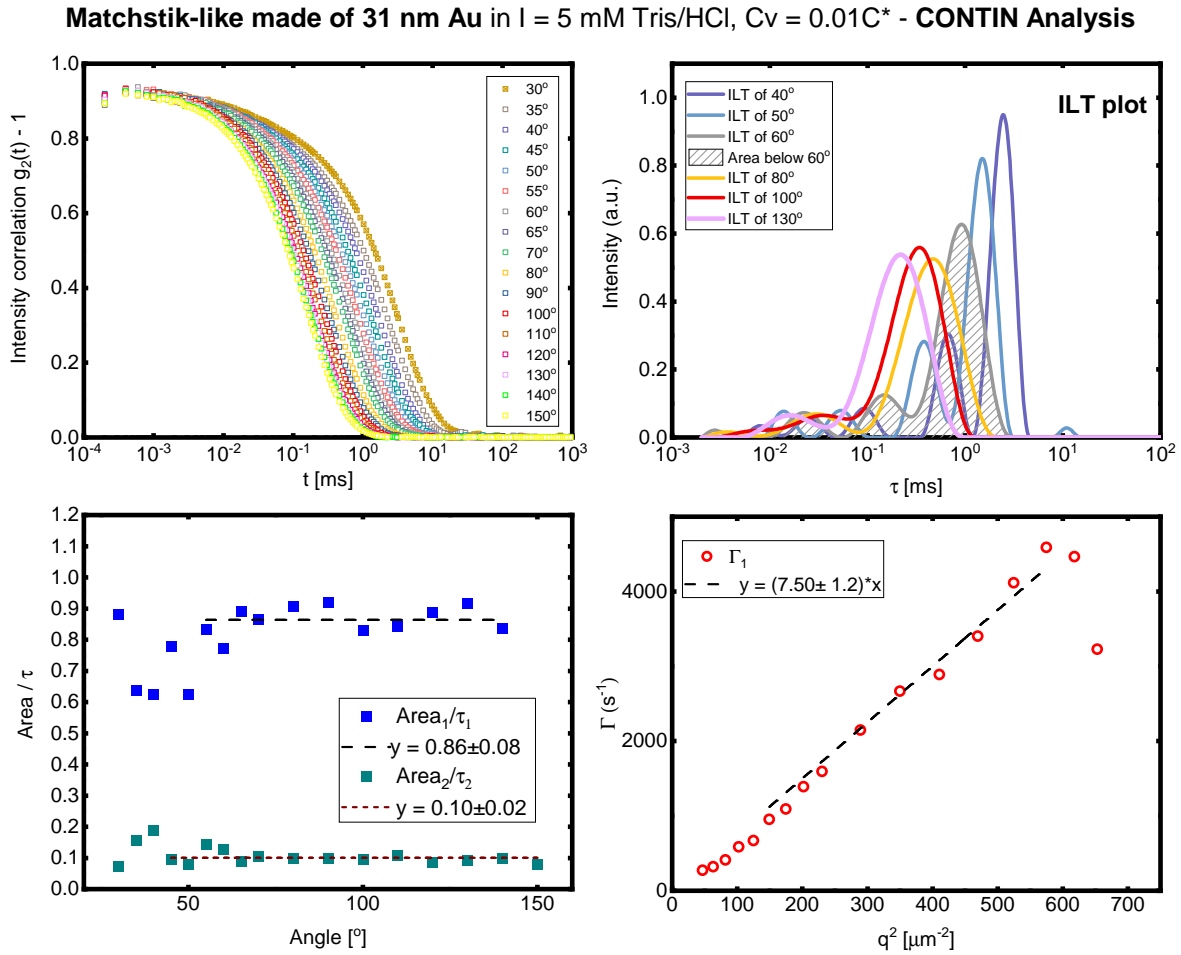


Figure 4.32: CONTIN analysis of matchstick-like particles made of $D = 31$ nm Au in $I = 5$ mM Tris/HCl buffer at $C_v = 0.01C^*$. The ILT computed in the range of angles $55^\circ \leq \theta \leq 130^\circ$ shows multiple peaks. The normalized parameter $Area/\tau$ indicates that the second contribution is not significant. From the q^2 dependence of Γ is obtained $D_T = 3.8 \pm 0.6 \mu\text{m}^2/\text{s}$.

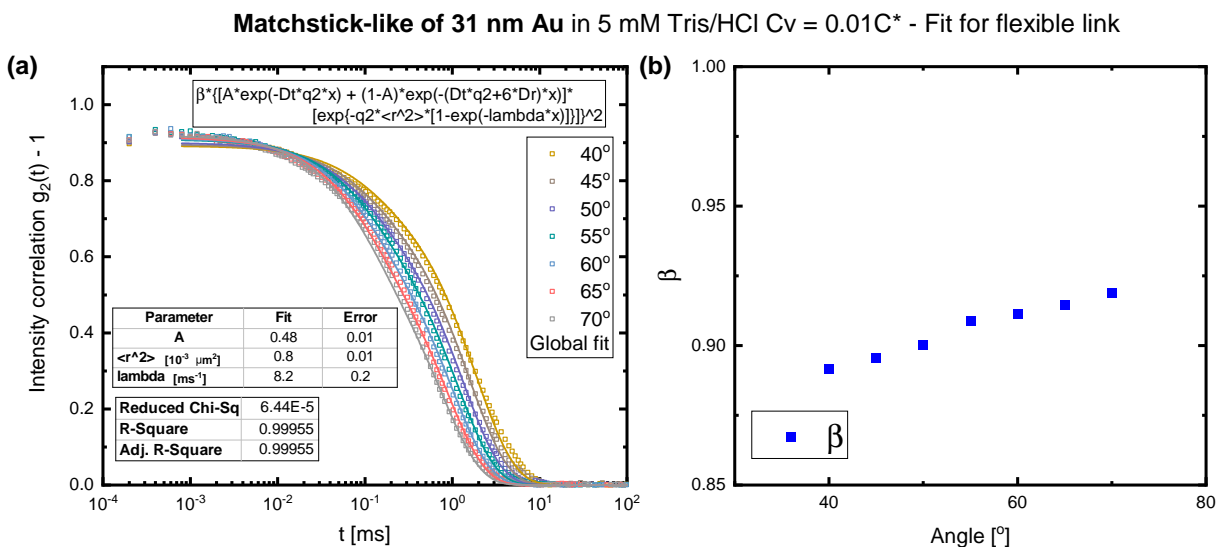


Figure 4.33: Global fit for the spring-bead model. (a) Intensity correlation function for matchstick-like particles at $C_v = 0.01C^*$. We obtain as global parameters $A = 0.48$, $\langle r^2 \rangle = 0.8 \times 10^{-3} \mu\text{m}^2$ and $\lambda = 8.2 \text{ ms}^{-1}$. (b) The free parameter β is plotted as function of the scattering angle θ .

- $C_v = 0.02C^*$

As shown in the ILT plot of figure 4.34, the distribution of the decay times exhibits only a main peak and a second peak of low contribution at shorter decay times. As the parameter $Area_2/\tau_2 < 0.1$, we discard the second peak. The q^2 dependence of Γ_1 shows an apparent change of slope for $\theta > 70^\circ$. This is consistent with the previous observations on other matchstick-like structures but contrast with the one for the same structure at lower concentration. The latter is accounted for the increase of statistical noise in that conditions. Here, we limit the range for the linear fit to $30^\circ < \theta < 70^\circ$ which results in a $D_T^{\text{eff}} = 3.2 \pm 0.4 \mu\text{m}^2/\text{s}$.

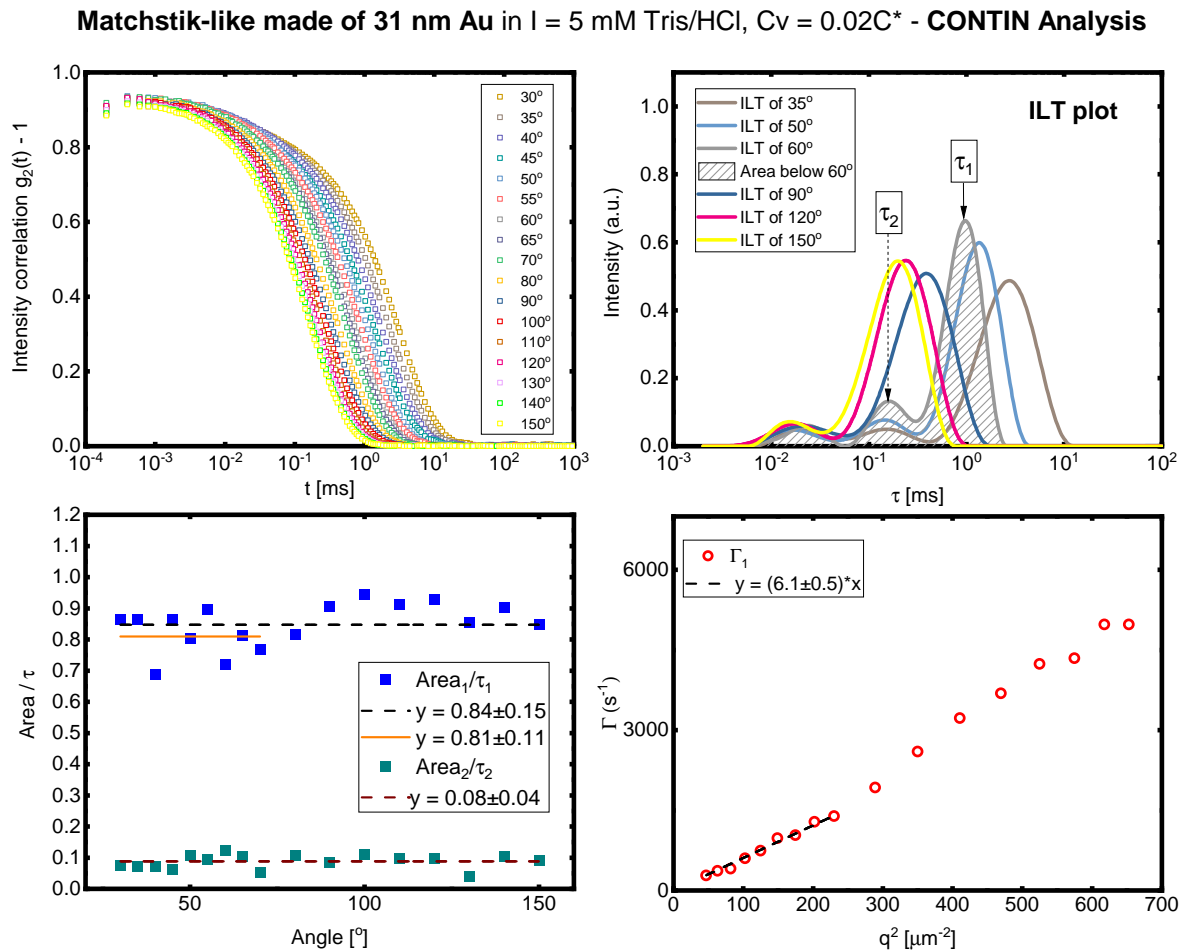


Figure 4.34: CONTIN analysis of matchstick-like particles made of Au NPs of $D = 31 \text{ nm}$ in $I = 5 \text{ mM Tris/HCl}$ buffer at $C_v = 0.02C^*$. The ILT computed in the range of angles $30^\circ \leq \theta \leq 150^\circ$ shows a main peak associated to τ_1 and a second peak of lower contribution related to τ_2 . From the q^2 dependence of Γ is obtained $D_T = 3.0 \pm 0.3 \mu\text{m}^2/\text{s}$.

The spring-bead model in the range of angles $35^\circ < \theta < 70^\circ$ is summarized in figure 4.35. The fit is of similar quality as for the case at lower concentration. The global parameters correspond to $A = 0.6$, $\langle r^2 \rangle = 0.85 \times 10^{-3} \mu\text{m}^2$ and $\lambda = 7.7 \text{ ms}^{-1}$. These results are used to estimate $rmsd = 29 \text{ nm}$, $k = 1176 k_B T / \mu\text{m}^2$ and $\gamma = 0.15 k_B T \text{ s} / \mu\text{m}^2$ which are in the error bar the same as the ones found at lower concentration.

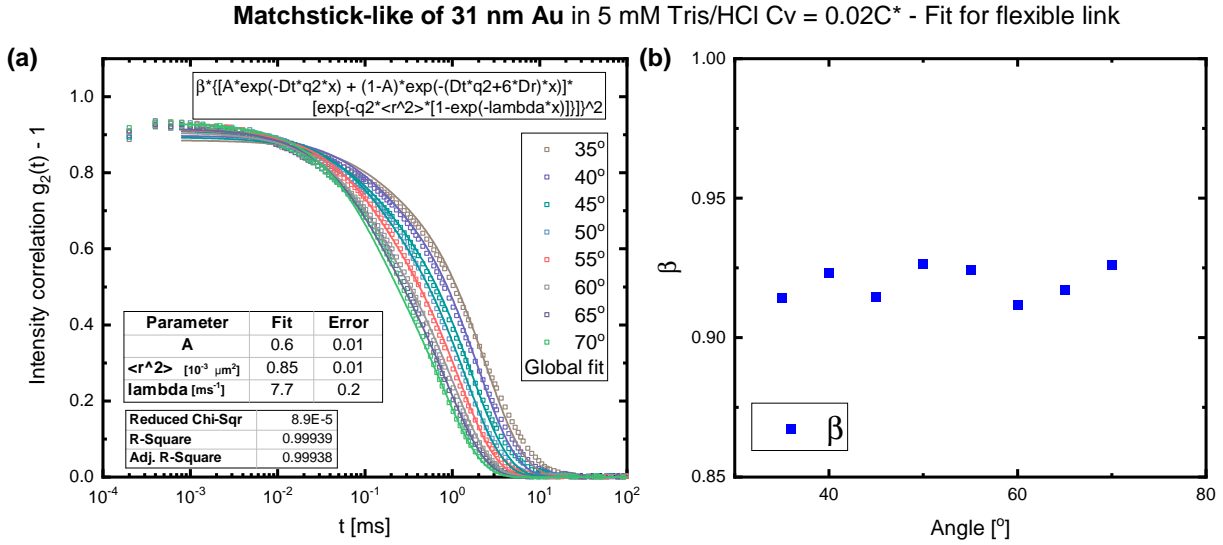


Figure 4.35: **Global fit for the spring-bead model.** (a) Intensity correlation function for matchstick-like particles at $C_v = 0.02C^*$. We obtain as global parameters $A = 0.6$, $\langle r^2 \rangle = 0.85 \times 10^{-3} \mu\text{m}^2$ and $\lambda = 7.7 \text{ ms}^{-1}$. (b) The free parameter β is plotted as function of the scattering angle θ .

- $C_v = 0.07C^*$

The results from CONTIN analysis, summarized in figure 4.36, show that the decay times distribution is formed by two peaks. A main peak at high decay time and a second peak if negligible contribution at shorter times. Under the same considerations of the previous cases, we limit the range for the linear fit dependence of q^2 to $30^\circ < \theta < 70^\circ$. The latter results in an effective $D_T^{\text{eff}} = 3.2 \pm 0.4 \mu\text{m}^2/\text{s}$.

In figure 4.37, we summarize our findings for the spring-bead model for the range of angles $35^\circ < \theta < 65^\circ$. The global fit does not recover the decay of low angles thus the quality of the fit is low compared with the ones for matchstick-like particles made of $D = 10$ and 18 nm Au NPs. For this case, we find as global parameters $A = 0.54$, $\langle r^2 \rangle = 0.85 \times 10^{-3} \mu\text{m}^2$ and $\lambda = 7.8 \text{ ms}^{-1}$ which result in $rmsd = 29 \text{ nm}$, $k = 1176 k_B T / \mu\text{m}^2$ and $\gamma = 0.15 k_B T \text{ s} / \mu\text{m}^2$. These findings are consistent with our observations for lower concentration.

From the previous results, we conclude that the effective diffusion and spring-bead model parameters of matchstick-like particles made of Au NPs of $D = 31 \text{ nm}$ are independent of the particle concentration. For the mean effective diffusion of this structure we consider the error bars of our measurements obtaining $D_T^{\text{eff}} = 3.4 \pm 1.0 \mu\text{m}^2/\text{s}$.

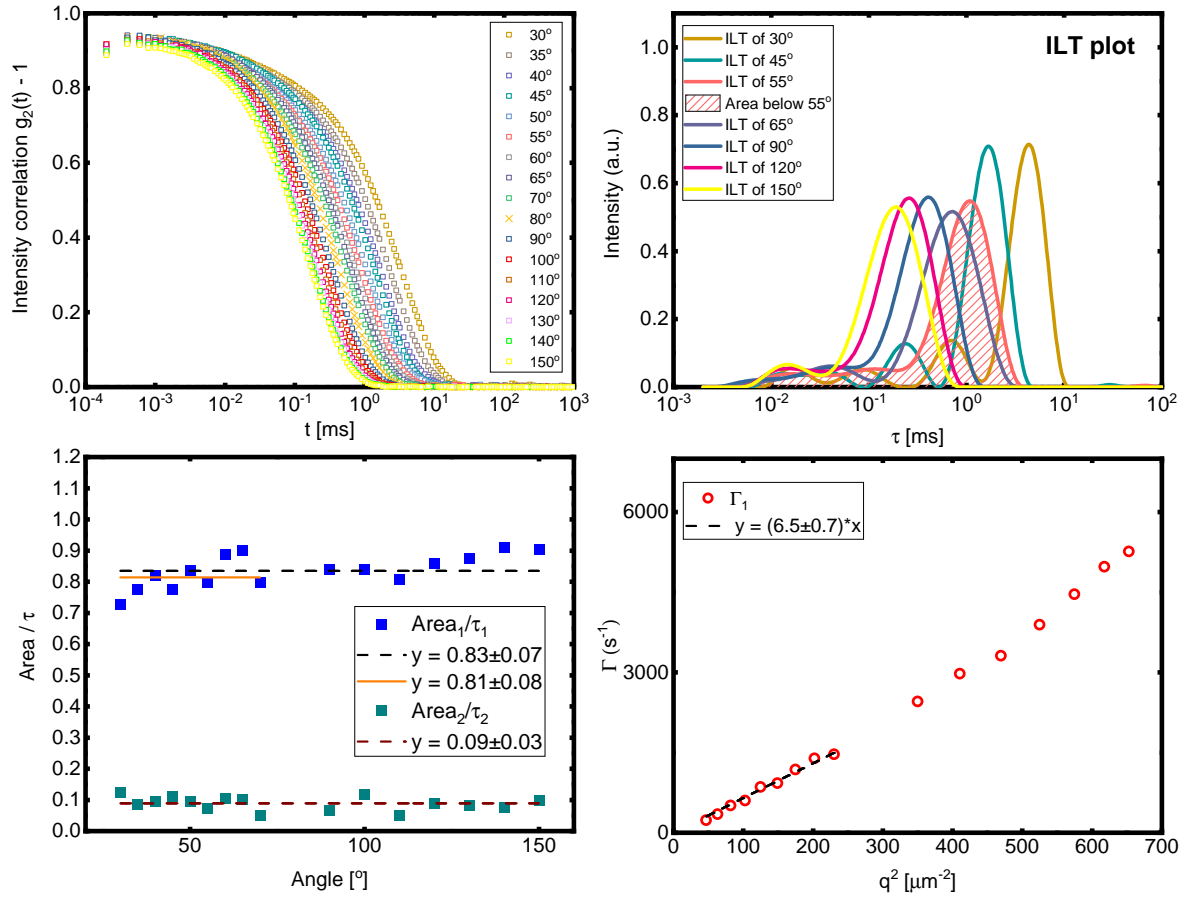
Matchstick-like made of 31 nm Au in I = 5 mM Tris/HCl, C_v = 0.07C* - CONTIN Analysis

Figure 4.36: CONTIN analysis of matchstick-like particles made of Au NPs of $D = 321 \text{ nm}$ in $I = 5 \text{ mM Tris/HCl}$ buffer at $C_v = 0.07C^*$. The ILT computed in the range of angles $30^\circ \leq \theta \leq 150^\circ$ shows a main significant peak. From the q^2 dependence of Γ is obtained $D_T = 3.2 \pm 0.4 \mu\text{m}^2/\text{s}$.

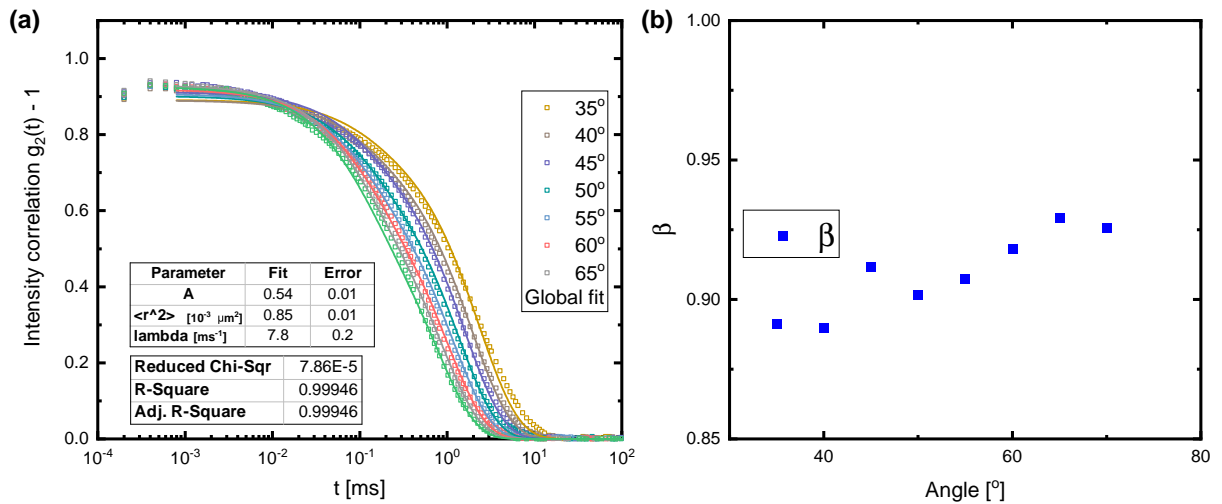
Matchstick-like of 31 nm Au in 5 mM Tris/HCl C_v = 0.07C* - Fit for flexible link

Figure 4.37: Global fit for the spring-bead model. (a) Intensity correlation function for matchstick-like particles at $C_v = 0.07C^*$. We obtain as global parameters $A = 0.54$, $\langle r^2 \rangle = 0.85 \times 10^{-3} \mu\text{m}^2$ and $\lambda = 7.8 \text{ ms}^{-1}$. (b) The free parameter β is plotted as function of the scattering angle θ .

Chapter 5

Towards the self-propulsion of hybrid colloidal particles

5.1	Artificial active particles at colloidal scale	104
5.1.2	Designing artificially self-propelled particles	104
5.2	Brownian motion versus Active Brownian motion	107
5.3	Hot Brownian motion	109
5.3.2	Experimental setup	111
5.4	Diffusion of Janus Au-Silica particles	112
5.5	Heat induced motion of matchstick-like particles	117
5.5.2	Effect of convention in the intensity correlation function	118
5.6	Discussion and conclusions	121

5.1 Artificial active particles at colloidal scale

Particles with experience a purely diffusive random walk, called “passive” Brownian particles differ from the so called “active” Brownian ones. According to the fluctuation-dissipation theorem [146], a passive particle keeps moving because the dissipation of energy caused by friction is compensated by the stochastic force in order to maintain a thermal equilibrium. However, an active Brownian particle take energy from their environment and use it as driving mechanism to execute non-equilibrium tasks such transport and self-propelled motility [147].

Nature provides many examples of active particles at the colloidal scale such as algae, sperm and other cells [148–150]. The most common example is given by bacteria such as *Escherichia coli* (E. coli) which exhibit ballistic motion as result of the transformation of chemical energy into mechanical movement [151]. Moreover, bacteria swarms are able to swim toward to the nutrition sources along their concentration gradients, leading to a joint migration of bacteria at the macroscale [152]. This mechanism called collective motion is observed in other active systems that experience as well motility-induced phase separation and giant fluctuations [153, 154]. The study of these intriguing phenomena is of interest for the fundamental understanding of the out-of equilibrium physics as well as for the development of smart devices and materials. Specifically, self-propelled particles at the colloidal/nano scale have attracted considerable attention for their potential applications in many fields such as drug delivery [155], sensing [101, 156] and biomedicine [157]. For this purpose, many artificial active particles at colloidal/nano scale, also called micro- or nano-motors/swimmers, have been developed with the aim of mimicking the structure and controlled motion of biological systems [158, 159]. But, how is the controlled motion achieved at the scale where the thermal fluctuations are so important? i.e., for nanoswimmers or at the nanoscale? How do we design an artificial motor with a selective direction?

5.1.2 Designing artificially self-propelled particles

In order to infer the requirements for a controlled motion at the colloidal scale, let’s recall the example of the movement of the E. coli bacteria. Bacteria contain several flagella (see figure 5.1). This hairlike appendages rotate in a clockwise or counterclockwise direction by energy consumption to promote the bacterial motility. As shown in figure 5.1, when the motion is counterclockwise multiple flagella unite into a bundle that functions as a propeller at the rear end of the cell body. Contrary, when one or more of the flagella rotate in the clockwise direction, the flagellar bundle disassembles and the cell “tumbles”, i.e., it performs a random walk in the same spot to change direction [160]. When the bundle re-forms, the bacterium “runs” in a new direction. In presence of a chemical gradient, bacterium switches between the tumbling and running mechanisms to direct their overall motion for instance to swim toward a source of nutrients [161, 162].

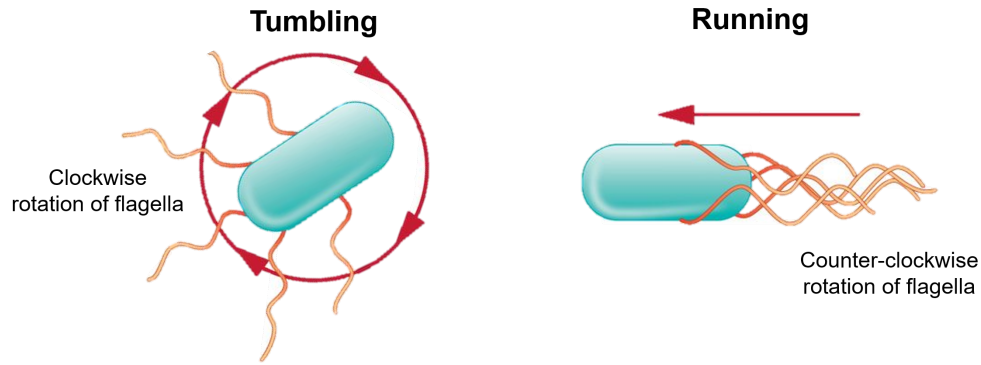


Figure 5.1: **Swimming mechanism of bacteria.** Clock-wise rotation of flagella results in a random re-orientation for of the bacteria while counter-clockwise rotation produces a straight motion.

From the previous example, it can be deduced that three different conditions need to be fulfilled for the self-propulsion of colloidal particles. First, an asymmetric shape is necessary to maintain orientation and to generate motion in a desired direction. Secondly, an energy should be injected and transferred into propulsion for instance by chemical or physical-chemical reactions or by a mechanical deformation of the device. And finally, a swimming strategy is required. This third condition arises from the fact that fluid dynamics at the colloidal/nano scale is dominated by viscous rather than inertial terms. This means that a purely reversible internal displacement is not associated with any net motion and that a propelled device must break the time-reversal invariance according to the “scallop theorem” [163, 164]. Many authors have worked in the modeling of different artificial architectures that can achieve self-propulsion considering the three points mentioned above. For example, nanorods/wire motors [165], tubular engines [166, 167] and Janus motors [98, 168, 169] that combine an intrinsic break of symmetry with a propulsion mechanism.

The next questions to formulate are, what is the role of the asymmetry? What conditions have to be tuned for the self-propulsion? First we need to describe how the propulsion is done. Because of the general features of small moving objects, the continuous motion of artificial active particles is usually associated with an effective power source such as light [170], temperature [169] or chemical fuels [168] (see figure 5.2). The type of fuel is linked to the nature of the motor which would diffuse accordingly to the propulsion mechanism. These mechanisms, illustrated in figure 5.2, include bubble propulsion, thermophoresis, electrophoresis and diffusiophoresis. One of the most studied mechanism is the self-diffusiophoresis associated to Janus particles. Typical Janus particles have two distinct faces. One of this faces consumes fuel in the surrounding solution leading to the motion of the particle. Let’s take as example Platinum-Gold (Pt-Au) Janus particles immersed in a fluid with a given concentration of hydrogen peroxide (H_2O_2) [168]. At the platinum side, the hydrogen peroxide is catalytically decomposed into water and oxygen. This chemical reaction generates protons in solution and electrons at the Pt end. The protons

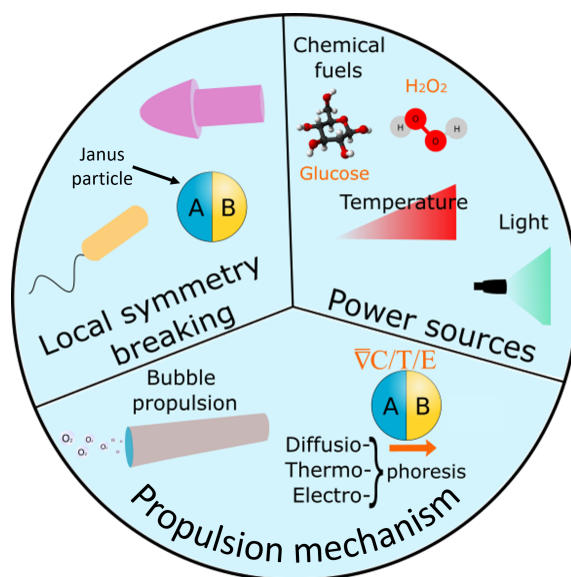


Figure 5.2: **Schematic representation of the controlled motion of artificial active particles.** First, a local symmetry breaking maintains the direction of the movement and secondly a combination of power source with a swimming strategy allows their movement.

and electrons are then consumed with the reduction of H_2O_2 on the Au end. The resulting ion flux induces motion of the particle relative to the fluid, propelling the particle toward the platinum end with respect to the stationary fluid. Similarly, for enzyme powered Janus particles [98], the decomposition of the fuel preferentially on one side of the particle generates a concentration gradient. Subsequently, as the decomposition reaches a critical point where the local concentration of the product is high, the product diffuses away resulting in the movement of the particle. From this comparison, it becomes clear that the asymmetry has an important role for the creation of a gradient and therefore the propulsion. Additionally, the type of fuel, concentration and nature of the particles are all the key factors to tune for the design of artificial active particles.

Here, we investigate the self-propulsion of one of our hybrid gold-virus systems described in chapter 2. These colloidal particles are made of rod-shaped viruses and spherical gold nanoparticles. Inspired by the intrinsic asymmetry of the matchstick-like particles we propose to study their potential self-propulsion by thermophoresis acquired when a green laser is irradiated to the suspension. When a gold nanoparticle (Au NP) is excited at its plasmonic resonance, a local change of temperature is created at its surroundings resulting in an effective increase of diffusion [171]. These phenomena, called “Hot Brownian motion”, could function as propulsion mechanism. As shown in figure 5.3, we expect that a local temperature gradient would be generated by the presence of the phage and by the absorption of laser at the gold nanobead end allowing the propulsion of the structure. In this chapter, we describe our investigations in this direction. First, the principles of the Hot Brownian motion are introduced. Then, the experimental setup used to inject thermal energy and to measure the diffusion of the structure is described. Next, we explore the thermophoresis associated to a system of Janus particles made of gold and silica. Finally, we present our observations in

the thermophoresis of our matchstick-like structures.

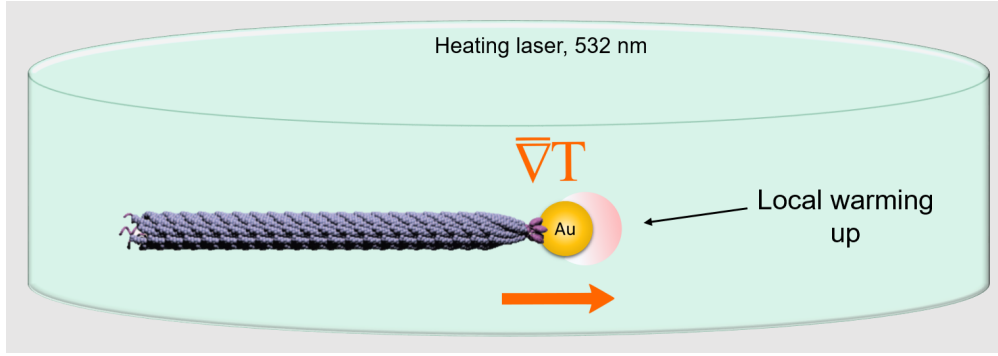


Figure 5.3: **Self-thermophoresis of matchstick-like particles.** Schematic drawing of a matchstick-like particle placed in a green laser path (green cylinder). The absorption of the gold nanoparticle generates a local gradient of temperature allowing the directed motion of the structure.

5.2 Brownian motion versus Active Brownian motion

As described in section 3.2.2, the Albert Einstein theory of Brownian motion establish that the Mean Squared Displacement (MSD) in n dimensions of a Brownian particle has a linear dependence on t (see equation 3.6) and is proportional to the diffusion coefficient D_T specific of the size, shape and surface properties of a colloidal particle [172] (see equations 1.1 and 3.7).

In an active diffusion, for which the motion is directed during a period of time, the particle experiences a displacement with the n -dimensional speed $V(n)$ altering the random walk of a particle. The MSD of these systems corresponds to [114]:

$$\text{MSD} = 2nD_T t + \frac{V^2(n)\tau^2}{2} \left(\frac{2t}{\tau} + e^{-2t/\tau} - 1 \right), \quad (5.1)$$

where $\tau = D_R^{-1}$ is the reciprocal rotational diffusion coefficient. From equation 5.1, it follows that the diffusion of an active Brownian particle has two limiting behaviors for $t \ll \tau$ and $t \gg \tau$ [114]. The first case, reduces equation 5.1 to:

$$\text{MSD} = 2nD_T t + V^2(n)t^2, \quad (5.2)$$

which is the combination of a passive diffusion and ballistic motion while for $t \gg \tau$:

$$\text{MSD} = 2nD_L t - \frac{V^2(n)\tau^2}{2} t, \quad \text{with} \quad D_L = D_T + \frac{V^2(n)\tau}{2n}, \quad (5.3)$$

the “long time diffusivity” which describes the enhanced diffusive motion that occurs due to Brownian rotation continuously and randomly changing the direction of propulsion. In figure 5.4, the two MSD regimes of an active Brownian particle are illustrated.

From the previous description it follows that $\tau = D_R^{-1}$ is a key parameter when the diffusion is measured. The possibility to access to this time determines if a measurement

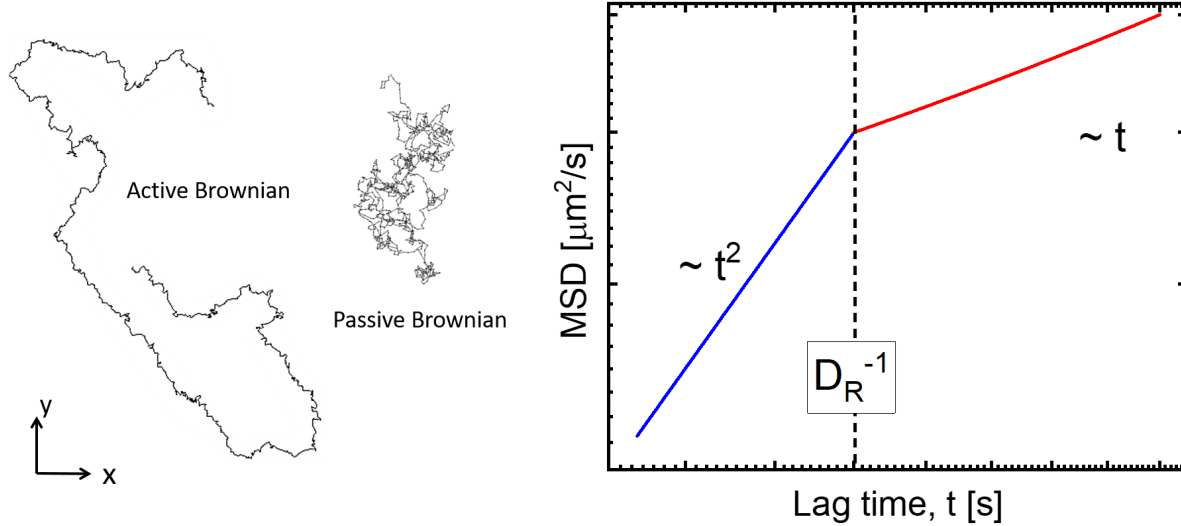


Figure 5.4: **Diffusion of an active Brownian particle.** **Left:** Example of typical active and passive trajectories projected in a 2D plane. **Right:** Typical MSD of an active Brownian particle according to equation 5.1. For lag time $t < D_R$ the active diffusion is ballistic and proportional to t^2 . As the time increases, the particle recovers a diffusive behavior of $\sim t$ with long diffusivity D_L .

corresponds to a system experiencing a ballistic diffusion or a long enhanced diffusivity. For example, when the MSD is calculated by single particle tracking as described in section 3.2 for a lag time shorter than $\tau = D_R^{-1}$, we have access to the ballistic regime and we are able to directly estimate the diffusion coefficient and velocity according to equation 5.2. However, for small nanoparticles whose $D_R \sim 1 \times 10^6 \text{ s}^{-1}$ (diameter of tens of nanometers) reaching times shorter than $\tau \sim 1 \times 10^{-6} \text{ s}$ requires specialized equipment such as a high speed camera to track the particles [173].

To overcome this limitation, Dynamic Light Scattering (DLS) has been used as an alternative method to investigate the active motion of colloidal and nano particles [98, 168]. As described in chapter 3, DLS allows us to directly obtain the translational and rotational diffusions of anisotropic particles representing the average dynamics of the whole system being probed. In DLS (see section 3.3), the first order correlation function $g_1(q, t)$ is related to the MSD by the relation [174]:

$$g_1(q, t) = \exp\left(-\frac{1}{6}q^2\text{MSD}\right). \quad (5.4)$$

From equation 5.4 and 3.13, it follows that for the three-dimensional case of spherical particles with ballistic motion (equation 5.2 for $n = 3$), the measured intensity correlation function reduces to:

$$g_2(q, t) - 1 = \beta \exp(-2q^2 D_T t - \frac{V^2}{3} q^2 t^2), \quad (5.5)$$

where V corresponds to the speed of the directed motion in 3D.

In this work, we have implemented DLS for the study of the active Brownian motion of our hybrid colloidal particles using as propulsion mechanism the gradient of temperature created when Au NPs are excited at their plasmonic resonance.

5.3 Hot Brownian motion

The diffusion of a colloidal particle that have an elevated temperature compared to the one of its solvent is called Hot Brownian motion (HBM) [171]. An example of colloidal particles which exhibits HBM are metal nanoparticles suspended on water that diffuse in the focus of a laser beam. Au NPs absorb light and convert it into heat when they are irradiated at the plasmonic resonance $\lambda \simeq 530$ nm [175]. As shown in figure 5.5, the heat emission creates a radially symmetric hot halo in the surrounding solvent causing a temperature and viscosity profiles around the NPs. The Brownian diffusion of these particles is then affected by the changes in temperature and viscosity resulting in a increase of apparent diffusion or HBM.

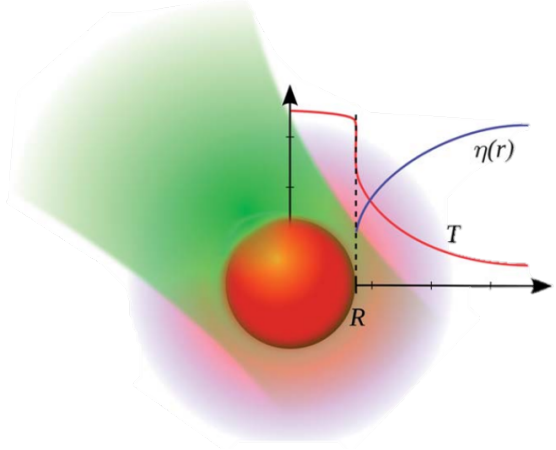


Figure 5.5: **Hot Brownian motion.** When a particle absorbs light and convert it into heat, the kinetics of the Brownian particle changes due to the local temperature $T(r)$ and viscosity profiles $\eta(r)$. Image was taken from reference [171].

This non-equilibrium thermal motion can be characterized for spherical particles of radius R by the effective translational and rotational diffusion coefficients [176]:

$$D_T^{\text{HBM}}(\Delta T) = \frac{k_B T_{\text{HBM}}^{\text{trans}}}{6\pi\eta_{\text{HBM}}R} \quad \text{and} \quad D_R^{\text{HBM}}(\Delta T) = \frac{k_B T_{\text{HBM}}^{\text{rot}}}{8\pi\eta_{\text{HBM}}R^3}, \quad (5.6)$$

which are given by different effective temperatures $T_{\text{HBM}}^{\text{trans}} \neq T_{\text{HBM}}^{\text{rot}}$

$$T_{\text{HBM}}^{\text{trans}}(\Delta T) \approx T_0 \left(1 + \frac{5}{12} \frac{\Delta T}{T_0} \right) \quad \text{and} \quad T_{\text{HBM}}^{\text{rot}}(\Delta T) \approx T_0 \left(1 + \frac{3}{4} \frac{\Delta T}{T_0} \right), \quad (5.7)$$

and by the effective viscosity, η_{HBM} , due to the temperature change ΔT [177]:

$$\frac{\eta_0}{\eta_{\text{HBM}}}(\Delta T) \approx 1 + \frac{193}{486} \left[\ln \frac{\eta_0}{\eta_\infty} \right] \frac{\Delta T}{(T_0 - T_{\text{VF}})} - \left[\frac{56}{243} \ln \frac{\eta_0}{\eta_\infty} - \frac{12563}{118098} \ln^2 \frac{\eta_0}{\eta_\infty} \right] \frac{\Delta T^2}{(T_0 - T_{\text{VF}})^2}. \quad (5.8)$$

In equations 5.7 and 5.8, T_0 and η_0 represent the solvent temperature and viscosity while T_{VF} and η_∞ are the solvent parameters which fulfill the Vogel-Fulcher equation used to describe the viscosity of liquids as function of temperature [178]:

$$\eta(T) = \eta_{\infty} \exp [A/(T - T_{VF})]. \quad (5.9)$$

In figure 5.6 (a) are plotted the $\eta_{\text{HBM}}(\Delta T)$ at initial room temperature ($T_0 = 293$ K) and $\eta(\Delta T + T_0)$ of water given by equation 5.9 for $A = 496.9$ K, $T_{VF} = 152$ K and $\eta_{\infty} = 0.029$ mPa \cdot s [171]. Note that $\eta_{\text{HBM}}(\Delta T)$ decreases at slower rate than the viscosity of water as the temperature rises. This, combined with the fact that T_{HBM} is smaller than $T_0 + \Delta T$, results in the lower value of D_T^{HBM} compared to the one corresponding to the same particle in a solvent at that temperature.

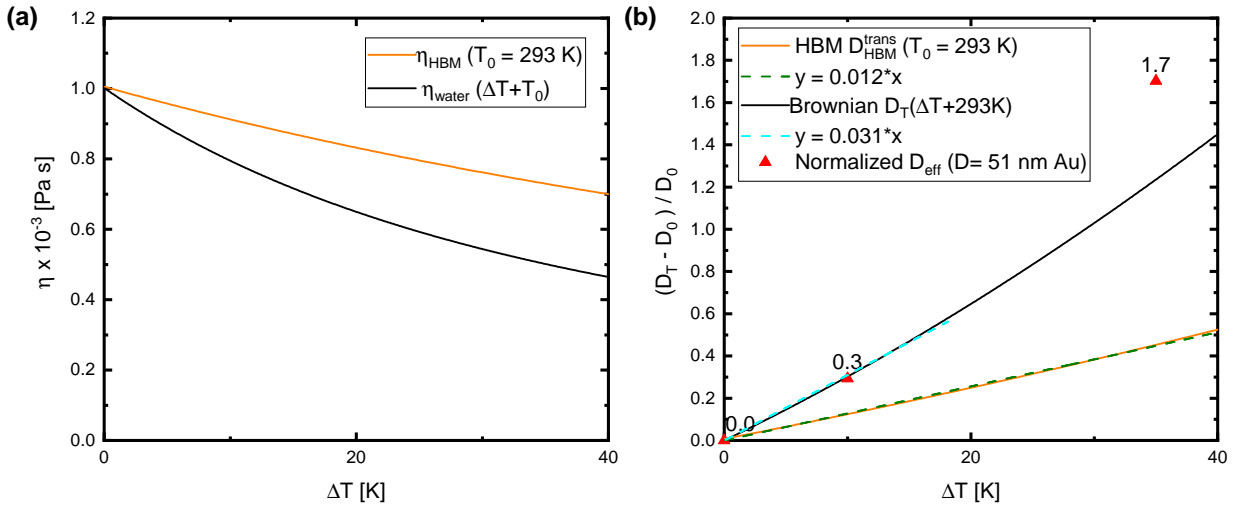


Figure 5.6: **Hot Brownian motion vs Brownian diffusion.** (a) Effective viscosity change of a water solvent at initial room temperature. (b) Normalized diffusion due to the increase of temperature. The data points correspond to the measured diffusion of $D = 51$ nm Au NPs at $T = 293, 303$ and 328 K.

Inserting equations 5.7 and 5.8 in 5.6 we get an expression for the translational diffusion coefficient as function of ΔT :

$$D_{\text{HBM}}(\Delta T) \approx \frac{k_B}{6\pi\eta_0 R} \left[T_0 + \left(\frac{5}{12} + \alpha T_0 \right) \Delta T + \left(\alpha \frac{5}{12} - \beta T_0 \right) \Delta T^2 - \frac{5}{12} \beta \Delta T^3 \right] \quad (5.10)$$

with α and β the prefactors of the second and third terms of equation 5.8 respectively. The normalized diffusion increase, $(D_T - D_0)/D_0$, is plotted in figure 5.6 (b) and compared with the one of a Brownian particle (equation 1.1) for a temperature increase $T_0 + \Delta T$ with $T_0 = 293$ K and the corresponding viscosity change $\eta(\Delta T + T_0)$. Note that in the range of $\Delta T \leq 20$ K, both diffusions have a linear dependence in ΔT . Moreover, the diffusion due to HBM is about a factor 2.5 lower than the simple Brownian diffusion for the same ΔT increase. These theoretical predictions have been compared with the experimentally measured equilibrium diffusion of $D = 51$ nm Au NPs obtained by DLS for bath temperatures $T = 293, 303$ and 328 K ($\Delta T = 0, 10$ and 35 K). As shown in figure 5.6 (b), the normalized diffusion increase

matches with the theoretical prediction accounting for the such temperature increase, for which the Au NPs does not undergo HBM.

5.3.2 Experimental setup

In order to induce the self-propulsion of our hybrid gold-virus structures through the injection of thermal energy, we have added a green laser in the path of our DLS setup (see figure 5.7). This laser, L2, is a $\lambda = 532$ nm green Diode-Dumped Solid-State (DPSS) laser Opus (Laser Quantum) of maximum power 1.2 W and typical beam waist 1 mm. As shown in figure 5.7, L2 shares the path of the typical Gaussian red laser beam ($\lambda = 632.8$ nm) L1, from the pinhole, D2, to the sample, S. Thus, a linear polarizer P1 and the pinhole D3 are incorporated to the path of the green laser in order to assure that this is also polarized and coherent. With this considerations, we are able to use the green laser as probe for the DLS measurements and as light source to induce thermophoresis. Since this reaches high power intensities, a Neutral Density (ND) filter of optical density 10, 20 or 30 has been placed in front of the detector C to protect it from excessive laser light income. In this configuration, we estimate that the beam diameter at the entrance of the DLS bath measured at low intensity corresponds to $d = 2a = 1.85 \pm 0.05$ mm.

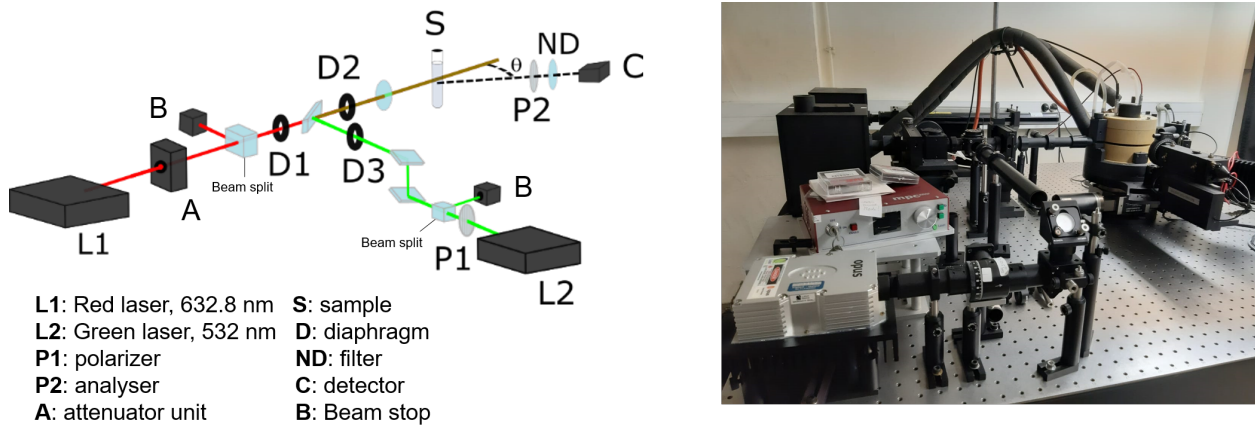


Figure 5.7: **Dynamic light scattering setup for the study of self-thermophoretic systems.** **Left:** Scheme of the optical configuration. **Right:** Picture of the actual setup.

When a spherical Au NP of radius R is irradiated by a light source, the temperature distribution surrounding it as function of the distance to its surface, r , is given by [179]:

$$\Delta T(r) = \frac{Q}{4\pi K r} = \frac{I_{heat}\sigma_{abs}(R)}{4\pi K r}, \quad \text{for } r \geq R, \quad (5.11)$$

K the surrounding medium's heat conductivity and $Q = I_{heat}\sigma_{abs}(R)$, the rate of dissipated or absorbed energy in terms of the heat flux density I_{heat} and optical absorption cross-section $\sigma_{abs}(R)$. The particle's surface temperature can be then calculated from equation 5.11 as: $T(R) = T_0 + \Delta T(R)$. In figure 5.8, it is shown the size dependence of $\sigma_{abs}(R)$ at $\lambda = 532$ nm (green) and $\lambda = 635$ nm (red) obtained from Mie's theory [180, 181]. Note that there is

a significant increase (at least one order of magnitude) of the absorption cross-section when the Au NPs are illuminated at the plasmonic resonance. Moreover, for bigger particles, a higher absorption cross-section is expected and hence a higher increase of $\Delta T(r)$.

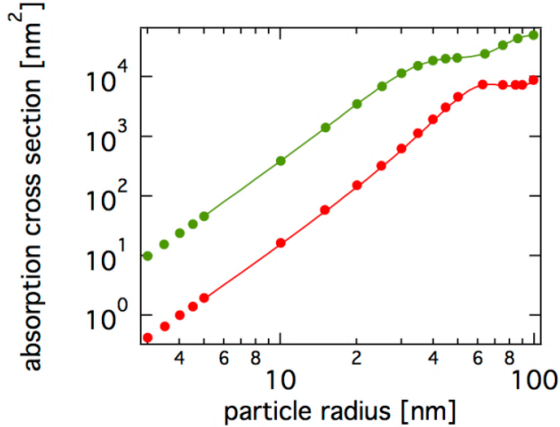


Figure 5.8: **Absorption cross-section.** (b) Size dependence of the $\sigma_{abs}(R)$ at $\lambda = 532$ nm (green) and 635 nm (red). The plot was taken from reference [182].

From equation 5.11, it follows that I_{heat} and $\sigma_{abs}(R)$ are the key parameters to vary in order to induce an increase of local temperature which results in HBM. For an optical system without loss, the heat flux density is given by:

$$I_{heat} = \frac{P}{s}, \quad (5.12)$$

with P the incoming beam power and $s = \pi a^2$ the cross-section of the laser beam. Considering the conditions of our experimental setup, i.e., $P = 1.2$ W and $a = 0.92$ mm, we estimate that a maximum heat flux of $I_{heat} = 4.4 \times 10^{-4}$ mW/ μm^2 can be injected to the sample.

5.4 Diffusion of Janus Au-Silica particles

In this section we report our findings on the induced thermophoresis of Janus gold-silica particles (Au-SiO₂). They have been produced by Chiara Moretti and Benjamin Abécassis at the ENS of Lyon, by the deposition of SiO₂ on the surface of Au NPs of diameter $D = 40 \pm 3.1$ nm [183]. In order to induce HBM and possibly self-propulsion to these Janus NPs, we have explored the dependence of the diffusion coefficient as function of laser intensity using a green laser ($\lambda = 532$ nm) in a range of beam power $5 < P < 1200$ mW. As control experiments, we have also studied the change in diffusion of core-shell Au-SiO₂ NPs and the raw Au NPs used to produce the Au-SiO₂ structures.

In figure 5.9 are shown the Janus and core-shell Au-SiO₂ NPs. The average sizes considering the longest axis measured from TEM images correspond to $D = 69 \pm 10$ nm and $D = 108.5 \pm 19$ nm for the Janus and core-shell NPs respectively.

Before the injection of thermal energy, we have measured by DLS their hydrodynamic diameter, diffusion coefficients and polydispersity index (PDI) using the red laser as probe beam. For this, the intensity correlation function of suspensions at particle concentration $C = 2.9 \times 10^9$ part/ml in a $I = 5$ mM Tris/HCl buffer have been measured in the range of angles $30^\circ < \theta < 150^\circ$ and running time 120 s. Knowing that the absorption cross-section for a red laser is at least one order of magnitude lower than the one of the green laser (see figure 5.8), we have used these results as the ones for incident power equal to zero (indicated

by red symbols in figure 5.12).

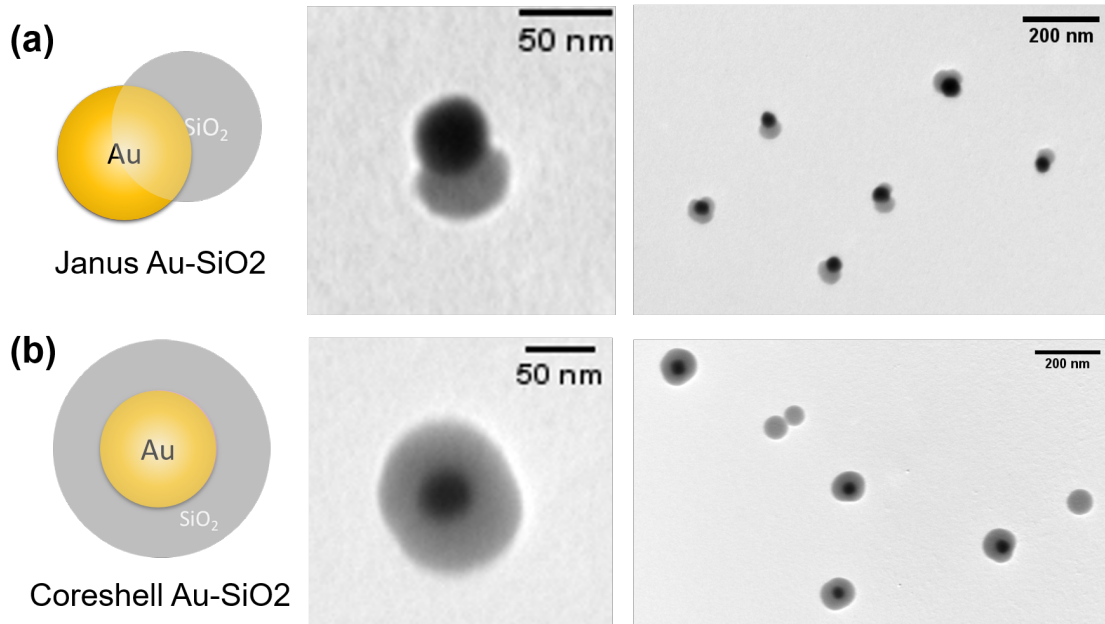


Figure 5.9: **Scheme and TEM images of the Au-SiO₂ nanoparticles.** (a) Janus NPs of average diameter $D = 69 \pm 10$ nm and (b) core-shell NPs of average diameter $D = 108.5 \pm 19$ nm.

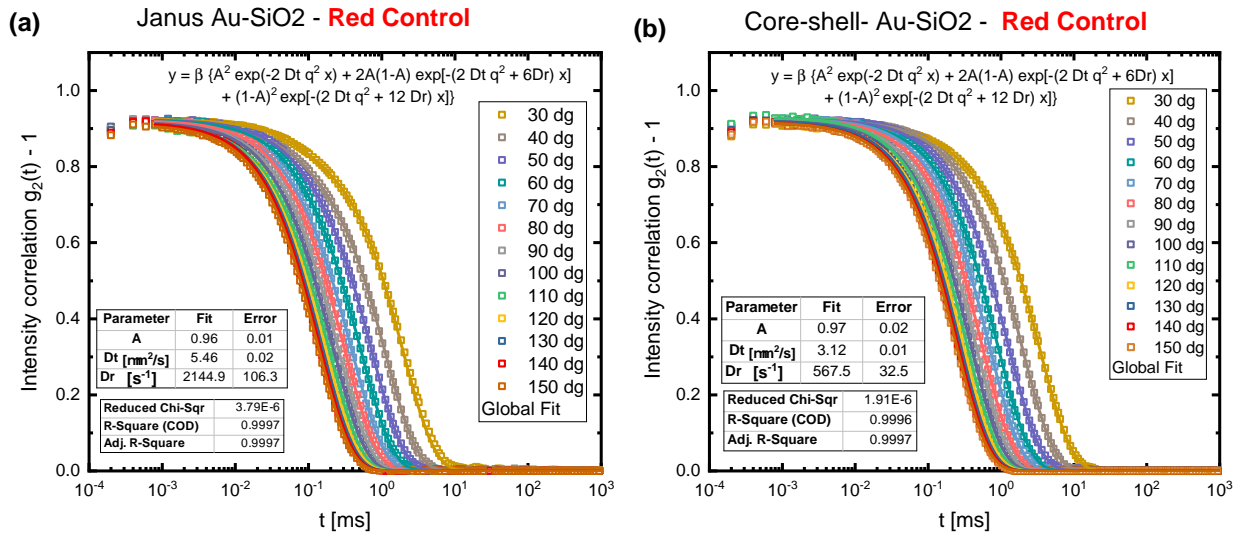


Figure 5.10: **Intensity correlation function of Au-SiO₂ NPs using a red laser as probe beam.** From the global fit for the (a) Janus and (b) core-shell NPs, the diffusion coefficient at room temperature $T_0 = 293$ K: $D_T = 5.5 \pm 0.1 \mu\text{m}^2/\text{s}$ and $D_T = 3.1 \pm 0.1 \mu\text{m}^2/\text{s}$ are obtained.

In figure 5.10 are plotted the intensity correlation functions and independent global fits (see section 3.3.4) of the Janus and core-shell Au-SiO₂ NPs. From the independent global fits (eq. 3.47) we have obtained $D_T = 5.5 \pm 0.1 \mu\text{m}^2/\text{s}$ and $3.1 \pm 0.1 \mu\text{m}^2/\text{s}$ as translational diffusion coefficients for the Janus and core-shell NPs respectively. For the raw Au NPs

of $D = 40$ nm (data not shown), we have found a $D_T = 9.1 \pm 0.1 \mu\text{m}^2/\text{s}$. These diffusion coefficients correspond to the ones of particles of hydrodynamic diameters $d_H = 77.6 \pm 1.3$ nm, 136.8 ± 0.4 nm and 46.9 ± 0.5 nm for the Janus, core-shell and raw Au NPs respectively. All are consistent with the expected double layer at these ionic conditions (for $I = 5$ mM, $\kappa^{-1} = 13.6$ nm). The fitting values of rotational diffusion coefficient obtained are $D_R = 2144.9 \pm 106.3 \text{ s}^{-1}$, $567.5 \pm 32.5 \text{ s}^{-1}$ and $5314.3 \pm 16.3 \text{ s}^{-1}$ for the Janus, core-shell and raw Au NPs respectively. The D_R of the Au-SiO₂ particles is in agreement with the expected according to equation 3.7 for their respective hydrodynamic diameters ($D_R = 2741.9 \text{ s}^{-1}$ and 500.5 s^{-1}). However, the rotational diffusion coefficient found for raw Au nanoparticles differs by more than a factor two from the theoretical value, $D_R = 12419.8 \text{ s}^{-1}$. This is attributed to the low geometrical and optical anisotropy of the raw Au NPs particles compared with the Janus and core-shell Au-SiO₂ ones. Using the cumulant method described in section 3.3.2.1, we have obtained for the raw Au, Janus and core-shell Au-SiO₂ NPs a PDI = 0.02, 0.1 and 0.1 respectively.

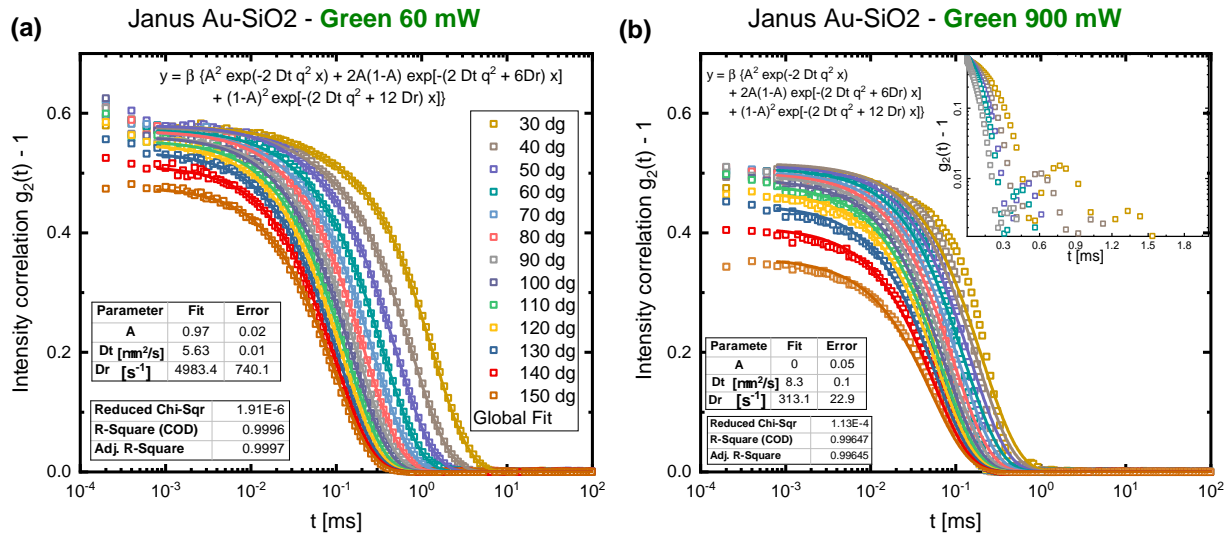


Figure 5.11: **Green laser excitation of Janus Au-SiO₂ NPs.** The intensity correlation functions and global fits are plotted for an incoming laser power (a) $P = 60$ mW and (b) $P = 900$ mW. For beam power above 600 mW the intensity correlation function has an oscillation pattern related to the convective flux velocity.

The intensity correlation functions obtained for each suspension at different beam power have been analyzed using the independent global fit. As show in figure 5.11, the coherence factor, β , i.e. the maximum value of $g_2(q, t) - 1$, when the green laser is used as probe beam is lower compared with the one using the red laser and varies with the scattering angle as well as with the laser intensity. This, attributed to the quality of the green laser, to the optical elements which could be not suitable for $\lambda = 532$ nm and to the optical alignment, slightly affects the accuracy of our measurements. In figure 5.12, we have summarized the translational and rotational diffusion coefficients as function of the input power. For the case of Janus and core-shell Au-SiO₂ NPs, we have observed a strong convection effect

above $P = 600$ mW. Note from the inset of figure 5.12 (b) that an oscillation pattern is found at long decay times. This is a signature of thermal convection whose pattern is related to the velocity of the convective flux [184] as we will discuss in section 5.5.2.

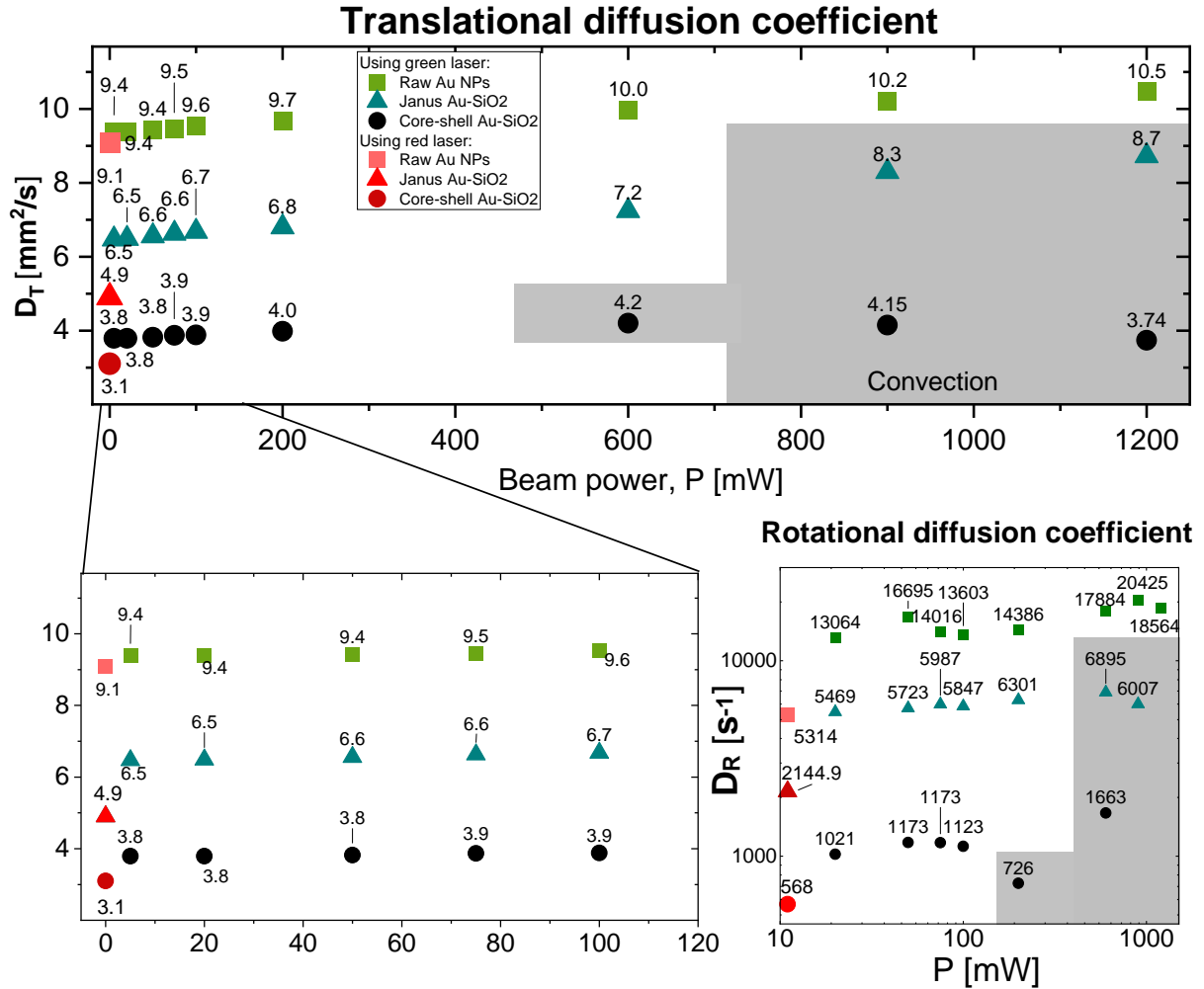


Figure 5.12: **Summary of translational and rotational diffusion coefficients as a function of incoming green laser beam power.** Suspensions of raw Au, Janus and core-shell Au-SiO₂ NPs experience an increase in the diffusion even at a low laser power (below 200 mW). Moreover, above 600 mW convection effects are observed indicated by the gray area.

As shown in figure 5.12, even at the low intensities the diffusions of the Au-SiO₂ systems are significantly higher than the ones obtained using the red laser as probe beam. In order to compare all the systems we have calculated the normalized parameter $(D_T - D_0)/D_0$ with D_0 the value of translational diffusion coefficient at the lowest green laser power. As shown in figure 5.13, for an incoming power below 200 mW the increase of diffusion is significant for all the systems. If we compare these experimental observations with the theoretical models of figure 5.6 (b), for which we find $(D_T - D_0)/D_0 = 0.012\Delta T$ for the theory of HBM, we estimate that in order to account for the observed increase of diffusion of the Janus Au-SiO₂ NPs at power 100 mW ($(D_T - D_0)/D_0 = 3.7 \times 10^2$), we must have a temperature change of $\Delta T \sim 3\text{K}$. According to equation 5.11, the latest result indicate that for $D = 40$ nm Au NPs

whose absorption cross-section is $\sigma_{abs}(20\text{nm}) = 3440 \text{ nm}^2$, the heat flux density is of about $I_{heat} \sim 1.3 \text{ mW}/\mu\text{m}^2$. However, from our experimental setup we expect to have a maximum $I_{heat} = 4.4 \times 10^{-4} \text{ mW}/\mu\text{m}^2$. Where does this difference come from? Can we account it for an active diffusion? Is it related to convective effects?

Since the highest increase is observed for the Janus particles, we have considered that the measured diffusion D_T corresponds to the long diffusivity D_L (equation 5.3) which for the active Brownian motion in 3D is written as:

$$D_T = D_{\text{HBM}} + \frac{V^2}{6D_R} \quad (5.13)$$

with D_{HBM} their effective HBM diffusion, D_R the rotational diffusion coefficient and V the speed of the directed motion. As effective D_{HBM} we have considered the one obtained for the core-shell Au-SiO₂ and raw Au NPs while for the D_R the rotational diffusion coefficient found from the global fits (see figure 5.12). As shown in figure 5.14, the speed obtained for the Janus Au-SiO₂ NPs is of around tens of micrometers per second. This means that the particles diffuse about a hundred of times its size in a second making questionable that this comes from an active motion.

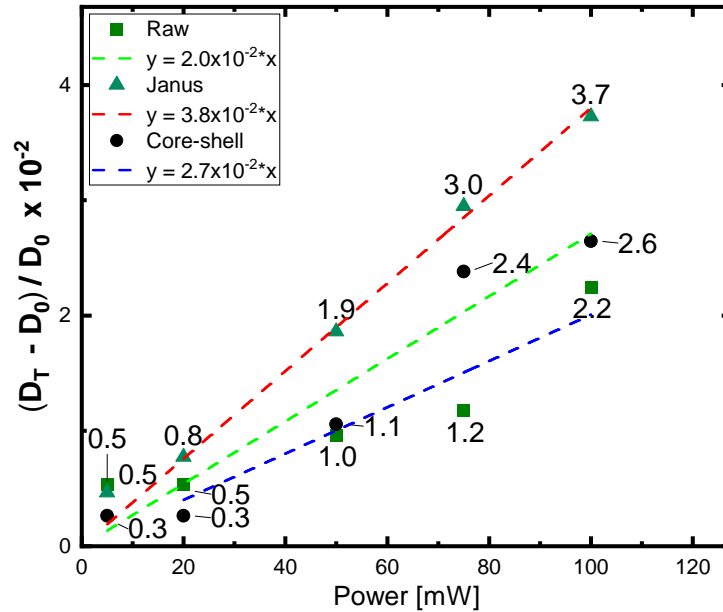


Figure 5.13: **Normalized increase of diffusion coefficients.** For suspensions of raw Au, Janus and core-shell Au-SiO₂ NPs in the range of power $P \leq 100 \text{ mW}$ a significant increase of diffusion is observed.

For comparison, we have estimated the speed in the convective regime clearly identified by the oscillation pattern in $g_2(q, t)$ ($P \geq 600 \text{ mW}$) using as global fit equation 5.5. The obtained speed, added to figure 5.14, follows the trend of the one obtained from the “active approach”. Thus, we conclude that the observed increase of diffusion at low intensities correspond to convective effects, which are not sufficiently strong to create the oscillation

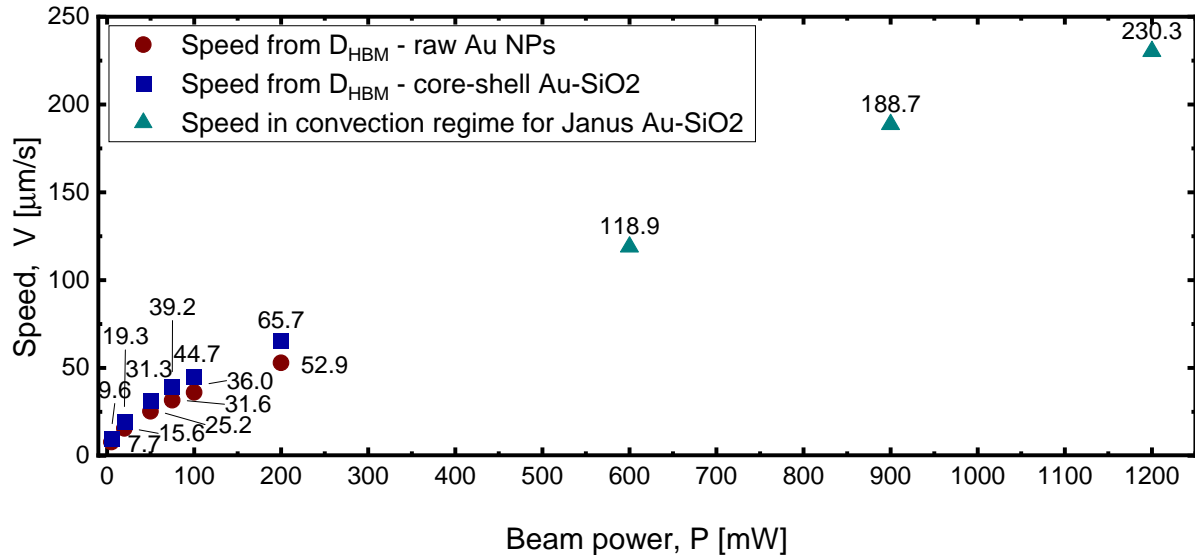


Figure 5.14: **Speed of the Janus Au SiO₂ NPs.** The speeds calculated from the ballistic motion approach are consistent with the typical speed found when convective effects are observed.

pattern in the intensity correlation function at long times but it does affect the diffusion of all the particles.

5.5 Heat induced motion of matchstick-like particles

In this section we investigate the induced thermophoresis in suspensions of matchstick-like particles made of 18 nm Au at particle concentrations $C = 0.01C^*$, $0.16C^*$ and $0.53C^*$ in a $I = 5$ mM Tris/HCl buffer at pH 8.2. Since the gold nanoparticles used to produce these matchstick-like structures are of smaller size than the previous example, the intensity of scattering signal is weak. In order to assure that this is higher than the electronic noise, we have only explored the range of incoming power of the green laser beam between $60 \leq P \leq 1200$ mW. For these experiments, we expect that due to the lower absorption cross-section ($\sigma_{abs} = 313.47$ nm²) and the presumably lower asymmetry induced by the grafted virus (compared to the silica shell of Janus NPs), we require a higher power in order to induce thermophoresis in the matchstick-like structures.

In figure 5.15, we have plotted the intensity correlation functions obtained for a sample at $C = 0.16C^*$ using a beam power $P = 60$ and 600 mW. These have been simultaneously analyzed using the spring-bead model described in section 4.3.1 which account for the flexibility of the p3 proteins of the virus tip (eq. 4.8). Note that for the lowest intensity tested, the quality of the fit is slightly lower than the one obtained using the red laser as probe beam (compare R-Square of figure 4.30). Moreover, as shown in figure 5.15 (b), convective effects are observed as the power increases and the quality of the fit is low (see inset). This observation indicates that the diffusion of the structure is dominated by the speed of the

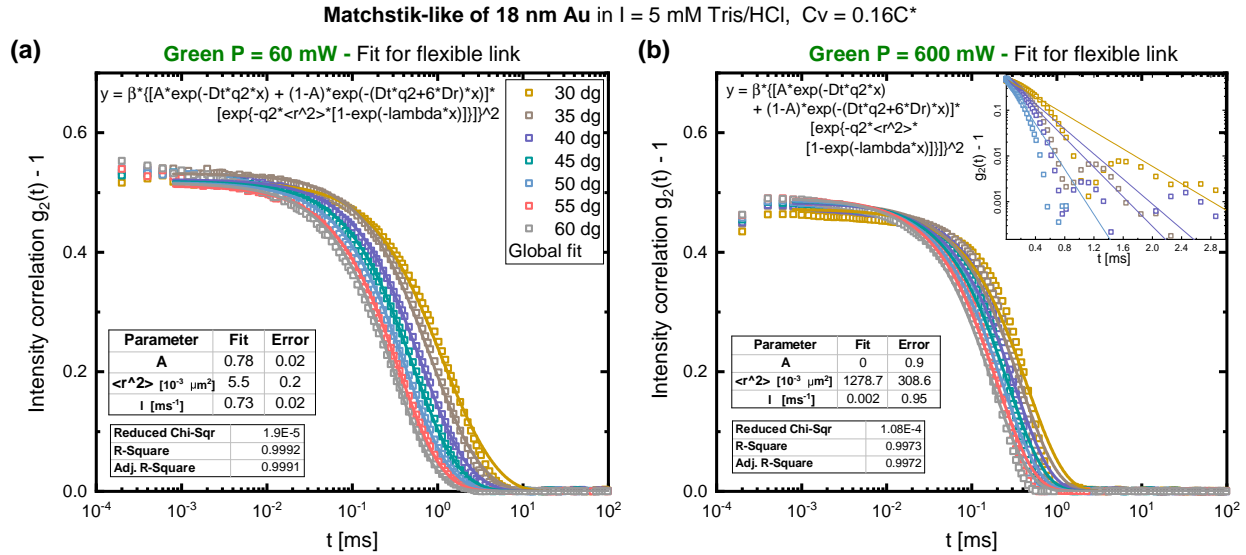


Figure 5.15: **Intensity correlation function of matchstick-like particles made of 18 nm Au NPs obtained using a green laser as probe beam.** (a) For power $P = 60$ mW and (b) $P = 600$ mW, the spring bead-model that accounts for the flexibility of the p3 proteins in the virus tips is not adequate as soon as convection effects are observed.

convective flux and thus we are not sensitive to the flexibility of the virus tip anymore.

In order to investigate the speed and apparent increase of diffusion as function of the income power, we have analyzed the intensity correlation function for samples at different particle concentration using the following approach for convective effects.

5.5.2 Effect of convection in the intensity correlation function

Let us consider a sample composed of spherical particles of dimension small compared to the wavelength moving at a convection flux velocity \mathbf{V} .

When a particle within the sample is illuminated by a laser beam of wavelength λ , the resulting electric field will have a frequency change due to the Doppler effect. Thus, the scattered electric field $\mathbf{E}_s(q, t')$ as seen by the detector (see figure 5.16) will have a scattered frequency ω_s given by [185] :

$$\omega_s = \omega + \Delta\omega_i + \Delta\omega_f, \quad (5.14)$$

where $\omega \equiv 2\pi c/\lambda$ is the frequency of the incident laser beam, $-\Delta\omega_i \equiv \omega(V_i n/c)$ the frequency lowering as seen by the moving particle and $\Delta\omega_f \equiv \omega(V_f n/c)$ the frequency increase as seen by the detector.

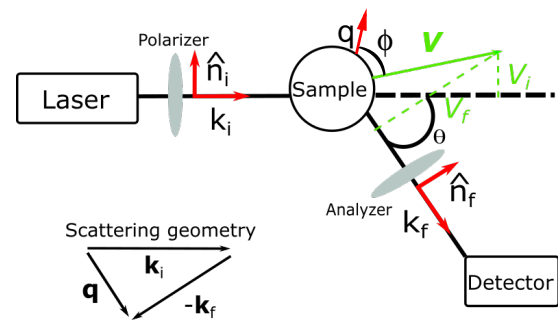


Figure 5.16: **Schematic representation of DLS scattering configuration.** For particles moving with speed \mathbf{V} the scattered electric field observed by the detector will have a frequency change due to the Doppler effect.

Note that the Doppler shifts are in terms of the velocity projections V_i and V_f in the directions of incidence and scattering respectively. Then, the scattering frequency is written in terms of the velocity \mathbf{V} as:

$$\begin{aligned}\omega_s &= \omega - \mathbf{k}_i \cdot \mathbf{V} + \mathbf{k}_f \cdot \mathbf{V} \\ &= \omega - (\mathbf{k}_i - \mathbf{k}_f) \cdot \mathbf{V} \equiv \omega - \mathbf{q} \cdot \mathbf{V},\end{aligned}\quad (5.15)$$

and therefore the scattered field is

$$\mathbf{E}_s(q, t) \sim E_0 \mathbf{k}_s e^{-i\omega t} e^{i\mathbf{q} \cdot \mathbf{V} t}, \quad (5.16)$$

where $\mathbf{q} = \mathbf{k}_i - \mathbf{k}_f$ is the scattering vector of magnitude $q = 4\pi n \sin(\theta/2)/\lambda$. From equations 3.12, 3.13 and 5.16, it follows that the intensity correlation function of an active particle measured by DLS is equal to an ensemble average of a phase factor $\exp(i\mathbf{q} \cdot \mathbf{V} t)$ [102].

In the simple case of a velocity gradient parallel to the convective flux, the change of phase in the intensity correlation function is reduced to [184]:

$$g_2(q, t) - 1 = 4\beta \cos^2(\cos(\phi)qVt) \exp(-2D_T q^2 t) \quad (5.17)$$

with ϕ the angle between the scattering vector \mathbf{q} and the speed \mathbf{V} .

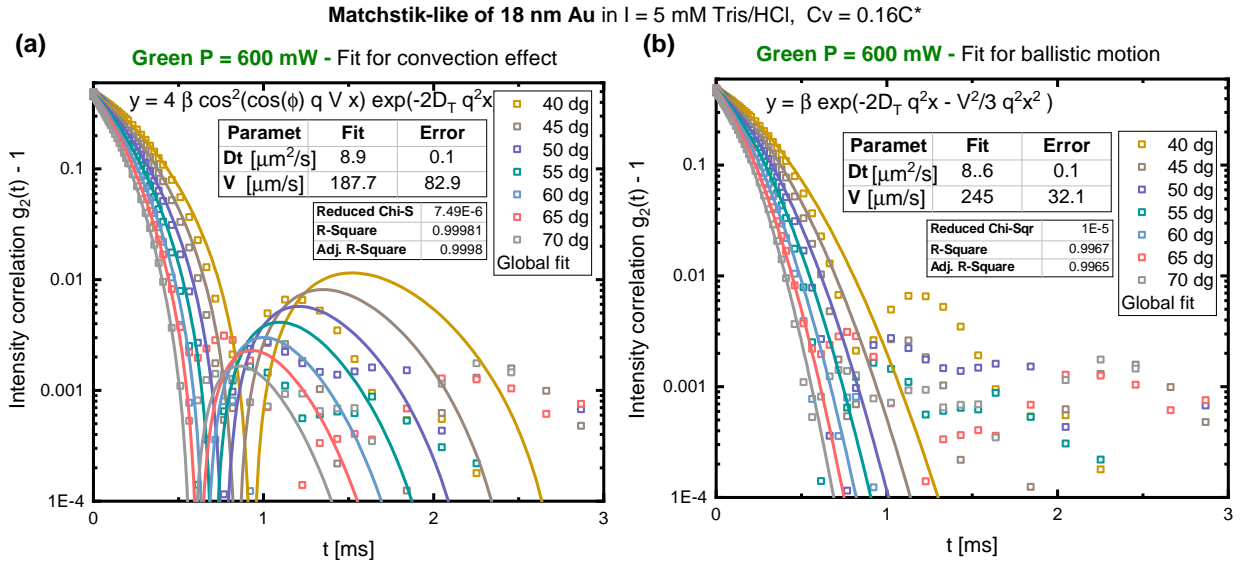


Figure 5.17: **Model for convection vs simple ballistic model.** The global fits of the convection model for free parameter ϕ (a) and ballistic motion (b) recover almost the same diffusion coefficient. The obtained speed for both models is in the same order of magnitude however, only the convection effect recover effectively the oscillation pattern.

In figure 5.17 (a) is shown the global fit using equation 5.17 to analyze our experimental data for $P = 600$ mW. Note that this model recovers properly the first decay related to the translational diffusion coefficient. However, the change of phase ϕ does not account completely for the oscillation pattern. This could be attributed to the fact that the convection flux is not necessary symmetric and thus the direction of the speed changes respectively for each measurement. This model is compared in figure 5.17 (b) with the one for simple ballistic

motion of equation 5.5. In the error bar, both models recover the same translational diffusion coefficient. However, a difference of $\sim 30\%$ is observed between the speeds obtained.

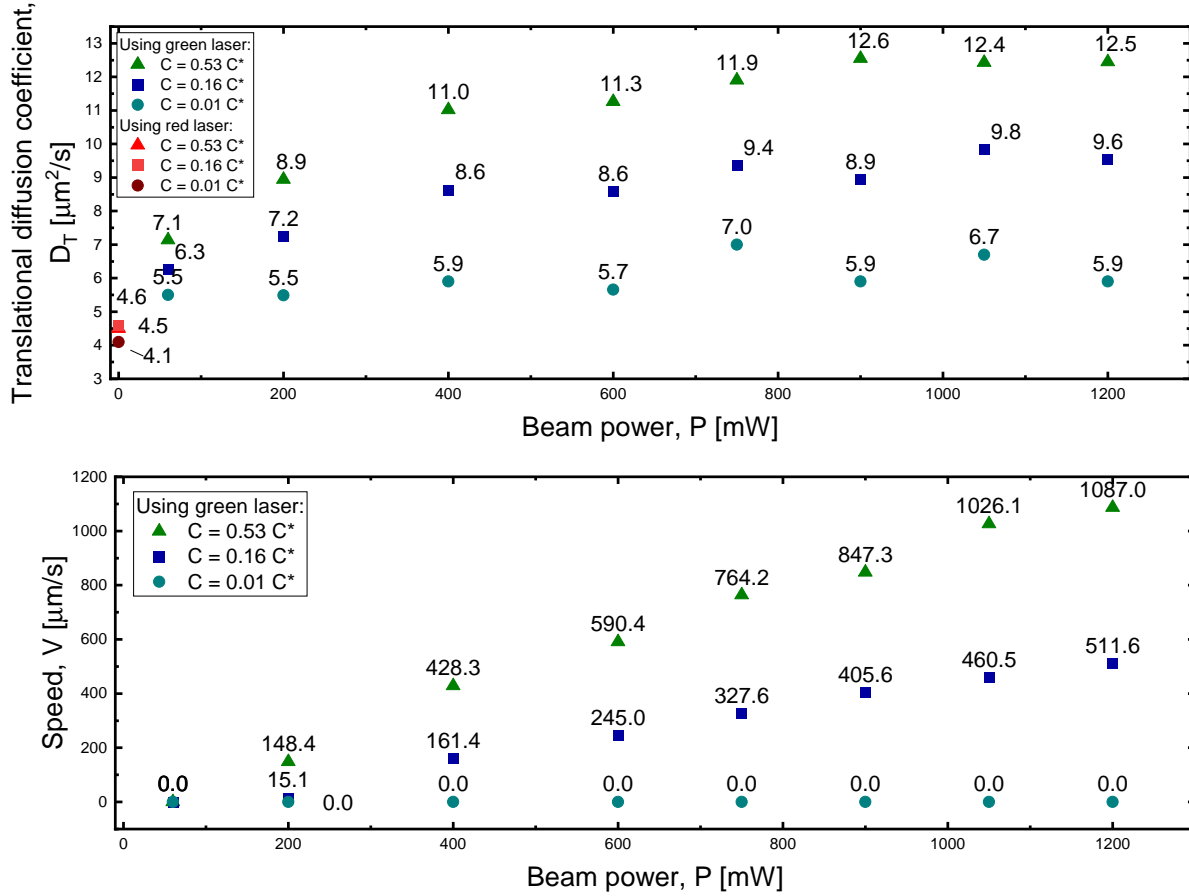


Figure 5.18: **Summary of the heat induced motion of matchstick-like particles made of 18 nm Au NPs.** Translational diffusion coefficient (top) and speed (bottom) obtained from the global fit equation 5.5 for different particle concentrations as function of the incident beam power.

For sake of simplicity, we have analyzed the samples at different particle concentration using the ballistic model of equation 5.5. The apparent diffusion coefficients and speeds found for each one are summarized in figure 5.18. As shown in the plot, from the lowest intensity there is a significant increase in the effective diffusion coefficient compared with the one measured using the red laser as probe beam. Moreover, a higher diffusion coefficient and speed is found as the particle concentration increases. Note that for $C = 0.01 C^*$, the global fit converges to a speed $V = 0$. However, an apparent increase of diffusion as the power increases is observed. This is similar to our findings on the Janus Au-SiO₂ NPs for which the convection effect is not as high to create the oscillation pattern in the intensity correlation function but still affects the particle diffusion. When we try to fit with equation 5.5, this does not account for such small speeds and hence it converges to zero but still corresponds to a convection effect.

Note that the speed increases significantly with the income green laser power even when we expect to have a lower change of temperature due to the smaller light absorption for this

nanoparticle size (in contrast with the Janus Au-SiO₂). This effect could be related to the possibility to orient our structures thanks to the vial “tail” making them more sensitive to weak flow or convection.

5.6 Discussion and conclusions

In this chapter we have explored the possibility to induce self-propulsion to anisotropic hybrid colloidal particles made of Au NPs. As propulsion mechanism, we have used the temperature and viscosity profiles created around Au NPs when these are irradiated at the plasmonic resonance combined with the structural asymmetry of Janus Au-SiO₂ NPs and matchstick-like gold-virus structures.

In order to inject thermal energy, we have implemented a DLS setup with a green laser beam of maximum power $I = 1.2$ W. This has been used as both probe beam and as energy source. For all our samples, we have observed an apparent increase of diffusion when we inject green light, i.e, when we irradiate the Au based hybrid colloids at the plasmonic resonance. However, this increase in diffusion cannot be accounted by the increase of temperature according to the incident power of our experimental setup. Thus, we have concluded that this is related to convective effects which influence the diffusion of our structures even at low power. For the matchstick-like structure, which could be easily aligned in the direction of the convective flow, we have measured a convection flux speed between tens and one thousand of micrometers per second despite the low light absorption of the nanoparticles attached to their tips.

It is known that absorption of laser radiation can lead to buoyancy or natural convection currents [184]. This effect could be attributed to the local heating of the liquid along the beam path [186] and to a possible thermal-lensing effect [187] which create a vertical temperature gradient and for some critical value, convection. The condition for the appearance of free convection is given by the Rayleigh number [186]:

$$Ra = \frac{g\alpha h^3 \Delta T}{\nu\chi} \quad (5.18)$$

where h is the characteristic length of the optical path and α , ν and χ the thermal expansion coefficient, kinematic viscosity and thermal diffusivity of the medium (for water: $\alpha = 2.1 \times 10^{-4}/K$, $\nu = 1 \times 10^{-6}$ m²/s and $\chi = 0.143 \times 10^{-6}$ m²/s). For the condition of our DLS experiment, for which the optical path corresponds to the size of the cylindrical cell of 1 cm, we estimate a $Ra \sim 1 \times 10^4$. This represent a significant value for which convection is expected [186].

Thus, in order to avoid convection effects, we suggest to work in thinner samples such as the ones prepared for optical microscopy. Using an optical microscope could sound promising from the point of view of the HBM theory, for which decreasing the beam size is translated as an increase of injected energy and hence of temperature (see equations 5.11 and 5.12).

However, concentrating light using a laser beam could induce optical forces/trapping on the particles due to the intensity gradient of the illumination [188]. The necessary condition to optically trap a particle of radius a is that the potential well of the gradient force trap should be much larger than the kinetic energy of the colloidal particles, i.e., $\exp(-U/k_B T) \ll 1$ [189], with the potential energy

$$U \propto \frac{2a^3 P}{w_0^2}, \quad (5.19)$$

proportional to the nanoparticle size, laser beam power P and beam waist w_0 . By using an objective lens we decrease w_0 resulting in an increase of potential energy of the trap. Thus, an optical microscopy setup to induce HBM to colloidal/nano particles is not trivial to do since it requires a fine-tuning of the experimental parameters in order to observe HBM and avoid optical trapping at the same time.

Chapter 6

Colloidal stars as model system of soft spheres

6.1	Soft colloidal particles	124
6.1.2	Phase diagram of soft colloids	124
6.2	Dynamics and structure of colloidal star particles	127
6.2.1	Dilute regime	129
6.2.2	Dense regime	133
6.3	Discussion and conclusions	140

6.1 Soft colloidal particles

The simplest colloidal systems consist of hard-spheres. These, led by their infinite repulsion at contact, exhibit an entropy driven phase behavior determined by the volume fraction [2]:

$$\phi = \frac{N}{V}V_{sph}, \quad (6.1)$$

defined as the fraction of the total volume, V , that is filled by N spheres of volume V_{sph} . Hard-spheres form close-packed structures with face-centered cubic (FCC) or hexagonal close packed (HCP) organization [190, 191] at relatively low volume fraction ($\phi \sim 0.58$) compared with particles such as polymers for which only liquid-like order is reached at very high volume fractions ($\phi > 1$). This is possible because in polymers the elasticity of the chains and the existence of interdigitation dominate their dynamics. The term “soft colloids” refers to the special class of particles with a dual character somewhere between polymers and hard spheres [192].

The “softness” of a colloidal particle, linked to the pair potential between them, could be interpreted as a degree of compression beyond its effective radius [193]. This can be achieved as a consequence of the steric mechanism to stabilize colloidal particles such as grafting polymers to their surface as well as from the particles themselves which could be elastic and deformable. Examples of soft colloids are microgels [36], micelles [194] and star polymers [195]. Recent studies in colloidal sciences address soft particles from a broad range of materials, chemical compositions and architectures such as the ones schematically illustrated in figure 6.1. These materials exhibit structural and mechanical properties that contrast from the ones of hard-spheres as result of their wide-ranging soft interaction potential at contact and beyond [196].

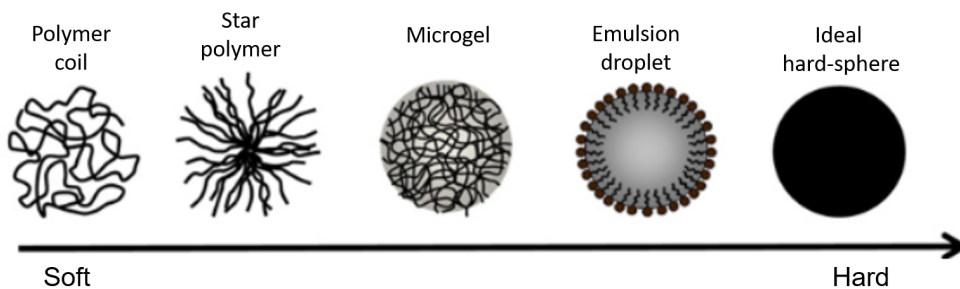


Figure 6.1: **Soft colloids.** Sketch of spherical soft colloidal particles with decreasing softness from left to right. Image was adapted from reference [196].

6.1.2 Phase diagram of soft colloids

The phase behavior of soft colloids exhibits similarities with the one of hard-sphere suspensions. As shown in figure 6.2, with increasing volume fraction, the hard spheres go from a disordered fluid phase to an ordered crystalline phase through an intermediate

fluid-crystal coexistence regime. Then, above a critical volume fraction of $\phi \sim 0.58$, a disordered amorphous glass whose particle positions are uncorrelated is formed. Moreover, beyond the upper limit of the glassy region, the particles are forced into contact in a jammed state. A similar sequence of phase transitions is undergone by soft colloids. However, significant quantitative differences are observed as the level of “softness” increases [196].

For example, colloidal star polymers made of a very small deformable core and a corona consisting of grafted long polymer arms, considered as ultra soft colloidal spheres, exhibit deformability, swelling/deswelling and interpenetration [192]. Thus, the location of phase transitions seems to occur at higher volume fractions than those of hard-spheres. Moreover, star polymers exhibit a narrower or even nonexistent phase coexistence region.

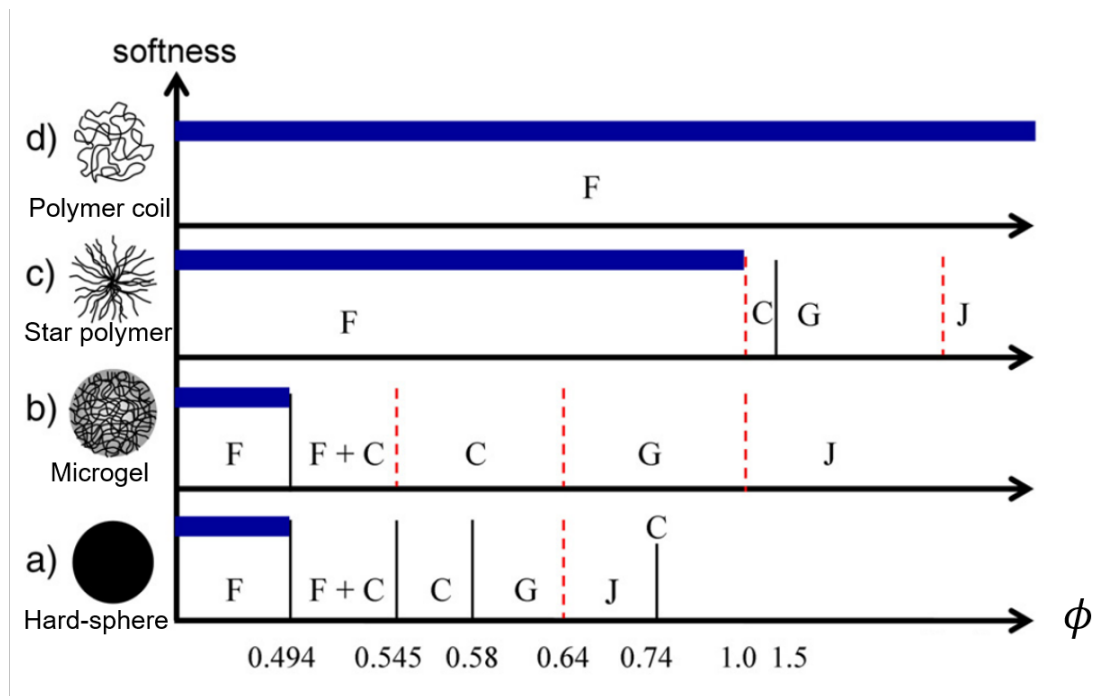


Figure 6.2: **Schematic phase diagram of soft colloids as function of their effective volume fraction.** The different states: fluid (F, the blue-shaded regions), crystal (C), coexistence (F + C), glass (G), and jammed (J) for **a)** hard spheres, **b)** microgels, **c)** star polymers and **d)** polymeric coils. The solid black vertical lines represent established transitions whereas red dashed lines those whose universality is still debatable. Image was adapted from reference [196].

In general, soft colloids exhibit an extended fluid phase as the softness increases. This is related to their soft repulsive potential at large and short inter-particle distances [197]. The fundamental understanding of phase formation in soft colloids is of interest to predict and control physical properties such as viscoelasticity [195].

In order to explore the phase diagram of colloidal particles, different methods have been used to increase the particle concentration and hence ϕ . The most simple approaches include the centrifugation of the suspension, for which the particles are sedimented and the supernatant is removed, and membrane ultra-filtration [198], for which part of the solvent goes away through the pores of the membrane while the colloids stay in a more

concentrated suspension. An alternative method to vary ϕ is to locally concentrate the structures by adding non-adsorbing hydrophilic polymer to the system, which induces an effective attraction between particles called *depletion*.

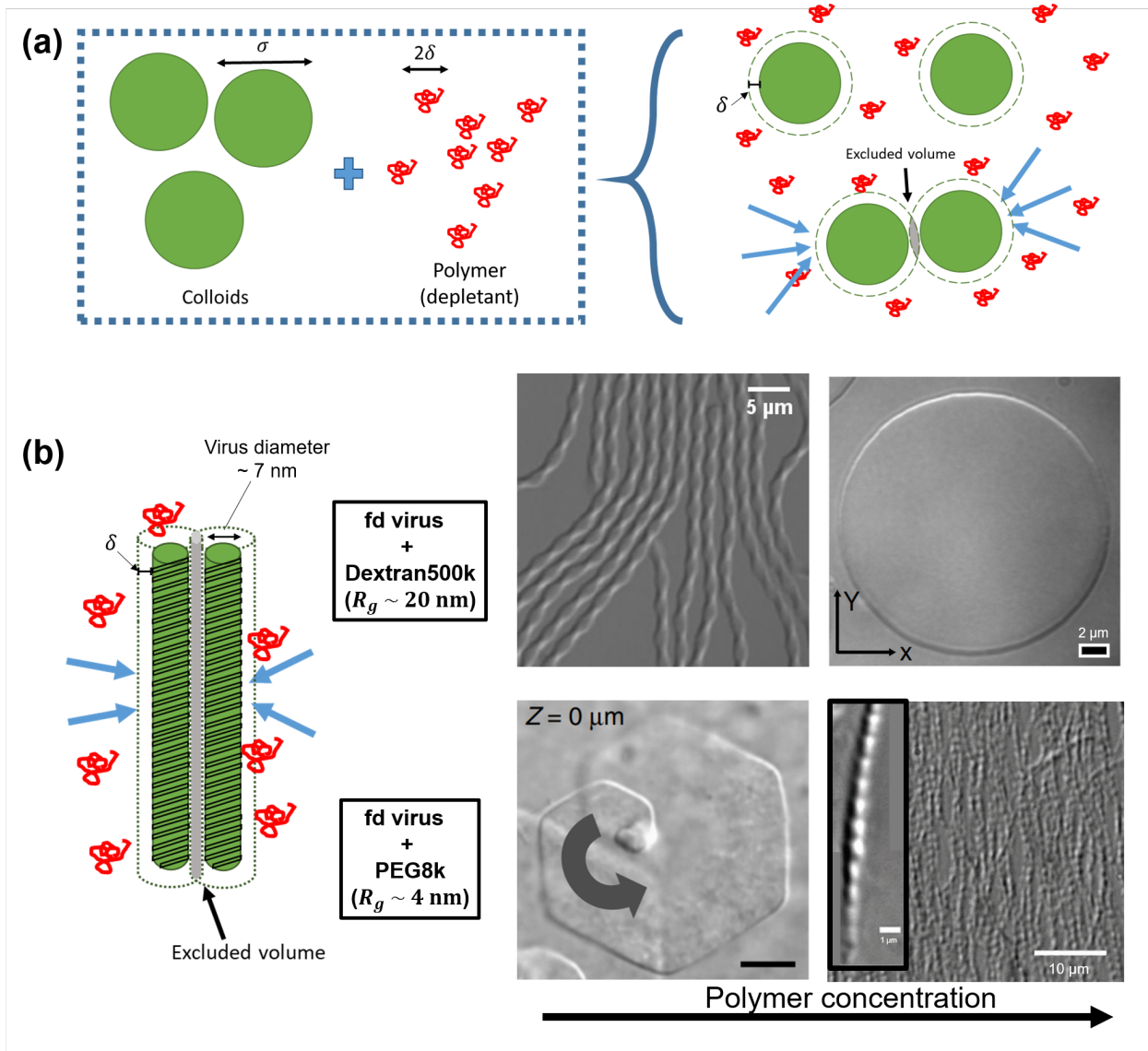


Figure 6.3: **Illustrations of depletion interaction.** (a) For a mixture of colloidal spheres of diameter σ and non-adsorbing polymer of diameter 2δ there is an excluded volume region inaccessible for the polymer associated with each colloid. Their overlap results in a decrease in the total volume available to the depletant. The maximization of entropy results in an effective attraction between colloidal particles. (b) The depletion of chiral rod-like viruses and Dextran polymer of radius of gyration $R_g \sim 20$ nm results in the formation of membranes[199] and twisted ribbons [200] as the polymer concentration increases while the one with PEG8k of $R_g \sim 4$ nm results in helical platelets [201] and smectic fibrils [202].

The depletion is an entropy driven phenomena associated with the size and concentration of the polymer (or depletant) mixed with colloids. As shown in figure 6.3(a), when spherical colloidal particles and polymers of diameters σ and 2δ respectively are mixed together, a depletion layer of thickness equal to the radius of the polymer is created around the colloids. Then, when two depletion layers overlap, i.e., when the colloids approach closer than 2δ , the

polymer cannot access the excluded volume formed. This results in a difference of osmotic pressure due to the increase of free volume available for the polymer. Since the entropy is maximized when the colloids are close to each other, their clustering is favored. Asakura and Oosawa were the first to develop a theory for the effective interaction between colloids and polymers [203] showing that its intensity and range are determined by the concentration and diameter of the depletant with respect to the colloid size respectively.

As shown in figure 6.3(b), the mixture of rod-like viruses of diameter ~ 7 nm and polymers of different size exhibits a rich variety of formed structures. For instance, in the presence of Dextran500k, a complex branched glucan polymer whose size is larger than the particle diameter, i.e., radius of gyration $R_g \sim 20$ nm, the rod-shaped viruses self-organize into structures with liquid-like order normal to the virus long axis such as membranes [199] and twisted ribbons [200]. Moreover, for a short-ranged depletion attraction, i.e., for a smaller size of the polymer such as Poly-Ethylene Glycol of molecular weight 8kDa (PEG8k) of $R_g \sim 4$ nm, the self-assembled structures are helical platelets [201] and smectic fibrils [202] which possess crystalline or long-ranged positional order in the three spatial dimensions. In the context of soft colloids, the question about the role of the softness in the behavior of soft colloid–polymer mixtures is raised.

In this chapter, we study the phase behavior of our hybrid colloidal star particles as model system of soft colloidal spheres. For this purpose, we have identified two regimes, a dilute regime for which the particles do not interact with each other and a dense regime for which there is interdigitation of the viral arms. The dynamics in both regimes has been studied by single particle tracking through optical microscopy observations. Moreover, in the dilute regime, our results are compared with the ones obtained by dynamic light scattering. After studying their dynamics, we have also explored the possibility to induce the self-assembly of these structures by tuning their interaction into an attractive one by depletion.

6.2 Dynamics and structure of colloidal star particles

In this section, we report our investigations on the dynamics of colloidal stars (CS) in dilute and dense regimes. As described in section 2.3.1, these hybrid structures are made of a gold nanoparticle (Au NP) core of $D = 51 \pm 6$ nm and a viral corona of average valency, i.e., the number of grafted viruses, $\langle n \rangle = 23 \pm 6$ (see figure 6.4). We have evidenced in chapter 4 that the p3 protein tips of the virus are flexible. Hence, the viral arms of the CS, which are linked to the Au NPs core by that tip, are allowed to re-orientate around it. Thus, we have first considered our CS as “soft” spheres of diameter equal to two virus length, i.e. $\sigma = 2 \mu\text{m}$.

According to the core-to-core distance between colloidal stars, R_a , we have *a priori* identified three different regimes: dilute, dense and overlap. As shown in figure 6.4, in the *dilute* regime R_a is higher than their diameter σ so star particles mostly do not interact with each other. In the *dense* regime, found between $1 \mu\text{m} < R_a < 2 \mu\text{m}$, we expect an

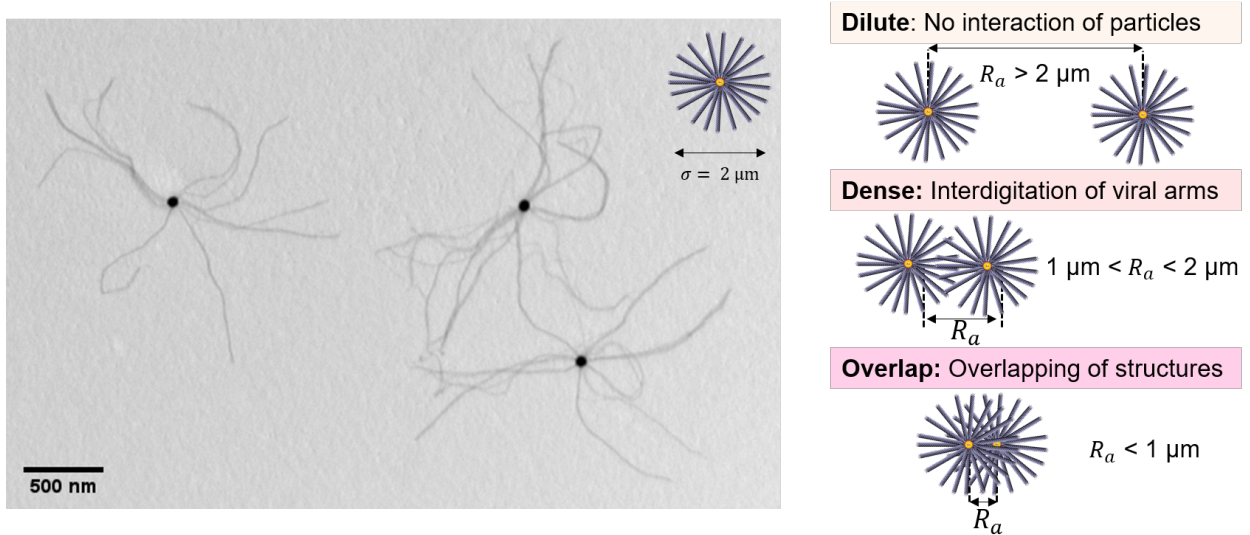


Figure 6.4: **Colloidal star particles.** TEM image (left) and expected regimes defined according to the core-to-core distance R_a (right).

interdigitation of viral arms and for $R_a < 1 \mu\text{m}$, we define the *overlap* regime.

The particle concentration of each of these three different regimes has been calculated as function of the optical density (OD) of the suspension considering the “nearest neighbor separation”, d_{nn} , of a face-centered cubic (FCC) crystal symmetry. As shown in figure 6.5, for the FCC crystal there are $n = 12$ nearest neighbors which are located from the reference point at a distance $d_{nn} = a/\sqrt{2}$. Thus, from equation 6.1, it follows that the nearest neighbor separation in this arrangement as function of the volume fraction is given by:

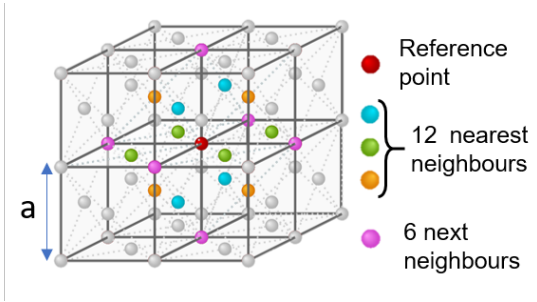


Figure 6.5: Sketch of a FCC crystal structure of typical length a .

$$d_{nn} = \left(\frac{16\pi}{\phi} \right)^{1/3} \frac{r}{\sqrt{2}}, \quad (6.2)$$

with r the radius of the spheres arranged in a FCC lattice. Assuming that for all concentrations the FCC organization is kept and hence the nearest neighbor separation is equal to the core-to-core distance, R_a , we substitute in equation 6.2, $\phi = N/V(4\pi\sigma^3/3)$, to get the relation as function of the colloidal star concentration N/V :

$$R_a = \left(\frac{12}{N/V} \right)^{1/3} \frac{1}{\sqrt{2}}. \quad (6.3)$$

In a suspension of colloidal stars, N/V is given in terms of the OD of the 51 nm Au NP core according to equation 2.2. Thus, it follows that:

$$\frac{N}{V} = \frac{OD_{520} N_A}{\varepsilon_{520}} \quad (6.4)$$

with N_A the Avogadro's number and $\varepsilon_{520} = 1.94 \times 10^{10} \text{ M}^{-1}\text{cm}^{-1}$ the specific extinction coefficient of Au NPs of diameter $D = 51 \text{ nm}$. From equations 6.3 and 6.4, we find that the OD for which the colloidal stars are at $R_a = 1 \mu\text{m}$ and $2 \mu\text{m}$, corresponding to the ones that delimit the dense regime, are $OD = 17.1$ ($5.3 \times 10^{14} \text{ part/ml}$) and 136.7 ($4.2 \times 10^{15} \text{ part/ml}$) respectively. Experimentally, we have explored the dynamics of colloidal stars in the range of $0.01 < OD < 140$. Moreover, we have chosen to work in a $I = 110 \text{ mM}$ Tris/HCl buffer at pH 8.2, with an associated Debye screening length of $\kappa^{-1} = 0.9 \text{ nm}$, in order to strongly screen the electrostatic repulsion between viruses to facilitate their interdigitation.

6.2.1 Dilute regime

In the dilute regime, for which the inter-particle interaction is negligible, we have studied the dynamics of the CS by means of single particle tracking using optical microscopy and dynamic light scattering. In figure 6.6 are shown confocal fluorescence microscopyⁱ images taken in a Zeiss LSM 980 microscope at a frame rate of 35 frames per second (fps). The snapshots evidence that beyond the rotational motion of the structure, the viral arms change their orientation thanks to the flexibility of the gold-virus link (p3 protein).

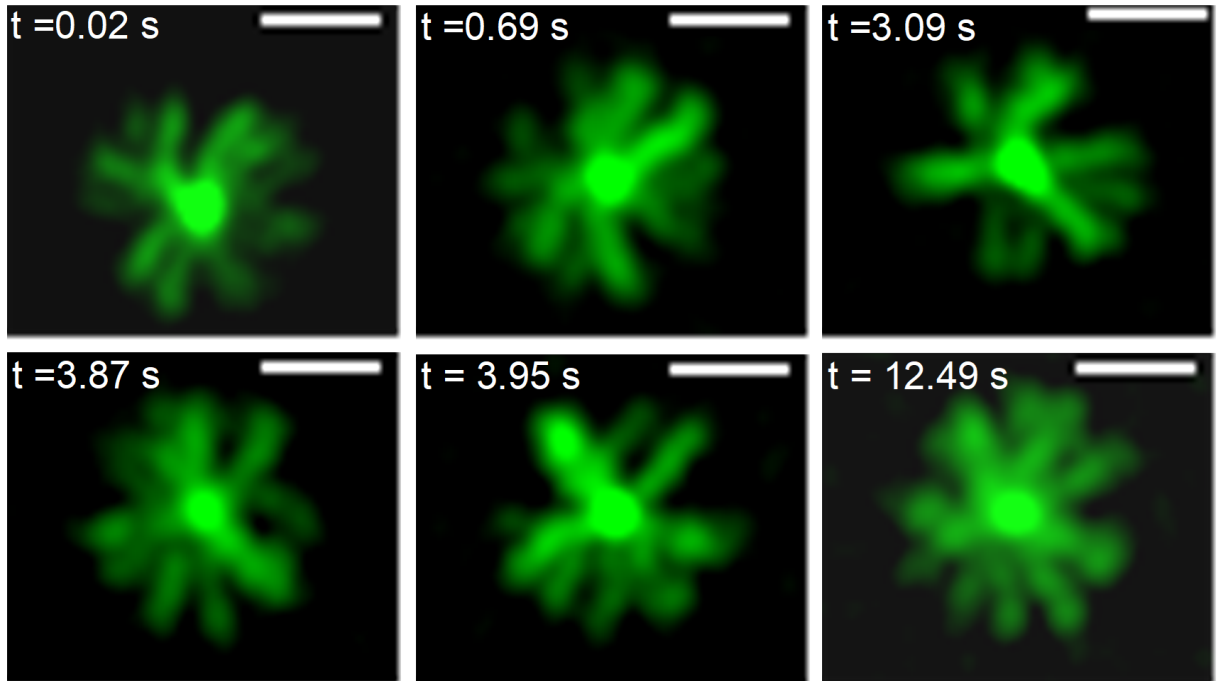


Figure 6.6: **Confocal fluorescence microscopy images of colloidal star particles.** Thanks to the flexibility of the gold-virus link, the viral arms change orientation freely in the dilute regime.

For suspensions at $OD = 0.03$ and $OD = 0.05$, we have measured the self-diffusion of the CS by single particle tracking as described in section 3.2.2 on one hand by fluorescence

ⁱConfocal microscopy is a advanced technique which offers 3D imaging increasing the optical resolution and contrast of a micrograph by means of a spatial pinhole [204].

(FLUO) microscopy at a frame rate of 195.57 fps and on the other hand, by dark field (DF) microscopy thanks to the Au NP in the core at a frame rate of 762 fps. Note from figure 6.7, that the position of the center of mass obtained from the DF observation is of higher accuracy than the one obtained from the FLUO observations. The latest statement stems from the fact that in order to obtain the center of mass position via FLUO microscopy we fit the signal coming from the moving labeled viral arms whereas by DF the position is determined from the Au NP core which is obtained with a sub-pixel accuracy thanks to the size and signal over noise ratio.

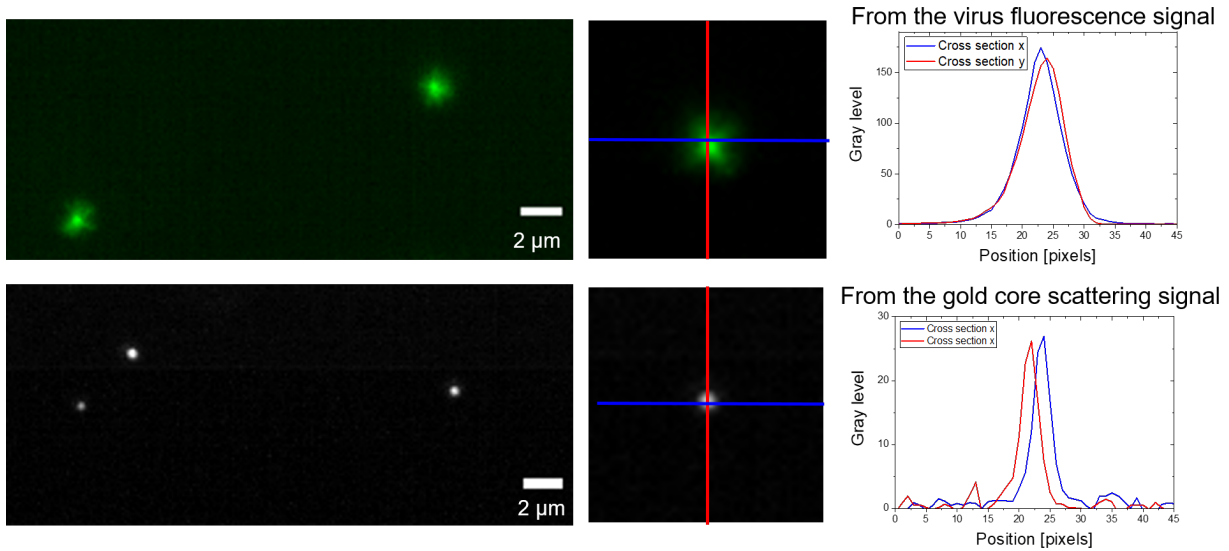


Figure 6.7: **Single particle tracking of colloidal star particles.** For the detection using fluorescence (FLUO), we determine the center of mass position from the intensity profile given by the labeled viral arms (top), while using dark-field (DF) from the scattering signal of the gold core (bottom).

In figure 6.8 are plotted the mean square displacements (MSD) obtained for DF and FLUO approximately from 60 and 110 traces respectively. Note that for this number of trajectories the statistical noise in the calculated MSD is high after ~ 2 s after which the MSD has therefore, no physical meaning. For the DF observations taken at a higher frame rate compared with the FLUO ones, we find two regimes: a subdiffusive regime of diffusion exponent, $\gamma \sim 0.5$ and, above the crossover time of $\tau = 50 \text{ ms}^{-1}$, a diffusive regime of $\gamma \sim 1$ (see section 3.2.2). This could be attributed on one hand to the lower time resolution given by the frame rate of the FLUO observation, or in the other hand, to an effect due to the internal degree of freedom coming from the flexibility of the gold-virus link. Using equation 3.6 for two dimensions, i.e., $n = 2$, we find $D_T = 0.25 \text{ } \mu\text{m}^2/\text{s}$ and $D_T = 0.30 \text{ } \mu\text{m}^2/\text{s}$ from the FLUO and DF microscopy experiments, respectively. According to equation 1.1, these diffusions correspond to the ones of spheres with diameter $\sigma = 1.7 \text{ } \mu\text{m}$ and $\sigma = 1.4 \text{ } \mu\text{m}$ respectively. The σ obtained from the FLUO observations is consistent with the expected size of CS, i.e., $\sim 2 \text{ } \mu\text{m}$, however the one from the DF deviates significantly. From the difference in the diffusion coefficients obtained $\Delta D = D_T^{\text{DF}} - D_T^{\text{FLUO}} = 0.05 \text{ } \mu\text{m}^2/\text{s}$ and the

cross over time of the DF observations $\tau = 50 \text{ ms}^{-1}$, we estimate the characteristic length $L = \sqrt{\Delta D \times \tau} = 50 \text{ nm}$ which is related to the internal degree of freedom of the Au NPs being probed by DF microscopy.

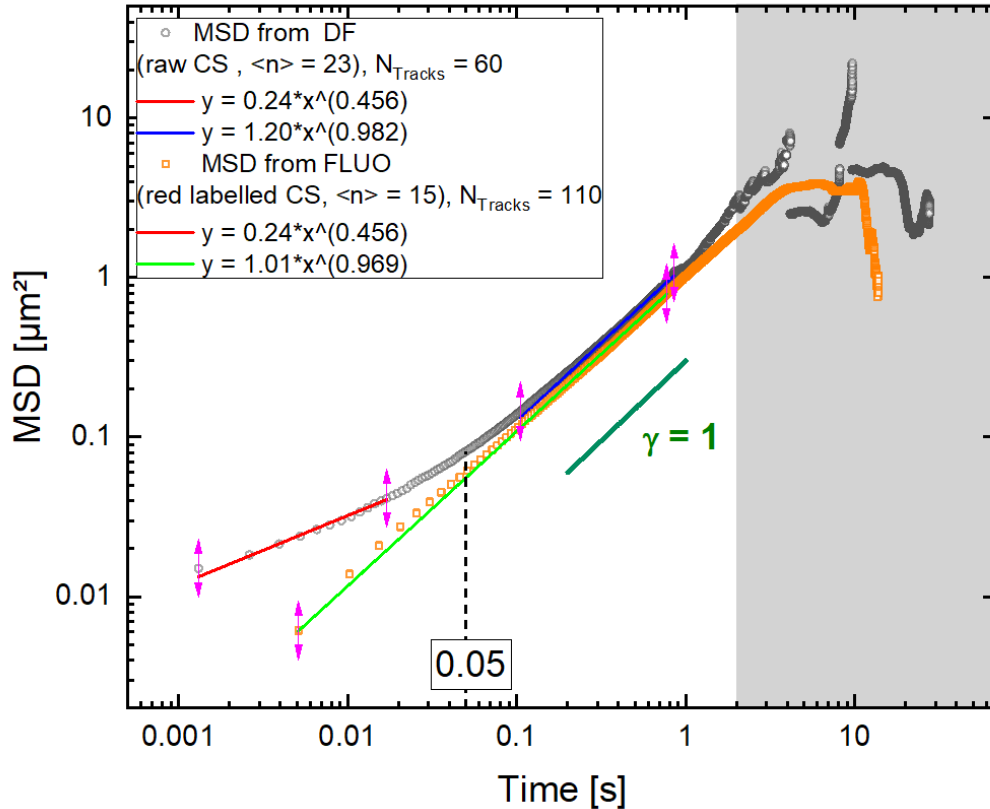


Figure 6.8: **MSD of colloidal star particles in the dilute regime.** The MSD obtained from the fluorescence (FLUO) observation for $OD = 0.03$, recorded at 196 fps, exhibits a single diffusive regime, from which we obtain $D_T = 0.25 \mu\text{m}^2/\text{s}$. From the dark-field measurements (DF) of $OD = 0.05$ at 762 fps, we find two regimes: one subdiffusive at short times, i.e., $\gamma \sim 0.5$ and one diffusive regime at longer times, i.e., $\gamma \sim 1$. The cross over time of these regimes is found at $\tau = 50 \text{ ms}^{-1}$. From the diffusive regime we obtain a translational diffusion coefficient of $D_T = 0.30 \mu\text{m}^2/\text{s}$. The gray region indicates the time for which the statistical noise is high for a proper determination of the MSD.

In chapter 4, we have shown that the Au NPs have an extra degree of freedom related to the flexible link at the virus tip to which we are sensitive by probing only the Au NPs involved in the hybrid structures. Here, we consider that the measured differences between the FLUO and DF observations, for which different components of the structure are probed, have the same origin. Thus, we have also studied the diffusion of the CS by dynamic light scattering (DLS). The intensity correlation function of a dilute suspension of CS at $OD = 0.05$ has been measured in the range of angles $30^\circ < \theta < 150^\circ$ and running time of 20 minutes.

Similarly to our observations in the matchstick-like structures of chapter 4, the scattering signal of the CS is mainly coming from the bead in their core. Hence, we have simultaneously fit our experimental data with the spring bead model of section 4.3.1, i.e., equation 4.8 with fixed parameters: $D_T = 0.25 \mu\text{m}^2/\text{s}$ and $D_R = 0.26 \text{ s}^{-1}$, corresponding to the diffusion obtained

via FLUO observations and the rotational one of the equivalent sphere according to equation 1.1 respectively.

The free parameter β is shown as function of the angle in figure 6.9(b). As global parameters, we find $A = 0.54$, $\langle r^2 \rangle = 4.3 \pm 0.1 \times 10^{-3} \mu\text{m}^2$ and $\lambda = 0.12 \pm 0.01 \text{ ms}^{-1}$. From these parameters, we obtain a root mean square displacement, $rmsd = 66 \text{ nm}$ which is compatible with our observations for matchstick-like structures and with the characteristic length obtained by single particle tracking. Moreover, using equations 4.6 and 4.7, we obtain a $\kappa = 232 k_B T / \mu\text{m}^2$ and a friction coefficient $\gamma = 1.9 k_B T \text{ s} / \mu\text{m}^2$ which is related to the effective diffusion of the bead $D_T^{\text{eff}} = k_B T / \gamma = 0.5 \mu\text{m}^2 / \text{s}$ which is self-consistent with the model. Note that the spring constant is similar to the one found for matchstick-like particles (see figure 4.18) which is in agreement with the fact that the flexibility is due to the p3 proteins of the viruses. However, the friction coefficient is of about one order of magnitude higher than the one found for matchstick-like particles: $\gamma = 0.28 k_B T \text{ s} / \mu\text{m}^2$. This difference can be interpreted as the friction mostly originates from the presence of viruses and it is proportional to the factor given by the valency of our CS, i.e., ~ 20 .

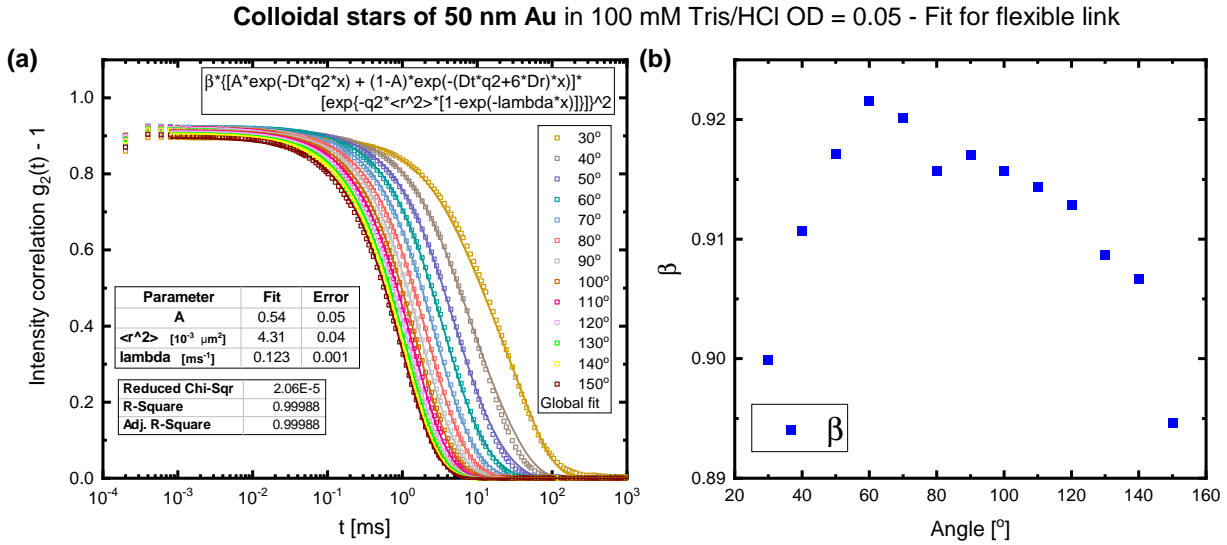


Figure 6.9: **Spring-bead model of colloidal stars.** (a) The intensity correlation function in the range of angles $35^\circ < \theta < 150^\circ$ is analyzed for fixed $D_T = 0.25 \mu\text{m}^2 / \text{s}$ and $D_R = 0.26 \text{ s}^{-1}$ corresponding to the translational and rotational diffusion coefficients obtained from the FLUO observations. The global parameters correspond to $\langle r^2 \rangle = 4.3 \pm 0.1 \times 10^{-3} \mu\text{m}^2$ and $\lambda = 0.12 \pm 0.01 \text{ ms}$. (b) The free parameter β is plotted as function of the scattering angle θ .

From these results, we conclude that when we probe the bead of the CS particles, the diffusion is also influenced by the flexibility at the virus tips and it is related to the number of viral arms forming the structure. The comparison between single particle tracking and dynamic light scattering evidence that the observations by DF microscopy are a most direct method to study the dynamics and internal degree of freedom of the Au NPs without the need of a model or input information about the system such as the case of DLS.

6.2.2 Dense regime

In order to investigate the diffusion and structure of the colloidal stars when the particle concentration is increased, we have centrifuged $\sim 500 \mu\text{l}$ of a suspension at initial $OD = 5.2$ in a 2 cm height Eppendorf tube for 2.5 hours and 2 500 g. These conditions have been chosen to carefully sediment the structures so they can be easily redispersed. After the centrifugation steps, the OD has been measured and the typical distance between particles estimated using equations 6.3 and 6.4. Lower concentrations have been reached by diluting with buffer the concentrated suspension.

We have studied the dynamics of suspensions of CS in the different regimes by DF microscopy for which we are able to track the center of mass of the structure located at the Au NPs core. For this purpose, the MSD has been calculated for the traces extracted from movies recorded at a frame rate of 762 fps. In figure 6.10 are shown DF images of suspensions at $OD = 1.2$, which is in the dilute regime, $OD = 10.7$, which is below the lower limit of the dense regime ($OD = 17$), and $OD = 122$, which is close to the high limit to the dense ($OD = 136.7$). In order to obtain the particle's positions, we have fixed the detection parameters in such a way that we only track the particles in focus, i.e., the ones whose shape is small and have high scattering signal.

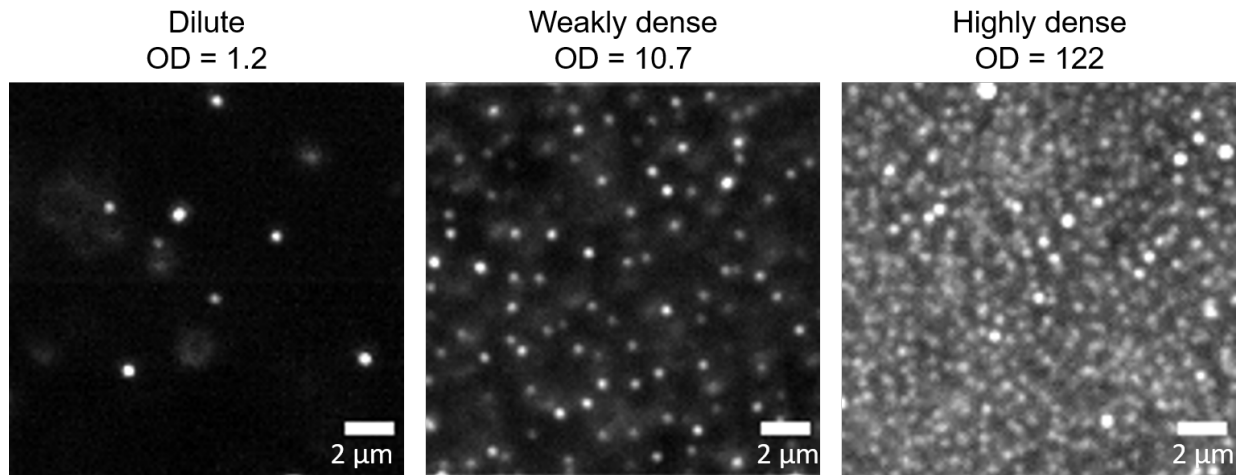


Figure 6.10: **Dark-field observations of colloidal stars at different regimes.** Using this technique, only the gold core at the center of the colloidal star structure are observed. As the particle concentration increases, a local ordering stars to appear.

In figure 6.11 are shown for the $OD = 122$, bright field (BF) and Differential Interference Contrastⁱⁱ (DIC) microscopy images at different magnifications. Note that for 100x magnification in the BF and DIC observations we are able to visualize the particle positions with some local organization. In order to have a better understanding of the overall behavior of the system, we have observed them at lower magnification. In the DIC image at 40x, we find a “layered” texture.

ⁱⁱDifferential interference contrast microscopy is a technique which enhances the contrast at interfaces between two regions of weak spatial variation of the refractive index [204].

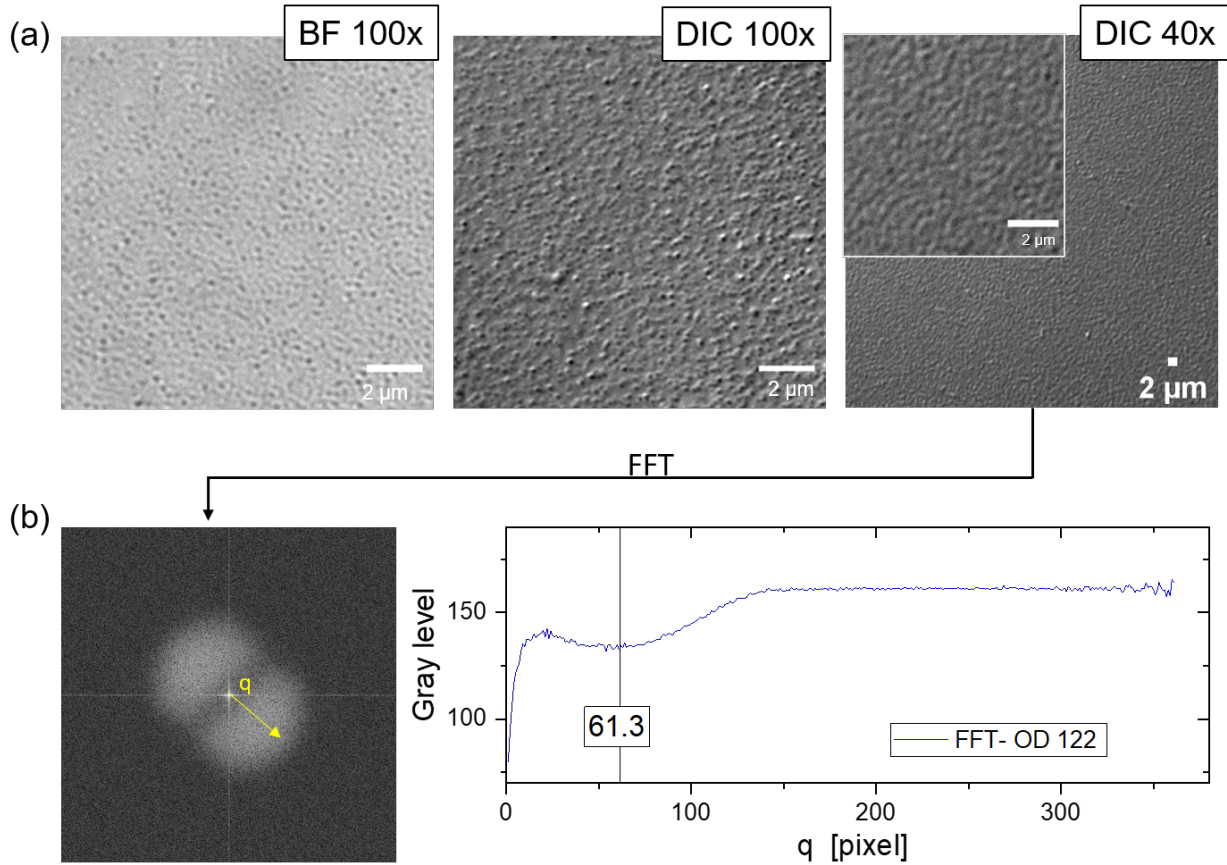


Figure 6.11: **Structure of colloidal stars at $OD = 122$.** (a) For the high magnification we only observe the position of the center of the particles. However, in a lower magnification we get a better picture of the global organization for which a layering texture is observed. (b) The Fast Fourier Transform (FFT) exhibits a maximum of intensity. This is translated to a typical distance of about $1.1 \mu\text{m}$ within the layers.

We have estimated the layer spacing from the Fast Fourier Transformⁱⁱⁱ (FFT) of the DIC image at magnification 40x using ImageJ software. As shown in figure 6.11 for a FFT image of size 512 pixels we find a broad intensity region in q which corresponds to the characteristic distance of the system. The radial integral of intensity shows a minimum at 61.3 pixels from the center. This value is related to the distance x in the real space by:

$$x = \frac{2n \times \text{FFT}(\text{size}) \times \text{Pixel size}}{q} \quad (6.5)$$

with n the binning, $\text{FFT}(\text{size})$ is the size of the FFT image. For a binning 1 and Pixel size = $0.065 \mu\text{m}$, we find that the typical distance between layers is $1.1 \mu\text{m}$ corresponding to the virus length scale. This evidence the local ordering of the structures at high OD.

From the DF videos, we have obtained the MSD for different concentrations. These are shown in figure 6.12. At long times, the MSD exhibits a diffusion exponent γ which is related to the diffusion rate D while at short times we find γ_2 related to the second diffusion rate

ⁱⁱⁱThe Fast Fourier Transform is an algorithm that computes the discrete Fourier transform to convert a signal from the real space to the reciprocal space [205].

D_2 . Note that as the OD increases the statistical noise at long times decreases as we loose less and less particles during the tracking.

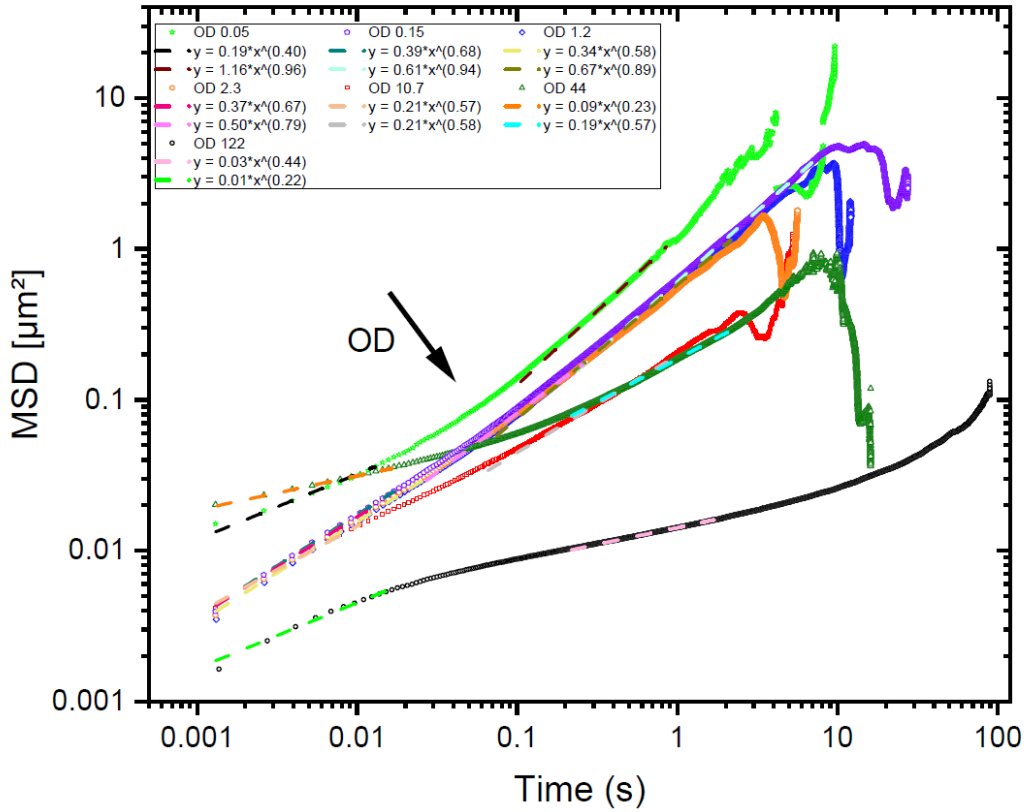


Figure 6.12: **MSD of colloidal star suspensions at different OD.** For a frame rate of 762 fps, all the curves exhibit two regimes. The diffusion rate and exponent D and γ_2 decreases as the OD increases. Moreover, for high OD the statistical noise is lower due to the ability to track longer trajectories of particles with slow diffusion.

In figure 6.13, we have collected the diffusion exponent and diffusion rates found for the two regimes. As shown in the figure 6.13(a), only above a core-to-core distance of $\sim 7 \mu\text{m}$, i.e., below $OD = 0.3$, the particles move in a diffusive regime of $\gamma \sim 1$. For higher OD , the diffusion rate and exponent decrease progressively into a state of limited motion. This, combined with the DIC observations suggest that at the $OD = 122$ we have a jammed state.

Note from figure 6.13(b), that at short times, γ_2 and D_2 , remain around the same value in the dilute regime and only decrease in the dense one. We believe that γ_2 and D_2 are related to the flexibility of the gold-virus links. The fact that these decrease only when $R_a < 2 \mu\text{m}$ is in agreement with the expected interdigitation of viral arms after which their reorientation and hence their diffusion is limited.

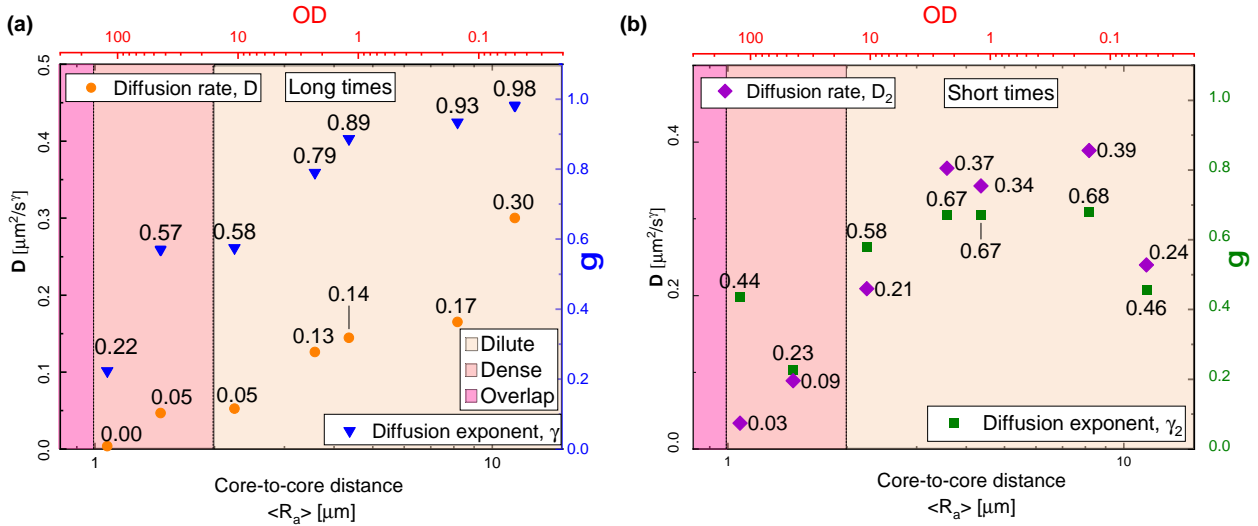


Figure 6.13: **Summary of diffusion rate and exponent for different OD.** At long times (a) γ and D and at short times (b) γ_2 and D_2 , are obtained from the MSD calculated for approximately 50 to 110 trajectories.

6.2.2.1 Self-organization induced by depletion attraction

In order to induce the self-organization of the colloidal stars, we have promoted their effective attraction by depletion using Dextran (Dex) and Polyethylene glycol (PEG/PEO) polymers of different molecular weights. For the PEG, whose radius of gyration is given by $R_g^{\text{PEG}} = 0.0215M_w^{0.583}$ [206], three different ones have been used: the PEG8k, PEG35k and PEO100k of $R_g = 4.0$ nm, 9.6 nm and 17.7 nm respectively. For the Dextran polymer whose radius of gyration is given by $R_g^{\text{Dex}} = 0.0215M_w^{0.583}$ [207], we have worked with Dex150k and Dex500k of $R_g = 10.9$ nm and 19.7 nm respectively. Note that the ranges of R_g partially matches between the two polymers. For polymers of about the same size, we expect to obtain a similar range of depletion interaction.

Stocks solutions of polymer in $I = 110$ mM Tris/HCl buffers have been prepared before adding it to the suspensions of CS containing 3 to 5 red labeled viral arms of the total valency of $\langle n \rangle = 23$ for their observation via optical microscopy.

In figure 6.14 are summarized the initial conditions explored for the different PEG/PEO polymers. For the three sizes, we have observed by DIC the self-assembly of colloidal stars into fiber-like structures which kinetics increases with by the CS concentration. For instance, at low concentrations the fiber structures are formed after a few days while at high concentrations they self-organize immediately after adding the polymer. As shown in figure 6.15, for the PEG8k the fibers are mostly single chains which, thanks to free arms that are not involved in the main chain, could form branches. For the PEG35k and PEO100k which induce a higher depletion range due to their bigger size, the fibers are mostly composed by multiple chains made of more than one Au NPs per layer (see scheme in figure 6.15).

In figure 6.17 are shown color DIC images of the fiber-like structures. Note that either for single or multiple chains, a pinkish color is highlighted at their nodes. These observations

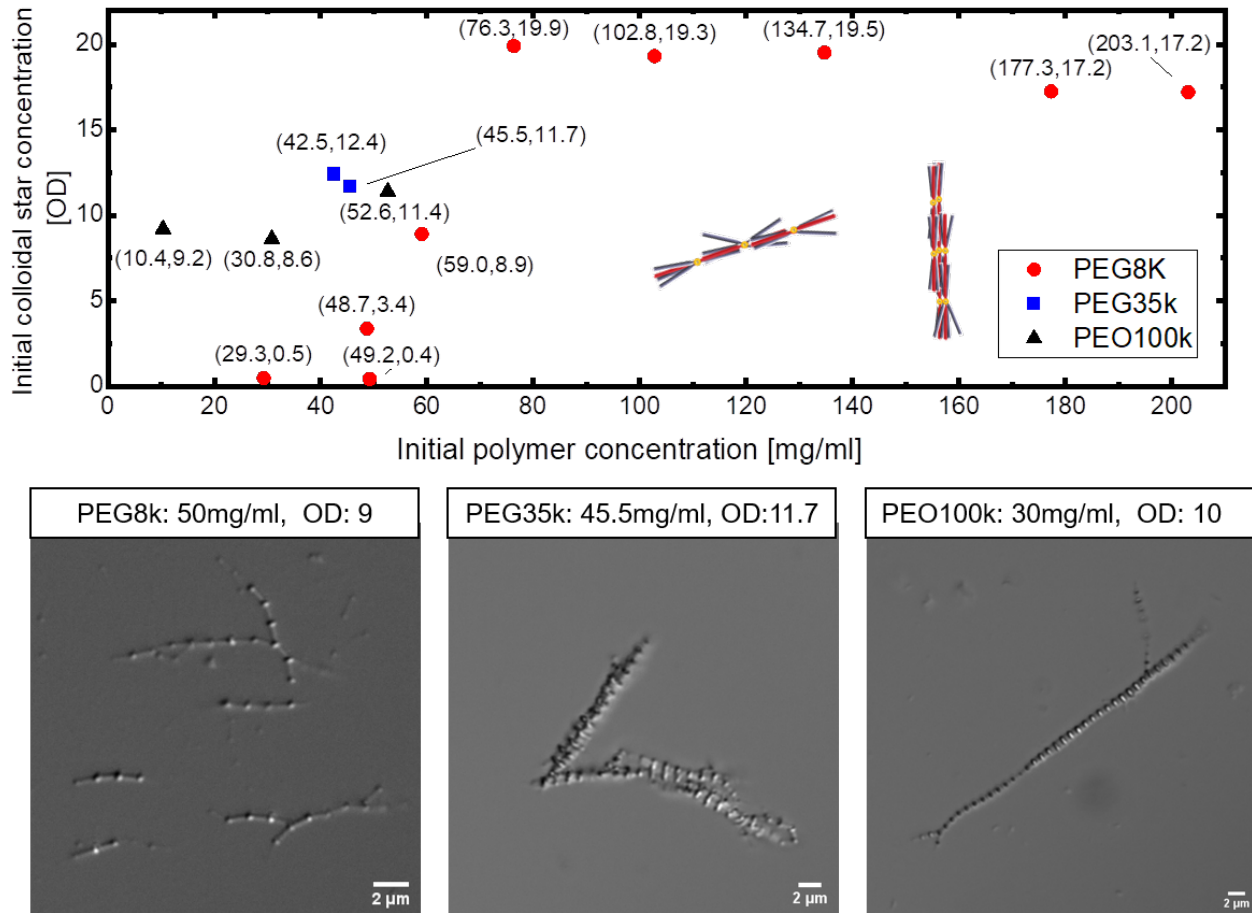


Figure 6.14: **Phase diagram as a function of the initial, i.e., just after mixing, colloidal stars and PEG/PEO concentrations.** For the three different sizes of PEG/PEO, i.e., $R_g = 4.0$ nm for $M_w = 8$ kDa, $R_g = 9.6$ nm for $M_w = 35$ kDa and $R_g = 17.7$ nm for $M_w = 100$ kDa, and independently of the CS concentration, we observe the formation of fiber-like structures. These are composed by single or multiple chains.

confirm that the nodes are made of Au NPs since it corresponds to their typical color in suspension. Using ImageJ software, we have estimated the distance between the Au NP layers by measuring the gray level for a given number of layers. The typical layer distance, as shown in figure 6.17(b), is obtained from the separation between two intensity minima. On average, we have found that the Au NPs are spaced by $1.0 \mu\text{m}$. This means that the local concentration of structures is in the dense regime for which there is interdigitation. Moreover, that the typical distance corresponds to the virus contour length indicates that they possess a lamellar or smectic order.

In order to investigate the organization of viruses within a fiber, we have compared images obtained using bright field (BF), dark-field (DF), differential interference contrast (DIC) and fluorescence (FLUO) microscopy. Example of these are shown in figure 6.16.

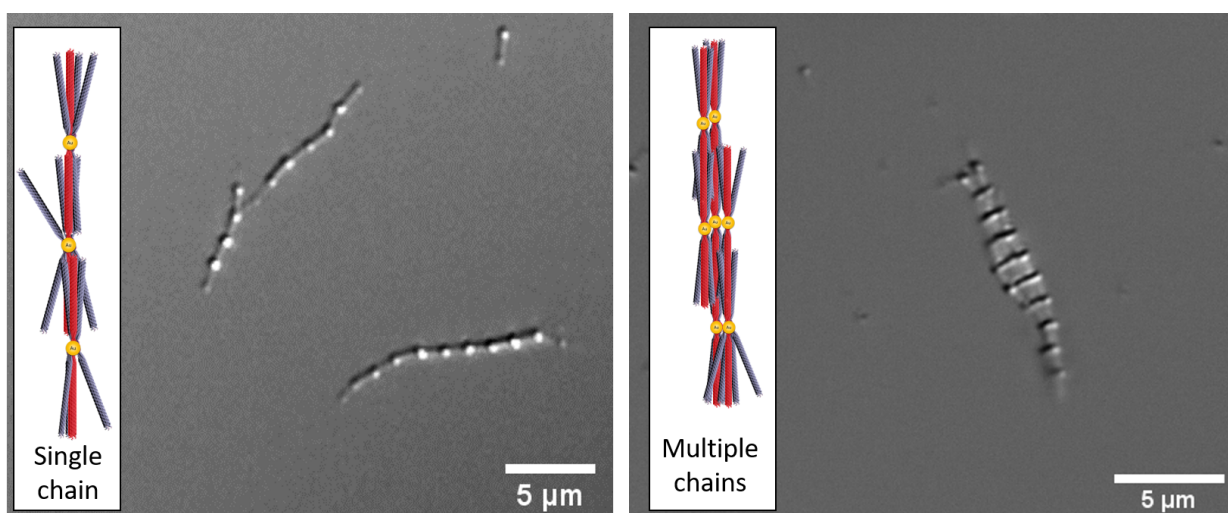


Figure 6.15: **Self-organization of colloidal stars into fiber-like structures.** **Left:** When PEG8k is added to a suspension of colloidal stars they mostly organized in single chains which can have branches. **Right:** For the PEG35k and PEO100k multiple chains share viruses from different colloidal stars.

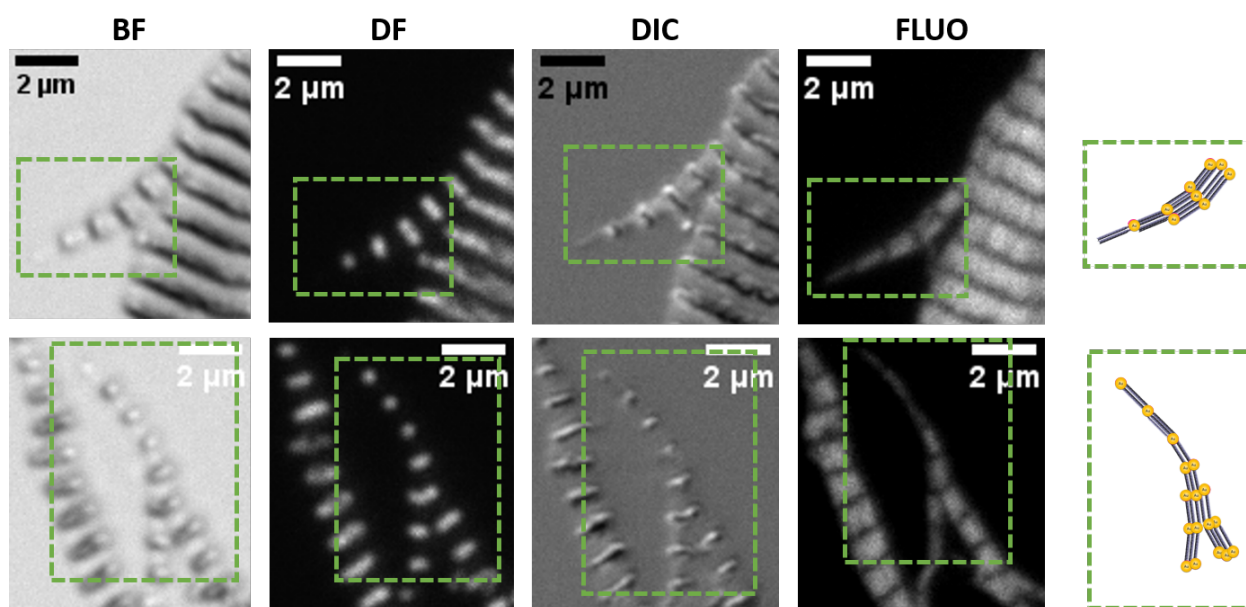


Figure 6.16: **Optical microscopy observations of fiber-like structures.** From left to right are shown bright field (BF), dark-field (DF), differential interference contrast (DIC) and fluorescence (FLUO) microscopy images of the same structure. Viruses from multiple stars organize into bundles perpendicularly aligned with respect to the layer of gold beads. Moreover, the beads seem very close to each other but not necessarily aggregated.

From the FLUO images, we have observed that viruses belonging to different colloidal stars are brought together into multiple thick bundles perpendicularly aligned to the Au NPs layer. As shown in the DF images, we can differentiate two or three separated beads in a layer, however, beads that are placed at a distance below the resolution of our microscope (~ 250 nm) look like a single bigger bead. We expect that the viruses grafted at the surface of the gold act as stabilizer so, as shown in figure 6.18, there is space between the beads of

a layer. For a better understanding of the Au NPs layer organization, Small-angle X-ray scattering (SAXS) experiments are suggested.

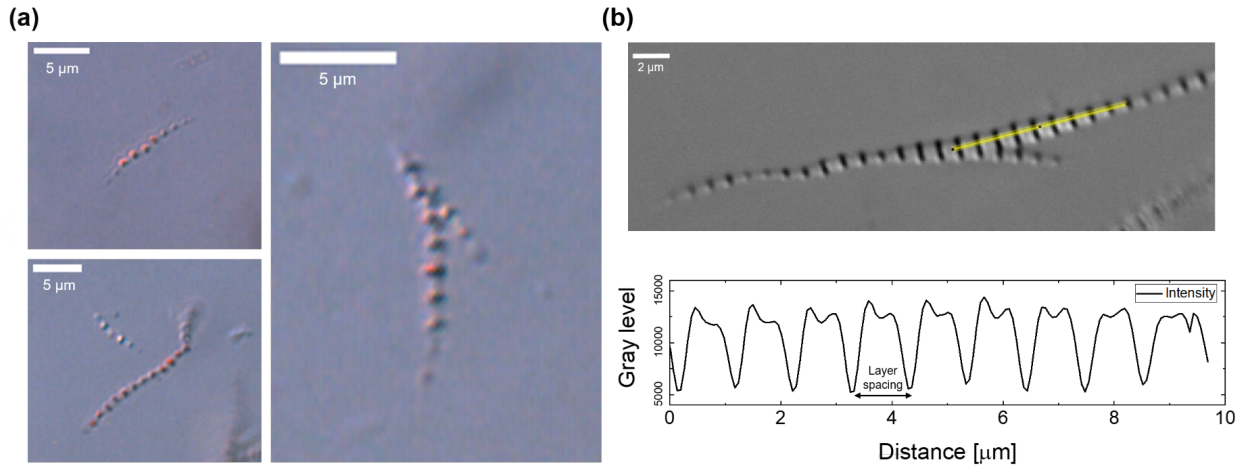


Figure 6.17: **Fiber-like structures.** (a) Color differential interference contrast (DIC) microscopy images of structures taken for a suspension prepared with PEG8k. The pinkish color comes from the absorption of gold nanoparticles. (b) The distance between the gold layers of a chain is obtained from the gray level of the DIC image. For a total of 9 layers we have measured a distance of $9.03 \mu\text{m}$ indicating that the layer spacing corresponds to $1.0 \mu\text{m}$.

As final step, we have tried to promote the organization of morphologies using Dextran polymer of different sizes. For this purpose, we have mixed CS suspensions with Dex150k and Dex500k whose radius of gyration are close to the ones of PEG35k and PEO100k respectively.

In figure 6.19 are summarized the different conditions prepared and observed by DIC microscopy. For all the suspensions, we have followed the evolution for weeks and not found the formation of any structures. However, we have observed the deposition of CS at the glass surface which could be related to an extra effect of depletion induced by the walls.

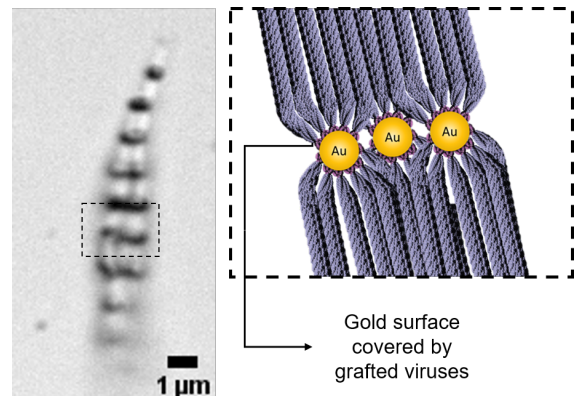


Figure 6.18: Bright field image of a fiber-like structure (left) and sketch of the expected Au NPs layer within it (right).

Considering that the range of depletion interaction is about the same order of magnitude due to the similarities in R_g for PEG and Dextran, we have expected that the self-organization results in similar fiber-like structures. However, we find that the chemical nature of the polymer influences the self-organization of our structures. Such behavior has not been so far seen for virus-based self-assemblies [200, 202, 208] at a fixed molecular weight. Thus, this effect could be associated with some polymer adsorption at the Au surface and certainly needs further investigation.

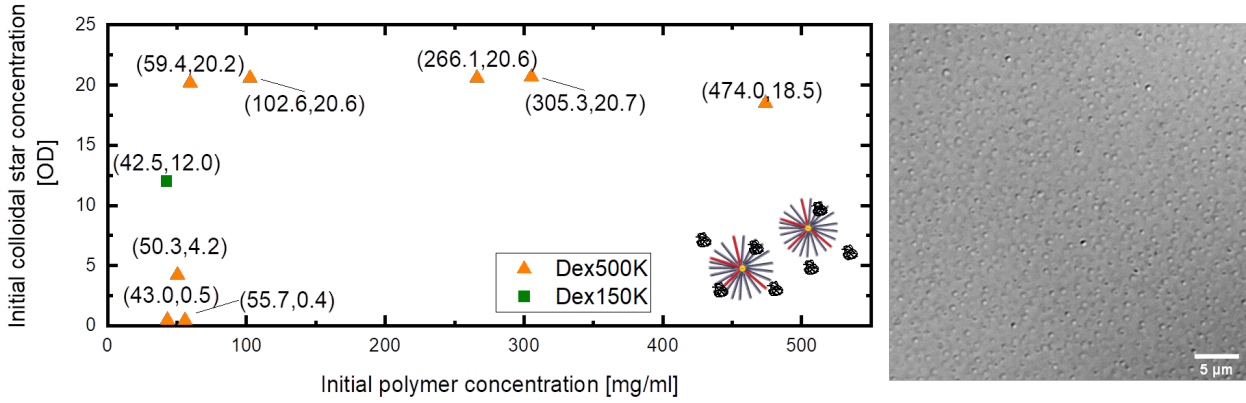


Figure 6.19: **Phase diagram as a function of the colloidal stars and Dextran concentrations.** For the different sizes of Dextran, i.e., $R_g = 10.9$ nm for $M_w = 150$ kDa and $R_g = 19.7$ for $M_w = 500$ kDa, (left) the structures do not exhibit any self-organization but only are deposited on the glass surface (right).

6.3 Discussion and conclusions

In this chapter we have investigated the dynamics and self-organization of colloidal star particles made of a single Au NP core and multiple viral arms in the dilute and dense regimes defined as a function of the core-to-core distance.

Thanks to the high scattering signal of the 51 nm Au NP at the core of the structure we are able to study their diffusion either by DLS in the dilute regime or by dark-field in both dilute or dense regimes. Moreover, thanks to the possibility to label the viral arms we also have observed them by fluorescence microscopy.

In the dilute regime, we have calculated by single particle tracking (SPT) the MSD in similar conditions using FLUO and DF microscopy. Our findings show that, similarly to the matchstick-like particles in chapter 4, we have evidenced some positional internal degree of freedom due to the virus tip flexibility. This is related to a subdiffusive regime ($\gamma < 1$) at short times in the MSD determined by DF. Moreover, the spring-bead model, shows to be adequate to fit the intensity correlation function obtained by DLS of the CS particles. From a practical point of view, we have found that the SPT using DF microscopy is the most direct way to study the CS dynamics since all the information can be extracted from the MSD calculation whereas in DLS there is the need of *a priori* knowledge of the system as well as of a proper model to interpret the intensity correlation function.

We have compared the diffusion exponent, γ , and diffusion rate, D , of the colloidal stars as function of the particle concentration. Our findings show that the dynamics of the structures is frozen in the dense regime suggesting the formation of a jammed state. Moreover, we also observe a decrease in the diffusion exponent γ_2 , related to the gold-virus link flexibility, when the core-to-core distance is below the sphere's diameter, i.e., $R_a < 2 \mu\text{m}$ which is consistent with the fact that the viral arms start to interdigitate.

Finally, we have explored as well the self-assembly of colloidal stars induced by depletion

using PEG/PEO and Dextran polymers. We have compared the influence in the type of polymer. Our results showed for PEG/PEO that the colloidal stars mostly organize in smectic-like fiber structures which could be conformed by single or multiple chains whose nodes are Au NPs beads spaced by one virus length. However, for Dextran of comparable size, our colloidal stars do not self-organize but only decorate the glass surfaces showing that the chemical nature of polymer has an influence in the resulting morphologies.

Chapter 7

General conclusions and perspectives

In this thesis we have studied different hybrid colloidal particles. These materials might acquire enhanced properties from the assets of its components as well as from their self-organization. Thanks to the rich optical properties of metal nanoparticles and to the versatility of bacteriophages to be genetically modified, we have chosen spherical gold nanoparticles (Au NPs) and rod-shaped viruses as building blocks of original hybrid structures. The optimized production and assembly of these colloids is of particular interest for their applications in different fields such as photonics [15], biomedicine [157] and nanotechnology [17]. For this purpose, we have investigated novel routes for the fabrication of specific morphologies as well as their dynamical and structural properties.

We have started in chapter 2 by exploring the genetic modification of M13 phages for the construction of hybrid colloidal particles. It has been shown, that these filamentous bacteriophages could be modified at their p3 tip proteins to display cysteine groups allowing for their binding to metal nanoparticles [55]. For example, the M13C7C mutant which possesses 13 amino acids inserted before its terminal amine (7 of them flanked by two cysteines) form disulfide bridges (Cys-Cys) which interact via a weak covalent bond with noble metals. This single tip modification has been successfully used to produce matchstick-like particles, diblock structures and colloidal star “molecules” [26]. However, the construction of more complex morphologies is limited by the single point of gold-virus interaction. To overcome this limitation, we have genetically modified the p7 proteins at the second virus tip with the same binding principle.

Our new mutants, M13s(*CgbpC*)₂ and M13l(*CgbpC*)₂ display a gold peptide between two cysteine groups at both virus tips. Since the p7 proteins are not as exposed as the p3 ones [42], a spacer has been encoded at the p7 proteins end in order to make them more accessible for interaction with gold. Their binding affinity has been tested by estimating the percentage of reacted tips with gold nanoparticles suspended in aqueous solvent. Our results show that the spacer of the M13l(*CgbpC*)₂ mutant, whose charge and length modify the accessibility of the disulfide bridges, promotes more efficiently their interaction with gold. However, in comparison with the p3 proteins it is necessary to strongly screen the electrostatic repulsion

of the gold and virus particles in order to promote their interaction. This indicates that the spacer and/or the encoded peptide could still be optimized. In a short time perspective, the spacer used to make the cysteine groups more exposed could be modified for example with higher negative charge which might result in the repulsion between proteins making them more “open” and then more exposed to the solvent. Moreover, a longer peptide containing two pairs of cysteine groups could also increase the probability of interaction with gold nanoparticles at that virus tip.

Thanks to this double tip binding ability of our new mutants, we have been able to produce a novel gold-virus colloid, the *dumbbell-like* structure made by a single virus with one bead attached to each tip. As a midterm perspective, one could explore the formation of liquid crystalline phases in suspensions of this structure increasing their concentration. In order to avoid aggregation of the nanoparticles at high concentrations, the PEGylation, i.e. the grafting of polymer Polyethylene glycol (PEG), could be performed at the gold surface.

As next step, we have studied the dynamical and structural properties of two of our hybrid colloids: the *matchstick-like* and *colloidal star particles*. An overview of the experimental techniques and principles involved for their characterization is described in chapter 3.

In chapter 4, the matchstick-like structure, composed by a single gold nanoparticle attached to a virus by one tip, has been studied by Dynamic Light Scattering (DLS). Thanks to the scattering signal of the Au NPs which prevails over the one of the viruses, we are able to study their self-diffusion by only probing the bead at the virus tip. We have investigated the influence of the nanoparticle size used to produce these structures and shown that the matchstick-like particles’ diffusion is independent of this parameter. However, we find a higher apparent diffusion coefficient than the one obtained by single particle tracking probing the virus in the structure. Thus, we have developed a spring-bead model to interpret our scattering signal. This model represents an extra degree of freedom on the bead’s diffusion given by its link with the p3 proteins which have been shown to be flexible [82]. The parameters obtained using this model are compatible with the length scale of the proteins proving that the higher diffusion measured when we probe the bead is a result of the tip flexibility.

Future investigations on this structure by means of optical microscopy techniques are recommended in order to corroborate our findings and predict the effect of flexibility for instance, when more than one virus is attached to a single nanoparticle (as in diblocks or colloidal stars). For such studies, fluorescence and dark field microscopy could be used for probing the virus and Au NPs components respectively. This could allow for the direct comparison on the diffusion of each element.

Thanks to our progress in the genetic modifications at the p7 tip proteins (distal end) we could also estimate by the same means their flexibility or rigidity. These proteins are not as exposed to the solvent as the p3 tip proteins (proximal end). Thus, an interesting

mid-term perspective is to study a monodisperse suspension of dumbbell-like structures using DLS and optical microscopy. Moreover, one could also develop a mutant which only binds Au NPs by the distal end for the fabrication of matchstick-like structures or diblocks to estimate their flexibility.

After the characterization on the Brownian dynamics of the matchstick like structure, we have explored the possibility to induce its self-propulsion or active motion. We describe in chapter 5 our investigation in the thermophoresis of this structure. When Au NPs are irradiated at the plasmonic resonance, their light absorption and heat release generate a decrease of viscosity and increase of temperature resulting in an enhanced diffusion. We have used this phenomenon, known as Hot Brownian motion (HBM) [171], as a possible propulsion mechanism for nanoparticles. Hence, we have implemented a green laser beam as light source and as probe beam of our DLS setup. Our observations on the matchstick-like structure as well as on hybrid Janus gold-silica nanoparticles show that the structures exhibit a significant increase of diffusion. However, this increase cannot be accounted by the temperature change predicted by the HBM theory for such nanoparticle size. Comparing our observations with spherical Au NPs and core-shell gold-silica NPs, we conclude that the increase of diffusion is due to convective effects. The creation of convection is expected on thick samples due to local heating up around the beam path or thermal-lensing effects [186, 187]. Hence, as short term perspective we suggest reducing the sample thickness for example to an optical microscopy cell. For this purpose, a specific setup has to be built. By means of an objective lens, the laser cross-section could be significantly reduced allowing the possibility to induce a higher change of temperature to the Au NPs. However, focusing a laser beam could generate an optical trapping effects [188]. Thus, the conditions to create an optical trap, given by the nanoparticle size, incoming power and beam waist [188] have to be balanced with the ones of the HBM theory (see equations 5.11, 5.12 and 5.19).

We have also tested other methods to induce the active motion of our matchstick-like structures by the decomposition of chemical fuels like hydrogen peroxide or glucose. To do so, we have attempted to graft thiol-functionalized enzymes (catalase and glucose oxidase) to the free gold nanoparticle surface of the hybrid particles. However, different complications have been faced. On one hand, the competition of the thiol groups and the weak covalent bonds of the gold-virus link have compromised the stability of the structure, i.e., they dissociate when the enzyme is in a big excess. On the other hand, chemical fuels such as hydrogen peroxide are oxidant agents which have destroyed the structures after a short period of time of adding the fuel to the sample. In a middle-term perceptive, we suggest to use for example already active Janus particles to produce matchstick-like structures and test their self-propulsion. We expect that the added viral “tail”, which decreases drastically the rotational diffusion of the hybrid structure, could promote their motion in an oriented direction for longer time.

In the last chapter, we have used the colloidal star “molecules” as model system of soft colloidal spheres and investigated their dynamics and self-organization in dense regimes. First, we have briefly explored their phase behavior as the particle concentration increases. The diffusion rate of the particles have been estimated by single particle tracking in dilute regime and dense regimes for which the viral arms start to interdigitate. Our results suggest the formation of a glassy state in the dense regime. We have also explored the possibility to induce the self-assembly of these structures by depletion. We have observed the formation of single chains and fiber-like structures which we have proven to result from the assembly of viral arms from different colloidal star molecules separated by beads. A short term perspective is to investigate the structural organization of the states found in the dense regime for example by X-ray diffraction. Once these colloidal glassy/crystal states are characterized, they might be used as templates for photonics sensor devices [15].

As a long time perspective of this work, one could use the double tip modified mutants to create oligomeric chains made of repeating gold-virus units, which could work as templates for nanowires [50], or for the construction of three-dimensional lattices structures with different symmetries which could have applications in photonics as resonators [15] (see figure 7.1).

Moreover, one could use the investigations done on the light and fuels response of these hybrid colloids for the fabrications of smart materials. For example a reconfigurable lattice structure which might change its optical or physical properties due to an external light or temperature stimulus.

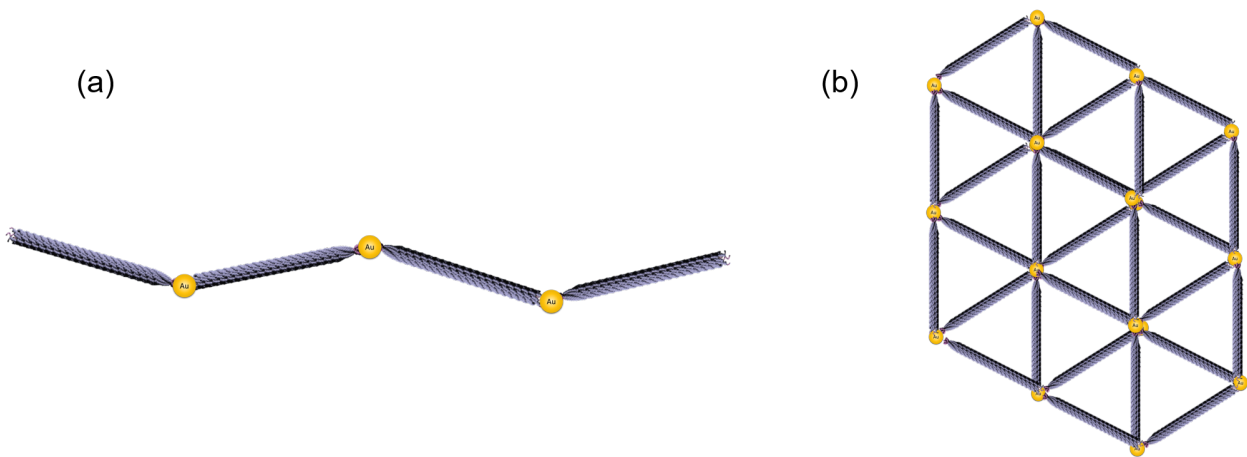


Figure 7.1: **Schematic representation of structures composed by double tip bound viruses.** (a) Oligomeric chain. (b) Lattice structure.

References

- [1] T. Graham, “X. Liquid diffusion applied to analysis,” *Philosophical Transactions of the Royal Society of London*, vol. 151, pp. 183–224, 1861.
- [2] W. C. Poon, “Colloidal suspensions,” in *The Oxford Handbook of Soft Condensed Matter*, 2012.
- [3] G. Avvisati, *Phase behaviour of colloidal molecules with anisotropic interactions*. PhD thesis, University Utrecht, 2017.
- [4] R. Brown, “XXVII. A brief account of microscopical observations made in the months of June, July and August 1827, on the particles contained in the pollen of plants; and on the general existence of active molecules in organic and inorganic bodies,” *The philosophical magazine*, vol. 4, no. 21, pp. 161–173, 1828.
- [5] A. Einstein, “Über die von der molekularkinetischen Theorie der Wärme geforderte Bewegung von in ruhenden Flüssigkeiten suspendierten Teilchen,” *Annalen der Physik*, vol. 322, no. 8, pp. 549–560, 1905.
- [6] J. Perrin, “Mouvement Brownien et réalité moléculaire,” *Annales de chimie et de Physique*, vol. 18, no. 8, pp. 5–114, 1909.
- [7] A. Yethiraj, “Tunable colloids: Control of colloidal phase transitions with tunable interactions,” *Soft Matter*, vol. 3, no. 9, pp. 1099–1115, 2007.
- [8] G. L. Hunter and E. R. Weeks, “The physics of the colloidal glass transition,” *Reports on progress in physics*, vol. 75, no. 6, p. 066501, 2012.
- [9] A. Kuijk, D. V. Byelov, A. V. Petukhov, A. Van Blaaderen, and A. Imhof, “Phase behavior of colloidal silica rods,” *Faraday discussions*, vol. 159, no. 1, pp. 181–199, 2012.
- [10] H. Maeda and Y. Maeda, “Liquid crystal formation in suspensions of hard rodlike colloidal particles: Direct observation of particle arrangement and self-ordering behavior,” *Phys. Rev. Lett.*, vol. 90, no. 1, p. 018303, 2003.

- [11] C. Fernández-Rico, T. Yanagishima, A. Curran, D. G. Aarts, and R. P. Dullens, “Synthesis of colloidal SU-8 polymer rods using sonication,” *Advanced Materials*, vol. 31, no. 17, p. 1807514, 2019.
- [12] E. Grelet, “Hexagonal order in crystalline and columnar phases of hard rods,” *Phys. Rev. Lett.*, vol. 100, p. 168301, 2008.
- [13] Z. Zhang and E. Grelet, “Tuning chirality in the self-assembly of rod-like viruses by chemical surface modifications,” *Soft Matter*, vol. 9, pp. 1015–1024, 2013.
- [14] Z. Dogic and S. Fraden, “Smectic phase in a colloidal suspension of semiflexible virus particles,” *Phys. Rev. Lett.*, vol. 78, no. 12, p. 2417, 1997.
- [15] J. Zhang, Z. Sun, and B. Yang, “Self-assembly of photonic crystals from polymer colloids,” *Current Opinion in Colloid & Interface Science*, vol. 14, no. 2, pp. 103–114, 2009.
- [16] A. La Porta, A. Sánchez-Iglesias, T. Altantzis, S. Bals, M. Grzelczak, and L. M. Liz-Marzán, “Multifunctional self-assembled composite colloids and their application to SERS detection,” *Nanoscale*, vol. 7, no. 23, pp. 10377–10381, 2015.
- [17] M. Liu, O. Voznyy, R. Sabatini, F. P. García de Arquer, R. Munir, A. H. Balawi, X. Lan, F. Fan, G. Walters, A. R. Kirmani, *et al.*, “Hybrid organic–inorganic inks flatten the energy landscape in colloidal quantum dot solids,” *Nature Materials*, vol. 16, no. 2, pp. 258–263, 2017.
- [18] M. H. Jazayeri, H. Amani, A. A. Pourfatollah, H. Pazoki-Toroudi, and B. Sedighimoghaddam, “Various methods of gold nanoparticles (GNPs) conjugation to antibodies,” *Sensing and bio-sensing research*, vol. 9, pp. 17–22, 2016.
- [19] R. Cao-Milán and L. M. Liz-Marzán, “Gold nanoparticle conjugates: Recent advances toward clinical applications,” *Expert opinion on drug delivery*, vol. 11, no. 5, pp. 741–752, 2014.
- [20] P. N. Njoki, I.-I. S. Lim, D. Mott, H.-Y. Park, B. Khan, S. Mishra, R. Sujakumar, J. Luo, and C.-J. Zhong, “Size correlation of optical and spectroscopic properties for gold nanoparticles,” *The Journal of Physical Chemistry C*, vol. 111, no. 40, pp. 14664–14669, 2007.
- [21] N. Sarfraz and I. Khan, “Plasmonic gold nanoparticles (AuNPs): Properties, synthesis and their advanced energy, environmental and biomedical applications,” *Chemistry–An Asian Journal*, vol. 16, no. 7, pp. 720–742, 2021.

- [22] K. Bolaños, M. J. Kogan, and E. Araya, "Capping gold nanoparticles with albumin to improve their biomedical properties," *International journal of nanomedicine*, vol. 14, p. 6387, 2019.
- [23] P. Huang, J. Lin, S. Wang, Z. Zhou, Z. Li, Z. Wang, C. Zhang, X. Yue, G. Niu, M. Yang, *et al.*, "Photosensitizer-conjugated silica-coated gold nanoclusters for fluorescence imaging-guided photodynamic therapy," *Biomaterials*, vol. 34, no. 19, pp. 4643–4654, 2013.
- [24] N. Uehara, "Polymer-functionalized gold nanoparticles as versatile sensing materials," *Analytical Sciences*, vol. 26, no. 12, pp. 1219–1228, 2010.
- [25] M. S. Strozyk, D. Jimenez-de Aberasturi, and L. M. Liz-Marzán, "Composite polymer colloids for SERS-based applications," *The Chemical Record*, vol. 18, no. 7-8, pp. 807–818, 2018.
- [26] A. de la Cotte, C. Wu, M. Trévisan, A. Repula, and E. Grelet, "Rod-like virus-based multiarm colloidal molecules," *ACS Nano*, vol. 11, no. 10, pp. 10616–10622, 2017.
- [27] Y. Lee, J. Kim, D. S. Yun, Y. S. Nam, Y. Shao-Horn, and A. M. Belcher, "Virus-templated Au and Au–Pt core–shell nanowires and their electrocatalytic activities for fuel cell applications," *Energy Environ. Sci.*, vol. 5, pp. 8328–8334, 2012.
- [28] S.-W. Lee, S. Lee, and A. Belcher, "Virus-based alignment of inorganic, organic, and biological nanosized materials," *Advanced Materials*, vol. 15, no. 9, pp. 689–692, 2003.
- [29] L. Jia, G. Zhao, W. Shi, N. Coombs, I. Gourevich, G. C. Walker, G. Guerin, I. Manners, and M. A. Winnik, "A design strategy for the hierarchical fabrication of colloidal hybrid mesostructures," *Nature Communications*, vol. 5, no. 1, pp. 1–8, 2014.
- [30] S. Merino, C. Martin, K. Kostarelos, M. Prato, and E. Vazquez, "Nanocomposite hydrogels: 3D polymer–nanoparticle synergies for on-demand drug delivery," *ACS nano*, vol. 9, no. 5, pp. 4686–4697, 2015.
- [31] R. K. Singh, K. D. Patel, J. H. Lee, E.-J. Lee, J.-H. Kim, T.-H. Kim, and H.-W. Kim, "Potential of magnetic nanofiber scaffolds with mechanical and biological properties applicable for bone regeneration," *PloS one*, vol. 9, no. 4, p. e91584, 2014.
- [32] S. Srivastava, D. Nykypanchuk, M. M. Maye, A. V. Tkachenko, and O. Gang, "Super-compressible DNA nanoparticle lattices," *Soft Matter*, vol. 9, pp. 10452–10457, 2013.
- [33] P. Horcajada, C. Serre, M. Vallet-Regí, M. Sebban, F. Taulelle, and G. Férey, "Metal–organic frameworks as efficient materials for drug delivery," *Angewandte Chemie International Edition*, vol. 45, no. 36, pp. 5974–5978, 2006.

- [34] Y. Yang, W. Zeng, P. Huang, X. Zeng, and L. Mei, "Smart materials for drug delivery and cancer therapy," *VIEW*, vol. 2, no. 2, p. 20200042, 2021.
- [35] E. C. Dreaden, L. A. Austin, M. A. Mackey, and M. A. El-Sayed, "Size matters: Gold nanoparticles in targeted cancer drug delivery," *Therapeutic delivery*, vol. 3, no. 4, pp. 457–478, 2012.
- [36] M. Karg, Y. Lu, E. Carbó-Argibay, I. Pastoriza-Santos, J. Pérez-Juste, L. M. Liz-Marzán, and T. Hellweg, "Multiresponsive Hybrid Colloids based on gold nanorods and Poly(NIPAM-co-allylactic acid) microgels. temperature- and pH-Tunable plasmon resonance," *Langmuir*, vol. 25, pp. 3163–3167, 2009.
- [37] D. Ghosh, Y. Lee, S. Thomas, A. G. Kohli, D. S. Yun, A. M. Belcher, and K. A. Kelly, "M13-templated magnetic nanoparticles for targeted in vivo imaging of prostate cancer," *Nature Nanotechnology*, vol. 7, no. 10, pp. 677–682, 2012.
- [38] K. J. Fowler, J. J. Brown, and V. R. Narra, "Magnetic resonance imaging of focal liver lesions: Approach to imaging diagnosis," *Hepatology*, vol. 54, no. 6, pp. 2227–2237, 2011.
- [39] T. A. Larson, J. Bankson, J. Aaron, and K. Sokolov, "Hybrid plasmonic magnetic nanoparticles as molecular specific agents for MRI/optical imaging and photothermal therapy of cancer cells," *Nanotechnology*, vol. 18, no. 32, p. 325101, 2007.
- [40] D. Oh, J. Qi, B. Han, G. Zhang, T. J. Carney, J. Ohmura, Y. Zhang, Y. Shao-Horn, and A. M. Belcher, "M13 virus-directed synthesis of nanostructured metal oxides for lithium–oxygen batteries," *Nano Lett.*, vol. 14, no. 8, pp. 4837–4845, 2014.
- [41] E. Pomerantseva, F. Bonaccorso, X. Feng, Y. Cui, and Y. Gogotsi, "Energy storage: The future enabled by nanomaterials," *Science*, vol. 366, no. 6468, p. eaan8285, 2019.
- [42] D. Marvin, M. Symmons, and S. Straus, "Structure and assembly of filamentous bacteriophages," *Progress in Biophysics and Molecular Biology*, vol. 114, no. 2, pp. 80–122, 2014.
- [43] R. Barderas and E. Benito-Peña, "The 2018 Nobel prize in chemistry: Phage display of peptides and antibodies.," *Anal. Bioanal. Chem.*, vol. 411, no. 12, pp. 2475–2479, 2019.
- [44] G. P. Smith, "Filamentous fusion phage: Novel expression vectors that display cloned antigens on the virion surface," *Science*, vol. 228, no. 4705, pp. 1315–1317, 1985.
- [45] M. A. Arap, "Phage display technology: Applications and innovations," *Genetics and Molecular Biology*, vol. 28, no. 1, pp. 1–9, 2005.

- [46] A. J. Bernal and W. G. Willats, "Plant science in the age of phage," *Trends in Plant Science*, vol. 9, no. 10, pp. 465–468, 2004.
- [47] G. P. Smith and V. A. Petrenko, "Phage display," *Chem. Rev.*, vol. 97, no. 2, p. 391–410, 1997.
- [48] Y. Huang, C.-Y. Chiang, S. K. Lee, Y. Gao, E. L. Hu, J. De-Yoreo, and A. M. Belcher, "Programmable assembly of nanoarchitectures using genetically engineered viruses," *Nano Lett.*, vol. 5, no. 7, p. 1429–1434, 2005.
- [49] K. T. Nam, B. R. Peelle, S.-W. Lee, and A. M. Belcher, "Genetically driven assembly of nanorings based on the M13 virus," *Nano Lett.*, vol. 4, no. 1, pp. 23–27, 2004.
- [50] C. Mao, C. E. Flynn, A. Hayhurst, R. Sweeney, J. Qi, G. Georgiou, B. Iverson, and A. M. Belcher, "Viral assembly of oriented quantum dot nanowires," *Proceedings of the National Academy of Sciences*, vol. 100, no. 12, pp. 6946–6951, 2003.
- [51] X. Cao, C. Tan, M. Sindoro, and H. Zhang, "Hybrid micro-/nano-structures derived from metal–organic frameworks: Preparation and applications in energy storage and conversion," *Chem. Soc. Rev.*, vol. 46, pp. 2660–2677, 2017.
- [52] G. T. Hess, J. J. Cragolini, M. W. Popp, M. A. Allen, S. K. Dougan, E. Spooner, H. L. Ploegh, A. M. Belcher, and C. P. Guimaraes, "M13 bacteriophage display framework that allows sortase-mediated modification of surface-accessible phage proteins," *Bioconjugate Chemistry*, vol. 23, no. 7, pp. 1478–1487, 2012.
- [53] E. Chow and J. Gooding, "Peptide modified electrodes as electrochemical metal ion sensors," *Electroanalysis*, vol. 18, no. 15, pp. 1437–1448, 2006.
- [54] K. Paramasivam, Y. Shen, J. Yuan, I. Waheed, C. Mao, and X. Zhou, "Advances in the development of phage-based probes for detection of bio-species," *Biosensors*, vol. 12, no. 1, 2022.
- [55] C. Wu, *Hybrid colloidal molecules from self-assembly of viral rod-like particles*. PhD thesis, Université de Bordeaux, 2018.
- [56] G. Å. Løset, N. Roos, B. Bogen, and I. Sandlie, "Expanding the versatility of phage display II: Improved affinity selection of folded domains on protein VII and IX of the filamentous phage," *PLoS One.*, vol. 6, no. 2, p. e17433, 2011.
- [57] C. Gao, S. Mao, G. Kaufmann, P. Wirsching, R. A. Lerner, and K. D. Janda, "A method for the generation of combinatorial antibody libraries using pIX phage display," *Proceedings of the National Academy of Sciences*, vol. 99, no. 20, pp. 12612–12616, 2002.

- [58] L. G. Caro and M. Schnös, “The attachment of the male-specific bacteriophage F1 to sensitive strains of *Escherichia coli*,” *Proceedings of the National Academy of Sciences of the United States of America*, vol. 56, no. 1, p. 126, 1966.
- [59] W.-J. Chung, D.-Y. Lee, and S. Y. Yoo, “Chemical modulation of M13 bacteriophage and its functional opportunities for nanomedicine,” *International journal of nanomedicine*, vol. 9, p. 5825, 2014.
- [60] A. B. Petrova, C. Herold, and E. P. Petrov, “Conformations and membrane-driven self-organization of rodlike fd virus particles on freestanding lipid membranes,” *Soft Matter*, vol. 13, pp. 7172–7187, 2017.
- [61] J. Rakonjac, N. J. Bennett, J. Spagnuolo, D. Gagic, and M. Russel, “Filamentous bacteriophage: Biology, phage display and nanotechnology applications,” *Current Issues in Molecular Biology*, vol. 13, no. 2, pp. 51–76, 2011.
- [62] K. Zimmermann, H. Hagedorn, C. C. Heuck, M. Hinrichsen, and H. Ludwig, “The ionic properties of the filamentous bacteriophages pf1 and fd,” *Journal of Biological Chemistry*, vol. 261, no. 4, pp. 1653–1655, 1986.
- [63] A. S. Khalil, J. M. Ferrer, R. R. Brau, S. T. Kottmann, C. J. Noren, M. J. Lang, and A. M. Belcher, “Single M13 bacteriophage tethering and stretching,” *Proceedings of the National Academy of Sciences*, vol. 104, no. 12, pp. 4892–4897, 2007.
- [64] L. Song, U.-S. Kim, J. Wilcoxon, and J. M. Schurr, “Dynamic light scattering from weakly bending rods: Estimation of the dynamic bending rigidity of the M13 virus,” *Biopolymers: Original Research on Biomolecules*, vol. 31, no. 5, pp. 547–567, 1991.
- [65] E. Barry, D. Beller, and Z. Dogic, “A model liquid crystalline system based on rodlike viruses with variable chirality and persistence length,” *Soft Matter*, vol. 5, pp. 2563–2570, 2009.
- [66] Y. A. Wang, X. Yu, S. Overman, M. Tsuboi, G. J. Thomas Jr, and E. H. Egelman, “The structure of a filamentous bacteriophage,” *Journal of molecular biology*, vol. 361, no. 2, pp. 209–215, 2006.
- [67] D. Boal and D. H. Boal, *Mechanics of the Cell*. Cambridge University Press, 2012.
- [68] B. Gibb, P. Hyman, and C. L. Schneider, “The many applications of engineered bacteriophages—An overview,” *Pharmaceuticals*, vol. 14, no. 7, p. 634, 2021.
- [69] J. C. Lessard, “Chapter seven - Molecular cloning,” in *Laboratory Methods in Enzymology: DNA*, vol. 529 of *Methods in Enzymology*, pp. 85–98, Academic Press, 2013.

- [70] N. Bhagavan, "Chapter 23 - Nucleic acid structure and properties of DNA," in *Medical Biochemistry*, pp. 521–543, San Diego: Academic Press, fourth edition ed., 2002.
- [71] C. R. Sanders, "Biomolecular ligand-receptor binding studies: Theory, practice, and analysis," *Nashville: Vanderbilt University*, pp. 1–43, 2010.
- [72] T. Ngo-Duc, Z. Alibay, J. Plank, J. Cheeney, and E. Haberer, "Gold-decorated M13 I-forms and S-forms for targeted photothermal lysis of bacteria," *ACS Appl Mater Interfaces.*, vol. 12, no. 1, p. 126–134, 2020.
- [73] D. Lee, H. Park, K. Koo, J. Lee, Y. Nam, W. Lee, and M. Yang, "Gold binding peptide identified from microfluidic biopanning: An experimental and molecular dynamics study," *Langmuir*, vol. 35, no. 2, pp. 522–528, 2019.
- [74] R. A. Blaik, E. Lan, Y. Huang, and B. Dunn, "Gold-coated M13 bacteriophage as a template for glucose oxidase biofuel cells with direct electron transfer," *ACS Nano*, vol. 10, no. 1, p. 324–332, 2015.
- [75] G. T. Hermanson, *Bioconjugate Techniques*. Academic Press, 2 ed., 2008.
- [76] Y. Xue, X. Li, H. Li, and W. Zhang, "Quantifying thiol–gold interactions towards the efficient strength control," *Nature Communications*, no. 5, p. 4348, 2014.
- [77] H. Grönbeck, A. Curioni, and W. Andreoni, "Thiols and disulfides on the Au(111) surface: The headgroup-gold interaction," *J. Am. Chem. Soc.*, vol. 122, pp. 3839–3842, 2000.
- [78] C. Wiedemann, A. Kumar, A. Lang, and O. Ohlenschläger, "Cysteines and disulfide bonds as structure-forming units: Insights from different domains of life and the potential for characterization by NMR," *Frontiers in Chemistry*, vol. 8, 2020.
- [79] W. Srila and M. Yamabhai, "Identification of amino acid residues responsible for the binding to anti-FLAG™ M2 antibody using a phage display combinatorial peptide library," *Appl. Biochem. Biotechnol.*, vol. 171, no. 3, pp. 583–9, 2013.
- [80] H. Kabayama, M. Takeuchi, N. Tokushige, S.-i. Muramatsu, M. Kabayama, M. Fukuda, Y. Yamada, and K. Mikoshiba, "An ultra-stable cytoplasmic antibody engineered for in vivo applications," *Nature Communications*, vol. 11, p. 336, 2020.
- [81] J. X. Huang, S. L. Bishop-Hurley, and M. A. Cooper, "Development of anti-infectives using phage display: Biological agents against bacteria, viruses, and parasites," *Antimicrobial Agents and Chemotherapy*, vol. 56, no. 9, pp. 4569–4582, 2012.
- [82] F. Karlsson, C. A. K. Borrebaeck, N. Nilsson, and A.-C. Malmberg-Hager, "The mechanism of bacterial infection by filamentous phages involves molecular interactions

- between TolA and phage protein 3 domains,” *Journal of Bacteriology*, vol. 185, no. 8, pp. 2628–2634, 2003.
- [83] T. Meyer and K. Geider, “Enzymatic synthesis of bacteriophage fd viral DNA,” *Nature*, vol. 296, no. 5860, pp. 828–32, 1982.
- [84] S. A. Berkowitz and L. A. Day, “Mass, length, composition and structure of the filamentous bacterial virus fd,” *Journal of Molecular Biology*, vol. 102, no. 3, pp. 531–547, 1976.
- [85] J. Buitenhuis, “Electrophoresis of fd-virus particles: Experiments and an analysis of the effect of finite rod lengths,” *Langmuir*, vol. 28, no. 37, pp. 13354–13363, 2012.
- [86] A. Repula, M. Oshima Menegon, C. Wu, P. van der Schoot, and E. Grelet, “Directing liquid crystalline self-organization of rodlike particles through tunable attractive single tips,” *Phys. Rev. Lett.*, vol. 122, p. 128008, 2019.
- [87] N. Raval, R. Maheshwari, D. Kalyane, S. R. Youngren-Ortiz, M. B. Chougule, and R. K. Tekade, “Chapter 10 - Importance of physicochemical characterization of nanoparticles in pharmaceutical product development,” in *Basic Fundamentals of Drug Delivery*, Advances in Pharmaceutical Product Development and Research, pp. 369–400, Academic Press, 2019.
- [88] T. Hendel, M. Wuthschick, F. Kettemann, A. Birnbaum, K. Rademann, and J. Polte, “In situ determination of colloidal gold concentrations with UV-Vis spectroscopy: Limitations and perspectives,” *Anal. Chem.*, vol. 86, no. 22, p. 11115–11124, 2014.
- [89] T. Ahmad, “Reviewing the tannic acid mediated synthesis of metal nanoparticles,” *Journal of Nanotechnology*, vol. 2014, 2014.
- [90] B. Contreras-Trigo, V. Díaz-García, E. Guzmán-Gutierrez, I. Sanhueza, P. Coelho, S. E. Godoy, S. Torres, and P. Oyarzún, “Slight pH fluctuations in the gold nanoparticle synthesis process influence the performance of the citrate reduction method,” *Sensors*, vol. 18, no. 7, p. 2246, 2018.
- [91] S. Bhattacharjee, “DLS and zeta potential – What they are and what they are not?,” *Journal of Controlled Release*, vol. 235, pp. 337–351, 2016.
- [92] C. A. Price, *Centrifugation in density gradients*. Academic Press, 2014.
- [93] Z. Dogic, A. Philipse, S. Fraden, and J. Dhont, “Concentration-dependent sedimentation of colloidal rods,” *J. Chem. Phys.*, vol. 113, no. 18, pp. 8368–8380, 2000.

- [94] W. O. Salivar, H. Tzagoloff, and D. Pratt, "Some physical-chemical and biological properties of the rod-shaped coliphage M13," *Virology*, vol. 24, no. 3, pp. 359–371, 1964.
- [95] A. Fernandez-Nieves and A. Manuel Puertas, *Fluids, Colloids and Soft Materials: An Introduction to Soft Matter Physics*. John Wiley & Sons, Inc., 2016.
- [96] S. W. Shin, J. S. Yuk, S. H. Chun, Y. T. Lim, and S. H. Um, "Hybrid material of structural DNA with inorganic compound: Synthesis, applications, and perspective," *Nano Convergence*, vol. 7, no. 2, 2020.
- [97] N. Geerts and E. Eiser, "DNA-functionalized colloids: Physical properties and applications," *Soft Matter*, vol. 6, no. 19, pp. 4647–4660, 2010.
- [98] X. Ma, A. Jannasch, U.-R. Albrecht, K. Hahn, A. Miguel-López, E. Schäffer, and S. Sánchez, "Enzyme-powered hollow mesoporous Janus nanomotors," *Nano Lett.*, vol. 15, no. 10, pp. 7043–7050, 2015.
- [99] D. G. Shchukin, G. B. Sukhorukov, and H. Möhwald, "Smart inorganic/organic nanocomposite hollow microcapsules," *Angewandte Chemie*, vol. 115, no. 37, pp. 4610–4613, 2003.
- [100] t. Duguet, C. Hubert, C. Chomette, A. Perro, and S. Ravaine, "Patchy colloidal particles for programmed self-assembly," *Comptes Rendus Chimie*, vol. 19, no. 1, pp. 173–182, 2016. Emerging Chemistry in France.
- [101] T. Patino, A. Porchetta, A. Jannasch, A. Lladó, T. Stumpp, E. Schäffer, F. Ricci, and S. Sánchez, "Self-sensing enzyme-powered micromotors equipped with pH-responsive DNA nanoswitches," *Nano Lett.*, vol. 19, no. 6, pp. 3440–3447, 2019.
- [102] B. J. Berne and R. Pecora, *Dynamic light scattering. With applications to chemistry, biology, and physics*. Courier Corporation, 2000.
- [103] S. Wolfgang, *Light Scattering from Polymer Solutions and Nanoparticle Dispersions*. Springer, 2007.
- [104] M. Tolan and M. Tolan, *X-ray scattering from soft-matter thin films: Materials science and basic research*, vol. 148. Springer, 1999.
- [105] S. Inoué and K. R. Spring, *Video Microscopy. The fundamentals*. No. 1, New York : Plenum Press, 1997.
- [106] H. Shen, L. Tauzin, R. Baiyasi, W. Wang, N. Moringo, B. Shuang, and C. Landes, "Single particle tracking: From theory to biophysical applications," *Chem. Rev.*, vol. 117, no. 11, pp. 7331–7376, 2017.

- [107] M. J. Saxton, “Single-particle tracking: Connecting the dots,” *Nature Methods*, vol. 5, p. 671–672, 2008.
- [108] Z. Ye, X. Wang, and L. Xiao, “Single-particle tracking with scattering-based optical microscopy,” *Anal. Chem.*, vol. 91, no. 24, p. 15327–15334, 2019.
- [109] M. Wiklund, H. Brismara, and B. Önfelta, “Acoustofluidics 18: Microscopy for acoustofluidic micro-devices,” *Lab on a Chip*, vol. 12, pp. 3221–3234, 2012.
- [110] M. Hu, C. Novo, A. Funston, H. Wang, H. Staleva, S. Zou, P. Mulvaney, Y. Xia, and G. V. Hartland, “Dark-field microscopy studies of single metal nanoparticles: Understanding the factors that influence the linewidth of the localized surface plasmon resonance,” *J. Mater. Chem.*, vol. 18, no. 17, pp. 1949–1960, 2008.
- [111] J. C. Crocker and D. G. Grier, “Methods of digital video microscopy for colloidal studies,” *Journal of Colloid and Interface Science*, vol. 179, no. 1, pp. 298–310, 1996.
- [112] M. P. Lettinga, L. Alvarez, O. Korculanin, and E. Grelet, “When bigger is faster: A self-Van Hove analysis of the enhanced self-diffusion of non-commensurate guest particles in smectics,” *J. Chem. Phys.*, vol. 154, no. 20, p. 204901, 2021.
- [113] L. Alvarez, M. P. Lettinga, and E. Grelet, “Fast diffusion of long guest rods in a lamellar phase of short host particles,” *Phys. Rev. Lett.*, vol. 118, p. 178002, 2017.
- [114] J. R. Howse, R. A. L. Jones, A. J. Ryan, T. Gough, R. Vafabakhsh, and R. Golestanian, “Self-motile colloidal particles: From directed propulsion to random walk,” *Phys. Rev. Lett.*, vol. 99, p. 048102, 2007.
- [115] F. C. MacKintosh, “Active diffusion: The erratic dance of chromosomal loci,” *Proceedings of the National Academy of Sciences*, vol. 109, no. 19, pp. 7138–7139, 2012.
- [116] F. Novotný and M. Pumera, “Nanomotor tracking experiments at the edge of reproducibility,” *Scientific reports*, vol. 9, no. 1, pp. 1–11, 2019.
- [117] A. Volk and C. J. Kähler, “Density model for aqueous glycerol solutions,” *Experiments in Fluids*, vol. 59, no. 5, pp. 1–4, 2018.
- [118] J. Stetefeld, S. A. McKenna, and T. R. Patel, “Dynamic light scattering: A practical guide and applications in biomedical sciences,” *Biophys. Rev.*, vol. 8, pp. 409–427, 2016.
- [119] K. Shätzel, “Light scattering - Diagnostic methods for colloidal dispersions,” *Advances in Colloid and Interface Science*, no. 46, pp. 309–332, 1993.

- [120] W. Burchard, "Static and dynamic light scattering from branched polymers and biopolymers," in *Light Scattering from Polymers*, (Berlin, Heidelberg), pp. 1–124, Springer Berlin Heidelberg, 1983.
- [121] J. D. Jackson, *Classical Electrodynamics*. John Wiley and Sons, 1999.
- [122] D. I. Svergun and M. H. J. Koch, "Small-angle scattering studies of biological macromolecules in solution," *Reports on Progress in Physics*, vol. 66, no. 10, pp. 1735–1782, 2003.
- [123] P. S. Russo, *Dynamic Light Scattering*, ch. 12. Oxford, 1993.
- [124] D. Lehner, H. Linder, and O. Glatter, "Determination of the translational and rotational diffusion coefficients of rodlike particles using depolarized dynamic light scattering," *Langmuir*, no. 16, pp. 1689–1695, 2000.
- [125] V. Uskoković, "Dynamic light scattering based microelectrophoresis: Main prospects and limitations," *Journal of Dispersion Science and Technology*, vol. 33, no. 12, 2011.
- [126] S.-J. Park and M.-K. Seo, *Chapter 1 - Intermolecular Force*, vol. 18 of *Interface Science and Technology*. Elsevier, 2011.
- [127] D. E. Koppel, "Analysis of macromolecular polydispersity in intensity correlation spectroscopy: The method of cumulants," *J. Chem. Phys.*, vol. 57, p. 4814, 1972.
- [128] B. J. Frisken, "Revisiting the method of cumulants for the analysis of dynamic light-scattering data," *Applied Optics*, vol. 40, no. 24, 2001.
- [129] B. Al-Qadi and T. Saiki, "Optical characterization and rotational dynamics observation of colloidal gold nanorods based on polarized light scattering microscopy," *Japanese Journal of Applied Physics*, vol. 49, no. 12, p. 125001, 210.
- [130] J. Rodríguez-Fernández, J. Pérez-Juste, L. M. Liz-Marzán, and P. R. Lang, "Dynamic light scattering of short Au rods with low aspect ratios," *The Journal of Physical Chemistry C*, vol. 111, no. 13, pp. 5020–5025, 2007.
- [131] I. Ermolina, H. Morgan, N. G. Green, J. J. Milner, and Y. Feldman, "Dielectric spectroscopy of tobacco mosaic virus," *Biochimica et biophysica acta*, vol. 1622, no. 1, pp. 57–63, 2003.
- [132] S. W. Provencher, "Inverse problems in polymer characterization: Direct analysis of polydispersity with photon correlation spectroscopy," *Makromol. Chem.*, vol. 180, pp. 201–209, 1978.

- [133] R. Tadmor, E. Hernández-Zapata, N. Chen, P. Pincus, and J. N. Israelachvili, “Debye length and double-layer forces in polyelectrolyte solutions,” *Macromolecules*, vol. 35, no. 6, pp. 2380–2388, 2002.
- [134] M. H. Rausch, J. Lehmann, A. Leipertz, and A. P. Fröba, “Mutual diffusion in binary mixtures of ionic liquids and molecular liquids by dynamic light scattering (DLS),” *Phys. Chem. Chem. Phys.*, vol. 13, no. 20, pp. 9525–9533, 2011.
- [135] V. P. Ananikov, “Organic–inorganic Hybrid Nanomaterials,” *Nanomaterials*, vol. 9, 2019.
- [136] T. Sawada, “Filamentous virus-based soft materials based on controlled assembly through liquid crystalline formation,” *Polymer Journal*, vol. 49, no. 9, pp. 639–647, 2017.
- [137] J. Wilcoxon and J. M. Schurr, “Dynamic light scattering from thin rigid rods: Anisotropy of translational diffusion of tobacco mosaic virus,” *Biopolymers*, vol. 22, no. 3, pp. 849–867, 1983.
- [138] J. Newman, H. Swinney, and L. Day, “Hydrodynamic properties and structure of fd virus,” *Journal of Molecular Biology*, vol. 116, no. 3, pp. 593–603, 1977.
- [139] J. F. Maguire, “Rotational dynamics of rigid rods. A dynamic light-scattering study,” *J. Chem. Soc., Faraday Trans. 2*, vol. 77, pp. 513–518, 1981.
- [140] S. Benson, J. Bamford, D. Bamford, and R. Burnett, “The X-ray crystal structure of P3, the major coat protein of the lipid-containing bacteriophage PRD1, at 1.65 Å resolution,” *Acta Crystallogr D Biol Crystallogr*, vol. 58, pp. 39–59, 2002.
- [141] L. R. Stingaciu, O. Ivanova, M. Ohl, R. Biehl, and D. Richter, “Fast antibody fragment motion: Flexible linkers act as entropic spring,” *Scientific reports*, vol. 6, no. 1, pp. 1–13, 2016.
- [142] G. E. Uhlenbeck and L. S. Ornstein, “On the theory of the Brownian motion,” *Physical Review*, vol. 36, no. 5, p. 823, 1930.
- [143] G. R. Kneller, “Quasielastic neutron scattering and relaxation processes in proteins: Analytical and simulation-based models,” *Phys. Chem. Chem. Phys.*, vol. 7, no. 13, pp. 2641–2655, 2005.
- [144] J. Lubkowski, F. Hennecke, A. Plückthun, and A. Wlodawer, “The structural basis of phage display elucidated by the crystal structure of the N-terminal domains of g3p,” *Nature structural biology*, vol. 5, no. 2, pp. 140–147, 1998.
- [145] T. J. Henry and D. Pratt, “The proteins of bacteriophage M13,” *Proceedings of the National Academy of Sciences*, vol. 62, no. 3, pp. 800–807, 1969.

- [146] R. Kubo, “The fluctuation-dissipation theorem,” *Reports on Progress in Physics*, vol. 29, no. 1, pp. 255–284, 1966.
- [147] C. Bechinger, R. Di Leonardo, H. Löwen, C. Reichhardt, G. Volpe, and G. Volpe, “Active particles in complex and crowded environments,” *Rev. Mod. Phys.*, vol. 88, p. 045006, 2016.
- [148] V. A. Vladimirov, M. S. C. Wu, T. J. Pedley, P. V. Denissenko, and S. G. Zakhidova, “Measurement of cell velocity distributions in populations of motile algae,” *Journal of Experimental Biology*, vol. 207, no. 7, pp. 1203–1216, 2004.
- [149] P. Thyberg and R. Rigler, “Rotational and translational motions of human spermatozoa: Angle dependence of dynamic laser light scattering,” *Eur. Biophys. J.*, vol. 23, p. 21–27, 1994.
- [150] L. K. Fritz-Laylin, “The evolution of animal cell motility,” *Current Biology*, vol. 30, no. 10, pp. R477–R482, 2020.
- [151] M. S. Kumar and P. Philominathan, “The physics of flagellar motion of *E. coli* during chemotaxis,” *Biophys. Rev.*, vol. 2, no. 1, pp. 13–20, 2010.
- [152] J. Gachelin, A. Rousselet, A. Lindner, and E. Clement, “Collective motion in an active suspension of *Escherichia coli* bacteria,” *New Journal of Physics*, vol. 16, no. 2, p. 025003, 2014.
- [153] G. S. Redner, M. F. Hagan, and A. Baskaran, “Structure and dynamics of a phase-separating active colloidal fluid,” *Phys. Rev. Lett.*, vol. 110, p. 055701, 2013.
- [154] J. U. Klamser, S. C. Kapfer, and W. Krauth, “Thermodynamic phases in two-dimensional active matter,” *Nature Communications*, vol. 9, p. 5045, 2018.
- [155] P. Degen, “Self-propelling capsules as artificial microswimmers,” *Current Opinion in Colloid & Interface Science*, vol. 19, pp. 611–619, 2014.
- [156] S. Campuzano, D. Kagan, J. Orozco, and J. Wang, “Motion-driven sensing and biosensing using electrochemically propelled nanomotors,” *Analyst*, vol. 136, pp. 4621–4630, 2011.
- [157] E. Karshalev, Y. Zhang, B. Esteban-Fernández de Ávila, M. Beltrán-Gastélum, Y. Chen, R. Mundaca-Urbe, F. Zhang, B. Nguyen, Y. Tong, R. H. Fang, L. Zhang, and J. Wang, “Micromotors for active delivery of minerals toward the treatment of iron deficiency anemia,” *Nano Lett.*, vol. 19, no. 11, pp. 7816–7826, 2019.
- [158] J. Zhang, E. Luijten, B. A. Grzybowski, and S. Granick, “Active colloids with collective mobility status and research opportunities,” *Chem. Soc. Rev.*, vol. 46, pp. 5551–5569, 2017.

- [159] L. K. Abdelmohsen, F. Peng, Y. Tu, and D. A. Wilson, “Micro-and nano-motors for biomedical applications,” *Journal of Materials Chemistry B*, vol. 2, no. 17, pp. 2395–2408, 2014.
- [160] F. Matthäus, M. Jagodič, and J. Dobnikar, “E. coli superdiffusion and chemotaxis–search strategy, precision, and motility,” *Biophysical Journal*, vol. 97, no. 4, pp. 946–957, 2009.
- [161] J. B. Kirkegaard and R. E. Goldstein, “The role of tumbling frequency and persistence in optimal run-and-tumble chemotaxis,” *IMA Journal of Applied Mathematics*, vol. 83, no. 4, pp. 700–719, 2018.
- [162] M. D. Egbert, X. E. Barandiaran, and E. A. Di Paolo, “A minimal model of metabolism-based chemotaxis,” *PLoS Computational Biology*, vol. 6, no. 12, p. 1001004, 2016.
- [163] E. M. Purcell, “Life at low Reynolds number,” *American Journal of Physics*, vol. 45, no. 1, pp. 3–11, 1977.
- [164] E. Lauga, “Life around the scallop theorem,” *Soft Matter*, vol. 7, pp. 3060–3065, 2011.
- [165] D. Pantarotto, W. R. Browne, and B. L. Feringa, “Autonomous propulsion of carbon nanotubes powered by a multienzyme ensemble,” *Chem. Commun.*, pp. 1533–1535, 2008.
- [166] X. Ma, A. C. Hortelao, A. Miguel-López, and S. Sánchez, “Bubble-free propulsion of ultrasmall tubular nanojets powered by biocatalytic reactions,” *J. Am. Chem. Soc.*, vol. 138, no. 42, pp. 13782–13785, 2016.
- [167] Z. Fattah, G. Loget, V. Lapeyre, P. Garrigue, C. Warakulwit, J. Limtrakul, L. Bouffier, and A. Kuhn, “Straightforward single-step generation of microswimmers by bipolar electrochemistry,” *Electrochimica Acta*, vol. 56, no. 28, pp. 10562–10566, 2011.
- [168] T.-C. Lee, M. Alarcón-Correa, C. Miksch, K. Hahn, J. G. Gibbs, and P. Fischer, “Self-propelling nanomotors in the presence of strong Brownian forces,” *Nano Lett.*, vol. 14, no. 5, p. 2407–2412, 2014.
- [169] H.-R. Jiang, N. Yoshinaga, and M. Sano, “Active motion of a Janus particle by self-thermophoresis in a defocused laser beam,” *Phys. Rev. Lett.*, vol. 105, p. 268302, 2010.
- [170] Q. Wang, R. Dong, C. Wang, S. Xu, D. Chen, Y. Liang, B. Ren, W. Gao, and Y. Cai, “Glucose-fueled micromotors with highly efficient visible-light photocatalytic propulsion,” *ACS Appl. Mater. Interfaces*, vol. 11, no. 6, p. 6201–6207, 2019.

- [171] D. Rings, M. Selmke, F. Cichos, and K. Kroy, "Theory of hot Brownian motion," *Soft Matter*, vol. 7, pp. 3441–3452, 2011.
- [172] G. G. Stokes, "On the effect of the internal friction of fluids on the motion of pendulums," *Transactions of the Cambridge Philosophical Society*, vol. 9, p. 8, 1851.
- [173] O. Otto, F. Czerwinski, J. L. Gornall, G. Stober, L. B. Oddershede, R. Seidel, and U. F. Keyser, "Real-time particle tracking at 10,000 fps using optical fiber illumination," *Opt. Express*, vol. 18, pp. 22722–22733, Oct 2010.
- [174] P. A. Hassan, S. Rana, and G. Verma, "Making sense of Brownian motion: Colloid characterization by dynamic light scattering," *Langmuir*, vol. 31, no. 1, pp. 3–12, 2015.
- [175] V. Amendola, R. Pilot, M. Frasconi, O. M. Maragò, and M. A. Iatì, "Surface plasmon resonance in gold nanoparticles: A review," *Journal of Physics: Condensed Matter*, vol. 29, no. 20, p. 203002, 2017.
- [176] D. Chakraborty, M. V. Gnann, D. Rings, J. Glaser, F. Otto, F. Cichos, and K. Kroy, "Generalised Einstein relation for hot Brownian motion," *EPL (Europhysics Letters)*, vol. 96, no. 6, p. 60009, 2011.
- [177] D. Rings, R. Schachoff, M. Selmke, F. Cichos, and K. Kroy, "Hot Brownian motion," *Phys. Rev. Lett.*, vol. 105, p. 090604, 2010.
- [178] G. Tammann and W. Hesse, "Die abhängigkeit der viscosität von der temperatur bie unterkühlten flüssigkeiten," *Zeitschrift für anorganische und allgemeine Chemie*, vol. 156, no. 1, pp. 245–257, 1926.
- [179] L. Jauffred, A. Samadi, H. Klingberg, P. M. Bendix, and L. B. Oddershede, "Plasmonic heating of nanostructures," *Chemical Reviews*, vol. 119, no. 13, pp. 8087–8130, 2019.
- [180] C. F. Bohren and D. R. Huffman, *Absorption and scattering of light by small particles*. John Wiley & Sons, 2008.
- [181] K. Metwally, S. Mensah, and G. Baffou, "Fluence threshold for photothermal bubble generation using plasmonic nanoparticles," *The Journal of Physical Chemistry C*, vol. 119, no. 51, pp. 28586–28596, 2015.
- [182] R. Schachoff, M. Selmke, A. P. Bregulla, F. Cichos, D. Rings, D. Chakraborty, K. Kroy, K. Günther, A. Henning-Knechtel, E. Sperling, and M. Mertig, "Hot Brownian motion and photophoretic self-propulsion," *The Open-Access Journal for the Basic Principles of Diffusion Theory, Experiment and Application*, 2016.
- [183] N. Castro, D. Constantin, P. Davidson, and B. Abécassis, "Solution self-assembly of plasmonic Janus nanoparticles," *Soft Matter*, vol. 12, no. 48, pp. 9666–9673, 2016.

- [184] W. Schaertl and C. Roos, "Convection and thermodiffusion of colloidal gold tracers by laser light scattering," *Physical Review E*, vol. 60, no. 2, p. 2020, 1999.
- [185] S.-H. Chen and F. R. Hallett, "Determination of motile behaviour of prokaryotic and eukaryotic cells by quasi-elastic light scattering," *Quarterly Reviews of Biophysics*, vol. 15, no. 1, p. 131–222, 1982.
- [186] S. Akhmanov, D. Krindach, A. Migulin, A. Sukhorukov, and R. Khokhlov, "Thermal self-actions of laser beams," *IEEE Journal of Quantum Electronics*, vol. 4, no. 10, pp. 568–575, 1968.
- [187] R. Rusconi, L. Isa, and R. Piazza, "Thermal-lensing measurement of particle thermophoresis in aqueous dispersions," *JOSA B*, vol. 21, no. 3, pp. 605–616, 2004.
- [188] Y. Harada and T. Asakura, "Radiation forces on a dielectric sphere in the Rayleigh scattering regime," *Optics communications*, vol. 124, no. 5-6, pp. 529–541, 1996.
- [189] A. Ashkin, J. M. Dziedzic, J. E. Bjorkholm, and S. Chu, "Observation of a single-beam gradient force optical trap for dielectric particles," *Optics letters*, vol. 11, no. 5, pp. 288–290, 1986.
- [190] Z. Cheng, P. Chaikin, W. Russel, W. Meyer, J. Zhu, R. Rogers, and R. Ottewill, "Phase diagram of hard spheres," *Materials & Design*, vol. 22, no. 7, pp. 529–534, 2001. Materials and Technologies for Space Exploration.
- [191] P. Pusey, W. C. Poon, S. Ilett, and P. Bartlett, "Phase behaviour and structure of colloidal suspensions," *Journal of Physics: Condensed Matter*, vol. 6, no. 23A, p. A29, 1994.
- [192] D. Vlassopoulos and M. Cloitre, "Suspensions of soft colloidal particles," in *Theory and Applications of Colloidal Suspension Rheology*, pp. 227–290, Cambridge University Press Cambridge, 2021.
- [193] D. Vlassopoulos and M. Cloitre, "Bridging the gap between hard and soft colloids," *Soft Matter*, vol. 8, no. 15, pp. 4010–4013, 2012.
- [194] Y.-S. Cho, G.-R. Yi, S.-H. Kim, D. J. Pine, and S.-M. Yang, "Colloidal clusters of microspheres from water-in-oil emulsions," *Chemistry of materials*, vol. 17, no. 20, pp. 5006–5013, 2005.
- [195] L. Gury, M. Gauthier, M. Cloitre, and D. Vlassopoulos, "Colloidal jamming in multiarm star polymer melts," *Macromolecules*, vol. 52, no. 12, pp. 4617–4623, 2019.
- [196] D. Vlassopoulos and M. Cloitre, "Tunable rheology of dense soft deformable colloids," *Current Opinion in Colloid & Interface Science*, vol. 19, no. 6, pp. 561–574, 2014.

- [197] C. Likos, H. Löwen, M. Watzlawek, B. Abbas, O. Jucknischke, J. Allgaier, and D. Richter, “Star polymers viewed as ultrasoft colloidal particles,” *Phys. Rev. Lett.*, vol. 80, no. 20, p. 4450, 1998.
- [198] P. Schratte, “Purification and concentration by ultrafiltration,” in *Protein Purification Protocols*, pp. 101–116, Springer, 2004.
- [199] E. Barry and Z. Dogic, “Entropy driven self-assembly of nonamphiphilic colloidal membranes,” *Proceedings of the National Academy of Sciences*, vol. 107, no. 23, pp. 10348–10353, 2010.
- [200] T. Gibaud, E. Barry, M. J. Zakhary, M. Henglin, A. Ward, Y. Yang, C. Berciu, R. Oldenbourg, M. F. Hagan, D. Nicastrò, *et al.*, “Reconfigurable self-assembly through chiral control of interfacial tension,” *Nature*, vol. 481, no. 7381, pp. 348–351, 2012.
- [201] B. Sung, A. de la Cotte, and E. Grelet, “Chirality-controlled crystallization via screw dislocations,” *Nature communications*, vol. 9, no. 1, pp. 1–7, 2018.
- [202] B. Sung, H. H. Wensink, and E. Grelet, “Depletion-driven morphological transitions in hexagonal crystallites of virus rods,” *Soft Matter*, vol. 15, no. 46, pp. 9520–9527, 2019.
- [203] S. Asakura and F. Oosawa, “On interaction between two bodies immersed in a solution of macromolecules,” *J. Chem. Phys.*, vol. 22, no. 7, pp. 1255–1256, 1954.
- [204] T. Lee, B. Senyuk, R. P. Trivedi, and I. I. Smalyukh, “Optical microscopy of soft matter systems,” *Fluids, Colloids and Soft Materials-An Introduction to Soft Matter Physics*, edited by Alberto Fernandez-Nieves Antonio Manuel Puertas (John Wiley & Sons), pp. 165–185, 2016.
- [205] H. J. Nussbaumer, “The fast fourier transform,” in *Fast Fourier Transform and Convolution Algorithms*, pp. 80–111, Springer, 1981.
- [206] S. Rad, J. Gao, H. J. Meiselman, O. K. Baskurt, and B. Neu, “Depletion of high molecular weight dextran from the red cell surface measured by particle electrophoresis,” *Electrophoresis*, vol. 30, no. 3, pp. 450–456, 2009.
- [207] K. Devanand and J. Selser, “Asymptotic behavior and long-range interactions in aqueous solutions of poly (ethylene oxide),” *Macromolecules*, vol. 24, no. 22, pp. 5943–5947, 1991.
- [208] Z. Dogic and S. Fraden, “Ordered phases of filamentous viruses,” *Current opinion in colloid & interface science*, vol. 11, no. 1, pp. 47–55, 2006.